

**Radar Studies of Natural and Artificial Waves and
Instabilities in the Auroral Ionosphere**

Thesis submitted for the degree of
Doctor of Philosophy
at the University of Leicester

Ranvir Singh Dhillon
Department of Physics and Astronomy
University of Leicester

January 2002

UMI Number: U148975

All rights reserved

INFORMATION TO ALL USERS

The quality of this reproduction is dependent upon the quality of the copy submitted.

In the unlikely event that the author did not send a complete manuscript and there are missing pages, these will be noted. Also, if material had to be removed, a note will indicate the deletion.



UMI U148975

Published by ProQuest LLC 2013. Copyright in the Dissertation held by the Author.
Microform Edition © ProQuest LLC.

All rights reserved. This work is protected against
unauthorized copying under Title 17, United States Code.



ProQuest LLC
789 East Eisenhower Parkway
P.O. Box 1346
Ann Arbor, MI 48106-1346

Radar Studies of Natural and Artificial Waves and Instabilities in the Auroral Ionosphere

Ranvir Dhillon

Abstract

The electron Pedersen conductivity instability (EPCI) was proposed by Dimant and Sudan (1995a, 1995b, 1995c) as an extension to accepted Farley-Buneman instability theory and was predicted to give rise to D-region radar echoes. Theoretical modelling of its growth rate and threshold velocity for varying flow and aspect angles is presented, together with evidence for a two-layer structure where the growth rate is maximised. Backscatter parameters obtained by two coherent radar systems, CUTLASS and STARE, are presented for two case studies where the data are consistent with an electrojet flow whose velocity exceeds the threshold value for EPCI excitation.

Backscatter parameters obtained from artificially generated FAIs for spatial sweeping and preconditioning experiments are also presented. Varying the illumination time of part of the heated patch affects the CUTLASS backscatter power corresponding to that patch. The variation in backscatter over CUTLASS range gates, for a heater beam with varying pointing direction, is shown to agree closely with the expected results obtained by modelling the heater beam intensity. It is shown that the CUTLASS backscatter power, for a given heater power, is dependent upon whether the ionosphere has previously been excited at a higher heater power.

A new longer-lag mode was run on CUTLASS for the October 1999 heating campaign and the ACF decorrelation and backscatter power decay time constants obtained from data collected when this mode was running were different by an order of magnitude. Turbulence characteristics were obtained from the artificial irregularity distribution. These are compared to a study performed by Villain et al. (1996) and the results are consistent with an artificial irregularity distribution that remained correlated for longer times than naturally occurring irregularity distributions.

Acknowledgements

For helping me construct and complete this thesis, special gratitude is reserved for the following:

Professor Stan Cowley, for allowing me to study in the Radio and Space Plasma Physics group;

The Particle Physics and Astronomy Research Council, for providing me with a research grant;

Professor Terry Robinson, for being my supervisor and for providing valuable insight into many areas of physics, including those related to my work;

Professor Mark Lester, for discussions on geophysics and various aspects of football, especially the anxiety-inducing performances of the mighty Leicester City;

Dr Tim Yeoman, for consultation on geophysical matters and radar operations;

Dr Steve Milan, Dr Darren Wright and Dr Jackie Davies, for help with general-purpose geophysics stuff and computing, and for providing miscellaneous information about CUTLASS, EISCAT and the heater;

Dr Paul Eglitis, for telling me all about auto-correlation functions;

Peter Chapman, for technical details regarding CUTLASS and the heater;

Dr Mike Rietveld, for operating the heater;

Professor Sandra Chapman, for supplying the modelling code used to simulate particle trajectories;

Roy Lewallen, for the EZNEC beam-modelling program;

Everyone associated with the operations of CUTLASS, EISCAT and STARE;

The Clarendon, the New Road Inn and the Old Horse, together with assorted other places, for providing alcoholic stress relief when required.

I would also like to thank all other members of the group, both past and present, who I have not acknowledged explicitly, for their valuable contributions and for making this such an interesting place to be. Thank you, everyone!

Lastly, I would like to thank the Almighty God, who has been with me throughout.

Contents

Chapter 1: Introduction to the Solar-Terrestrial Environment

- 1 Overview
- 1.1 The Solar Wind
- 1.2 The Magnetosphere
- 1.3 The Ionosphere
- 1.4 The Auroral Ionosphere and the Electrojet
- 1.5 Ionospheric Plasma Waves and Irregularities
- 1.6 Aims of the Current Study

Chapter 2: Theory of Ionospheric Irregularities

- 2.1 Introduction
- 2.2 The E-region Farley-Buneman Instability (FBI)
- 2.3 The Electron Pedersen Conductivity Instability (EPCI)
 - 2.3.1 Inclusion of Energy Effects and the EPCI
 - 2.3.2 EPCI Expressions Derived from Kinetic Theory
 - 2.3.3 Simplified Fluid Theory Summary of the EPCI
- 2.4 E-region Non-linear Theory
- 2.5 Additional Instabilities in the High Latitude Ionosphere
- 2.6 Radio Wave Propagation and Non-linear Effects in the F-region
- 2.7 The Parametric Decay Instability (PDI) and Other Related Effects
- 2.8 Artificially Generated Field-aligned Irregularities in the F-region
 - 2.8.1 The Thermal Oscillating Two-Stream Instability (TOTSI): Overview
 - 2.8.2 Coupling between Electromagnetic and Electrostatic Waves via Irregularities
 - 2.8.3 Differential Ohmic Heating
 - 2.8.4 Thermal Effects and Density Modifications

- 2.8.5 Growth Rates and Thresholds
- 2.8.6 Comparison of Heating Models
- 2.9 Plasma Turbulence in the Ionosphere
 - 2.9.1 F-region Plasma as a Turbulent Fluid
 - 2.9.2 The Lagrangian Auto-correlation Function
 - 2.9.3 Collective Wave Scattering Theory
- 2.10 Summary

Chapter 3: Review of Natural and Artificial Irregularity Observations

- 3.1 Introduction
- 3.2 E-region Radar Echoes from Naturally Occurring Irregularities
 - 3.2.1 Type I and Type II Signatures
 - 3.2.2 Type III and Type IV Radar Echoes
- 3.3 Possible Observations of the EPCI
 - 3.3.1 Rocket Campaign Measurements
 - 3.3.2 Radar Measurements
- 3.4 Observations of Ionospheric Modification Effects
 - 3.4.1 Observations of Anomalous Absorption
 - 3.4.2 Plasma Lines, Ion Lines and Other Measurements
- 3.5 Measurements of the Radar Backscatter Auto-correlation Function
- 3.6 Summary

Chapter 4: Instrumentation and Experimental Techniques

- 4.1 Introduction
- 4.2 Coherent and Incoherent Radar Scatter
 - 4.2.1 Forward Scatter and Backscatter
 - 4.2.2 Coherent and Incoherent Scatter
- 4.3 The CUTLASS Radar System
 - 4.3.1 CUTLASS Overview

- 4.3.2 The CUTLASS Pulse Sequence
- 4.3.3 Auto-correlation Functions (ACFs)
- 4.3.4 Interferometric Techniques for the
Determination of Altitude
- 4.4 The STARE VHF System
- 4.5 The EISCAT Radar System
 - 4.5.1 EISCAT Overview
 - 4.5.2 EISCAT Measurement Programs
 - 4.5.3 EISCAT Derived Parameters
- 4.6 Ionospheric Modification and the EISCAT Heating
Facility
 - 4.6.1 The Heater Arrays
 - 4.6.2 The Heater Transmitters
 - 4.6.3 Heater Modulation Types
 - 4.6.4 Propagation of Heater Radio Waves
- 4.7 Summary

Chapter 5: Theoretical Calculations of EPCI Characteristics and Wave-induced Diffusion in the E-region

- 5.1 Introduction
- 5.2 Combined FBI and EPCI Characteristics
 - 5.2.1 Predicted Threshold Velocities given by Two
Different Theories
 - 5.2.2 Growth Rate Predictions
 - 5.2.3 Aspect Angle Dependence of the Growth Rate
 - 5.2.4 Comparison between Theoretical Predictions
- 5.3 Chaotic Diffusion in the E-region
 - 5.3.1 Wave-induced Collision Processes
 - 5.3.2 Covariance and Diffusion Results
- 5.4 Summary

Chapter 6: Observations of Naturally Occurring Irregularities in the Lower Ionosphere

- 6.1 Introduction
- 6.2 Physical Processes Responsible for Natural Irregularities in the Lower Ionosphere
- 6.3 The Myopic Campaign Data Set
- 6.4 Radar Echo Characteristics
- 6.5 Two Case Studies of D-region Echo Occurrence
 - 6.5.1 Case Study 1: 22nd November 1997
 - 6.5.2 Simultaneously Collected Finland Data
 - 6.5.3 Comparison of Backscatter Parameters
 - 6.5.4 STARE Data Intervals
- 6.6 Case Study 2: 13th February 1998
- 6.7 Summary of the Case Studies
- 6.8 Attempts to Measure the Convection Electric Field
- 6.9 Summary

Chapter 7: Radar Backscatter from Artificially Generated FAIs

- 7.1 Introduction
- 7.2 Use of CUTLASS and EISCAT
- 7.3 Overview of Spatial Sweeping Experiments
 - 7.3.1 Spatial Sweeping
 - 7.3.2 Modelling of the Heater Beam
 - 7.3.3 CUTLASS Range Gate Profiles of the Heater Beam
 - 7.3.4 Persistent Backscatter Observed at the Centre of the Beam
- 7.4 Preconditioning of the Ionosphere
- 7.5 The CUTLASS Longer-lag Mode and Associated Parameters
 - 7.5.1 Characteristics of Heating Data
 - 7.5.2 The CUTLASS Longer-Lag Mode

Contents

- 7.5.3 Differences between Normal-lag and Longer-lag Data
- 7.5.4 Backscatter Decay Time Constants
- 7.5.5 ACF Decorrelation Time Constants
- 7.5.6 F-region Plasma Treated as a Turbulent Fluid
- 7.6 Summary

Chapter 8: Conclusions and Future Work

- 8.1 Introduction
- 8.2 Present Work Undertaken in this Thesis
 - 8.2.1 Modelling Instability Characteristics and Anomalous Diffusion
 - 8.2.2 D-region Radar Echoes
 - 8.2.3 F-region Radar Echoes
- 8.3 Future Work
 - 8.3.1 Possible Observations of the EPCI
 - 8.3.2 Artificially Generated FAIs

References

Chapter 1

Introduction to the Solar-Terrestrial Environment

1. Overview

The Sun is the main driver of terrestrial surface processes. For instance, from everyday experience, it is known that the Sun provides the ultimate source of energy for biological processes. The Sun is also responsible for effects at higher altitudes, e.g. the weather and associated atmospheric phenomena. At even higher altitudes, the partial plasma that forms the ionosphere is also strongly affected by solar radiation. This thesis describes ionospheric waves, instabilities and other effects that occur at these high altitudes.

1.1 The Solar Wind

The temperature and associated pressure of the Sun's outer atmosphere, the solar corona, is a lot higher than that of interplanetary space. Because of this, the corona expands outwards and the constituent coronal plasma is carried out into space. It travels almost radially outwards at speeds of around $400\text{-}700\text{ km s}^{-1}$ and consists of mainly protons and electrons. The streaming plasma is known as the solar wind and its number density is around 10 particles per cubic centimetre at a distance of 1 astronomical unit (AU) from the Sun. The prevailing plasma conditions may be approximated by assuming an ideal magnetohydrodynamic situation. It follows that the plasma carries the Sun's magnetic field, also known as the interplanetary magnetic field (IMF), with it as it travels away from the Sun. Because the Sun rotates with a period of 27 days, the IMF assumes a spiral configuration known as the Parker spiral and, at a distance of 1 AU, makes an angle of around 45° with the radial direction in the ecliptic plane. The speed of the solar wind depends upon magnetic activity on the Sun, with speeds reaching up to 800 km s^{-1} being observed. In the solar magnetic equatorial plane, a current sheet exists that separates oppositely-directed magnetic field lines, and the orientation of this current sheet with respect to the ecliptic plane varies as the Sun rotates.

The IMF may be characterised by employing a Cartesian coordinate system whose z-direction is taken to describe the North-South component where North has the same sense as that corresponding to terrestrial North, with negative values referring to a southwards

direction. It is mainly this IMF component that is responsible for driving coupling between the solar wind and the magnetosphere-ionosphere system that exists at the Earth.

1.2 The Magnetosphere

The magnetosphere is defined as the region that is controlled by the terrestrial magnetic field and forms a cavity in the travelling solar wind. The boundary of the magnetosphere is termed the magnetopause and separates solar wind plasma from magnetospheric plasma. The size of the magnetosphere is dependent upon fluctuations in the solar wind strength, although the distance to the nose of the magnetopause is of the order of 10 Earth radii (R_E). The flow of the solar wind past the magnetosphere stretches the magnetosphere in the anti-sunwards direction, thus forming the magnetotail, which can stretch to 1000 R_E in length (Villante, 1975). Figure 1.1 shows the Earth's magnetosphere.

Upon its arrival ahead of the Earth, the solar wind is travelling at supersonic velocities. When it encounters the magnetosphere, it is slowed abruptly and a bow shock is formed ahead of the magnetopause, a feature similar to that caused by the flight of a supersonic aircraft through the air.

The nature of the interaction between the IMF and the Earth's field at the magnetopause is determined by the direction of the IMF. If it has a southward component, opposite to the northward-directed terrestrial field, a process known as magnetic reconnection may occur. During magnetic reconnection, the solar wind field lines and the Earth's field lines diffuse across the magnetopause and reconnect with each other, thus changing the field topology and resulting in the IMF being directly coupled to the terrestrial magnetic field. In addition to the coupling of the magnetic fields, reconnection allows the solar wind plasma to enter the magnetosphere. The plasma particles may then travel down the polar cusps and impact the upper atmosphere. If reconnection has occurred, then as the solar wind flows away from the Sun, it drags the Earth's field back with it. This causes the field lines to flow anti-sunwards over the poles. Magnetic flux is conserved by the migration of field lines in a sunwards direction at lower magnetic latitudes. This return flux results from reconnection that occurs in the magnetotail. This cycle of flux migration is known as the Dungey cycle (Dungey, 1961). In addition to the Dungey cycle, rapid reconnection events known as substorms occur in the magnetotail. These allow hot plasma to travel down the magnetic field lines on the nightside into the auroral zones in either hemisphere.

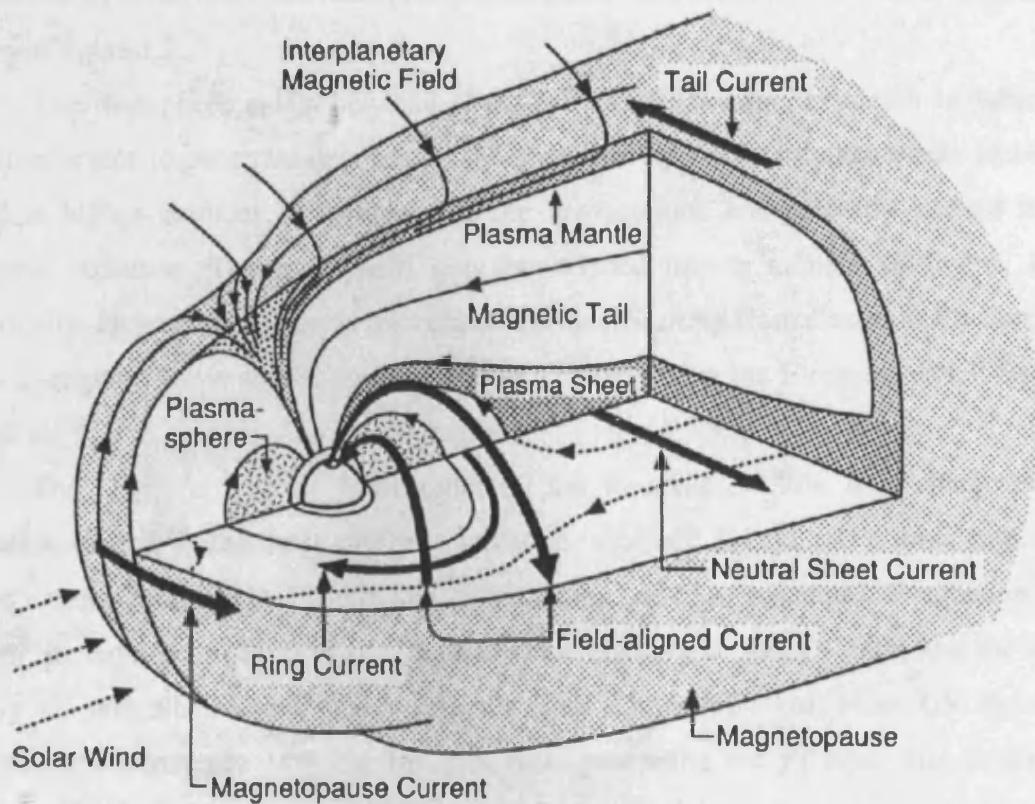


Figure 1.1: The Earth's magnetosphere, the region controlled by the terrestrial magnetic field (Kivelson and Russell, 1995).

1.3 The Ionosphere

The Earth's upper atmosphere is continually bombarded by radiation from the Sun. This radiation contains constituents from a large part of the electromagnetic spectrum, including the high-energy end. This high-energy radiation ionises the upper atmosphere and produces an ionised region known as the ionosphere. It is a very complex region and knowledge of both neutral-gas and plasma dynamics is necessary in order to attempt to understand its behaviour. The ionospheric temperature and electron concentration profiles are shown in figure 1.2.

The ionosphere exists between about 60 and 1000 km. The depth to which solar radiation is able to penetrate depends on the photon energy. Since lighter atoms and ions are found at higher altitudes, it follows that the heavier ions are generally ionised by more energetic radiation. The ionosphere may be divided into a number of layers, labelled historically, each of which has its own characteristics. Starting from closest to the Earth, there is the D-region. Above this is the E-region and above this is the F-region, which forms two layers, the F₁ and F₂ layers, during the daytime.

The D-region extends from about 60 km to about 90 km. It is characterised by ionisation caused by the most energetic radiation, e.g. hard X-rays and cosmic rays. The E-region extends from 90 to 150 km and is formed by softer X-rays and UV radiation. In this region, the daytime electron density profile slope changes at about 110km and the ions are mainly O⁺ and NO⁺. The F-region extends from 150 to 500 km. Most UV radiation is absorbed from between 150 and 180 km, thus generating the F₁ layer that exists in the daytime. The F₁ layer is composed mainly of O⁺ ions and a maximum exists in the electron density profile at about 170 km. The electron density in the F₂ layer is relatively high. This occurs because the rate at which ions are lost decreases with altitude more quickly than the rate at which ions are produced. The densities of ions and electrons in the ionosphere are determined mainly by a balance between production and loss processes, with transport of the plasma constituents assuming a less important role. Transport only becomes an important loss process above the F₂ peak, i.e. the topside ionosphere. Finally, it should be noted that diffusion processes become more important at higher altitudes, as the neutral density decreases.

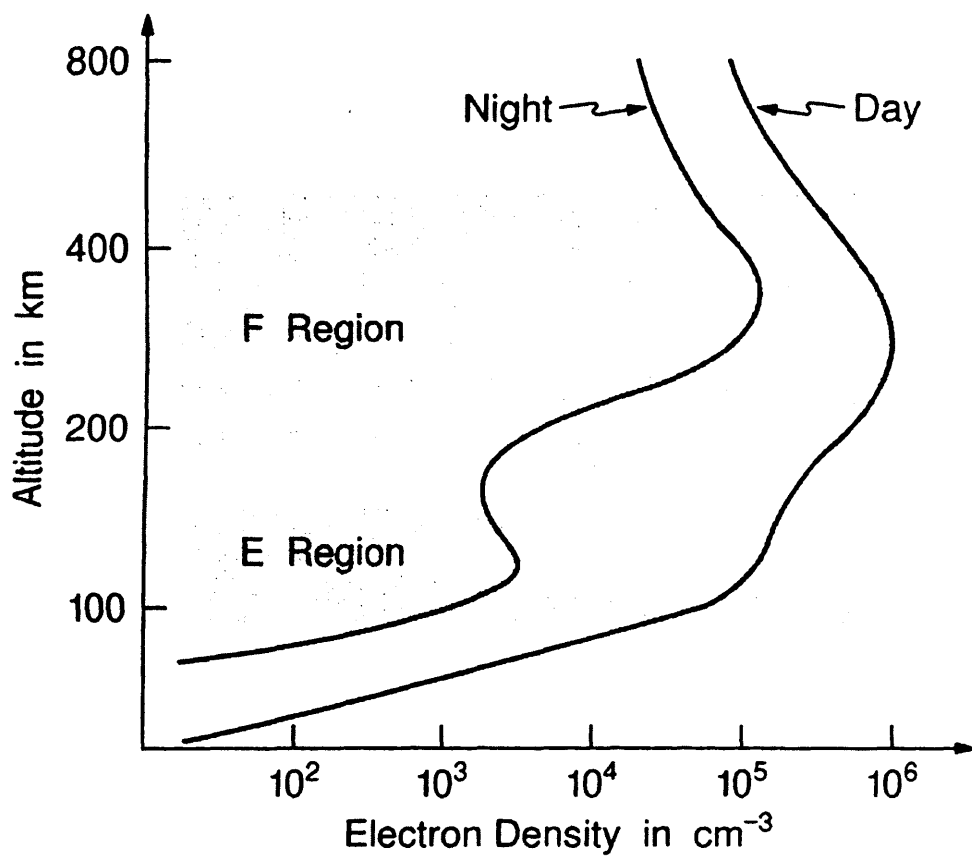


Figure 1.2: The electron concentration in the Earth's ionosphere, showing the E-region and F-region for daytime and night-time conditions (Baumjohann and Treumann, 1997a).

1.4 The Auroral Ionosphere and the Electrojet

At auroral latitudes, the large-scale morphology of ionospheric processes is determined by the interaction between the IMF and the terrestrial magnetic field leading to magnetospheric convection. The convective flow of plasma has an associated electric field, which is able to map down the magnetic field lines into the ionosphere, leading to ionospheric convection. Figure 1.3 shows the equipotential contours of the high-latitude electric field. At F-region altitudes, the gyrofrequencies of ions and electrons are much higher than the corresponding ion-neutral and electron-neutral collision frequencies. Since the guiding centres of moving charged particles are constrained to move with the magnetic field, in the absence of collisions, it follows that both ions and electrons convect with the magnetic field at the $\mathbf{E} \times \mathbf{B}$ drift velocity. Relative motion between ions and neutrals leads to the frictional heating of the ions, which in turn modifies the chemical composition in the F-region through an increase in recombination (e.g. St.-Maurice and Torr, 1978).

In the E-region, the flow of ions is damped due to collisions with neutral particles as the ion-neutral collision frequency is much higher than it is in the F-region. Therefore, although there is a magnetic field present, the ions cannot be guided by it as they collide with neutral particles far too frequently. The ions, therefore, may be considered to be stationary in the frame of the neutrals. The electron-neutral collision frequency, however, is still very small compared to the electron gyrofrequency and the electron flow is not seriously damped by the presence of the neutrals. Therefore, there is strongly damped ion motion and almost completely undamped electron motion. An alternative way to describe this is in terms of ionospheric conductivities in the E-region that arise from the nature of the particle motion. The electron Pedersen conductivity is essentially zero as is the ion Hall conductivity. The electrons can move fairly freely, but the ions cannot. This leads to relative motion between the ions and electrons, i.e. a current, known as the auroral electrojet. It is an electron Hall current and moves at the $\mathbf{E} \times \mathbf{B}$ drift speed. Additional complications arise regarding current closure, but these may be neglected in the present discussion.

The E-region current flow is enhanced by particle precipitation. This causes increased ionisation and helps to maintain the conducting layer through which the electrojet flows. In addition, large convection electric fields in the E-region lead to an increase in the plasma temperature mainly through Joule heating, which through collisions also affects the neutral atmosphere. Another source of the E-region electric field is the forced motion of charged particles across field lines by collisions with neutrals.

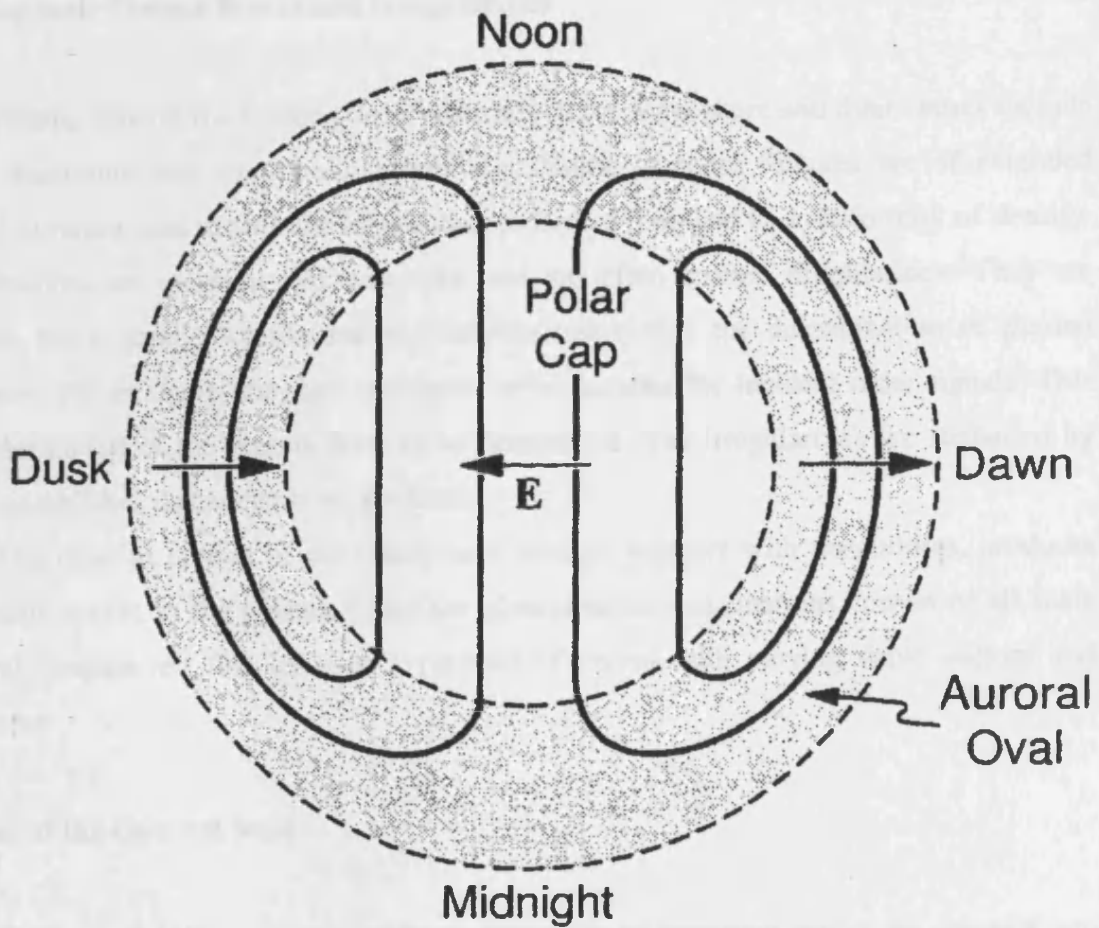


Figure 1.3: The potential contours across the polar cap associated with ionospheric convection, itself driven by magnetospheric convection (Baumjohann and Treumann, 1997a).

The convection electric field may vary quite considerably from one time to another, depending on magnetospheric conditions and the direction of the IMF. Therefore, the associated $E \times B$ drift can be quite different depending on the time of observation. As a final note, it is instructive to note that less than 1% of the atoms in the ionosphere are actually ionised.

1.5 Ionospheric Plasma Waves and Irregularities

Plasma density fluctuations occur naturally in the ionosphere and their causes include thermal variations and ionospheric instabilities. Some of these features are of extended temporal duration, and remain for longer than processes that lead to a uniformity of density. These features are coherent and wave-like and are often termed irregularities. They are important for a number of reasons and their existence aids the determination of plasma parameters. For example, they act as sources of backscatter for incident radar signals. This allows the nature of the plasma flow to be determined. The irregularities are sustained by plasma instabilities that occur in the medium.

The random motion of the ionospheric plasma, together with instabilities, produces electrostatic waves in the plasma. Since the plasma density fluctuations consist of all scale sizes and frequencies, this leads to a plethora of waves with varying wave vectors and frequencies.

1.6 Aims of the Current Study

Plasma instabilities, and their effects, constitute an important part of the research into space plasmas. Many different types of plasma instability exist and this work will concentrate upon only a small subset. There are two types of instability generation mechanism that will be discussed in this thesis: naturally occurring instabilities in the D and E regions of the ionosphere and artificially generated instabilities in the F-region.

Chapter 2 presents the theory behind the instabilities, both natural and artificial, whose effects are described in this work. The first part of the chapter concerns the Farley-Buneman and the electron Pedersen conductivity instabilities that occur in the E-region and D-region, respectively. In reality, both of these instabilities may be described by a single theory, and it will be shown that the decisive factor is the inclusion of terms relating to the Electron Pedersen conductivity. The second part of the chapter describes the theory behind

artificially generated irregularities in the F-region, with the primary driving mechanism being the thermal oscillating two-stream instability. The third part of the chapter, related also to the effects of artificially generated instabilities, concerns the effects of plasma turbulence and how these may be related to the auto-correlation functions associated with coherent backscatter radar measurements.

Chapter 3 presents a review of previous work that has been done on the observations of the instability types whose properties were given in Chapter 2. Both natural and artificial instabilities are considered. Chapter 4 describes the instruments and facilities used to make measurements that relate to field-aligned irregularities in the auroral ionosphere. Chapter 5 presents threshold velocity values and growth rates of D-region and E-region instabilities obtained from the theory given in chapter 2.

The next two chapters present data. Data from the D and E-regions are presented in chapter 6, in order to determine whether the electron Pedersen conductivity instability has been observed and two case studies are presented. Chapter 7 is concerned with the F-region and presents data relating to ionospheric modification. The latter part of the chapter is concerned with turbulence parameters and their determination from radar data.

Chapter 2

Theory of Ionospheric Irregularities

2.1 Introduction

Chapter 1 described the basic processes of solar-terrestrial interactions, with the solar wind driving magnetospheric convection that, via the coupling between the magnetosphere and the ionosphere, also causes ionospheric effects. The work presented in this thesis concerns natural and artificial waves, instabilities, field-aligned irregularities (FAIs) and other associated effects in the ionosphere. Two situations are considered: naturally occurring waves and instabilities in the auroral electrojet and altitudes below it, and artificially generated waves and instabilities in the F-region. This chapter describes the theoretical foundations behind the generation of FAIs in various parts of the ionosphere.

2.2 The E-region Farley-Buneman Instability (FBI)

The plasma in the auroral E-region, at altitude ranges of approximately 95-130 km, consists of magnetised electrons and collisional unmagnetised ions that may be considered to be at rest in the neutral frame. The flow of electrons gives rise to an ionospheric current system, generally taken to flow at altitudes around 110 km called the auroral electrojet. The gradient-drift and Farley-Buneman instabilities occur in this region. The description of E-region instabilities focuses on the Farley-Buneman instability (FBI), also called the modified two-stream instability (MTSI). Electrostatic waves are produced when the relative electron-ion flow speed in the auroral electrojet exceeds a certain threshold value. These waves then produce field-aligned irregularities (FAIs), plasma density inhomogeneities that have a large spatial extent along magnetic field lines, but a comparatively small extent across them. The FBI was proposed, independently, by Farley (1963) and Buneman (1963). Farley's approach used kinetic theory to derive the parameters associated with the instability, whereas Buneman's argument was founded upon fluid theory. Kinetic theory includes more of the important physics but is complex. The use of fluid theory provides simpler equations but its validity is confined to cases where the flowing plasma may be validly considered to be a fluid, i.e. at longer wavelengths and scale sizes where the particulate nature of the plasma may be ignored.

Comprehensive reviews of work on E-region electrojet instabilities were conducted by Fejer and Kelley (1980), Farley (1985) and Haldoupis (1989). The characteristic irregularity properties have been derived using linear theory, which describes a simplified approximation where only the values of parameters at the threshold conditions are considered. It is useful for describing the onset and initial growth of instability mechanisms but cannot be used to describe the stabilisation of instabilities. The later evolution of instabilities requires consideration of non-linear effects that become important when the amplitude of the generated waves becomes large and more complex physical processes must be included.

Instabilities are characterised by their thresholds and growth rates, which are derived by considering the equations of motion. The following derivation is taken from Fejer et al. (1984a) and describes E-region Farley-Buneman and gradient drift instabilities. Both instabilities were described using a unified approach and their properties were obtained by deriving the fluid dispersion relation for electrostatic waves.

The ion and electron continuity and momentum equations are given by

$$\frac{\partial N}{\partial t} + \nabla \cdot (N\mathbf{V}) = Q - \alpha N^2 \quad (2.1)$$

$$m \left(\frac{\partial}{\partial t} + \mathbf{V} \cdot \nabla \right) \mathbf{V} = q(-\nabla\phi + \mathbf{V} \times \mathbf{B}) - \frac{\nabla P}{N} - m\nu\mathbf{V} \quad (2.2)$$

where the operator on the left hand side of equation (2.2) is the convective derivative, which gives the time derivative of a quantity along a particle trajectory in phase space. Also, Poisson's equation is

$$\epsilon_0 \nabla^2 \phi = e(N_e - N_i) \quad (2.3)$$

After linearising these equations, assuming quasi-neutrality and perturbations proportional to $e^{i(\mathbf{k}\cdot\mathbf{r}-\omega t)}$ in the rest frame of the ions, a dispersion relation is obtained. If nearly field-aligned irregularities are assumed, ($k_{\perp} \gg k_{\parallel}$) where \mathbf{k} is the irregularity wave vector and the parallel and perpendicular components refer to directions parallel and perpendicular to the geomagnetic field, then the following dispersion relation results

$$\left[v_i - i \left(\omega - \frac{\Omega_i}{kL_N} \right) \right] (\bar{\omega} - \mathbf{k} \cdot \mathbf{V}_d) + \left\{ \bar{\omega} [\Omega_i^2 + (v_i - i\omega)^2] + ik^2 C_s^2 \left[v_i - i \left(\omega - \frac{\Omega_i}{kL_N} \right) \right] \right\} \left(\frac{\psi}{v_i} - \frac{i}{kL_N \Omega_i} \right) = 0 \quad (2.4)$$

The quantity ψ is defined as

$$\psi = \frac{V_e V_i}{\Omega_e \Omega_i} \left(1 + \frac{\Omega_e^2}{V_e^2} \sin^2 \beta \right) \quad (2.5)$$

and the aspect angle, β , is the angle between the direction perpendicular to the magnetic field and the irregularity wave vector, \mathbf{k} . Here, $\mathbf{V}_d = \mathbf{V}_e - \mathbf{V}_i$ is the relative electron-ion drift velocity and is almost equal to \mathbf{V}_e as $\mathbf{V}_i \approx \mathbf{0}$ in the E-region. In (2.4), ν_e and ν_i are the electron-neutral and ion-neutral collision frequencies, and Ω_e and Ω_i are the electron and ion gyrofrequencies. Also, $\nu_i \gg \Omega_i$, $\Omega_e \gg \nu_e$ and $\mathbf{V}_d \approx \mathbf{E} \times \mathbf{B} / B^2$, i.e. \mathbf{V}_d may be taken as the $\mathbf{E} \times \mathbf{B}$ drift velocity without loss of significant accuracy. Applying these conditions leads to the simplification of the dispersion relation, giving

$$\bar{\omega} - \mathbf{k} \cdot \mathbf{V}_d + \left(\bar{\omega}(\nu_i - i\omega) + ik^2 C_s^2 \right) \left(\frac{\psi}{\nu_i} - \frac{i}{kL_N \Omega_i} \right) = 0 \quad (2.6)$$

and $\bar{\omega}$ is given by

$$\bar{\omega} = \omega + i2\alpha N_0 \quad (2.7)$$

Apart from $\bar{\omega}$, which includes the effects of recombinational damping, this expression is well known, e.g. Sudan et al. (1973), and the fluid theory used to derive it is valid when $\nu_i^2 \gg \omega_r^2$. For smaller wavelengths and/or drift velocities much larger than C_s , kinetic theory is required. The irregularity frequency, ω_r , comes from assuming that $\omega = \omega_r + i\gamma$, where γ is the growth rate, and it is also assumed that $\omega_r \gg \gamma$. Expressions for ω_r and γ are obtained as follows

$$\omega_r = \frac{kV_d \cos \theta}{1 + \psi} = \frac{\mathbf{k} \cdot \mathbf{V}_d}{1 + \psi} \quad (2.8)$$

$$\gamma = \frac{1}{1 + \psi} \left[\frac{\psi}{\nu_i} (\omega^2 - k^2 C_s^2) + \frac{\omega_r \nu_i}{kL_N \Omega_i} \right] - 2\alpha N_0 \quad (2.9)$$

L_N is the electron density gradient scale length, given by

$$L_N = \left(\frac{1}{n_0} \frac{dn_0}{dx} \right)^{-1} \quad (2.10)$$

Also, θ , known as the flow angle, is the angle between \mathbf{k} and \mathbf{V}_d . Finally, C_s is the ion-acoustic speed, given by

$$C_s = \sqrt{\frac{k_B (\gamma_e T_e + \gamma_i T_i)}{m_i}} \quad (2.11)$$

The isothermal case, given by $\gamma_e = \gamma_i = 1$, ignores the effects of temperature gradients, leading to the neglect of terms involving ∇T . This commonly used approach results in important physics, such as energy exchange, being ignored. Gurevich and Karashtin (1984) have analysed temperature perturbations for altitudes in the upper E-region and have concluded that adiabatic compression is the cause. If adiabatic conditions apply then γ_e and γ_i equal 5/3. Kissack et al. (1997) have investigated the effects of electron thermal effects on the threshold phase speed required to excite the instability. This led to the definition of an effective γ_e that described an intermediate state between adiabatic and isothermal conditions. St.-Maurice and Kissack (2000) obtained adiabatic results only when frequencies low enough for heat conduction to be ignored were used.

When density gradients are absent, i.e. $L_N \rightarrow \infty$, the two equations reduce to the standard FBI relationship, leading to a threshold condition given by

$$V_d \cos \theta > C_s (1 + \psi) \quad (2.12)$$

This derivation has shown how FBI waves may arise when the threshold condition given by (2.12) is satisfied and this situation applies for flow along the electrojet. The two derivations of the FBI require separate theories and only Buneman's fluid theory version has been considered here. Robinson and Honary (1990) presented a kinetic theory formulation of the FBI that accounted for non-linear resonance broadening effects. The predictions of this theory on radar observations were also considered.

Apart from the derivation given above, others also exist, e.g. Rogister and D'Angelo (1970) and Kelley (1989). Stubbe (1989) presented a general formulation of E-region electrostatic waves using methods from both fluid theory and kinetic theory. E-region irregularity electric field and density perturbations are illustrated in figure 2.1. Figure 2.1(a) shows the instability mechanism for the FBI for night-time conditions and figure 2.1(b) shows the mechanism for the gradient drift instability for daytime conditions.

2.3 The Electron Pedersen Conductivity Instability (EPCI)

The generally well-accepted theory of the FBI has been discussed in detail in many publications. However, the usual derivation does not include the effects of the electron Pedersen conductivity since its value is negligibly small at E-region altitudes. Upon inclusion of the electron Pedersen conductivity, the effects of the FBI are augmented by the inclusion of D-region irregularities that propagate preferentially in a direction that bisects those of the flow direction and the convection electric field.

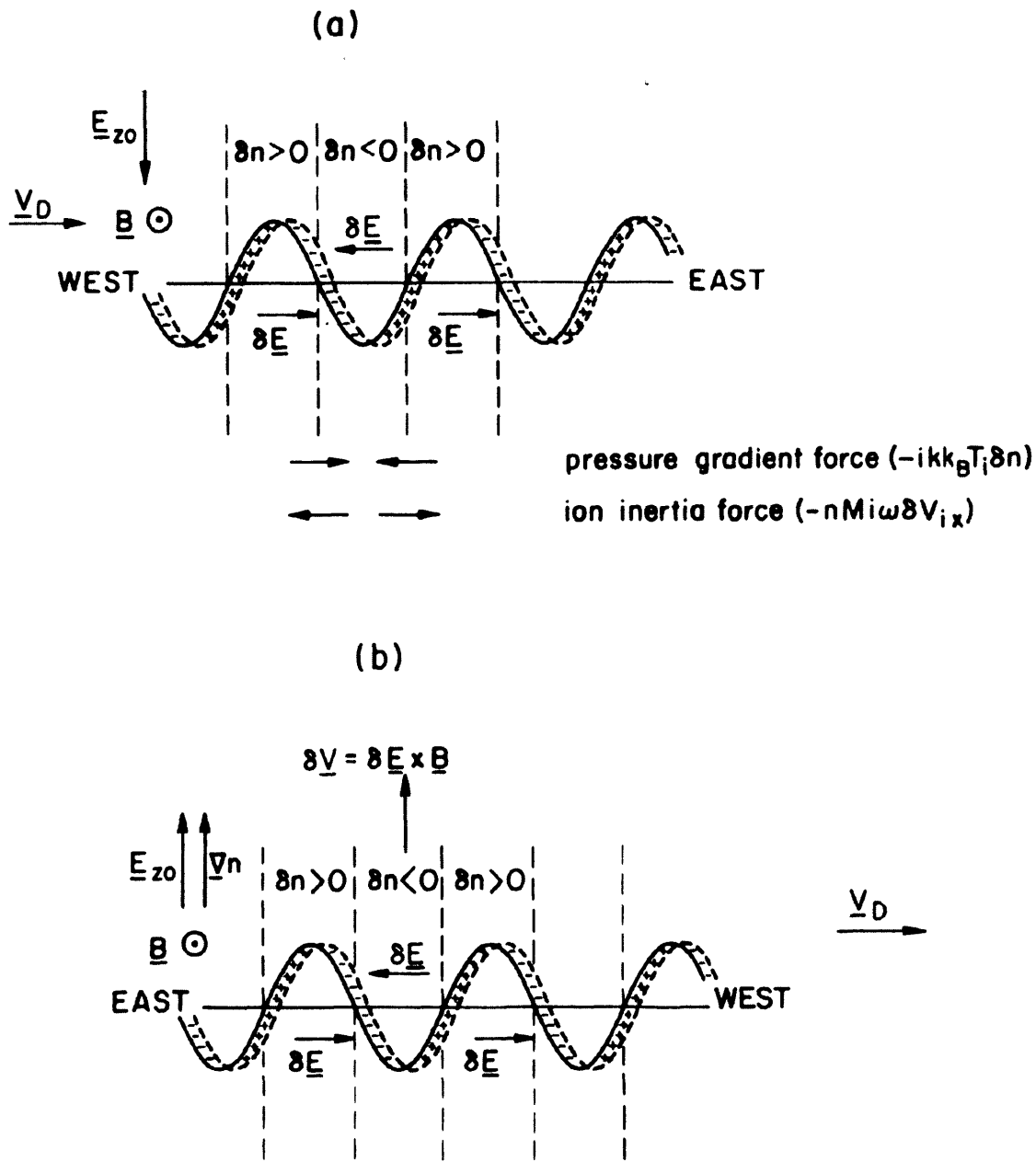


Figure 2.1: The electric field and density perturbations associated with (a) the FBI during night-time conditions and (b) the gradient-drift instability during daytime conditions (Kelley, 1989).

The kinetic theory of the D-region instability was given by Dimant and Sudan (1995a, 1995b and 1995c) but this presentation left the underlying physical processes unclear. Hence, a more physical explanation was later given (Dimant and Sudan, 1997). The new theory predicted a zone of instability centred at the bisector of the convection electric field, E , and the $E \times B$ drift direction, and as for the FBI most effects occur in a plane perpendicular to the terrestrial magnetic field. The waves generated by the instability exceed several metres in length. The novel feature of this instability is that the waves may be excited at altitudes lower than that at which FBI waves are supported, and also where no other low-frequency instabilities may be excited.

2.3.1 Inclusion of Energy Exchange Effects and the EPCI

The conventional FBI is driven by processes associated with the ion inertia. The EPCI is associated with the Ohmic heating of electrons by a perturbed electric field. There are two ways that this gives rise to the instability. Firstly, the sign of the plasma pressure perturbation is opposite to that of the density perturbation. This mechanism depends upon the flow angle, it is stabilising when $k \cdot E$ is positive and destabilising when it is negative. Secondly, the excitation may be caused by thermal perturbations of the electron Pedersen conductivity, due to monotonically increasing temperature dependence of the electron-collision frequency. Thermal perturbations such as these are caused by small secondary temperature modulations that are shifted in phase with respect to the density perturbations and occur as a result of slow $E \times B$ advection of the temperature modulations. This effect always acts to destabilise and is independent of the sign of the flow angle and the threshold drift velocity has two minima near the bisectors between the directions of $\pm E$ and V . The minima are asymmetric because of the first mechanism described above.

The density, δN , and temperature, δT_e , perturbations are illustrated in figure 2.2. N and T_e are positive in the upper half-space and negative in the lower half-space. The temperature and density variations are superimposed on the plane of vectors orthogonal to B and their directions are shown by arrows. Local directions of the perturbation electric field, δE , are shown for adjacent extrema of δN and δT_e . The instability should occur for altitudes from approximately 75-105 km, and is excited most favourably for the case of low-altitude, small phase velocity waves where the electron Pedersen conductivity is large. The upper-D/lower-E regions provide optimal conditions for excitation of the instability, which also generates FAIs. The FBI and this new instability are then described by the same equations,

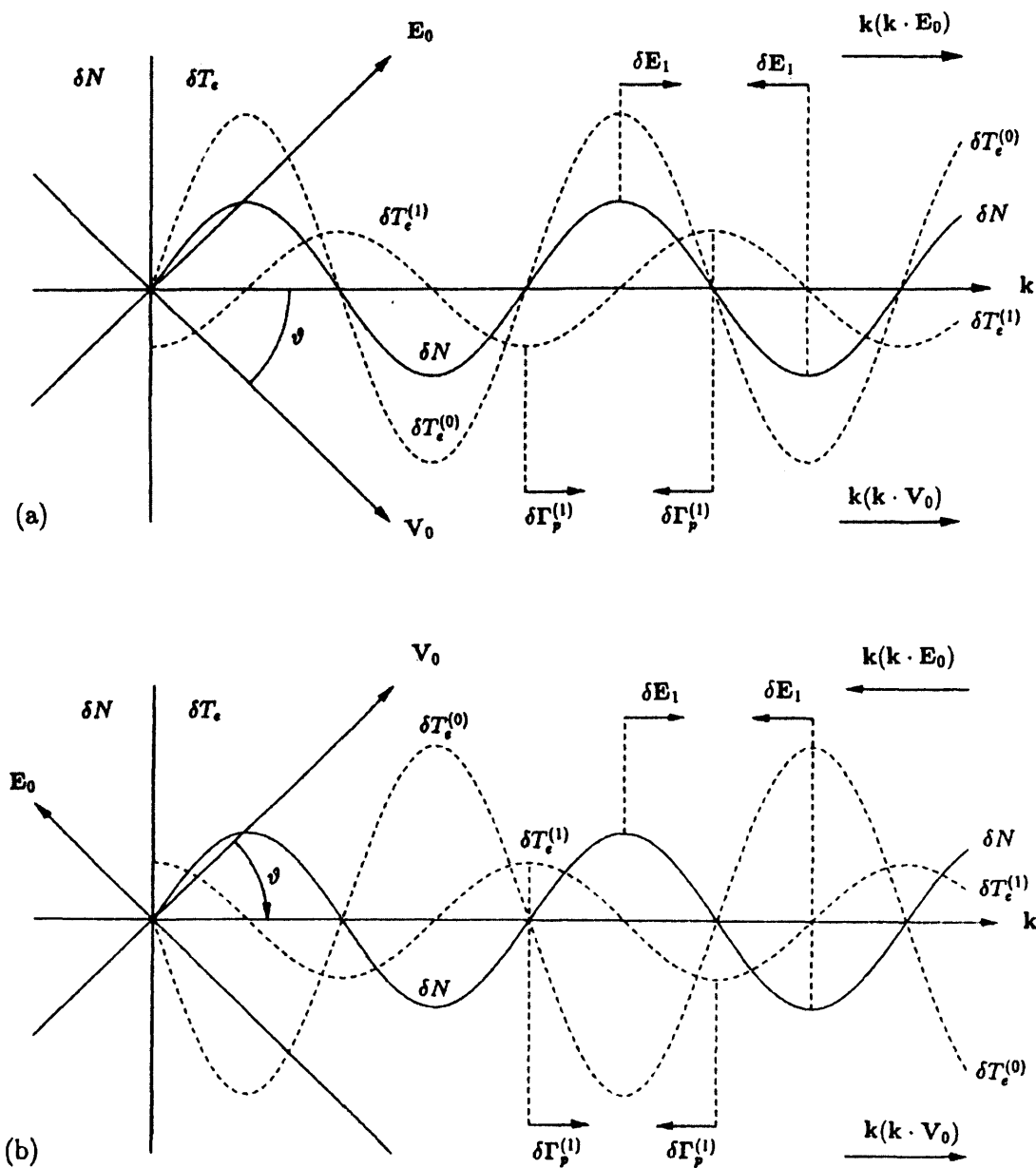


Figure 2.2: The density and field perturbations for a combined theory that incorporates the EPCI (Dimant and Sudan, 1997). The temperature perturbations, δT_e , and density perturbations, δN , are shown in the direction of \mathbf{k} in the wave frame. N and T_e are positive in the upper half-space and negative in the lower half-space. The variations in N and T_e are superimposed on the plane of vectors orthogonal to \mathbf{B} and their directions are shown by arrows. Two cases for (a) positive flow angles and (b) negative flow angles are shown.

and hence are two manifestations of a single instability. However, each case occurs in its own characteristic altitude range and it is still useful to consider the two cases as separate instabilities. This new D-region instability was denoted as the Electron Pedersen Conductivity Instability (EPCI) by Robinson (1998).

2.3.2 EPCI Expressions Derived from Kinetic Theory

Dimant and Sudan (1995c) gave an expression for the growth rate of the instability

$$\gamma \approx \frac{\psi(kv_{Ti})^2}{(1+\psi)^3 v_{in}} \left[\frac{4}{45} \eta^2 \tau^2 + \eta \left(1 - \frac{8}{9} \frac{\tau(1+\psi)}{1+4x/15} \right) - 2(1+\psi)^2 \right] \quad (2.13)$$

where

$$\tau = \rho \tan \theta, \quad \rho = \frac{5v_{in}}{\Omega_e \delta_{en}}, \quad \eta = \left(\frac{V}{v_{Ti}} \right)^2 \cos^2 \theta, \quad x = \frac{k_{\parallel}^2 \Omega_e^2}{k_{\perp}^2 v_{en}^2} \quad (2.14)$$

and V and v_{Ti} correspond to the relative plasma drift velocity and ion thermal velocity respectively. The threshold drift velocity is given by the standard technique of setting the growth rate to zero and then solving for the value of the velocity. The resulting expression is

$$\frac{V}{v_{Ti}} \approx \sqrt{\frac{D + \sqrt{D^2 + (32/45)\rho^2 \tan^2 \theta (1+\psi)^2}}{(8/45)\rho^2 \sin^2 \theta}} \quad (2.15)$$

where

$$D = \frac{8}{9} \rho \tan \theta \frac{1+\psi}{1+4x/15} - 1 \quad (2.16)$$

This expression is valid at all altitudes where the FBI occurs and also takes into account effects at lower altitudes. Dimant and Sudan (1997) simplified their approach to the EPCI, in order to make the physics behind the processes more comprehensible, and to provide more of a physical insight into the processes that occur in the EPCI, which involve an extended energy equation that adds the effects of heat transfer.

2.3.3 Simplified Fluid Theory Summary of the EPCI

Robinson (1998) applied fluid equations to obtain a simplified version of the EPCI that retained the basic features of the instability mechanism. Fluid theory may be applied for long wavelength and low frequency situations given by

$$\omega - \mathbf{k} \cdot \mathbf{V}_e \ll \eta_e \quad (2.17)$$

where ω is the wave frequency, η_e is the inelastic electron-neutral collision frequency, \mathbf{k} is the wave vector and \mathbf{V}_e is the electron drift velocity. The important addition to standard FBI theory is provided by a modification to the equation of energy conservation, with the addition of an electron Pedersen heating term, given by

$$H = \epsilon N_e \nu_e m_e V_e^2 \quad (2.18)$$

where the factor, ϵ , may be set to zero or one, thus turning the effects of the term off or on, corresponding to the equations for the FBI or the EPCI, respectively.

Figure 2.3 depicts the configuration of the \mathbf{E} -field, \mathbf{B} -field, electron-drift and irregularity propagation directions. \mathbf{V} refers to the $\mathbf{E} \times \mathbf{B}$ drift driven by magnetospheric convection, where \mathbf{E} is the convection electric field. The equations for the FBI/EPCI used by Robinson (1998) are presented below. Standard notation is used with the addition of η_e , the inelastic electron-neutral collision frequency.

A low-frequency approximation has been applied in order to obtain simple expressions for the frequency, and hence the phase speed, and the growth rate. These are given by

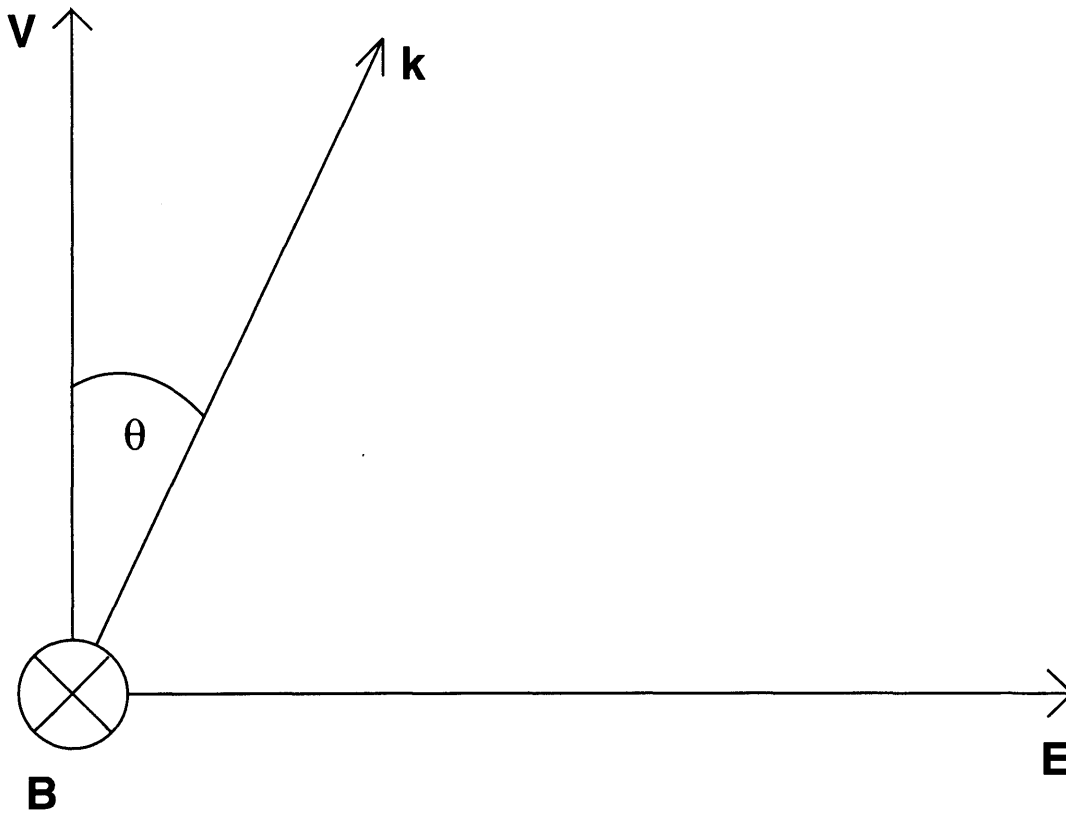
$$\frac{\omega}{k} = \frac{\hat{\mathbf{k}} \cdot \mathbf{V}_{e0}}{1 + \psi} \quad (2.19)$$

$$\begin{aligned} \gamma = & \frac{\psi k^2}{(1 + \psi)^3 \nu_{in}} \left(V_{e0}^2 \cos^2 \theta - C_s^2 (1 + \psi)^2 \right) \\ & - \frac{\psi k^2}{(1 + \psi)^3 \nu_{en}} (1 + \psi) \frac{V_{e0}^2 \sin 2\theta}{\Omega_e \eta_e} \end{aligned} \quad (2.20)$$

The phase velocity of the EPCI irregularities is given by the same expression as that for the FBI. Hence, the two wave velocities are the same, although it should be remembered that ψ has a higher value at D-region altitudes, perhaps of the order of 1000.

The expression for the growth rate is modified from the usual FBI expression by the addition of an extra term due to electron Pedersen heating. This term contains a component proportional to $\sin 2\theta$, where θ is the angle between the flow direction and the irregularity propagation direction. It is this term that gives rise to the EPCI.

There are a number of important differences between the FBI and the EPCI, including the direction in which waves are excited. For the FBI, the waves propagate with a maximum around the $\mathbf{E} \times \mathbf{B}$ drift direction. For the EPCI, the maximum occurs in the bisector direction between the electric field and the $\mathbf{E} \times \mathbf{B}$ drift velocity direction. The values of the electron Pedersen conductivity, included for the EPCI, confirm that the growth rate is highest along the bisector direction for altitudes around 75-105 km.



\mathbf{V} = electron $\mathbf{E} \times \mathbf{B}$ drift

\mathbf{E} = convection electric field

\mathbf{B} = terrestrial magnetic field

\mathbf{k} = irregularity wave vector

θ = flow angle

Figure 2.3: The configuration of the fields and drift and wave propagation directions for the FBI and EPCI. The FBI is most favourably excited in the E-region when $\theta \approx 0^\circ$ and the EPCI is most favourably excited in the D-region when $\theta \approx 45^\circ$.

As discussed by Dimant and Sudan, the EPCI excites longer-wavelength, lower-frequency irregularities with wavelengths of ten of metres most effectively. This is another difference between the EPCI and the FBI. Referring to (2.20), the threshold is given by setting γ to zero and then solving for the velocity. As described by Robinson (1998), the threshold velocities are proportional to $\sqrt{1+\psi}$ for $\theta = -\pi/2$, rather than $(1+\psi)$, which is the case when $\theta = 0$. The dependence of the growth rate and threshold velocity on the flow angle and the aspect angle are described in chapter 5.

2.4 E-region Non-linear Theory

As mentioned above, use of linear theory provides only an approximation to the true situation. The linear theory describes the primary growth characteristics for the instability when it is first excited. However, it makes no provision for the termination of the growth stage, which must happen at some stage as an instability can only grow as long as there is a source of energy driving it. The solution to this is provided by a process involving anomalous collisions (Sudan, 1983). These are instances of momentum transfer between electrons and plasma waves and their effects are described by an anomalous electron collision frequency, ν_e^* . Anomalous collisions and the associated frequency may be characterised by considering wave-wave interactions and weak turbulence (Baumjohann and Treumann, 1997b), where the three waves involved in the interaction satisfy the conditions, $k_1 = k_2 + k_3$ and $\omega_1 = \omega_2 + \omega_3$. In the linearised equations given above, ν_e is replaced by $\nu_e + \nu_e^*$ leading to the phase speed of the irregularities saturating at the ion-acoustic speed and the expression for the phase velocity is modified as follows

$$V_{ph} = \frac{\omega}{k} = \frac{V_d \cos \theta}{1 + \psi + \psi^*} \approx C_s \quad (2.21)$$

where

$$\psi^* = \frac{\nu_e^* V_i}{\Omega_e \Omega_i} \quad (2.22)$$

The significance of non-linear effects was highlighted by Robinson (1994) who considered the effects of an enhanced anomalous wave-enhanced collision frequency on the heating effects of Farley-Buneman waves in the auroral E-region and concluded that it was associated with strong plasma flows. A further consequence of anomalous collisions is anomalous diffusion and a possible mechanism partially responsible for this will be presented in chapter 5.

2.5 Additional Instabilities in the High Latitude Ionosphere

The discussion so far has centred on the E-region Farley-Buneman instability together with an extension of it into the D-region. Other ionospheric instabilities also exist, e.g. the velocity shear instability that exists along the convection reversal boundary (e.g. Kintner, 1976). It is related to the Kelvin-Helmholtz instability and is known to increase the quantity and the amplitude of field-aligned irregularities. Ionospheric plasma is a turbulent fluid and this turbulence can cause other instabilities and associated effects. The focus in the next section is on F-region effects associated with the artificial modification of the ionosphere.

2.6 Radio Wave Propagation and Non-linear Effects in the F-region

The plasma in the F-region may be considered to be effectively collisionless since the mean free path of the electrons is much larger than the scale-size of the perturbing wave. The propagation of radio waves into the F-region is described well by Evans (1969). HF radio waves, launched almost vertically, propagate in two modes in the ionosphere, the ordinary (O) mode and the extraordinary (X) mode. These modes correspond to solutions of the Appleton-Hartree dispersion relation, which is given by

$$n^2 = 1 - \frac{X}{1 - \frac{Y^2 \sin^2 \theta}{2(1-X)} \pm \left\{ \left(\frac{Y^2 \sin^2 \theta}{2(1-X)} \right)^2 + Y^2 \cos^2 \theta \right\}^{\frac{1}{2}}} \quad (2.23)$$

where the refractive index is given by $n = kc/\omega_f$. Also, $X = (\omega_p/\omega_f)^2$, $Y = \Omega/\omega_f$, and the electron gyrofrequency is given by $\Omega = eB_0/m_e$. In addition, ω_p is the plasma frequency, ω_f is the frequency of the radio waves and θ is the angle between the wave vector and the ambient magnetic field. O-mode waves are reflected at the altitude where $X = 1$, which corresponds to

$$\omega_f = \omega_p = \left(\frac{e^2 n_e}{4\pi^2 \epsilon_0 m_e} \right)^{\frac{1}{2}} \quad (2.24)$$

X-mode waves are reflected at the altitude where $X = 1 \pm Y$. In most cases, X-mode waves are reflected at the lower altitude, where $X = 1 - Y$. However, at auroral latitudes, the energy in the X-mode may be transferred to a wave that reaches the altitude where $X = 1 + Y$. This wave is called the Z-mode and has been described by Mjølhus (1990). It should be noted that this coupling to the Z-mode requires an inhomogeneous ionosphere, i.e. it will not occur if the ionosphere is stratified. At the altitude of reflection, the group velocity of the waves

vanishes, leading to a large increase in the electric field strength. This results in a standing wave, leading to a spatially periodic wave field that may be approximated by an Airy function. There is an increase in the field strength where the amplitude of the standing wave is highest. This increase is called swelling and has been described by Lundborg and Thidé (1986). Swelling increases the amplitude of the wave field such that it exceeds the threshold required for instability onset.

At the upper-hybrid resonance height, typically 6 km below the O-mode reflection height, the electric field vector of the propagating radio wave changes direction such it becomes perpendicular with the terrestrial magnetic field and the wave is circularly polarised. As a consequence of this field orientation, coupling can occur between electromagnetic and electrostatic waves, leading to amplification of the electrostatic waves and the onset of plasma instabilities. For most situations, O-mode waves are of most importance because X-mode waves are reflected at altitudes below that at which electromagnetic-electrostatic coupling occurs.

At the upper-hybrid altitude, the wave frequency of the electromagnetic waves equals the upper-hybrid frequency, ω_u , given by

$$\omega_u^2 = \omega_p^2 + \Omega^2 \quad (2.25)$$

Bernstein modes that do not generate irregularities may also be excited by the electromagnetic waves at the upper-hybrid height. O-mode waves incident at greater than the Spitz angle are also reflected below the vertical reflection angle, although if the angle of incidence is close to this value, then the O-mode wave may couple to the Z-mode. The Spitz angle, θ_s , is given by

$$\theta_s = \sin^{-1} \left(\sqrt{\frac{Y}{1+Y}} \cos \theta_m \right) \quad (2.26)$$

and corresponds to a discontinuity or cusp in the ray path. The angle θ_m is the local magnetic dip angle, which is equal to 78° for Tromsø. Taking Ω as 1.35 MHz, then $\theta_s \approx 6^\circ$ for $\omega_f = 4$ MHz and $\theta_s \approx 4.5^\circ$ for $\omega_f = 8$ MHz.

In addition to the effects mentioned above, there are other physical processes that affect the propagation of radio waves into the F-region. Collisional heating of electrons in the electric field of the wave results in Ohmic or non-deviative absorption, because $n \approx 1$ and there is little bending of the ray or absorption of the radio wave. This thermal effect is most pronounced in the D-region, at altitudes from 70-80 km, and increases with power. Although this is not an F-region effect, it causes absorption that can reduce the power reaching the F-

region. Finally, it should be noted that other non-linear effects occur when the power of the radio waves is high.

2.7 The Parametric Decay Instability (PDI) and Other Related Effects

Coupling occurs between electromagnetic and electrostatic waves at the O-mode reflection height and interaction between the electrostatic waves drives an instability known as the parametric decay instability (PDI).

The primary driver behind the PDI is the ponderomotive force, which is proportional to $\nabla|E|^2$ and described in detail by Kohl et al. (1993). Upon excitation of the PDI, a three-wave interaction occurs, leading to an electromagnetic wave coupling to an electron-acoustic wave and an ion-acoustic wave. The PDI results in the deposition of energy in the F-region electron gas, leading to anomalous absorption and an increase in the temperature, although the effect is weak because most of the energy in the electromagnetic pump wave drives processes at the upper-hybrid height and does not reach the reflection height. Furthermore, the daughter waves produced by the instability then interact with one another repeatedly, thus providing an example of turbulence and leading to a process known as cascading, where the energy is spread amongst more and more waves. Via cascading, the energy in the system, which sustains and amplifies the instability, may be dissipated.

A further consequence resulting from the excitation of Langmuir waves is the production of stimulated electromagnetic emission (SEE). Scattering of the Langmuir waves, from low frequency electrostatic waves, results in the transmission of electromagnetic waves (Thidé et al., 1982) that propagate out of the interaction region and may be observed at the ground. A prominent feature in SEE spectra is the continuum, a usually asymmetric spectrum with a peak at the frequency of the heater pump wave. This is thought to be caused by the cumulative effects of the electromagnetic waves, produced by Langmuir waves via the PDI, scattered from ion-acoustic waves.

2.8 Artificially Generated Field-aligned Irregularities in the F-region

The theory of the generation of artificial FAIs is considered in this section. The mechanism responsible for the FAIs is the thermal oscillating two-stream instability (TOTSI), also known as the thermal parametric instability (TPI). It occurs because of coupling between electromagnetic and electrostatic waves, similar to the parametric decay instability (PDI) that

was discussed above, although the FAIs are an integral part of the coupling mechanism and the feedback is thermal as opposed to ponderomotive. Hagfors (1984) described the propagation of electromagnetic waves in a cold magnetised plasma in which FAIs are present.

2.8.1 The Thermal Oscillating Two-Stream Instability (TOTSI): Overview

In the TOTSI regime, one of the decay products is a non-propagating periodic structure in the frame of the terrestrial magnetic field. Anomalous absorption occurs at the density gradients of FAIs. The FAIs can occur naturally, but are enhanced by a pressure gradient force caused by differential heating of plasma waves, resulting in a resonance when the heater frequency is close to the upper hybrid frequency. Thermal effects, based upon the Ohmic heating of electrons, are responsible for the excitation of the instability. Figure 2.4 shows an overview of the processes that occur in order to excite the TOTSI.

Chen (1974) described a non-thermal form of the oscillating two-stream instability that relies upon ponderomotive effects. Both the thermal and non-thermal versions of the oscillating two-stream instability involve the displacement of plasma from regions of high wave field intensity. However, the thermal version of the instability affects the plasma indirectly. Excess heating is present in regions where the wave field is high, causing an increase in temperature. This demonstrates that the similarity between the two types of non-linearity is not complete. Indeed, the thermal case is dissipative, resulting in thermodynamically irreversible theories, whereas the ponderomotive force may be included in reversible theories.

The derivation that follows comes from the work of Dysthe et al. (1983). The model of the TOTSI consists of four parts: the electrostatic response, the differential Ohmic heating of the electron gas, thermal conduction and modification of the density.

2.8.2 Coupling between Electromagnetic and Electrostatic Waves via Irregularities

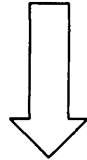
Consider a long wavelength O-mode electromagnetic wave, whose amplitude is given by

$$E_0 e^{i\omega t} + c.c. \quad (2.27)$$

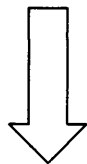
and a planar density perturbation given by

$$n = n_0(\mathbf{r}) + \delta n(x) \quad (2.28)$$

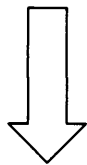
Natural waves and density perturbations are always present because of random thermal fluctuations in the plasma.



After switch-on of the heater, the electromagnetic pump wave is able to transfer energy to electrostatic waves near the upper-hybrid height, where the coupling occurs at the density perturbation.



The excited electrostatic waves then interact with the electromagnetic wave, leading to a beat heating effect that increases the size of the original density perturbation, thus leading to observable large-amplitude field-aligned irregularities or striations.



The size of the irregularities is limited by anomalous absorption, where the energy of the electromagnetic wave is going into the excited electrostatic waves.

Figure 2.4: The processes that occur when the thermal oscillating two-stream instability (TOTSI) is excited. Other theories of heating also exist.

The variation of n_0 is assumed to be much slower than that of δn along the x direction. The density perturbation causes an electrostatic polarised electric field perturbation that is oriented in the x direction. Assuming that the wave field is stationary, the total electric field is given by

$$\nabla \times (\nabla \times \mathbf{E}) - \frac{\omega^2}{c^2} \boldsymbol{\varepsilon} \cdot \mathbf{E} = \mathbf{0} \quad (2.29)$$

where $\boldsymbol{\varepsilon} = \boldsymbol{\varepsilon}(n)$ is the local dielectric tensor. Splitting the tensor and the electric field into background and perturbation parts, subtracting and then taking the divergence leads to

$$\nabla \cdot (\boldsymbol{\varepsilon} \cdot \mathbf{E}_1) = -\nabla \cdot (\delta \boldsymbol{\varepsilon} \cdot \mathbf{E}_0) \quad (2.30)$$

To facilitate the discussion, a one-dimensional model will be utilised. The previous equation becomes

$$\frac{\partial}{\partial x} (\varepsilon_{xx} E_x) = -\frac{\partial}{\partial x} (\delta \boldsymbol{\varepsilon} \cdot \mathbf{E}_0)_x \quad (2.31)$$

and linearising and integrating, results in

$$\varepsilon_{00x} E_x = \frac{X}{1-Y^2} \frac{\delta n}{n_0} (E_{0x} + iY E_{0y}) \quad (2.32)$$

where X , Y , ω_p and Ω were defined above. The constant of integration may be eliminated by defining δn and n_0 such that the mean of δn vanishes in the x direction. The y direction is considered to be perpendicular to the magnetic field and the x direction. Using the slow spatial variation of ε_{xx0} and a finite electron-neutral collision frequency, a final expression for the electric field may be obtained

$$E_x = -\frac{\xi/L + i\delta}{|\Delta|^2} (E_{0x} + iY E_{0y}) \frac{\delta n}{n_0} \quad (2.33)$$

where

$$\Delta = -\varepsilon_{xx0}, \quad \delta = \frac{\nu_e}{\omega} \frac{1+Y^2}{1-Y^2}, \quad L^{-1} = \frac{1}{n_0} \frac{dn_0}{d\xi} \quad (2.34)$$

ξ is a vertical coordinate and L is the scale length. This model is illustrative and a more accurate two-dimensional model should be used if a correct description of the electrostatic response is required.

2.8.3 Differential Ohmic Heating

For the complex field amplitude of the heater wave, the Ohmic heating is given by

$$Q = 2\mathbf{E}^* \cdot \boldsymbol{\sigma}^H \cdot \mathbf{E} \quad (2.35)$$

where σ^H is the Hermitian part of the conductivity tensor. Applying the standard technique of splitting this into equilibrium and perturbation quantities and utilising the previous one-dimensional model together with an expression for the conductivity tensor, the first-order heating term is given by

$$Q_1 = -\frac{\nu}{2\pi} \frac{1}{|\Delta|^2} \left(\frac{\xi}{L} R_1 + \delta R_2 \right) \frac{\delta n}{n_0} \quad (2.36)$$

where

$$R_1 = 2(\sigma_{\perp} |E_{0x}|^2 + Y\mu |E_{0y}|^2) + i(Y\sigma_{\perp} + \mu)(E_{0y}^* E_{0x} - E_{0y} E_{0x}^*) \quad (2.37)$$

$$R_2 = Y(E_{0y}^* E_{0x} + E_{0y} E_{0x}^*) \quad (2.38)$$

where $\mu = 2Y/(1-Y^2)$ and $\sigma_{\perp} = (1+Y^2)/(1-Y^2)$. Denoting the upward wave by

$$U = E_0^+ \exp[i(\omega t - k\xi)] + E_0^+ \exp[-i(\omega t - k\xi)] \quad (2.39)$$

and the downward wave by

$$D = rE_0^+ \exp[i(\omega t + k\xi + \phi)] + rE_0^+ \exp[-i(\omega t + k\xi + \phi)] \quad (2.40)$$

the following expression may be derived

$$\int_{-\infty}^{\infty} Q_1 dz = \frac{1}{\cos \alpha} \int_{-\infty}^{\infty} Q_1 d\xi = -3\nu_e \frac{m}{M} n_0 T_0 l \frac{\delta n}{n_0} P \quad (2.41)$$

where P is given by

$$P = \frac{1}{6} \frac{M}{m} \frac{1}{n_0 T_0} \frac{L}{\cos \alpha} \left[2r \sin \phi R_1 + (1 + r^2 + 2r \cos \phi) R_2 \right] \quad (2.42)$$

and r corresponds to the relative amplitude of the reflected wave, i.e. $0 < r < 1$. Also, α is the angle between the magnetic field and the vertical direction. Das and Fejer (1979) considered the case of a standing wave, consisting of the transmitted and reflected heating waves, and concluded that such a standing wave was essential for the excitation of the heating effect. Dysthe et al. (1983), demonstrated that the instability may still be excited when the reflected wave is not considered, i.e. when $r = 0$. Das and Fejer ignored the term containing Y in (2.33), and therefore did not consider the heating effects for cases where $r = 0$.

Because the region where heating occurs is much smaller than the region where the density and temperature perturbations propagate, the heating may be represented by a thin plane. The thermal conduction processes are derived by considering the electron temperature perturbation. Also taking into account the density perturbations allows the relevant parameters of the instability, e.g. the growth rate, to be calculated. Assuming that the x direction makes an angle, θ , with the magnetic meridian plane, electric field components may

be defined both parallel and perpendicular to it, such that both are perpendicular to \mathbf{B} . This allows (2.42) to be written as

$$P = \frac{2}{3} \left(\frac{M}{m} \right)^{\frac{1}{2}} \frac{L}{l_c \cos \alpha} \frac{|E_{0p}^+|^2}{n_0 T_0} P_0 \quad (2.43)$$

where

$$P_0 = r \sin \phi (a - b \cos^2 \theta) + \frac{c}{2} (1 + r^2 + 2r \cos \phi) \cos \theta \sin \theta \quad (2.44)$$

$$a = \frac{1 + Y^2 + 2Y^2 \Gamma^2 + Y(3 + Y^2) \Gamma}{1 - Y^2} \quad (2.45)$$

$$b = \frac{(1 + 3Y^2)(1 - \Gamma^2)}{1 - Y^2} \quad (2.46)$$

$$c = Y(1 - \Gamma^2) \quad (2.47)$$

and

$$\Gamma = \frac{1}{2Y} \tan^2 \alpha \left[\left(1 + \frac{4Y^2 \cos^2 \alpha}{\sin^4 \alpha} \right)^{\frac{1}{2}} - 1 \right] \quad (2.48)$$

2.8.4 Thermal Effects and Density Modifications

Considering transport theory and introducing skew coordinates, with x defined as previously and ζ pointing vertically in the magnetic meridian plane, leads to the following expression for the electron temperature perturbation

$$\begin{aligned} \delta_{T\parallel} \frac{\partial^2 T}{\partial \zeta^2} + \delta_{N\parallel} \frac{\partial^2 N}{\partial \zeta^2} - \frac{3}{2} (\gamma + \delta_T) T + N(\gamma - \delta_N) \\ - p^2 (\delta_{T\perp} T + \delta_{N\perp} N) = 3PN \delta(\zeta) \end{aligned} \quad (2.49)$$

where

$$p = Kl_{\perp}, \quad l_{\perp} = \left(\frac{M}{m} \right)^{\frac{1}{2}} r_e = \left(\frac{T_e}{T_i} \right)^{\frac{1}{2}} r_i \quad (2.50)$$

where K is a spatial frequency in the x direction, e.g. $A = A_0 \cos Kx$, for the temperature and density perturbations, and r_e and r_i are the electron and ion gyroradii, respectively. There is a similar equation for density modifications

$$\begin{aligned} \varepsilon_{T\parallel} \frac{\partial^2 T}{\partial \zeta^2} + \varepsilon_{N\parallel} \frac{\partial^2 N}{\partial \zeta^2} - \frac{3}{2}(\gamma + \delta_T)T + N(\gamma - \delta_N) \\ - (p^2 \varepsilon_{T\perp} + \gamma)N = 0 \end{aligned} \quad (2.51)$$

In (2.49) and (2.51), $T = \delta T/T_e$ and $N = \delta n/n_0$. This pair of equations must be solved for γ , the growth rate, according to a consistency condition, together with the constraints $T, N \rightarrow 0$ as $|\zeta| \rightarrow \infty$. The solution to these equations has the form

$$T = T_{01} \exp(-\kappa_1 |\zeta|) + T_{02} \exp(-\kappa_2 |\zeta|) \quad (2.52)$$

$$N = N_{01} \exp(-\kappa_1 |\zeta|) + N_{02} \exp(-\kappa_2 |\zeta|) \quad (2.53)$$

Away from $\zeta = 0$, the two differential equations are homogeneous and a determinant may be constructed in order to obtain the relationship between T_{0i} and N_{0i} , $i = 1, 2$. This determinant then imposes the condition

$$P = F(\gamma, p^2) \quad (2.54)$$

where

$$F(\gamma, p^2) = a \frac{\sqrt{GH + 2H\sqrt{H}}}{\sqrt{H + dp^2}} \quad (2.55)$$

and

$$d = \frac{\varepsilon_{T\perp}}{\varepsilon_{T\parallel}}, \quad a = \frac{2}{3} \delta_{T\parallel} \left(\frac{\varepsilon_{N\parallel}}{\varepsilon_{T\parallel}} - \frac{\delta_{N\parallel}}{\delta_{T\parallel}} \right) \quad (2.56)$$

G and H are quadratic and quartic expressions for p , respectively, and also each contain γ . The two cases for weakly and strongly ionised plasma (Dysthe, 1983) have the same power threshold condition, satisfied by $P > P_{thr}$, and this is given by

$$P_{thr} = F(0,0) = \left[a \left(\delta_T \frac{\varepsilon_{N\parallel}}{\varepsilon_{T\parallel}} - \frac{2}{3} \delta_N \right) \right]^{\frac{1}{2}} \quad (2.57)$$

2.8.5 Growth Rates and Thresholds

As for the D-region and E-region instability mechanisms, the thresholds and growth rates characterise the instability and are obtained by assuming that density and temperature perturbations tend to zero as ζ tends to infinity. The resulting solutions provide a determinant that may be calculated in order to obtain the required parameters. The threshold electric field for the excitation of the instability is given by

$$\frac{|E_{0thr}|^2}{n_0 T_0} = k_3 k_4 \left(\frac{m}{M} \right)^{\frac{1}{2}} \frac{l_c}{L} \quad (2.58)$$

where k_3 is given by

$$k_3 = \frac{3}{4} \left[a \left(\delta_T \frac{\epsilon_{N\parallel}}{\epsilon_{T\parallel}} - \frac{2}{3} \delta_N \right) \right]^{\frac{1}{2}} \quad (2.59)$$

and k_4 is given by

$$k_4 = \frac{\cos \alpha}{P_0} \quad (2.60)$$

This threshold, whose expression is taken directly from Dysthe et al. (1983), equates to electric field values of the order of 1 mV m^{-1} . For the growth rate, the e-folding time is given by

$$\tau \sim k_5 \frac{M}{m} \frac{1}{v} \frac{|E_{thr}|^4}{|E|^4} \quad (2.61)$$

where

$$k_5 = k_1 a \left(\delta_T \frac{\epsilon_{N\parallel}}{\epsilon_{T\parallel}} - \frac{2}{3} \delta_N \right) \quad (2.62)$$

and $k_1 \approx 0.4$.

The quantity P_0 , given in (2.44), may be decomposed into an amplitude part and a phase part, ϕ . When heating begins, the plasma density changes in time, leading to the reflection and upper-hybrid heights also changing. This leads to a change in the phase, ϕ , as time passes. If the rate of change of the phase is larger than the growth rate of the thermal instability, then the threshold condition is not satisfied and the instability is not excited.

Partly because of their low group velocity, the daughter electrostatic waves associated with the TOTSI deposit their energy in a localised region near the upper-hybrid height. Robinson (1989) measured a peak $\Delta T_e/T_e$ of about +50%, indicating that heating due to anomalous absorption is the dominant mechanism causing an increased temperature. The effects of the increased temperature on the electron density depend on the altitude at which the heating takes place. At altitudes greater than 200 km, there is a predominance of O^- ions, and the enhanced temperature results in an increased conversion to NO^+ . This recombines with electrons more easily, thus resulting in a decrease in the density (Rietveld, 1993). The diffusion of the hot plasma away from the active regions also leads to a decrease in the density.

2.8.6 Comparison of Heating Models

Several basic types of FAI growth are described in the literature. The first type requires the power of the heating wave to exceed a threshold value, but does not impose any further conditions on the presence of FAIs (e.g. Das and Fejer, 1979). The second type of growth mechanism depends on the product of the heater power and the FAI amplitude (e.g. Inhester et al., 1981), producing explosive irregularity growth when the threshold condition is exceeded. A combination of the two mechanisms, whereby the first mechanism increases the irregularity amplitude until it exceeds the threshold required for the second mechanism to become operative, may explain FAI generation suitably.

Das and Fejer (1979) ignored the expression given by R_2 in (2.38), and therefore assumed that a standing wave must be present for heating to occur. Dysthe et al. (1983) showed that this requirement was unnecessary. Vas'kov and Gurevich (1976; 1978) considered an explosive instability that requires the presence of an initial field-aligned irregularity whose amplitude must exceed a certain threshold value. The instability then results in the scattering of the heating wave, producing electrostatic waves. Vas'kov and Gurevich considered heating effects by discussing a single field-aligned irregularity, whereas the approach by Dysthe and Das and Fejer assumed a spatially periodic structure. The different approaches lead to the same conclusions in most cases. However, non-linear effects where the sum of independent solutions is not a solution to the problem lead to different results for the two cases. Inhester et al. (1981) considered the case of periodic structures that scatter the electromagnetic heater wave into Langmuir waves. They demonstrated that an instability may be excited by the scattered Langmuir waves, irrespective of the reflected heater wave. Vas'kov and Gurevich assumed a scale size of around one metre perpendicular to the magnetic field, with the group velocity of the Langmuir wave being a minimum in this direction. Pre-existing irregularities, which are required for this mechanism to work, may be amplified during the excitation of the instability. Inhester (1982) considered a thermal modulational instability that grows explosively, as mentioned above. The basic physical process, scattering into Langmuir waves, is the same for all the processes mentioned. Inhester's approach is again based upon isolated FAIs, which may be considered independently. The scattering takes place at an altitude immediately below the upper-hybrid height. The process of irregularity generation becomes more complex when considering the non-linear evolution of the instability and this may be done by considering two FAIs. These result in scattering into Langmuir waves, and these may then interact adding to the initial heat

intensity that originates from the instability, thus maintaining the original instability. More recent work by Gurevich et al. (1996) considered the case where the density of the magnetised ionospheric plasma increased slowly in the vertical direction. From their analysis, the temperature of the striations embedded within the plasma was found to be several times higher than the background temperature, whereas the density perturbation was found to remain small.

2.9 Plasma Turbulence in the Ionosphere

Turbulence relating to plasma instabilities generally involves large amplitude waves, typically one or two orders of magnitude greater than random thermal fluctuations. Coupling occurs amongst them, giving rise to daughter waves and hence leading to a re-distribution of the available energy amongst more and more waves. Turbulence is often associated with the excitation of F-region instabilities generated by heating the ionosphere. For example, Thornhill and terHaar (1978) have considered the limiting case where the frequency of the resulting electrostatic waves becomes so close to the plasma frequency that further decay becomes energetically impossible.

2.9.1 F-region Plasma as a Turbulent Fluid

A specific definition of turbulence that applies to fluid flow is now considered. Flowing ionospheric plasma is taken to be an incompressible turbulent fluid, allowing turbulence characteristics to be defined for the flow. The following discussion presents the Lagrangian description of fluid flow following the approach of Monin and Yaglom (1971).

Fluid motion is usually described using an Eulerian regime, where the velocity, \mathbf{u} , at some time, t , is given by

$$\mathbf{u} = \mathbf{u}(\mathbf{X}, t) \quad (2.63)$$

where $\mathbf{X} = (X_1, X_2, X_3)$ and X_1 , X_2 and X_3 are fixed. Under this regime, the motion is considered in terms of the spatial coordinates, without consideration of how a fluid element will move in time. The velocity is measured and given a value at a particular position, and the subsequent and preceding motion of the fluid element that passes through that position is ignored. This treatment is perfectly sufficient for the case of steady or laminar flow, where fluid streamlines may be defined, as the variation of the fluid velocity from one position to another occurs in a well defined and predictable way. Using classical theory, the Eulerian variables,

$\mathbf{u}(\mathbf{X},t)$, may be determined, at least in principle, for all times $t > t_0$, provided the initial values are known, i.e. $\mathbf{u}(\mathbf{X},t_0) = \mathbf{u}_0(\mathbf{X})$. The situation is more complex when turbulent motion is considered.

The notion of turbulence in this respect is similar to that in everyday situations, such as the airflow behind an aeroplane or a lorry that is moving quickly. In cases such as these, streamlines do not exist and fluid flow is better described using the Lagrangian description. The Lagrangian description of fluid flow depends upon following the flow of fluid elements after some initial time, $t = t_0$. The fluid element is defined as having linear dimensions that are much larger than the typical inter-particle distance, where the particles are the electrons and ions that constitute the plasma. In addition to this, the fluid element is considered to be small enough for its internal velocity and pressure to be considered constant. Also, the fluid element is assumed to move as a whole and to not suffer noticeable deformation, therefore allowing it to be considered as a point. The Lagrangian description is a more natural regime under which to consider the fluid motion, since the fluid elements are followed as they move in time. However, the Eulerian description is mathematically and analytically more simple. Consequently, Lagrangian fluid equations are rarely used for specific calculations.

At this point, it is worth clarifying the situation regarding variables. Starting with spatial coordinates, \mathbf{x} denotes the Eulerian position, which is independent of t . \mathbf{X} refers to the Lagrangian coordinates and these are a function of time, since they represent the motion of a fluid element. Thus, for all $t > t_0$, $\mathbf{X} = \mathbf{X}(\mathbf{x},t)$ corresponds to all possible positions of the fluid element and describes a family of trajectories. Each trajectory may be labelled according to the value of \mathbf{X} at $t = t_0$, i.e. \mathbf{x} . Also, \mathbf{V} is the Lagrangian velocity and \mathbf{u} is the Eulerian velocity and the two are related by the expressions given below. It should be remembered that the Eulerian and Lagrangian velocities are equal when $t = t_0$.

The full Lagrangian characteristic of an incompressible fluid is the function $\mathbf{X}(\mathbf{x},t)$, which gives the coordinates of all fluid elements in terms of some parameter, \mathbf{x} . Theoretically, it is possible to determine the value of $\mathbf{X}(\mathbf{x},t)$, for all $t > t_0$, in terms of the initial velocities, $\mathbf{V}(\mathbf{x},t)$, where

$$\mathbf{V}(\mathbf{x},t) = \frac{\partial \mathbf{X}(\mathbf{x},t)}{\partial t} \quad (2.64)$$

Therefore, for the initial time t_0 ,

$$\mathbf{V}(\mathbf{x},t_0) = \left[\frac{\partial \mathbf{X}(\mathbf{x},t)}{\partial t} \right]_{t=t_0} \quad (2.65)$$

Eulerian and Lagrangian characteristics are related by

where u' represents the fluctuations of the Eulerian velocity. From this expression, it is clear that the variance depends on the fluctuations in the Eulerian velocity and the Lagrangian ACF. The shape and actual functional dependence of the Lagrangian ACF are not important (Monin and Yaglom, 1971), the only requirement is that $R_L(s)$ should decrease in value quickly. Therefore, it is possible to choose a Lagrangian ACF that facilitates computation. The following function is suitable

$$R_L(s) = e^{-s/T_L} \quad (2.72)$$

where T_L is the Lagrangian correlation time defined from the ACF by the following

$$T_L = \int_0^{\infty} R_L(\tau) d\tau \quad (2.73)$$

Substituting this definition for the Lagrangian ACF, given by (2.72), into (2.71) gives the following

$$\overline{\Delta^2} = 2\overline{u}^2 \int_0^{\tau} (\tau - s) e^{-s/T_L} ds \quad (2.74)$$

and after integration, the final expression is

$$\overline{\Delta^2} = 2\overline{u}^2 T_L^2 \left(\frac{\tau}{T_L} + e^{-\tau/T_L} - 1 \right) \quad (2.75)$$

Turbulence parameters may now be derived, including the diffusion coefficient, D , given by

$$D = \overline{u}^2 \cdot T_L \quad (2.76)$$

and the correlation length, L , is given by

$$L = (D \cdot T_L)^{1/2} = \overline{u} \cdot T_L \quad (2.77)$$

2.9.3 Collective Wave Scattering Theory

The characteristics of ACFs have been examined in terms of collective wave scattering by Grésillon and Cabrit (1991), Grésillon et al. (1992) and Hanuise et al. (1993). For the backscatter conditions that apply to coherent radar systems, the signal collected at a time, t , is the Fourier transform of the plasma susceptibility. This may be written as (Landau and Lifchitz, 1969)

$$s(t) = \int_V \chi(\mathbf{x}, t) e^{-i\mathbf{k} \cdot \mathbf{x}} d\mathbf{x}^3 \quad (2.78)$$

When the probing electromagnetic wave has a frequency larger than the plasma frequency and the electron gyrofrequency, and the wave is O-mode polarised and propagating

orthogonally to the terrestrial magnetic field, then an approximate expression may be obtained for the plasma susceptibility. This is given by (Quemada, 1968)

$$\chi(\mathbf{x}, t) = -\frac{n(\mathbf{x}, t)}{n_c} \quad (2.79)$$

where $n(\mathbf{x}, t)$ is the local fluctuating plasma density and n_c is the constant density for which the plasma frequency is equal to the frequency of the probing radio wave. Inserting this approximation into the expression for the Fourier transform allows the signal frequency spectrum to be calculated from its temporal correlation

$$\langle s(t)s^*(t + \tau) \rangle = \frac{1}{n_c^2} \int_V \int_V \langle e^{-i\mathbf{k} \cdot (\mathbf{x}_1 - \mathbf{x}_2)} [n(\mathbf{x}_1, t) dx_1^3] [n(\mathbf{x}_2, t + \tau) dx_2^3] \rangle \quad (2.80)$$

Plasma motion conserves particles. Therefore, the integration over \mathbf{x}_2 at time $t + \tau$ may be replaced by an integration over \mathbf{x}_2' , the position the same volume element occupied at time t .

In the transformation, the volume element is moved by a vector $\Delta(\mathbf{x}_2', \tau)$, where

$$\Delta(\mathbf{x}_2', \tau) = \mathbf{x}_2 - \mathbf{x}_2' \quad (2.81)$$

and the number of particles is conserved, such that

$$n(\mathbf{x}_2, t + \tau) dx_2^3 = n(\mathbf{x}_2', t) dx_2'^3 \quad (2.82)$$

Substituting this into the expression for the temporal correlation leads to

$$\langle s(t)s^*(t + \tau) \rangle = \frac{1}{n_c^2} \int_V \int_V \langle e^{-i\mathbf{k} \cdot (\mathbf{x}_1 - \mathbf{x}_2')} [n(\mathbf{x}_1, t) dx_1^3] [n(\mathbf{x}_2', t) dx_2'^3] e^{i\mathbf{k} \cdot \Delta(\mathbf{x}_2', \tau)} \rangle \quad (2.83)$$

This expression may be simplified for cases where the plasma displacement, $\Delta(\mathbf{x}_2', \tau)$, is statistically independent of the local number density, $n(\mathbf{x}_2', t)$. Such a situation applies in many areas of space plasma physics, including linear, transverse electromagnetic waves, longitudinal electrostatic waves and incompressible turbulent fluid flow, including frozen-in two-dimensional MHD plasma motion. The simplification allows the averaging operator to be factorised, leading to two different statistical moments.

$$\begin{aligned} \langle s(t)s^*(t + \tau) \rangle = \\ \frac{1}{n_c^2} \left\langle \int_V \int_V e^{-i\mathbf{k} \cdot (\mathbf{x}_1 - \mathbf{x}_2')} [n(\mathbf{x}_1, t) dx_1^3] [n(\mathbf{x}_2', t) dx_2'^3] \right\rangle \cdot \langle e^{i\mathbf{k} \cdot \Delta(\mathbf{x}_2', \tau)} \rangle \end{aligned} \quad (2.84)$$

The first averaged term is proportional to the 'form factor',

$$\Sigma(\mathbf{k}) = \frac{1}{N} \left\langle \int_V \int_V e^{-i\mathbf{k} \cdot (\mathbf{x}_1 - \mathbf{x}_2')} [n(\mathbf{x}_1, t) dx_1^3] [n(\mathbf{x}_2', t) dx_2'^3] \right\rangle \quad (2.85)$$

where N is the total number of scattering particles and is independent of time. The second averaged term is related to the probability distribution, $P(\Delta|\mathbf{x}_2', \tau)$, of the displacement, Δ , for

position \mathbf{x}_2' during time τ . It is now assumed that the spatial fluctuations of the plasma are statistically uniform. Hence, the probability is not a function of the initial position, so that

$$P(\Delta | \mathbf{x}_2', \tau) = P(\Delta | \tau) \quad (2.86)$$

The second averaged term from the expression given above is the statistical characteristic of the probability distribution, $P(\Delta | \tau)$. This is defined as the Fourier transform of the probability distribution of the scattering wave vector, \mathbf{k} .

$$\hat{P}^*(\mathbf{k}, \tau) = \langle e^{i\mathbf{k} \cdot \Delta(\mathbf{x}_2', \tau)} \rangle = \int e^{i\mathbf{k} \cdot \Delta} P(\Delta | \tau) d\Delta \quad (2.87)$$

Grésillon et al. (1992) and Hanuise et al. (1993) have studied two limiting cases where the ACF and the spectrum may be related to the turbulent motion of the fluid. In the limit of long correlation length, the probability distribution is related directly to that of the fluid velocity. Conversely, for a short correlation length, the probability distribution is related to that of a random walk.

Assuming stationary isotropic two-dimensional turbulent flow, for ionospheric plasma, the probability distribution may be considered to be Gaussian, resulting in

$$P(\Delta | \tau) = (2\pi\overline{\Delta^2})^{-3/2} e^{-\Delta^2/\overline{\Delta^2}} \quad (2.88)$$

Substituting this expression into that for the statistical characteristic, gives

$$\langle e^{i\mathbf{k} \cdot \Delta} \rangle = e^{-\overline{\Delta^2} k^2 / 2} \quad (2.89)$$

The previously obtained expression for $\overline{\Delta^2}$, given by (2.71)-(2.75), allows the ACF to be written as the following

$$\langle s(t)s^*(t+\tau) \rangle_t = \frac{N^2}{n_c^2} \Sigma(\mathbf{k}) e^{k^2 DT_L (\tau/T_L + e^{-\tau/T_L} - 1)} \cdot e^{i\mathbf{k} \cdot \mathbf{u} \tau} \quad (2.90)$$

and finally, the modulus of the ACF is given by

$$A(\tau) = \left| \langle s(t)s^*(t+\tau) \rangle_t \right| = \Gamma(\mathbf{k}) e^{k^2 DT_L (\tau/T_L + e^{-\tau/T_L} - 1)} \quad (2.91)$$

and it is the modulus that may be compared to measured ACFs. There are two limiting cases for the modulus, the Gaussian corresponding to $\tau \ll T_L$ given by

$$A(\tau) = \Gamma(\mathbf{k}) e^{-(1/2)(D/T_L)k^2\tau^2} \quad (2.92)$$

and the exponential corresponding to $\tau \gg T_L$ given by

$$A(\tau) = \Gamma(\mathbf{k}) e^{-k^2 DT_L \tau} \quad (2.93)$$

2.10 Summary

This chapter has provided a description of the theoretical aspects of irregularity studies as presented in this thesis. The basic discussion began with the accepted theory for the Farley-Buneman instability, in terms of the well-known derivation in terms of fluid theory. Following on from this was the electron Pedersen conductivity instability, an enhanced version of the Farley-Buneman instability that encompasses D-region instabilities. The second major part of this chapter then described artificially generated instabilities in the F-region, reviewing the theory behind the thermal oscillating two-stream instability. Finally, ionospheric plasma treated as a flowing turbulent fluid was described, relating turbulence parameters associated with the plasma to the auto-correlation function that is calculated from the backscattered signal detected by the radar system that is used to diagnose the ionosphere.

Chapter 3

Review of Natural and Artificial Irregularity Observations

3.1 Introduction

The need to diagnose the ionosphere remotely has led to the development of techniques involving radar systems, which operate by detecting backscatter from ionospheric FAIs. It has been known since the 1950s that the angle of incidence of transmitted radio waves is directly related to the efficiency of the backscatter from the field-aligned plasma inhomogeneities that form the irregularities. Booker et al. (1955) discussed the elongation of E-region irregularities by electron precipitation, together with scale sizes and other phenomena. It is now known that the scale sizes then predicted, 5-10 m along the field and 1 m across, were far too small. However, the theory presented by Booker (1956) is still useful as it contains a good description of the scattering of radio waves from FAIs. Booker considered the scattering cross-section of plasma irregularities caused by the presence of the terrestrial magnetic field. Because of the increased mobility along the magnetic field, the irregularities elongate in a direction parallel to the field. This creates a characteristic electric charge distribution that scatters the incident radio wave into a direction where the angle of incidence equals the angle of scattering, similar to specular reflection. Therefore, if the incident radio wave is perpendicular to the local terrestrial magnetic field, then the radio wave will be scattered back along the direction from which it came.

Field-aligned irregularities (FAIs) were first identified in radar studies of equatorial backscatter obtained by Bowles et al. (1960, 1963). A large set of observations has been collected over time and this has formed the basis for a number of review papers considering various aspects of ionospheric irregularities, including those that occur in the E-region (Fejer, 1979; Fejer and Kelley, 1980; Hanuise, 1983; Fejer, 1985; Fejer and Providakes, 1987). The mechanisms leading to naturally occurring irregularities in the F-region remain unclear at present, whereas artificially generated irregularities in the F-region have been attributed to the thermal oscillating two-stream instability. E-region irregularities result mainly from the gradient drift and Farley-Buneman instabilities. Naturally occurring D-region irregularities may be caused by the electron Pedersen conductivity instability. The Farley-Buneman, electron Pedersen conductivity and thermal oscillating two-stream instabilities have been discussed in the previous chapter.

3.2 E-region Radar Echoes from Naturally Occurring Irregularities

3.2.1 Type I and Type II Signatures

Radar echoes observed in the E-region have been classified according to spectral type and four radar echo types were originally identified and designated as Type I, II, III and IV. Haldoupis (1988) provided a good review of observations of these radar echoes and their characteristics and Sudan (1983) gave a more detailed discussion and overview of echo types. The general terminology used in describing radar echoes was originally developed for equatorial observations. Type I and II radar echoes were identified and classified according to the observing geometry and the characteristics of the Doppler spectrum. This nomenclature was extended to the auroral region and the equatorial backscatter echo definitions were retained.

Backscatter spectra obtained from coherent and incoherent radar spectra, together with the techniques used to calculate them, are described in detail in the following chapter on instrumentation and measurement techniques. A backscatter spectrum is obtained by plotting the backscatter power versus the Doppler velocity. Type I echoes are characterised by narrow single-peak spectra, with spectral widths of around 50 m s^{-1} , whose peaks are located at approximately the ion-acoustic speed, whereas Type II echoes are characterised by small Doppler shifts and wide spectra, corresponding to spectral widths of $200\text{-}400 \text{ m s}^{-1}$. Figure 3.1 shows typical Type I and Type II echoes.

Type I and II radar echoes types have been identified with specific plasma irregularity generation mechanisms. Type I echoes are caused by primary plasma waves corresponding to the Farley-Buneman instability and Type II echoes are caused by secondary plasma waves, corresponding to the excitation of the gradient-drift instability on the primary Farley-Buneman waves. Primary waves corresponding to the gradient-drift instability also exist but are rare in the E-region. Further evidence that these radar echoes are associated with specific irregularity generation mechanisms is obtained by considering additional facts, e.g. the existence of a threshold electric field that corresponds to electron drift at around the ion acoustic speed (Tsunoda and Presnell, 1976; Moorcroft, 1979; Cahill et al., 1978). The dependence of backscatter properties on the strength and location of the auroral electrojet has been studied (Greenwald et al., 1973; 1975; Haldoupis et al., 1982).

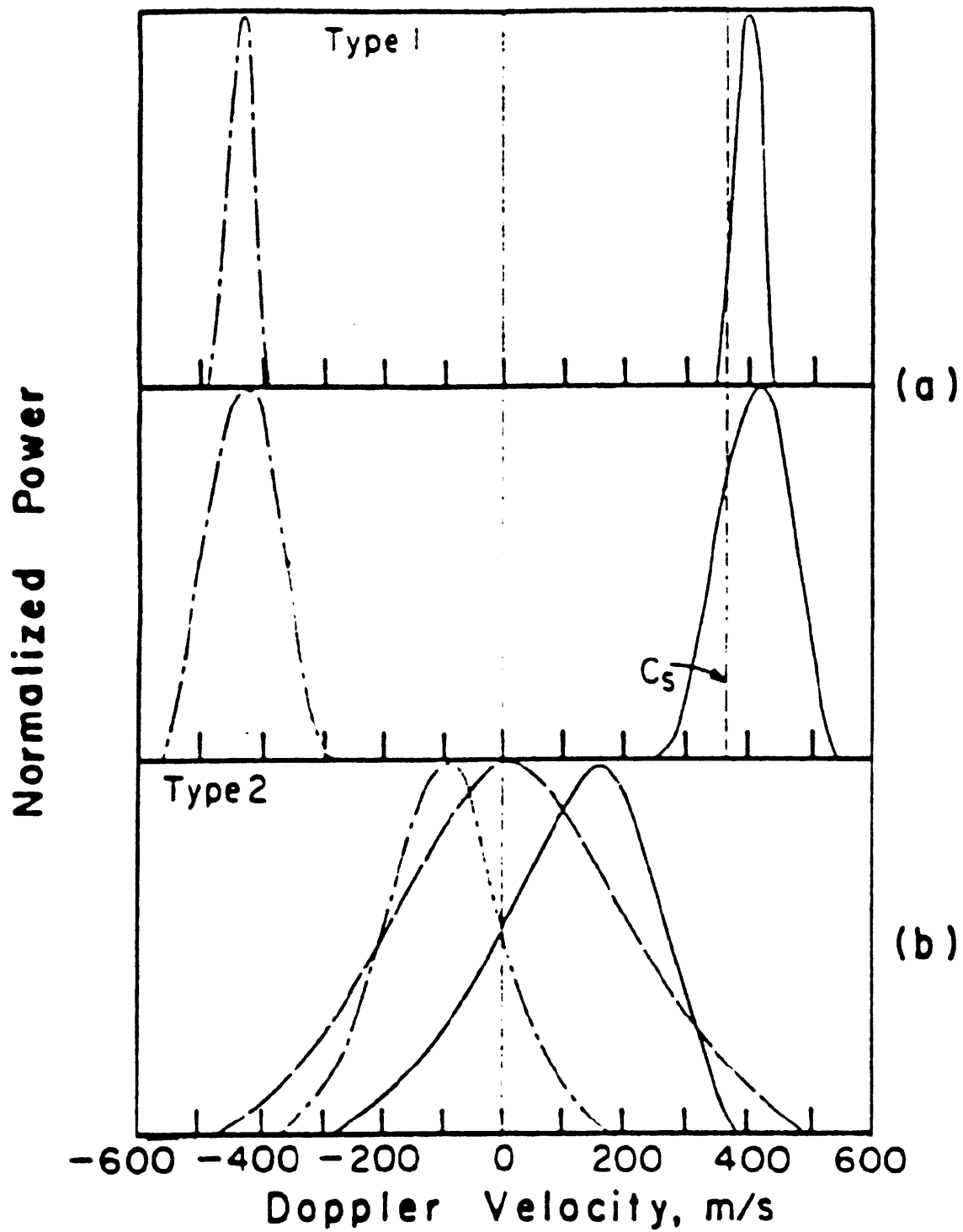


Figure 3.1: Spectra corresponding to Type I and Type II auroral backscatter radar echoes (Haldoupis, 1989).

3.2.2 Type III and IV Radar Echoes

Type I and II radar echoes have well defined signatures and have been associated with particular plasma waves and instabilities. Other types of radar echo exist in addition to these, and this section briefly describes two of them, Type III and IV signatures. Type III echoes are related to high intensity signals that have very narrow spectra. The frequency Doppler shifts of the signals preferentially have values either in the range 50-70 Hz, or less often, from 20 Hz to 40 Hz. These shifts correspond approximately to ion cyclotron frequencies, or their harmonics, of the main ion types in the plasma. Therefore, if the Doppler shift is converted to a Doppler velocity, its peak value will depend on the wavenumber, and hence the wavelength, that the observing radar is using. It appears that Type III echoes are not as aspect sensitive as Type I and II echoes. Haldoupis et al. (1987) have reported that Type III echoes were seen during more disturbed conditions. Fejer et al. (1984b) proposed that they were caused by ion-cyclotron waves generated by strong field-aligned currents originating from altitudes in the upper E-region well above the electrojet. Indirect optical evidence of field-aligned current involvement also exists (Providakes et al., 1985; Prikryl et al., 1987) as well as in situ rocket measurements of ion-cyclotron oscillations (Ogawa et al., 1981; Bering, 1983).

Haldoupis and Sofko (1979) observed Type IV echoes during disturbed conditions in the post-midnight sector. The backscatter spectrum consisted of two components, a broad part centred around 500 m s^{-1} and corresponding to Type I characteristics, and a narrow part, centred around 1100 m s^{-1} . According to Haldoupis and Sofko, the component that is shifted more strongly must have originated from extremely localised scattering regions during unusual plasma conditions. Further evidence of this distinct new echo type was provided by Providakes (1985) and Fejer et al. (1986) who used a portable interferometer to record observations taken during the disturbed conditions in the post-midnight sector. Fejer et al. suggested that Type IV echoes represent a case of the Farley-Buneman instability, where the ion-acoustic speed is raised significantly due to anomalous electron heating conditions. This interpretation assumes very high electron temperatures in excess of 2000 K. Figure 3.2 demonstrates the primary features of Type III and Type IV radar echoes.

The previous work on spectral types so far described was conducted mainly with VHF radar systems. The existing data set was enlarged by Milan and Lester (2001), who conducted a thorough study of spectral types in the HF band. Milan and Lester have presented evidence for five backscatter populations in the auroral electrojet. Evidence consistent with Type I and

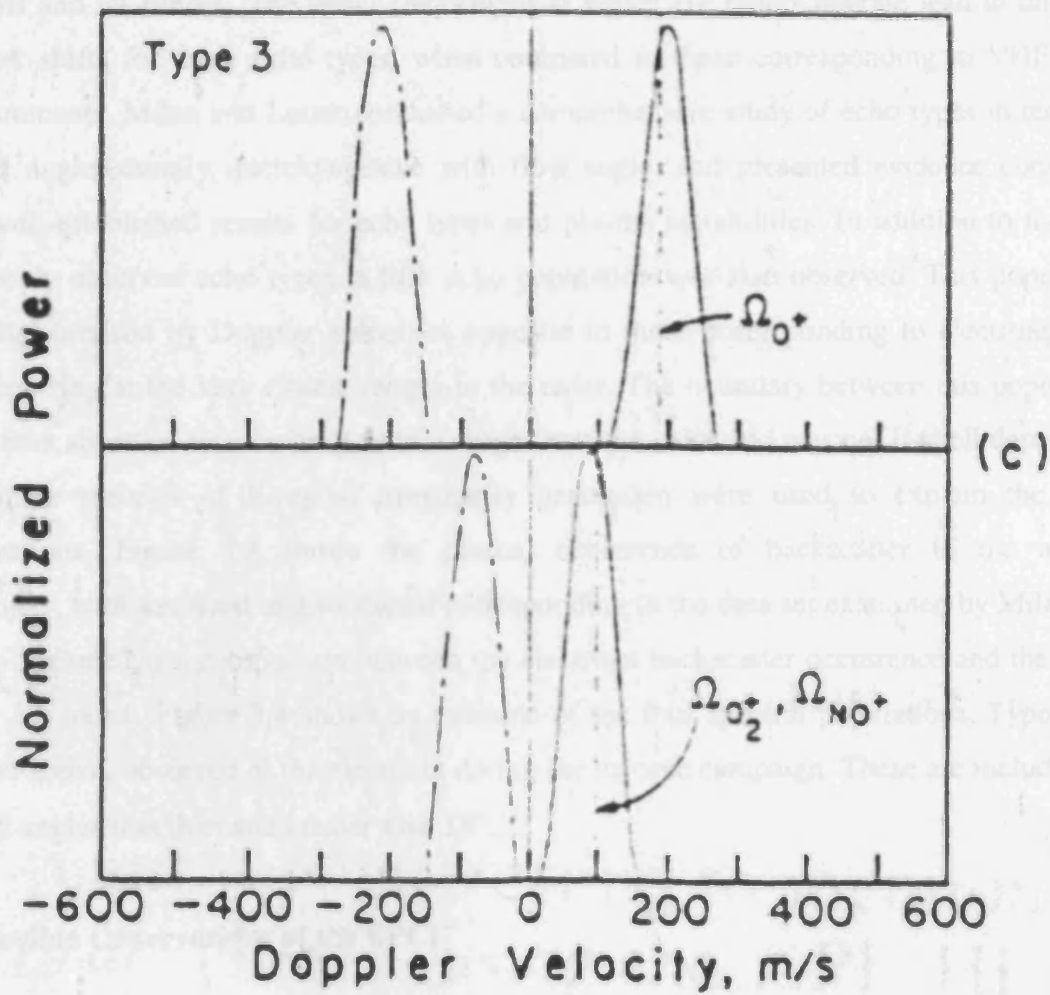


Figure 3.2(a): Type III radar echoes observed by a radar operating at 50 MHz (Haldoupis, 1989).

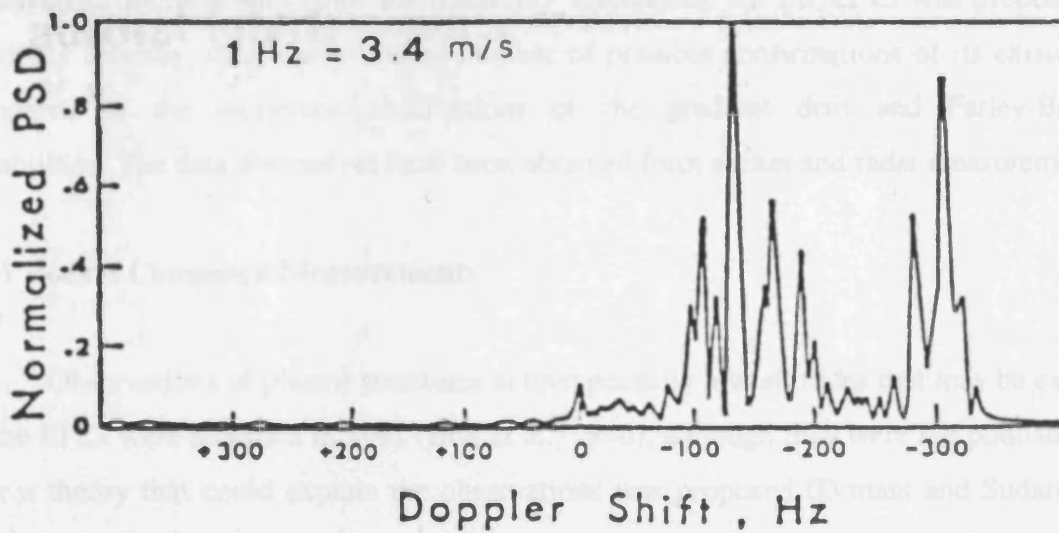


Figure 3.2(b): A Type IV radar echo observed at 42 MHz (Haldoupis and Sofko, 1979)

Type II echoes was presented, together with Doppler shift measurements consistent with Type III and IV echoes. The lower frequencies at which HF radars operate lead to different Doppler shifts for these echo types, when compared to those corresponding to VHF radar measurements. Milan and Lester conducted a comprehensive study of echo types in terms of L-shell angle, usually interchangeable with flow angle, and presented evidence consistent with well-established results for echo types and plasma instabilities. In addition to the four commonly observed echo types, a fifth echo population was also observed. This population was characterised by Doppler velocities opposite to those corresponding to electrojet flow and occurring at the very closest ranges to the radar. The boundary between this population and others appeared to occur at a certain range from the radar and was not L-shell dependent. Non-linear theories of E-region irregularity generation were used to explain the radar observations. Figure 3.3 shows the diurnal occurrence of backscatter in the auroral electrojets, both eastward and westward corresponding to the data set examined by Milan and Lester. Included is a comparison between the electrojet backscatter occurrence and the value of the Kp index. Figure 3.4 shows an example of the four spectral populations, Types I-IV defined above, observed in the electrojet during the myopic campaign. These are included for L-shell angles less than and greater than 35° .

3.3 Possible Observations of the EPCI

Since the proposal of the EPCI (Dimant and Sudan, 1995a, 1995b, 1995c) and the further clarification of its driving mechanisms (Dimant and Sudan, 1997; Robinson, 1998), possible observations of this D-region instability have been noted and these are now described in more detail. Since the instability mechanism for the EPCI was proposed only relatively recently, there are a limited number of possible confirmations of its existence, as compared to the numerous observations of the gradient drift and Farley-Buneman instabilities. The data themselves have been obtained from rocket and radar measurements.

3.3.1 Rocket Campaign Measurements

Observations of plasma structures at unexpectedly low altitudes that may be explained by the EPCI were recorded in 1991 (Blix et al., 1996), although they were not published until after a theory that could explain the observations was proposed (Dimant and Sudan 1995a, 1995b and 1995c).

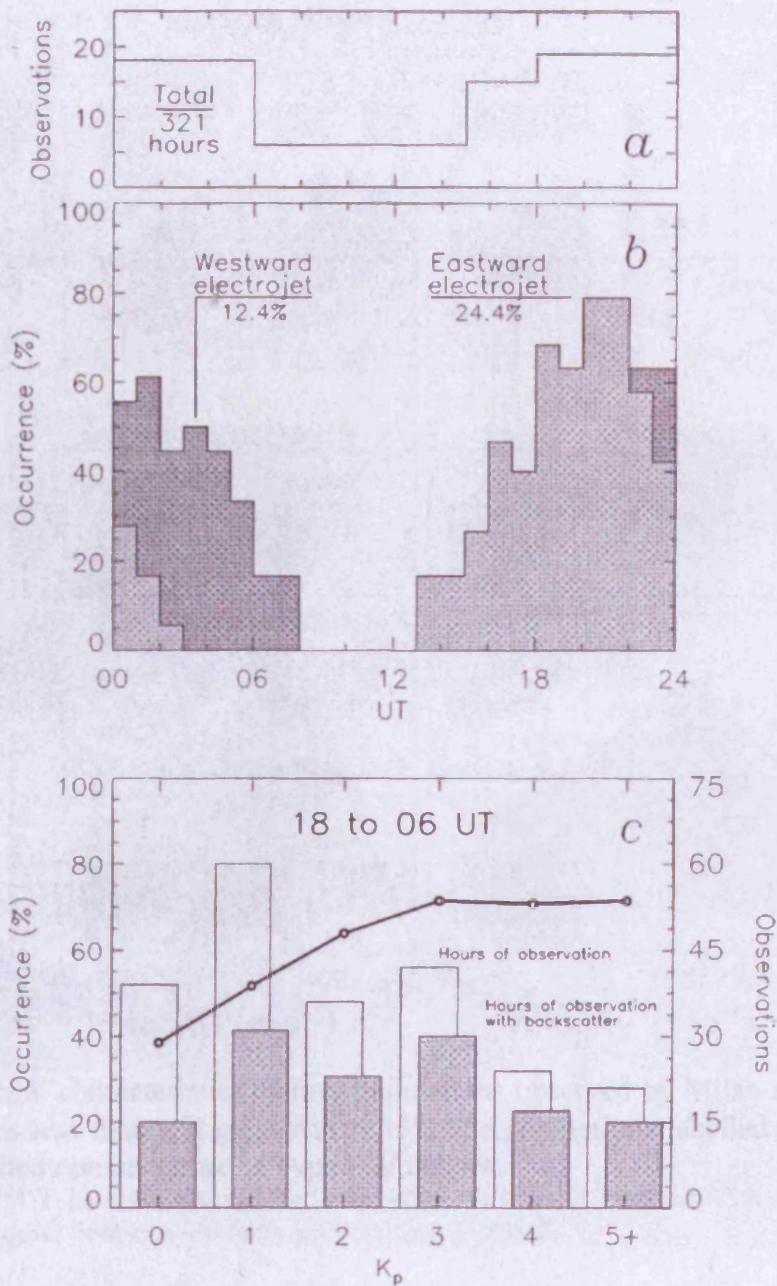


Figure 3.3: This figure shows results presented by Milan and Lester (2001). (a) The diurnal backscatter coverage in the westward and eastward auroral electrojets. Most observations were conducted from 1800 to 0600 UT. (b) Backscatter occurrence in both electrojets during the myopic campaign. (c) A comparison between the number of electrojet observations and the K_p index.

During the middle of September/October 1991, a major campaign called MISTAR-91 was organized. This campaign consisted of a set of scientific missions with instruments to measure the nature of the ionospheric plasma environment and their included plasma probes (that measured ion and electron density fluctuations) (Daly et al., 1996). Figure 3.5 shows the geometry of the orbit together with the configuration of the conjugate electric field and the magnetic field. Also shown in the figure are the two detectors along which the ICAI is carried out. As usually, in conjunction with the rocket salvoes, the DiSCAT radar

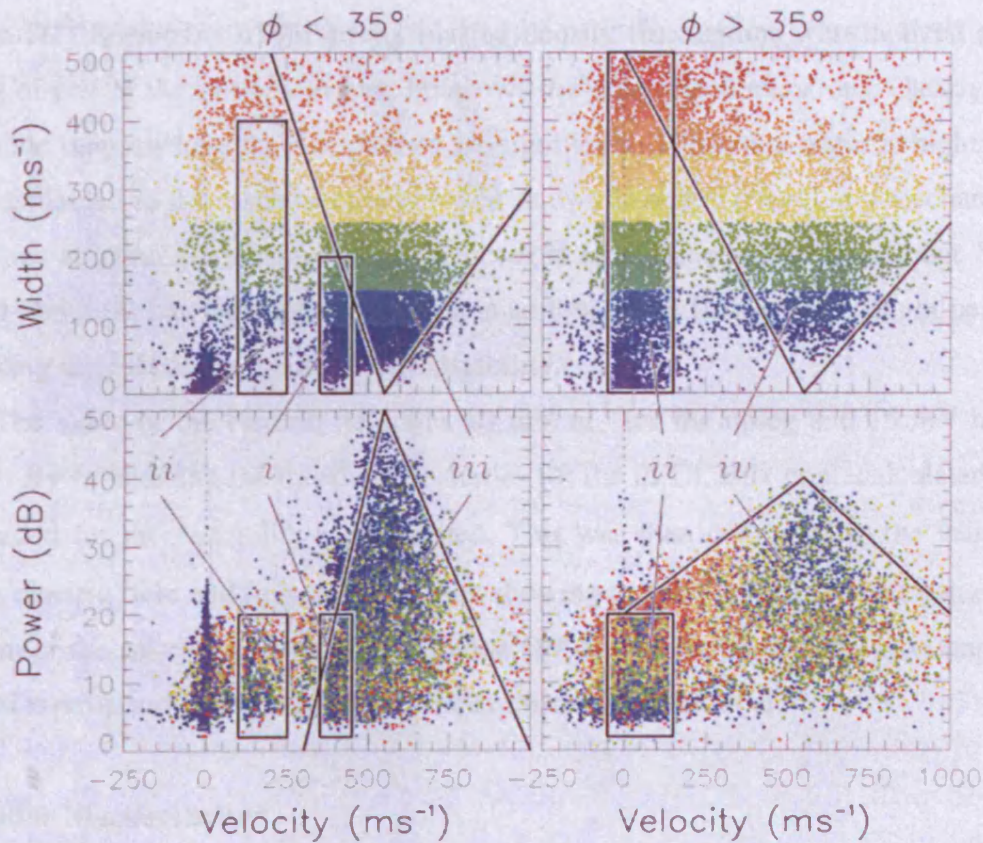


Figure 3.4: Spectral characteristics of four populations observed by Milan and Lester (2001) for L-shell angles less than and greater than 35°. The populations labelled i-v correspond to the well-established nomenclature of Type I-IV echoes.

During the months of September/October 1991, a rocket campaign called METAL-91 was undertaken. This campaign consisted of a set of sounding rockets with instruments to measure the nature of the ionospheric plasma environment and these included plasma probes that measured ion and electron density fluctuations (Blix et al., 1990). Figure 3.5 shows the trajectory of the rocket, together with the configuration of the convection electric field and the terrestrial magnetic field. Also shown in the figure are the two bisectors along which the EPCI is excited most favourably. In conjunction with the rocket salvoes, the EISCAT radar system, described in the next chapter, was used to measure the ambient convection electric field. On 30th September 1991, strong plasma density fluctuations were noticed during the downleg of one of the salvoes. Figure 3.6 shows these density fluctuations. Clearly, there are two altitude ranges where the fluctuations are significant. Those that occur at higher altitudes may be explained as the result of ordinary well-known E-region irregularity mechanisms. The fluctuations at lower altitudes were seen to occur at an altitude greater than about 78 km, but less than about 90 km. Because the altitude is so low, these fluctuations cannot be described by invoking the FBI or the gradient-drift instability.

The value of the electric field was 50 mV m^{-1} for the upleg and 75 mV m^{-1} for the downleg. By considering the threshold velocities for the EPCI, Blix et al. calculated the value of ψ needed for the instability to be excited. This was then compared to the value derived from the electric field and flow velocity, thus showing that the value of ψ was consistent with excitation of the instability. Dimant and Sudan (1995c) predicted that the wavelength should be tens of metres and these predictions were confirmed by Blix et al.

3.3.2 Radar Measurements

The proposal of the theory for the EPCI by Dimant and Sudan allowed other unexplained former measurements to be re-appraised. The EPCI should be more readily observed with lower frequency radar systems that operate at HF ranges rather than VHF ranges. A case in point concerns measurements taken on 12th August 1983, and was described by Tsunoda et al. (1997). This study was undertaken using a 12.3 MHz radar situated at Søndre Strømfjord, Greenland. The radar was used to probe the D-region, in order to search for FAIs. Because of the propagation and refraction of radio waves, the D-region could only be examined for southerly azimuths, as orthogonality with the terrestrial magnetic field could only be obtained for downcoming radio waves. Tsunoda et al. used the Greenland magnetometer chain and the incoherent scatter radar to obtain values for the electric field and

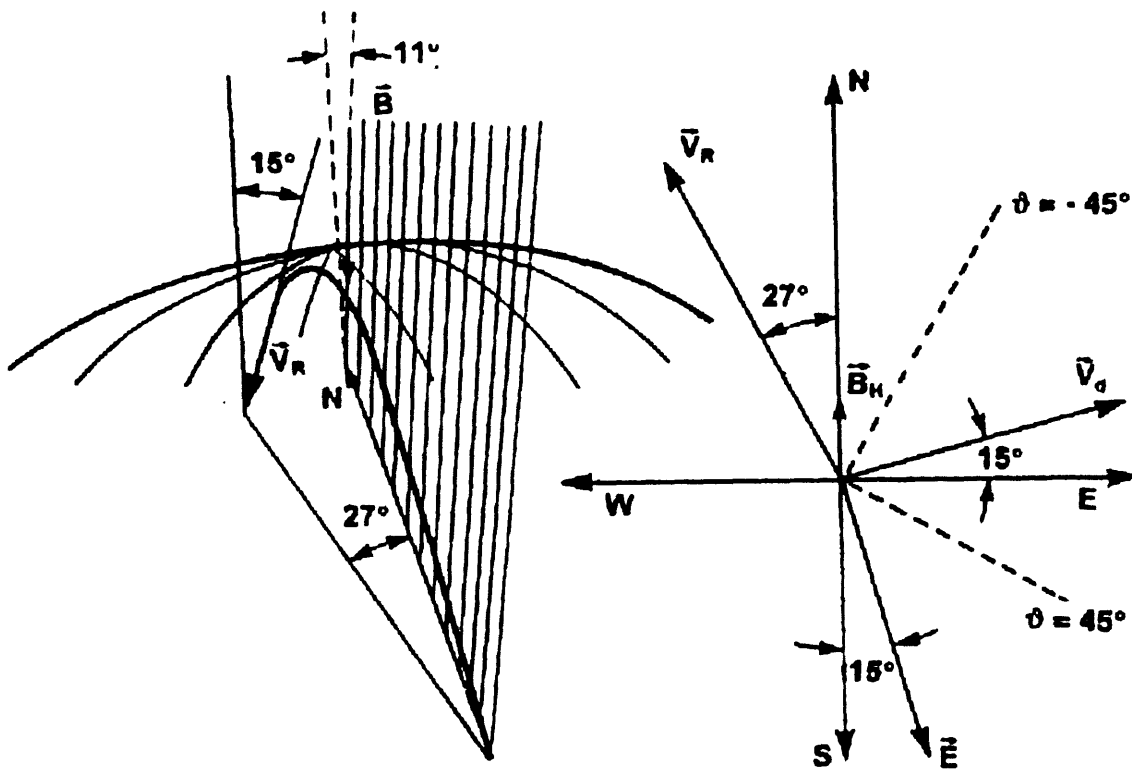


Figure 3.5: The rocket trajectory of flight L-T13 during the METAL-91 rocket campaign. Unusual plasma density fluctuations were observed during the flight. The sectors corresponding to positive and negative flow angles are shown on the right (Blix et al., 1996).

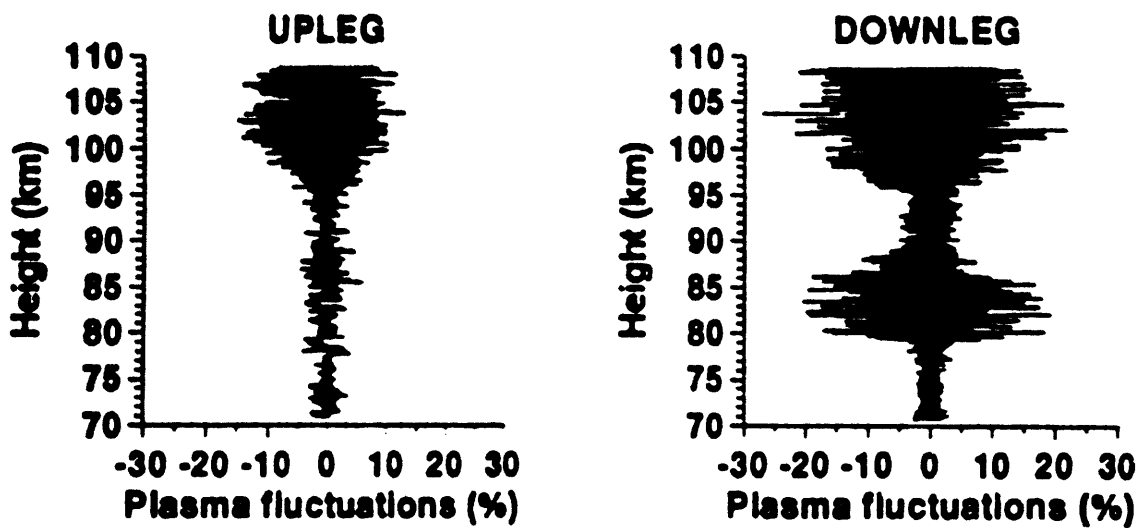


Figure 3.6: Unusual D-region plasma fluctuations were observed during the downleg of the L-T13 rocket flight. No such fluctuations were observed for the upleg (Blix et al., 1996).

the drift velocity. This was done with the assumption that the magnetometer variations were the result of an overhead Hall current associated with convective flow.

Based on this assumption, a range of radar echoes were observed and classified, including the Type I and II echoes that have been described above. Type I echoes at an altitude around 95 km and Type II echoes at an altitude around 90 km were observed. The convection electric field was quite large during the event described, 50 to 100 mV m⁻¹, and thus the Type I echoes may be explained in terms of the FBI. However, the Type II echoes occur at altitudes too low to be explained by instability mechanisms such as the FBI or the gradient drift instability. In addition, ray-tracing techniques were utilised in order to determine correctly the altitude from which the echoes with southerly azimuths originated and confirm that this altitude lay within the D-region. Apart from the data presented in this thesis, these have been the only observations consistent with excitation of the EPCI.

3.4. Observations of Ionospheric Modification Effects

In the F-region, the high-power radio waves transmitted into the ionosphere cause the generation of FAIs and the time taken to reach the maximum amplitude, the backscatter power at which the irregularities are maintained and the time they take to decay after heater switch-off provide indications of how the ionosphere responds to the heating process.

As well as Tromsø, observations have also been made at Sura, Platteville and Arecibo. Thome and Blood (1974) considered radio frequency backscatter from FAIs generated by the Platteville heater, capable of transmitting radiation at frequencies from 3-10 MHz, located at the Boulder Magnetic Observatory and observed by HF and VHF radars located at White Sands, New Mexico. Echoes were observed only after sunset, when the local plasma frequency over the heater site was of the order of 5 MHz. Fialer (1974) considered heating caused by O-mode waves and concluded that the strength of the backscatter decreased for cases where observations away from the direction of orthogonality to the terrestrial magnetic field were made. Observations were made using both HF and VHF waves. Minkoff et al. (1974) investigated field-aligned structures generated by ionospheric modification, together with plasma line and centre line scattering. Minkoff's instruments included a mobile bistatic receiver flown aboard a KC-135 aircraft. This provided a means of reception for VHF/UHF signals, at frequencies of 157.5 and 435 MHz, and also HF signals, at frequencies of 15 and 30 MHz. The 30 MHz signals were localised in an area about 200 km across in the North-South direction, whereas the 15 MHz signals were observed at larger

distances from the heater. Carpenter (1974) again examined results obtained by the Platteville facility. VHF and UHF measurements were utilised and it was found that the backscatter irregularity cross-section depended upon the observation frequency, with the most intense backscatter being observed for the lowest frequency used, the 49.8 MHz signal. Observations were also made at 157.5, 423.3 and 435 MHz. Meltz et al. (1974) developed a theory for ionospheric heating using the Platteville and Arecibo measurements as a basis. Cragin and Fejer (1974) considered the generation of large-scale FAIs in connection with the purely growing mode.

Using the heater at Arecibo, Noble and Djuth (1990) reported simultaneous observations of HF-enhanced plasma waves and artificial FAIs. Their experiment was conducted in order to determine whether artificially generated plasma turbulence affected the growth of artificial FAIs. It was found that initially the levels of plasma line associated turbulence and FAI intensity were linearly dependent on the HF heater power. However, the turbulence reached a saturation value whereas the FAI intensity continued to increase with the heater power. Coster et al. (1985) considered the growth and decay times for artificially generated FAIs created by the Arecibo heater. Evidence existed for two decay-time constants. The second longer time constant was associated with a diffusion process.

Using data obtained by the heating facility at Tromsø, Bond et al. (1997) considered CUTLASS observations of artificially generated FAIs and the CUTLASS system is described in the next chapter. The horizontal extent of the heating region was found to be 170 ± 50 km. A threshold electric field value for the instability was calculated from the data and this was found to be between 0.1 and 0.01 V m^{-1} . Hedberg et al. (1986) examined the HF backscatter cross-sections for artificial FAIs. This work followed on from observations of HF backscatter associated with heating at Tromsø (Hedberg et al., 1983). The observations were made at Kiruna, Lycksele and Uppsala, at frequencies of 3, 7, 14, 15.6 and 17 MHz. The rise and decay times were found to be frequency dependent, being longer for lower radar frequencies. The strongest echoes were obtained when the F-region maximum plasma frequency, given by the value of foF2, was close to the frequency of the heater wave. Eglitis et al. (1998) compared the drift speeds of artificially generated FAIs as measured by CUTLASS and EISCAT and found a close correlation between the two.

Hysell et al. (1996) examined results obtained from a modification experiment conducted using the Sura heater in Russia. After heater switch off, the decaying FAI backscatter power profiles, seen using the UTR-2 radio telescope in Ukraine, were found to be consistent with two time constants. Yampolski et al. (1997) also examined results from the

Sura heater. HF pulsed and continuous wave observations of FAIs over the heater were made and a variety of effects were seen, including the evolution of irregularities and turbulence contained within the heater volume.

3.4.1 Observations of Anomalous Absorption

Anomalous absorption is a generic term that describes processes that result in a reduction in the amplitude of radio waves reflected from the F-region. It is a well-known effect associated with ionospheric modification by high power radio waves, although it occurs for all electromagnetic waves that reach the upper-hybrid height. It is characterised by the reduced amplitude of diagnostic waves and is explained by the scattering of electromagnetic waves into electrostatic waves, thus removing energy from the incident electromagnetic wave. Various measurements of anomalous absorption have been made, including those from diagnostic transmitter/receiver systems (Cohen and Whitehead, 1970; Utlaut and Violette, 1974). It should be noted that only O-mode radio waves are affected by heater-induced absorption. The heating of the electrons in the F-region observed during ionospheric modification experiments is thought to be dominated by anomalous absorption (Robinson, 1989).

3.4.2 Plasma Lines, Ion Lines and Other Measurements

The work in this thesis focuses upon field-aligned irregularities, and so emphasis has been placed on irregularity observations. However, observations of other aspects related to ionospheric modification also exist and these are now briefly discussed. During the transmission of high-power radio waves, there is an enhancement in the strengths of the ion line and the plasma line, explained in chapter 4, present in the spectra obtained by incoherent radar measurements. Carpenter (1974) identified two types of scatter created during ionospheric modification by the Platteville heater. The first type is characterised by the backscatter frequency being equal to the transmitted radar frequency and is termed centre line scatter. The second type of scatter originates from propagating plasma waves and the backscatter spectrum contains sidebands above and below the radar frequency, displaced by the heater frequency. Langmuir waves affect the backscatter by Doppler shifting it both up and down and these shifted lines are commonly known as plasma lines. In addition to the Platteville measurements, plasma line features were also observed at Arecibo (Gordon and

Carlson, 1974). Further observations include those made by Duncan and Sheerin (1985), Djuth et al. (1986), Robinson (1989) and Isham et al. (1996). Isham et al. investigated the frequency difference between the plasma line enhanced by the heater radio waves and the plasma line enhancement caused by the action of photoelectrons and found evidence that this frequency difference was related to the presence of plasma waves.

Results have also been obtained with instruments that measure at optical wavelengths. Suprathermal electrons generated by Langmuir waves that are excited by the heater ought to excite enhanced air glow because of greater collisional excitation of red and green line emission. Such observations have been made (Bernhardt et al., 1989), although there have also been negative results (Henriksen et al., 1984).

Experiments involving sounding rockets made in late 1982, in order to study in situ the magnetic and electric fields of the heater wave and associated heater-excited waves in and around the heated patch. Rose et al. (1985) reported the absence of the expected swelling and the electron temperature followed closely the modulation of the heater power and suprathermal electrons were found only in short bursts.

Satellites can also be used to detect the waves produced by modulated heating of the lower ionosphere that propagate into the magnetosphere and upper ionosphere. The most recent of these was conducted using 3 Hz modulation of the Tromsø heater, with the resulting particle precipitation created by the waves being detected by the FAST satellite (Wright et al., 2000; Robinson et al., 2000).

3.5 Measurements of the Radar Backscatter Auto-correlation Function

Part of the work that will be presented in Chapter 7 concerns auto-correlation functions (ACFs) of backscatter signals from artificially generated FAIs. The theory behind this work was presented in Chapter 2. Villain et al. (1996), following on from work undertaken by Hanuise et al. (1993), conducted a study of ACFs relating to naturally occurring ACFs. The system they used was SHERPA, which has very similar capabilities and specifications to the SuperDARN radars (Greenwald et al., 1995) including the CUTLASS system that is described in Chapter 4. Villain et al. found that 80% of the ACFs were best fitted by Lorentzian decay profiles, with the remaining 20% being more accurately described by Gaussian decay profiles.

3.6 Summary

This chapter has served to highlight the previous research that has been carried out regarding naturally occurring and artificially generated FAIs in the D/E and F-regions. Frequently observed E-region echoes, Type I and Type II, were reviewed, together with other echo types, i.e. Type III and Type IV, and their characteristics were presented. Possible observations of the EPCI, consisting of radar studies and rocket campaign measurements, were then presented. Observations of artificially generated FAIs occurring mainly in the F-region were reviewed and other associated effects were briefly described.

Chapter 4

Instrumentation and Experimental Techniques

4.1 Introduction

Chapters 2 and 3 described the theoretical aspects of the generation of FAIs and previous work on their detection. This chapter describes the radio systems that detect ionospheric irregularities used to collect the data used in this thesis, together with a system that creates irregularities.

The ionospheric plasma is located at altitudes of a few hundred kilometres and, apart from rockets and satellites that only make measurements sporadically, in situ measurements are difficult to obtain. Radar systems provide a means of obtaining information about ionospheric parameters by remote sensing and the transmitted radio waves are scattered by plasma waves and irregularity structures in the ionosphere.

There are two types of radar system described in this chapter, coherent backscatter radar systems called CUTLASS (Milan et al., 1997a) and STARE (Greenwald et al., 1978), and an incoherent backscatter system called EISCAT (Rishbeth and Williams, 1985). CUTLASS operates in the HF range of 8-20 MHz, the EISCAT radars operate at various frequencies in the VHF, from 30-300 MHz, and UHF bands and STARE operates at around 140 MHz. An HF ionospheric heating facility that is collocated with the EISCAT radar systems is described in addition to the radar systems.

The geographic location of the systems discussed in this chapter is shown in figure 4.1, together with the field-of-view of the radars. It contains the EISCAT UHF, VHF and heating facility, all located near Tromsø, Norway. The EISCAT site is about 1000 km away from CUTLASS Finland and about 2000 km away from CUTLASS Iceland.

4.2 Coherent and Incoherent Radar Scatter

4.2.1 Forward Scatter and Backscatter

Bragg scatter is observed when the scattered radio waves from irregularity structures combine constructively. This situation is similar to X-ray diffraction from solid crystalline

arrangement, where the Bragg condition is satisfied, Figure 4.2 shows the scattering of radio waves from F₂ when the Bragg condition is satisfied.

Consider the case when k_i is the wave-vector of the incident radio waves and k_s is the

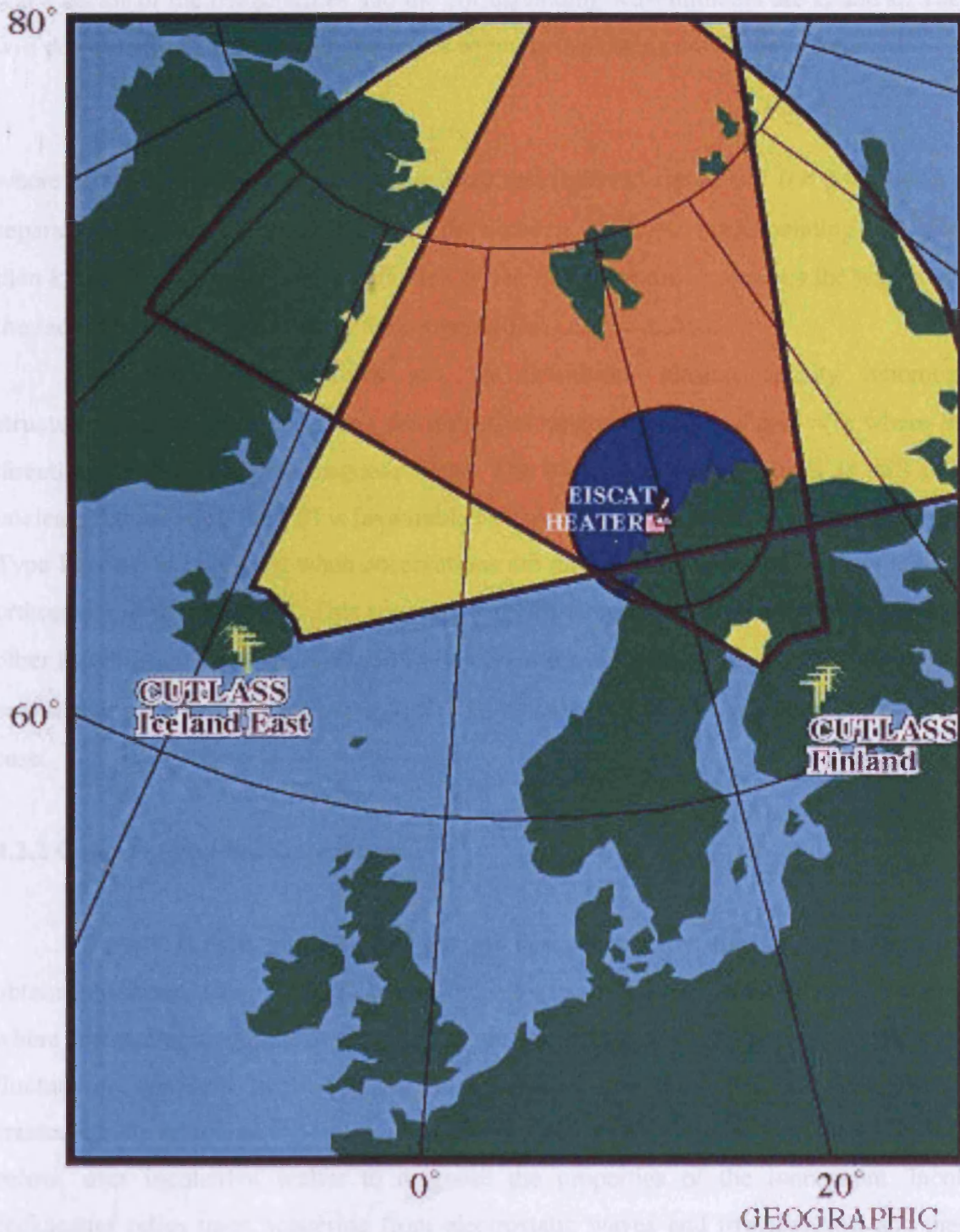


Figure 4.1: The location and experimental arrangement of CUTLASS and EISCAT. The heating facility is co-located with the EISCAT transmitter/receiver dish, Tromsø, Norway.

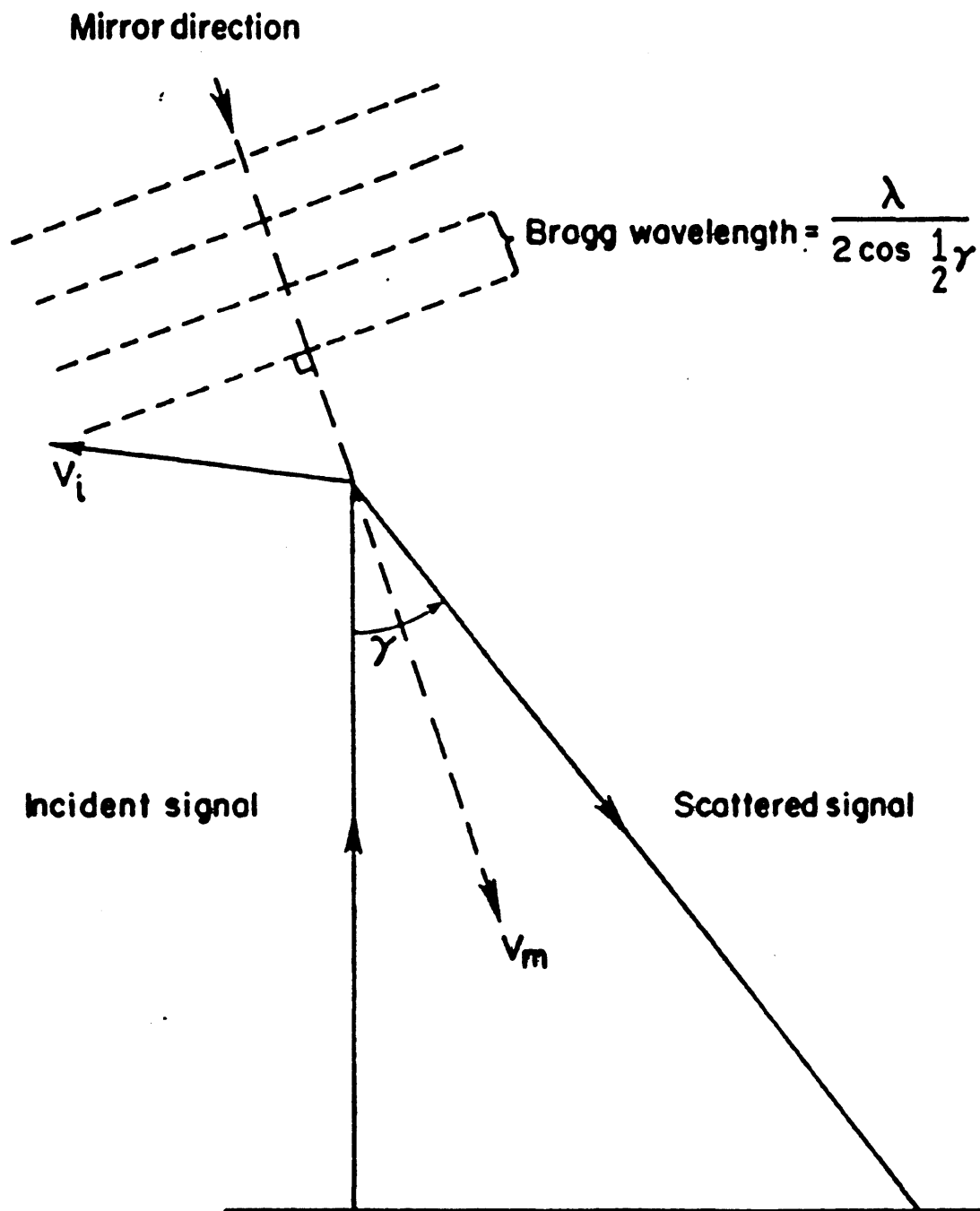


Figure 4.2: Bragg backscatter corresponding to the forward scatter case, where the receiver site is spatially separated from the transmitter site. Bragg backscatter is utilised by both coherent and incoherent radar systems (Rishbeth and Williams, 1985).

Weakly ionised plasma consists of a mixture of ions, electrons and neutral particles. The presence of positive charges gives rise to electrostatic shielding around each electron, thus cancelling out electrostatic effects. This is called Debye shielding and there is a characteristic scale length associated with this shielding process, called the Debye length, and is defined as follows

$$L_D = \left(\frac{\epsilon_0 k_B T_e}{e^2 n_e} \right)^{\frac{1}{2}} \approx 69 \left(\frac{T_e}{n_e} \right)^{\frac{1}{2}} \quad (4.2)$$

where e is the charge of an electron and T_e and n_e are the electron temperature and electron number density, respectively. The size of the Debye length in the ionosphere varies from a few millimetres to tens of centimetres. Basically, for scale lengths much smaller than the Debye length, particles may be considered to be isolated and not affected by each other electrostatically.

True incoherent scatter would result from electromagnetic radiation with wavelengths much smaller than the Debye length, where the electrons are treated as isolated particles, and is an example of Thompson scatter. However, this treatment is invalid because the electrons are coupled to the ions and hence cannot be treated as individual particles. For wavelengths much larger than the Debye length, scattering occurs from electrostatic waves that are generated by thermal ion motion and electrostatic coupling. This type of scattering process is actually quasi-coherent scattering, although it is known as incoherent scatter, where the backscatter is again of the Bragg type as discussed above.

An incoherent scatter spectrum is constructed from the backscattered radio waves received by the radar. This spectrum contains parts originating from scattering processes involving ion and electron acoustic waves propagating towards and away from the radar. The ion lines in the spectrum, caused by scattering from ion-acoustic waves, are Doppler shifted by a few kHz, whereas the electron-acoustic waves cause electron lines that are shifted by a few MHz. The ion lines are broadened by Landau damping because the ion-acoustic wave velocity lies within the Maxwellian distribution of the ions. This allows broadening to take place, leading to the familiar double-humped spectrum. The electron lines (plasma lines) are not broadened by Landau damping. Also, the entire spectrum may be shifted due to bulk motion of the plasma. The lines present in the spectrum are all a result of backscatter from electrons and the ion signature is present because the electrons are coupled to the ions. An incoherent scatter spectrum is shown in figure 4.3.

4.3 The CUTLASS Radar System

4.3.1 CUTLASS Overview

SuperDARN is a network of 12E radars (Greenwald et al, 1995) that are designed to investigate the coupling between the ionosphere and the magnetosphere. The CUTLASS (Co-

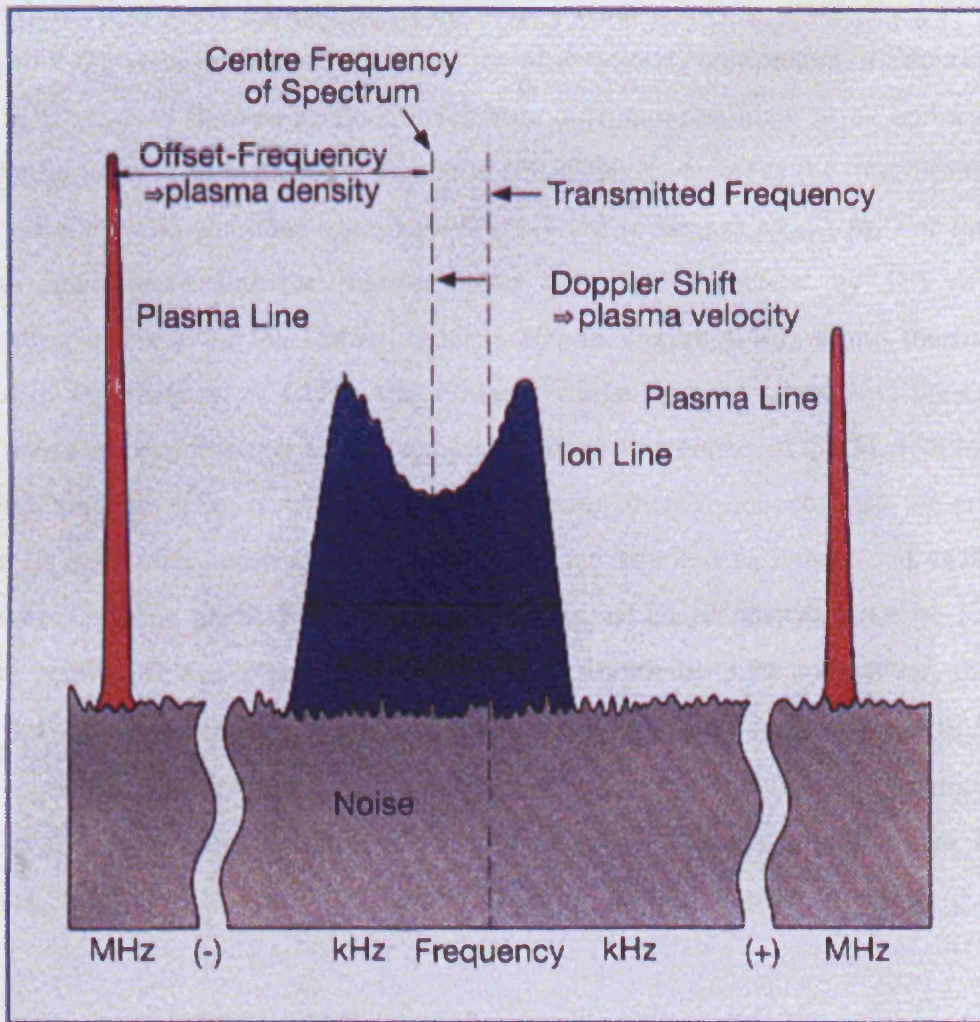


Figure 4.3: A typical incoherent scatter spectrum, from which parameters such as the ion-acoustic speed and electron density may be obtained (EISCAT operations brochure, 1995).

The frequency range of CUTLASS is such that the radio waves suffer refraction by magnetospheric plasma as they propagate through it. The effect is more pronounced for higher altitudes, i.e. refraction in the F-region is more severe than that in the E-region. The refraction increases the range over which orthogonality of the radar beam with the terrestrial

4.3 The CUTLASS Radar System

4.3.1 CUTLASS Overview

SuperDARN is a network of HF radars (Greenwald et al, 1995) that are designed to investigate the coupling between the ionosphere and the magnetosphere. The CUTLASS (Co-operative UK Twin-Located Auroral Sounding System) radars, sited at Hankasalmi in Finland and Pykkvibær in Iceland, constitute the most easterly component of SuperDARN.

There are two antenna arrays at each site, a 16-antenna main array and a 4-antenna interferometer array. The main array transmits and receives, whereas the interferometer array can only receive. The antennae within each array are separated by 15 m. For the Finland radar, the main array and the interferometer array are separated by 185 m and the corresponding distance for the Iceland radar is 100 m. Figure 4.4(a) shows the main array, composed of 16 antennae, of CUTLASS Finland, whilst figure 4.4(b) shows the main array together with the interferometer array, which comprises 4 antennae, of CUTLASS Iceland.

The antenna array is phased, i.e. the phasing matrix concentrates the transmitted power in 16 azimuthal pointing directions, which are labelled as beams and each beam is divided into 75 range gates. Hence the field-of-view of each radar consists of 1200 range cells. The centres of the beams are separated in azimuth by 3.24° . However, the angular width of the beams, in azimuth, is frequency dependent and varies from about 3° to 5° .

The range of the scatter is determined from the time taken for the transmitted power to travel to and return from the target. The range gates are typically 45 km in size, leading to a maximum range of 3550 km, and the range of the backscatter return is given by

$$r = r_f + r_l N \quad (4.3)$$

where r_f is the range to the first gate, r_l is the gate length and N is the number of the range gate. N ranges from 0 to 74, corresponding to the 75 range gates and r_l is either 15 km or 45 km depending on the mode. In the study presented in chapter 6, the myopic scan mode, designed to examine near-range processes more fully, was the main mode used and r_l was 15 km.

The frequency range of CUTLASS is such that the radio waves suffer refraction by the ionospheric plasma as they propagate through it. The effect is most pronounced for higher altitudes, i.e. refraction in the F-region is more severe than that in the E-region. The refraction increases the range over which orthogonality of the radar beam with the terrestrial

magnetic field may be observed, such that it is far larger than that of VHF radar systems, e.g. STARR.

Data are collected on a burst-by-burst basis and the dwell-time, the time for which pulses are collected from a particular direction, is usually 7 seconds. For 10-beams, it follows



Figure 4.4(a): The CUTLASS Finland array. The main array is visible in this photograph.



Figure 4.4(b): The CUTLASS Iceland array. Both the main array and the interferometer array are shown.

magnetic field may be obtained, such that it is far larger than that of VHF radar systems, e.g. STARE.

Data are collected on a beam-by-beam basis and the dwell-time, the time for which data are collected from a particular direction, is usually 7 seconds. For 16 beams, it follows that a complete scan is performed in 112 s. However, the scanning schedule is arranged such that new scans begin on a minute boundary, i.e. there are 8 seconds of idle time. In addition to the 7-second normal scan mode, higher resolution 1-second and 3-second scan modes also exist.

4.3.2 The CUTLASS Pulse Sequence

The CUTLASS system derives backscatter parameters from the collected return signal. It does this by utilising signal processing techniques that calculate quantities from the auto-correlation function, or ACF, which is derived from the backscattered signal received by the radar.

SuperDARN radar systems transmit and receive a standard pulse scheme consisting of 7 pulses. In order to appreciate fully the construction and treatment of this pulse scheme, it is useful to define a few characteristic times. The following discussion is based upon a normal scan. The length of the range gate is given by $cT_p/2$, where T_p is the pulse length, typically 300 μs and corresponding to 45 km range gates. Therefore, there is a 45 km ambiguity in the position of the backscatter. A similar expression applies to the actual range of the return, $cT_f/2$, where T_f is the time of flight of the radio waves to the target and back. The basic lag separation, which is the smallest time difference between pulses, is 2400 μs . This is important for the calculation of the ACF, as described below. The third important time scale is the integration time and gives rise to the temporal resolution of the data. This is just given by the dwell-time, 7 seconds for the normal scan, since this is the time between measurements being made. Figure 4.5 shows the pulse sequence and the lags that are used to calculate the ACF.

4.3.3 Auto-correlation Functions (ACFs)

To study how the ACF is related to the properties of irregularities, it is helpful to consider the simplified situation where the backscatter return pulses all emanate from the same plasma irregularity located at a fixed point in space. The return signal from a single

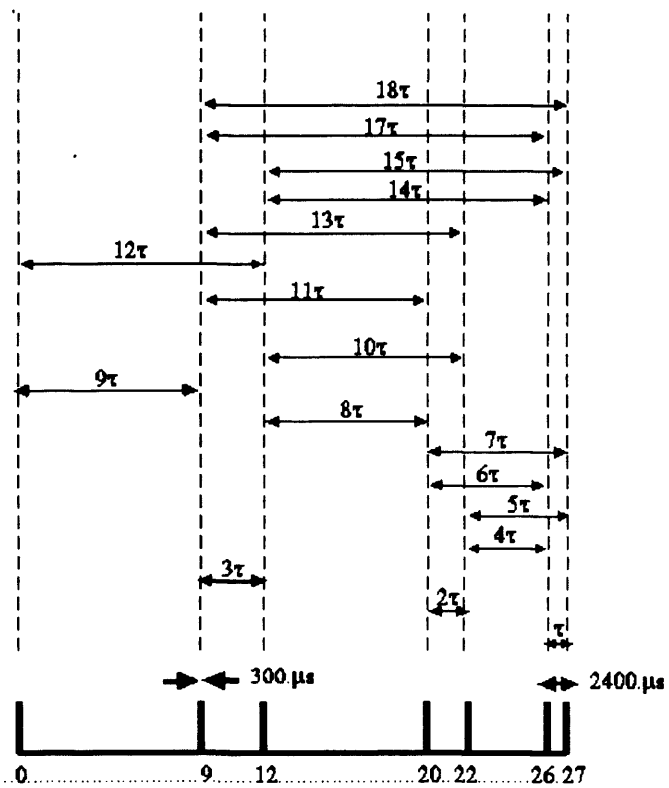


Figure 4.5: The SuperDARN pulse scheme. The standard pulse sequence consists of seven pulses. The pulse is $300\ \mu\text{s}$ in length and the smallest sampling time is usually $2400\ \mu\text{s}$. The lags used to obtain the ACF are also shown. The ACF is calculated by calculating products of phase and amplitude from various pulse pairs (Provan, 1998).

pulse, from which little physical information is obtained because the evolution of the irregularity cannot be determined, is given by

$$R(t) = A(t)e^{i(\omega t + \phi)} \quad (4.4)$$

Combining this with a reference signal, given by $R_f(t) = e^{-i\omega t}$, the following expression results

$$\langle R_f^* R \rangle = A(t)e^{i\phi} \equiv A(t) \cos \phi + iA(t) \sin \phi \quad (4.5)$$

giving an expression for the phase and amplitude parts of the signal. Defining the real part as x and the imaginary part as y results in the following expressions for amplitude and phase

$$A(t) = \sqrt{x^2 + y^2} \quad (4.6)$$

$$\tan \phi = \frac{y}{x} \quad (4.7)$$

To calculate the full ACF, it is only necessary to consider all the pulse pairs and their correlation products, leading to

$$F(n, t) = \langle R^*(t)R(t + n\tau) \rangle \quad (4.8)$$

where n is a non-negative integer corresponding to the lag number and τ is the lag time.

For the simplified case considered here, the temporal variation of the ACF obtained from the irregularities may be described by

$$I(t) = I_0 e^{-i(\omega + i\gamma)t} \quad (4.9)$$

The amplitude of the ACF is a decaying sinusoid, with a period of $2\pi/\omega$ and a decay rate of γ . This assumption is accurate for samples from a fixed irregularity region that can be described by (4.9). Thus, irregularity properties could be extracted directly from the ACF.

However, the actual return from the radar is more complex. A scattering volume is defined by the range extent for a range cell, together with the angular beam widths in azimuth and elevation. The scattering volume contains irregularities of different wavelengths and amplitudes, which grow, decay and propagate at different rates. The detection of these irregularities changes the ACF such that it does not correspond to the idealised situation given by (4.9). Due to the nature of the transmission process for many pulses, there will inevitably be cross-range noise and this may affect the quality of the data. Cross-range noise occurs when backscatter from different ranges reaches the radar simultaneously, leading to ambiguity regarding the range of the backscatter.

To obtain decorrelation information, it is necessary to fit a function to the ACF, thus allowing backscatter parameters to be obtained from it. The two types of function that are usually used correspond to exponential and Gaussian decorrelations. The exponential

decorrelation corresponds to a Lorentzian spectrum and the Gaussian decorrelation corresponds to a Gaussian spectrum and this relationship follows from Fourier transform theory. As an example, expressions for the decorrelation profiles are as follows

$$\text{Exponential} = e^{-i(\omega-i\gamma)t} \quad (4.10)$$

$$\text{Gaussian} = e^{-i\omega x - (\sigma)^2} \quad (4.11)$$

where the spatial and temporal variations correspond to all the irregularities whose effects are detected. In addition to these, a function that approximates the two common decorrelation profiles, for the limits of small and large decorrelation time, may be fitted. The theory behind this was described in chapter 2 and results using it are presented in chapter 7. Figure 4.6 shows the relationship between the ACF and the spectrum. Together they form a Fourier transform pair. The spectral width corresponding to the exponentially decorrelating ACF is usually taken as 2γ , whereas a common value for the spectral width corresponding to the Gaussian ACF, is given by 3.3σ (Baker et al., 1986), with γ and σ defined by (4.10) and (4.11).

Another way to obtain information is to consider moments of the spectrum. As an example, the first moment is given by

$$M_1 = \varpi = \int_{-\infty}^{\infty} \omega F(\omega) d\omega \quad (4.12)$$

and corresponds to the mean Doppler shift, from which the mean phase speed is obtained. However, this is difficult in practice and other techniques are used to obtain information from the ACF. For example, the Doppler velocity may be obtained by performing a linear fit on the phase values corresponding to various pulse pairs. If the irregularities are correlated over longer than the travel time, then the phase speed is related to the phase change that is calculated from a comparison of the pulse signals. The following expression then applies

$$\Delta\phi = \frac{2T_p V_{ph}}{\lambda} 2\pi \quad (4.13)$$

where $2T_p V_{ph}$ is the distance moved by the phase front provided the irregularities remain correlated for longer than T_p . Also, V_{ph} is the phase speed of the observed plasma irregularity.

4.3.4 Interferometric Techniques for the Determination of Altitude

The interferometer array was mentioned above when the configuration of the radar arrays was discussed. The functions of the interferometer are described in detail by André et al. (1998) and, especially, Milan et al. (1997b). This work concentrated upon, respectively,

Date: 09-10-86 Time: 05:48:40 Beam: 13 Freq: 12.4 MHz

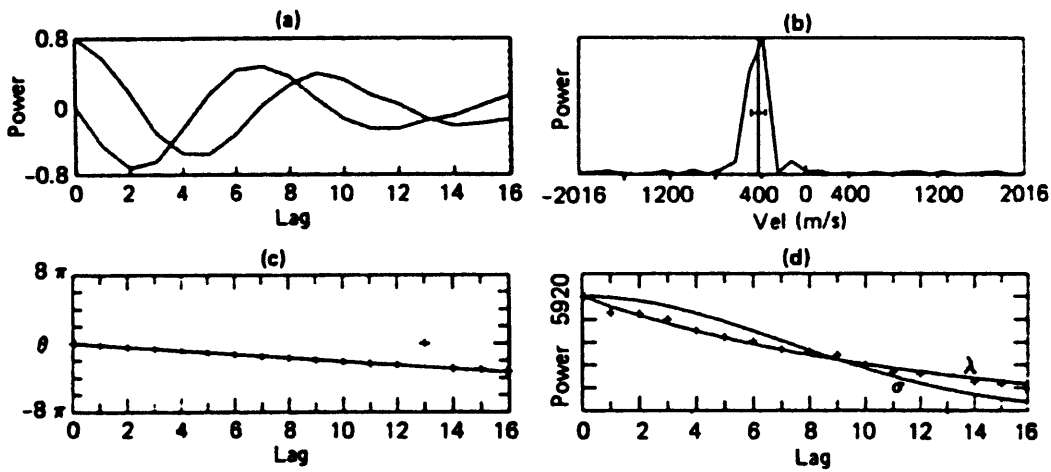


Figure 4.6: A summary of ACF and spectrum relationships (Villain et al., 1987). (a) The real and imaginary parts of an ACF. (b) A Doppler spectrum obtained from a Fourier transform of the ACF. (c) Phase as a function of lag (d) Power variation of the ACF as a function of lag.

the role of the interferometer in detecting and correctly identifying backscatter from meteor trails, and also backscatter originating from behind the radar. The following description of the interferometer follows the approach undertaken by Milan et al.

The CUTLASS interferometer consists of 4 receiving antennae and these are situated either behind or in front of the main array. The backscattered signal arrives at the interferometer array at a slightly different time to that taken to reach the main array. This time difference leads to a phase lag, Ψ , given by

$$\delta P = \frac{\Psi}{k} = \frac{\Psi \lambda}{2\pi} \quad (4.14)$$

where k is the wavenumber of the return signal and λ is the corresponding wavelength. Figure 4.7 shows a schematic of the main and interferometer arrays, together with an example of the beam direction. Using spherical geometry, it follows from $\angle BOC$ that $d' = d \cos \phi$, where d' is the projection of the path difference onto the array separation and d is the array separation. Also, ϕ is the value of the azimuthal angle. The elevation angle is Δ , equal to $\angle AOB$, and it follows that

$$\cos \Delta = \frac{\delta P}{d'} = \frac{\Psi}{kd \cos \phi} \quad (4.15)$$

The azimuthal pointing direction is a function of the elevation angle, from which the following relationship is derived

$$\cos^2 \Delta \cos^2 \phi + \sin^2 \Delta = \cos^2 \phi_0 \quad (4.16)$$

where ϕ_0 is the azimuthal pointing direction when $\Delta = 0$. Combining the previous two expressions leads to an expression for the elevation angle

$$\sin \Delta = \left(\cos^2 \phi_0 - \frac{\Psi^2}{k^2 d^2} \right)^{\frac{1}{2}} \quad (4.17)$$

This is the primary equation used for interferometric analysis. There are problems with this approach as $\lambda \ll d$ and hence $\Psi \gg 2\pi$. This leads to 2π ambiguities when trying to determine the phase lag. The phase lag measured by the radar is Ψ_0 , where $-\pi \leq \Psi_0 < \pi$, and Ψ is related to Ψ_0 by

$$\Psi = \Psi_0 + 2n\pi \quad (4.18)$$

and n is a non-negative integer to be determined. Ψ takes its maximum value when $\Delta = 0$, leading to

$$\Psi_{\max} = kd' = kd \cos \phi_0 \quad (4.19)$$

The value of θ is usually obtained by assuming that the main phase lag lies between the maximum allowable phase lag and the first of the 3 π ambiguities. Therefore

$$\theta_{max} = 2\pi - 4\pi \lambda / P_{max} \quad (4.20)$$

This assumption is true when $d < \lambda_{max}$, where λ_{max} is the value of the elevation angle corresponding to $P = P_{max} = 2\pi$. From this, the following relationship may be obtained

$$\sin \theta_{max} = \frac{2\pi}{\lambda_{max}} \quad (4.21)$$

As mentioned above, $d = 100$ m for CUTLASS Iceland and $d = 185$ m for CUTLASS Finland. These values of the array separation lead to $\lambda_{max} = 45^\circ$ and 35° , respectively, for a frequency of 10 MHz. If the return signal has $d > \lambda_{max}$ then it is aliased and such data may not be usable by default.

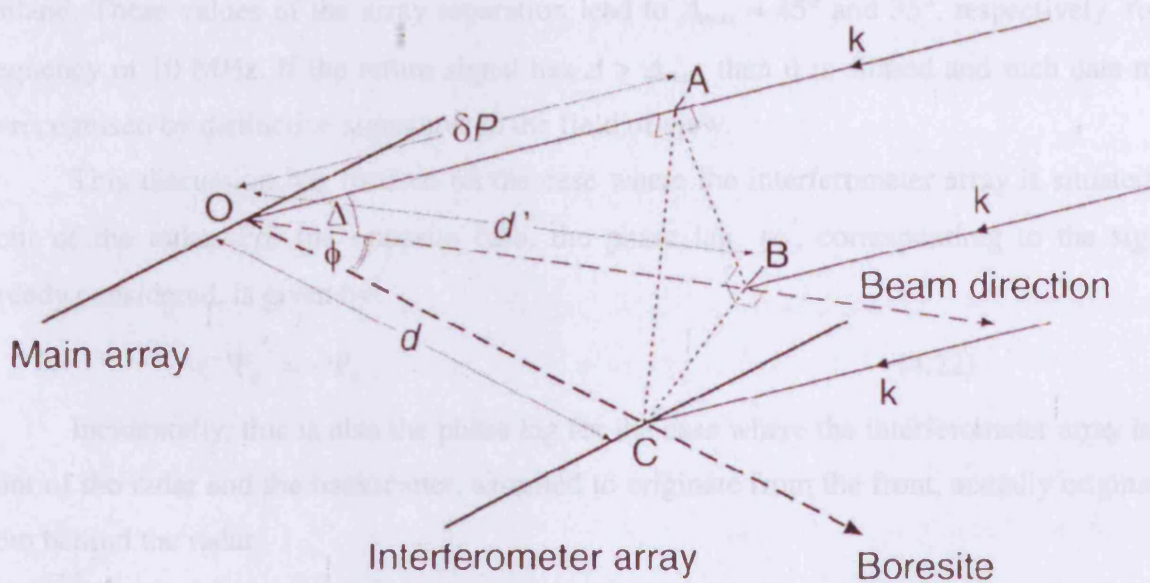


Figure 4.7: The spherical geometry that is applied in order to calculate the elevation angle of backscatter return received by the main and interferometer arrays. By applying basic assumptions regarding the propagation of the signal, the altitude of the backscatter may then be calculated (Milan et al., 1997).

where h is the altitude of the target, R is the radius of the Earth, r is the range to the backscatter signal and θ the elevation angle in degrees. It should be noted that the determination of the altitude using the spherical propagation of the radio waves through the ionosphere. Although this is a valid approximation at lower altitudes, it is not as reliable at higher altitudes, e.g. for the F-layer. This is because the amount of refraction is higher at higher altitudes, as the radio waves have to travel through a larger portion of the ionosphere.

The calculation of the altitude is important as it helps to determine the origins of the backscatter, i.e. possible ionospheric mechanisms that generate irregularities may be identified. The utility of calculating the altitude will be shown in chapter 5, where backscatter return

The value of n is usually obtained by assuming that the true phase lag lies between the maximum attainable phase lag and the first of the 2π ambiguities. Therefore

$$\Psi_{\max} - 2\pi < \Psi \leq \Psi_{\max} \quad (4.20)$$

This assumption is true when $\Delta < \Delta_{\max}$, where Δ_{\max} is the value of the elevation angle corresponding to $\Psi = \Psi_{\max} - 2\pi$. From this, the following relationship may be obtained

$$\cos \Delta_{\max} = \frac{\Psi_{\max} - 2\pi}{\Psi_{\max}} \quad (4.21)$$

As mentioned above, $d = 100$ m for CUTLASS Iceland and $d = 185$ m for CUTLASS Finland. These values of the array separation lead to $\Delta_{\max} \approx 45^\circ$ and 35° , respectively, for a frequency of 10 MHz. If the return signal has $\Delta > \Delta_{\max}$, then it is aliased and such data may be recognised by distinctive signatures in the field of view.

This discussion has focused on the case where the interferometer array is situated in front of the radar. For the opposite case, the phase lag, ψ_0' , corresponding to the signal already considered, is given by

$$\Psi_0' = -\Psi_0 \quad (4.22)$$

Incidentally, this is also the phase lag for the case where the interferometer array is in front of the radar and the backscatter, assumed to originate from the front, actually originates from behind the radar.

After the elevation angle has been computed, it may be used to obtain a value for the altitude. This is done by using the cosine rule, with appropriate expressions for the distances involved, leading to

$$h = \sqrt{R^2 - \left\{ 2Rr \cos \left[\frac{(90 + \Delta)\pi}{180} \right] - r^2 \right\}} - R \quad (4.23)$$

where h is the altitude in km, R is the radius of the Earth, r is the range to the backscatter signal and Δ is the elevation angle in degrees. It should be noted that the determination of the altitude assumes rectilinear propagation of the radio waves through the ionosphere. Although this is a valid approximation at lower altitudes, it is not as reliable at higher altitudes, e.g. for the F-region. This is because the amount of refraction is higher at higher altitudes, as the radio waves have to travel through a larger portion of the ionosphere.

The calculation of the altitude is important, as it helps to determine the origins of the backscatter, i.e. possible instability mechanisms that generate irregularities may be identified. The utility of calculating the altitude will be shown in chapter 6, where backscatter return

from lower altitudes, 80 km to 100 km, is presented and a possible explanation in terms of the electron Pedersen conductivity instability is proposed.

4.4 The STARE VHF System

The STARE (Scandinavian Twin Auroral Radar Experiment) radar system is a bistatic coherent VHF system and its components are located at Midsandn near Trondheim, Norway and Hankasalmi, Finland. There are 18 antennae and the radio waves are phased such that 8 pointing directions arise. The field-of-view consists of 8 beams with 50 range gates per beam. The range to the first gate is 495 km and the range gates are 15 km in length. The maximum range is 1230 km. The system operates by taking data at 20 s intervals. All 8 beams are scanned simultaneously and the integration period of the data is 20 s. The frequency of the observing radio waves is fixed at 140 MHz for the Trondheim radar and 143.8 MHz for the Hankasalmi radar.

The system measures three parameters, the Doppler velocity, the backscatter power and the ACF from which the spectral width may be determined. Since STARE is a VHF system, irregularities with much smaller wavelengths are observed. Another effect of the higher frequency is that the radio waves are not refracted to the same extent as those for HF systems. This results in the radar field-of-view being limited to the E-region. The STARE field-of-view is shown in figure 4.8 and the antennae that form the STARE Trondheim radar are shown in figure 4.9.

4.5 The EISCAT Radar System

4.5.1 EISCAT Overview

The EISCAT (European Incoherent SCATter) radar system utilises the principles of incoherent scatter. The particular component relevant to this thesis is the transmitter/receiver system, illustrated in figure 4.10, located at Ramfj rmoen, near Troms , Norway, hereafter called simply Troms . The radar dish is a 32 m diameter paraboloid with an area of about 570 m² and a half-power angular beam width of 0.6°. The dish is steerable in azimuth and elevation. The system can operate at any of 16 frequencies that are spaced at 0.5 MHz intervals around the central frequency of 933.5 MHz. In theory observations from ranges of

STARE antenna lobes

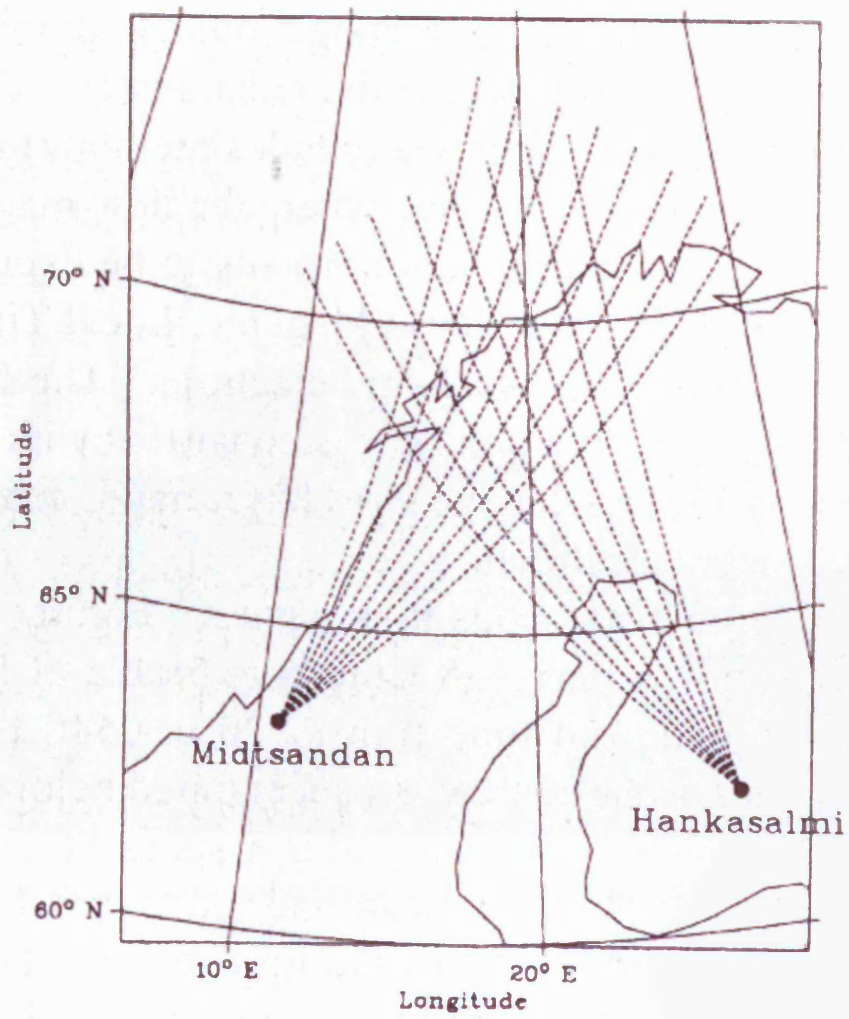


Figure 4.8: The field-of-view of the STARE radar system together with the sites at which the two components of STARE are situated (Nielsen et al., 1999).

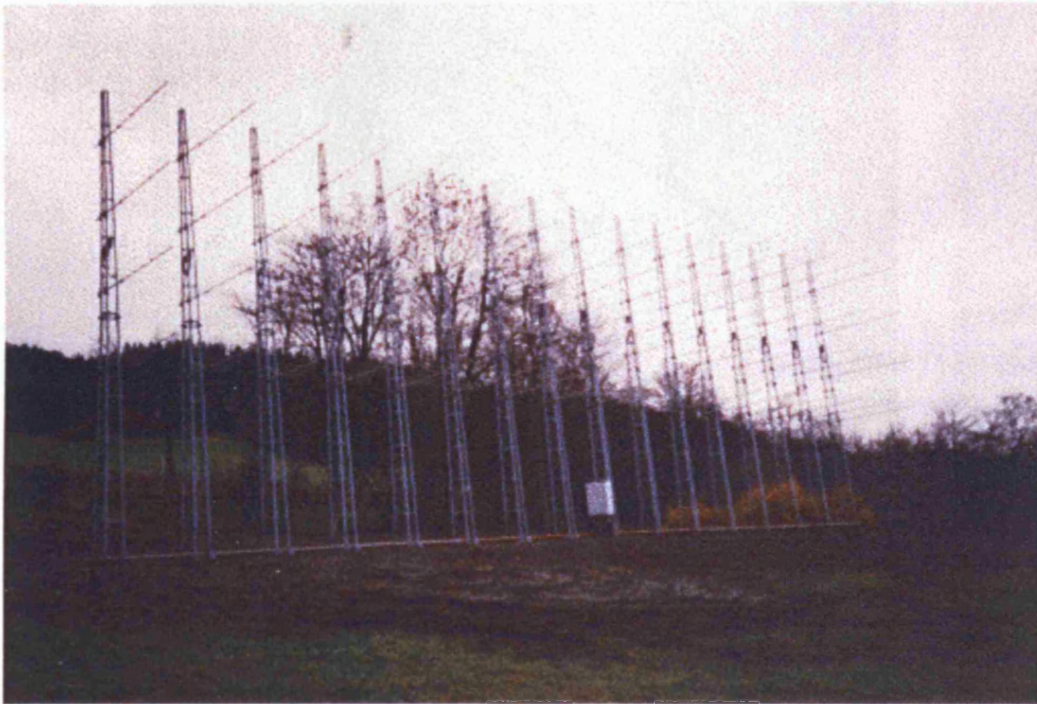


Figure 4.9: The antenna array at the Trondheim site for the STARE radar system.



Figure 4.10: The EISCAT UHF transmitter/receiver dish located at Tromsø, Norway.

80-1500 km ought to be possible, but the power consumption of the radar restricts this range to 600 km.

The transmitter/receiver dish is part of a tristatic UHF system, whose constituents include two receiver dishes, sited at Sodankylä in Finland and Kiruna in Sweden. Because of oblique propagation and the projection of the electric field components onto the observing direction, the remote sites at Sodankylä and Kiruna receive elliptically polarised radiation when circularly polarised radiation is transmitted at Tromsø. A monostatic VHF system is also located at Tromsø and two additional monostatic UHF systems, which comprise the ESR (EISCAT Svalbard Radar), are located at Longyearbyen, Spitsbergen, in the Svalbard archipelago to the north of Norway.

4.5.2 EISCAT Measurement Programs

The EISCAT operating modes are determined by computer programs that control the observation direction, data sampling rate and other characteristics. These programs are divided into Special Programs, designed for specific purposes, and Common Programs, designed to provide a general-purpose data collection. Some of the data discussed in chapter 7 of this thesis were collected whilst CP-1, a common program, was running. The version used in this study is called CP-1-K. It is a program where the remote site receivers sample a spatial volume at an altitude of 278 km, and the pointing direction of the antenna is usually field-aligned at this altitude, but may be varied as appropriate. A single long pulse, power profile and alternating code are all transmitted. The range gates are 22 km in length for the long pulse that is used to measure parameters in the F-region. The data integration time is usually 10 s, but can be shortened to 5 s when required. The power profile is obtained by transmitting a single short pulse to obtain the lag-0 power and the alternating code is a Barker-coded pulse sequence.

As for CUTLASS, the EISCAT system parameters are calculated from an auto-correlation function, or ACF. The values of the lags are calculated by averages and there are fewer estimates of the longer lags. This is because there are fewer return signals that can be correlated to give the longer lags. This leads to a less accurate estimate of the longer lags and an uneven spatial distribution for the longer lags. It is possible to overcome these problems by gating the signal after the ACF cross-products have been evaluated.

If the received signal is gated over a certain length of time, t , there will be a contribution from a height range of ct , where c is the speed of light. This in turn provides a

height resolution of $ct/2$, which must be less than the ionospheric scale height, h , so that the altitudinal dependence of parameters may be measured accurately. This means that the transmission length ought to be less than $2h/c$, implying that for smaller scale heights over which the electron density varies, e.g. the E-region, the pulse length should be smaller. This requirement for short pulses is counterbalanced by the need for a good signal to noise ratio, which requires longer pulses.

4.5.3 EISCAT Derived Parameters

The derivation of parameters from EISCAT spectra and ACFs has been described in some detail by Rishbeth and Williams (1985). The parameter α is important in incoherent scatter theory and appears in the expression for the received backscatter power. It is defined by

$$\alpha = \frac{4\pi L_D}{\lambda} \quad (4.24)$$

where λ is the observing wavelength and L_D is the Debye length. True incoherent scatter corresponds to $\alpha \geq 10$, but the usual case considered is given by $\alpha \ll 1$. The electron number density is proportional to the received power. The separation of the two broader peaks, as shown in figure 4.3, is proportional to the ion-acoustic speed. The ratio of the electron temperature to the ion temperature is related to the width and sharpness of the peaks. As mentioned above, the bulk plasma velocity is determined from the Doppler shift of the whole spectrum. The use of the tristatic system allows a determination of the vector velocity.

Further calculation of parameters continues by fitting the ACF to a function computed from theory. Initially, estimates of parameters are obtained from the ACF, e.g. the value of the ACF at the first minimum is proportional to the ratio of electron and ion temperatures. These latter approximations are used to correct the value of the electron density.

The electron density, ion drift-velocity and ion and electron temperatures are calculated on a routine basis. A number of additional parameters may be derived indirectly from those that are measured directly. A list of the parameters obtained by EISCAT is given in figure 4.11.

PARAMETERS MEASURED BY INCOHERENT SCATTER

Directly-derived parameters:-

Strength of the echo	is proportional to	Electron concentration N
Separation of two peaks	is proportional to	$\sqrt{(T_i + T_e)/M_i}$
Spectral Slope at 1/2-power	is sensitive to	Ion composition (hence M_i)
Sharpness of the peaks	is sensitive to	(T_e/T_i)
Mean Doppler shift	is proportional to	Component of v_p, the plasma velocity
Spectral width (E-region)	is sensitive to	Ion-neutral collision frequency ν_{in}
Spectral Shape (E-region)	depends on	$\Psi_i = \frac{\lambda}{4\pi r_i} = \nu_{in} \lambda \sqrt{\frac{m_i}{2k_B T_i}} = \frac{\nu_{in}}{\nu_{ia}}$

iv) Indirectly-derived parameters:-

(T_i / M_i)	+	M_i	\Rightarrow	Ion temperature T_i
T_i	+	(T_e / T_i)	\Rightarrow	Electron temperature T_e
T_i	+	ν_{in}	\Rightarrow	Neutral temperature T_n
N	+	ν_{in}	\Rightarrow	Pedersen and Hall Conductivity Σ_p and Σ_H
v_p (F-region)	+	Magnetic field	\Rightarrow	Electric field \underline{E}
v_p (F-region)	-	$\underline{E} + \nu_{in}$	\Rightarrow	Neutral wind
Σ_p and Σ_H	-	\underline{E}	\Rightarrow	Pedersen and Hall currents \underline{J}_p and \underline{J}_H
\underline{J}_p	-	\underline{E}	\Rightarrow	Joule heating

Figure 4.11: Directly and indirectly derived EISCAT parameters.

4.6 Ionospheric Modification and the EISCAT Heating Facility

The ionospheric heating facility (Stubbe and Kopka, 1979; Stubbe et al., 1982; Rietveld et al., 1993) is collocated with the EISCAT radar systems situated at Ramfjordmoen, near Tromsø, Norway (69.6° N, 19.2° E, $L = 6.2$, magnetic dip angle $I = 78^{\circ}$). It operates at around 4-8 MHz and is used to generate artificial FAIs. A good description of the heater's technical specifications, together with an overview of operation, is provided by Rietveld et al. (1993) and previous descriptions (Stubbe and Kopka, 1979; Stubbe et al., 1982) were updated in this paper. The heating facility consists of an array of crossed-dipole antennae and is used to transmit high-power radio waves into the ionosphere. The transmitted radio waves then modify the ionosphere leading to the production of waves and instabilities, together with FAIs. Figure 4.12 shows a picture of the EISCAT site and the UHF and VHF antennae are clearly visible. The heater array is visible in the bottom left hand corner of the picture. Figure 4.13 shows a schematic layout of the heater experiment, with the heater irregularities being observed by CUTLASS and EISCAT.

4.6.1 The Heater Arrays

The heating facility consists of three antenna arrays. Originally, these were capable of transmitting in a frequency range from 2.75-8 MHz. Array 1 consists of 12 rows of 12 antennae and has a frequency range of 5.5-8 MHz, but, before a storm blew it down, used to be the lowest frequency array. Arrays 2 and 3 contain 6 rows of 6 antennae. Array 2 operates in the frequency range 3.85-5.65 MHz, and array 3 operates in the frequency range 5.5-8 MHz. The heater beam transmitted by array 1 has an angular width of 7° , whereas the beams from arrays 2 and 3 have an angular width of 14.5° . These values for the angular width assume that all transmitters are operating. Figure 4.14 shows an example of the crossed-dipole antenna that is used in the heater array, together with a layout of the three arrays.

4.6.2 The Heater Transmitters

The energy radiated by the heater arrays is supplied by the transmitters, via transmission lines. Each of the 12 transmitters is supplied by a frequency synthesiser and function generator unit. Originally, the specified maximum power of each transmitter was 125 kW, however the actual maximum power is 100 kW. The frequency synthesiser is locked



Figure 4.12: The EISCAT site at Tromsø. The UHF and VHF EISCAT incoherent scatter radars are visible in the upper part of the diagram. The lower left of the picture shows a part of the heater array. This is controlled from the heater building visible in the lower right of the picture.

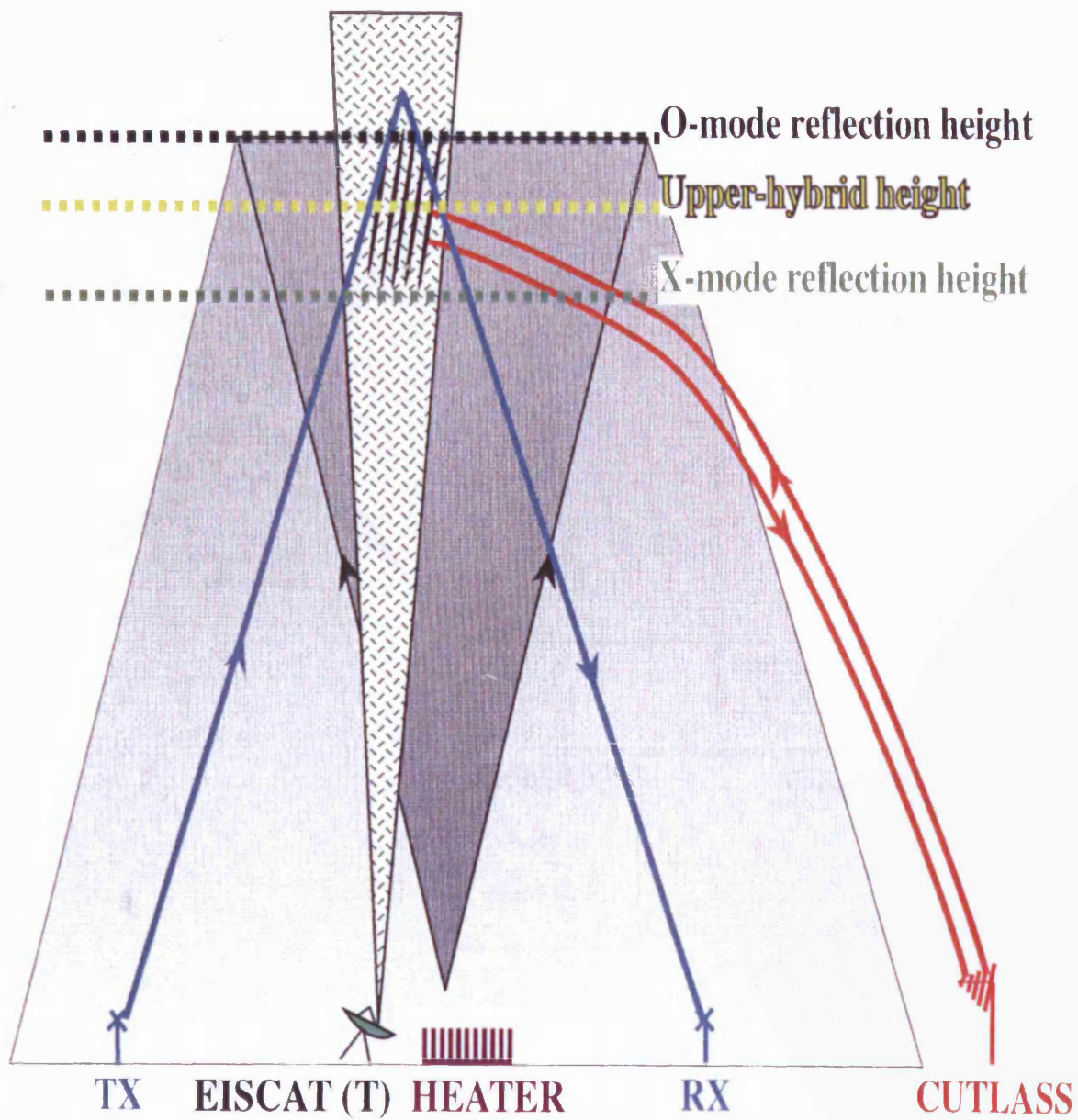


Figure 4.13: The instrumental arrangement for a typical ionospheric modification experiment (Bond, 1997).

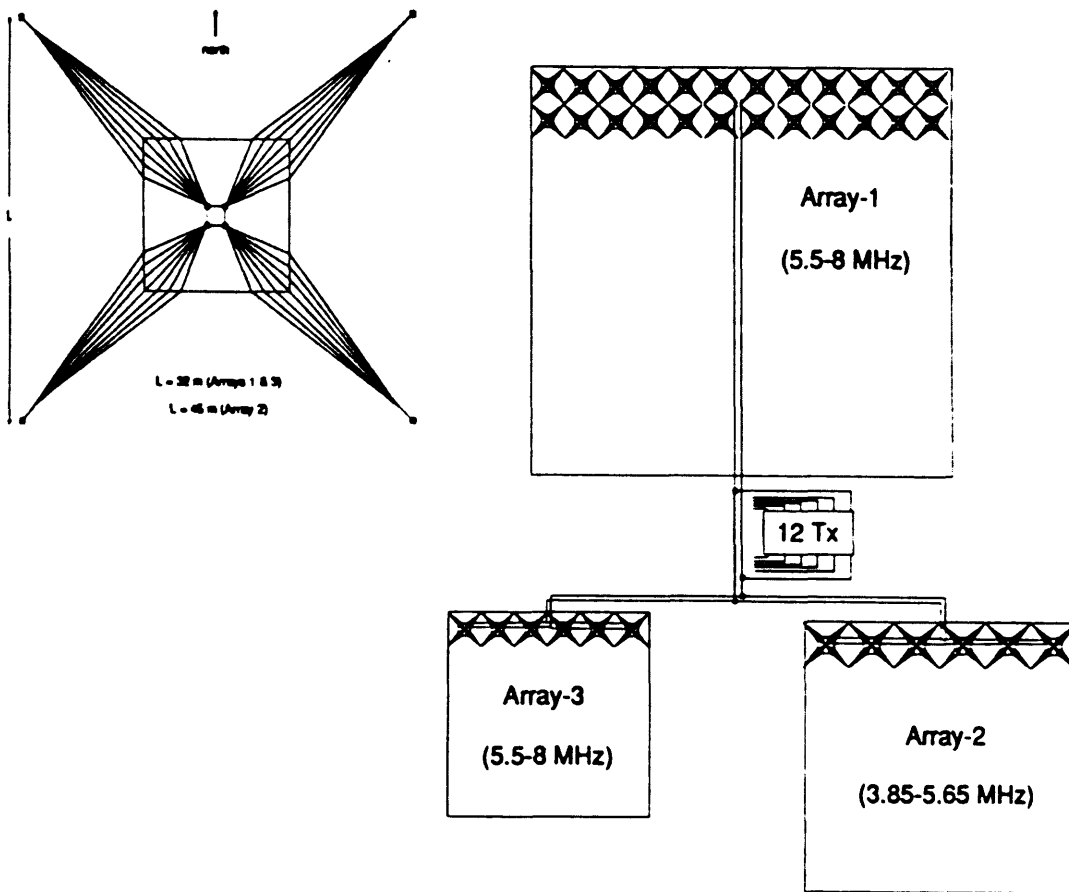


Figure 4.14: The EISCAT transmitter array together with an example of a crossed-dipole antenna (Rietveld et al., 1993).

to a common reference frequency that is locked to the EISCAT clock. The frequency, amplitude and phase of each transmitter may be programmed. This is controlled by a PC, formerly a Commodore PET microcomputer. A pair of transmitters is used to control a row of crossed linear full-wave dipole antennae. One antenna of each pair is fed by one transmitter and the perpendicular linear antenna is fed by the other transmitter. Changing the relative phases between pairs of transmitters allows the direction of the beam to be varied. If fewer transmitters are in operation then the angular widths of the beams increase. The output power should be limited for the larger deflections, as the standing wave ratio and reflected power in the antennae increases as the deflection increases. Also, the circular polarisation of the radiation is effected by introducing a 90° phase-shift between the two halves of each row. For linear polarisation, each of the 12 transmitters can emit different frequencies. However, for circular polarisation, 2 frequencies can be used for groups of 6 transmitters, or 3 frequencies for groups of 4 transmitters, or 6 frequencies for groups of 2 transmitters. The higher harmonics are suppressed by the antenna impedance and the 50 Hz mains hum is also suppressed.

4.6.3 Heater Modulation Types

It is often necessary to modulate the transmitted heater pump wave in some way. This may involve varying the power, polarisation or beam angle. This section describes the various ways in which the output of the heater beam may be modulated. These include modulating the direction as well as the frequency.

The amplitude and phase of the radio frequency signal may be altered by applying a voltage to two inputs on the transmitter and the heater may be switched on and off in this way. Usually, the power is reduced so that it is 37.5 dB below the value of the full power. Sometimes this level of reduction is not large enough and the power may be reduced further by switching in 70 dB of attenuation. After the signal is sent to supply full power to the heater, the time to actually achieve this is 5 μ s. This delay time limits the modulation pulse length to 20 μ s.

For regular modulation sequences, where minimum on or off times of 1 s are required, a microcomputer is used to supply a modulating voltage when complicated modulation patterns are required. The modulation range may be varied from 0.001-9999 Hz for modulated waveforms of fixed frequency or 200-6550 Hz for swept frequencies. Because of resonances in the transmitter power supply, frequencies ranging from 15-200 Hz should not

be used. An example of an experiment that utilises modulation is that where D-region and E-region heating creates waves that stimulate field-aligned particle flow that may be detected by the FAST satellite (Wright et al., 2000; Robinson et al., 2000). Increasing the power in regular steps is a common requirement for experiments and may be done by retuning the heater. This is done most efficiently by supplying the radio frequency synthesiser with a different modulation voltage that is automatically calculated by the computer. This allows 40 power intervals in 2.5% steps to be programmed. Smaller power steps may be obtained by performing the initial tune-up at a lower 'full' power level.

For the case where the polarisation of the radio waves must be altered between X-mode and O-mode, it is only necessary to reverse the phase of the appropriate 6 transmitters and this may be done almost instantly. It is possible to change the pointing direction of the beam in meridional directions by varying the phases between pairs of transmitters driving each row of antennae. In a similar way, the use of varying voltages allows the beam to be widened.

4.6.4 Propagation of Heater Radio Waves

The radiation that propagates through the ionosphere is either O-mode or X-mode polarised. The height at which the radio waves are reflected depends on the plasma frequency of the ionosphere. Reflection occurs when the wave frequency is below the critical frequency. The reflection frequency for X-mode waves in the E-region is labelled as f_xE . Similarly, the reflection frequency for O-mode waves is labelled as f_oE . The corresponding frequencies for the F_1 layer are termed f_oF1 and f_xF1 . Finally, the frequencies of reflection in the F_2 layer, and the most important in terms of heating, are f_xF2 and, especially, f_oF2 . Observations of the effects of O-mode and X-mode heating (Robinson et al., 1997) indicate that O-mode heating is most effective for generating FAIs because, for a given frequency, the altitude for O-mode reflection is higher than the upper-hybrid region and the X-mode reflection altitude is lower. However, X-mode heating is more efficient as regards transferring energy into the ionospheric plasma (Robinson, 1989). The value of f_oF2 gives an indication of the optimum frequency at which to heat. For the present emphasis upon irregularity generation, the process is most effective when a heater frequency just below f_oF2 is used. This is because f_oF2 is the highest frequency that is reflected, and heating just below this frequency will excite the ionosphere at the altitude where the upper-hybrid resonance occurs, leading to the creation of FAIs.

Heating carried out at frequencies less than the F-region maximum plasma frequency, given by the value of foF2, is known as overdense heating, whereas heating conducted at frequencies above the plasma frequency is termed underdense heating. For the case of radio wave propagation in free space, the energy flux, F , and electric field, E , are given by the following expressions

$$F = 7.96 \times 10^{-5} \frac{ERP}{R^2} \quad (4.25)$$

$$E = 0.25 \frac{\sqrt{ERP}}{R} \quad (4.26)$$

where ERP is the effective radiated power measured in kW, F is in W m^{-2} and E is in V m^{-1} , and R is the range from the transmitter in km. The ERP is defined as the antenna gain multiplied by the maximum power transmitted. For arrays 2 and 3 and an altitude of 250 km, typical values are $E = 0.5 \text{ V m}^{-1}$ and $F = 1.5 \text{ mW m}^{-2}$. The actual power delivered to the F-region is dependent upon the amount of absorption in the underlying D-region. This may be quite substantial during auroral disturbances, e.g. substorms and enhanced precipitation, and may act to inhibit heating experiments.

4.7 Summary

The experimental techniques that may be utilised in order to detect ionospheric effects have been presented in this chapter. The main focus has centred on coherent and incoherent radar systems to diagnose the effects that occur in the ionosphere. In addition to this, the heating facility, collocated with the EISCAT system, situated at Ramfjordmoen, near Tromsø, Norway has been described.

Chapter 5

Theoretical Calculations of EPCI Characteristics and Wave-induced Diffusion in the E-region

5.1 Introduction

This chapter contains the results of theoretical calculations concerning two key topics considered in this thesis: the effects of altering the flow and aspect angles on the growth rate and threshold velocity of the D-region electron Pedersen conductivity instability (EPCI), and the simulation of particle trajectories describing a possible anomalous diffusion mechanism.

As described in chapter 2, the EPCI is excited most favourably along the bisector direction between the convection electric field direction and the relative ion-electron drift direction. The effects of changing the flow and aspect angles on the irregularity characteristics have been examined and the results obtained from this analysis are presented below.

The particle trajectories are defined by equations (5.1)-(5.9), given in section 5.3, and describe a possible diffusion mechanism caused by wave-particle interactions that could lead to an enhancement in the anomalous collision frequency. It has been proposed that this enhancement leads to saturation of the Farley-Buneman instability such that the phase speed of E-region Farley-Buneman irregularities is limited to the ion-acoustic speed.

5.2 Combined FBI and EPCI Characteristics

The characteristics of the EPCI for different instability regimes were studied by varying the flow angle for different flow speeds and examining the effect this had on the growth rate. The aspect angle dependence of the EPCI was then determined by increasing the aspect angle, for six values of the flow angle and a fixed drift speed. This procedure was repeated for three different drift speeds. The figures presented below show the characteristics for the theories of the combined FBI/EPCI. The values for the elastic ion-neutral and electron-neutral collision frequencies used to model the altitude dependence of the irregularity characteristics, together with the inelastic electron-neutral collision frequency, were calculated for electron and ion temperatures of 200 K from the equations given in Schunk and Nagy (1978). The values were obtained for altitudes from 50-150 km and derived

properties such as ψ were obtained from these calculated values. The chosen values for the ion and electron temperatures give rise to an ion-acoustic speed of around 340 m s^{-1} , where the isothermal case has been assumed. Finally, the magnitude of the terrestrial magnetic field was taken as $5 \times 10^{-5} \text{ T}$.

5.2.1 Predicted Threshold Velocities given by Two Different Theories

The growth rate for 20 m waves, excited by the Farley-Buneman instability, together with the threshold velocity values are shown in figure 5.1. As for the figures below, the growth rate and flow speed have been plotted for flow angles from -90° to $+90^\circ$. The region of instability in the $k-E-V$ plane is symmetrical about the $E \times B$ drift direction, V , so the results for positive flow angles are identical to those for negative flow angles.

EPCI characteristics are illustrated by comparing the growth rates and the threshold values of the velocities for different flow angles. The flow angle range includes the directions for which the EPCI should be excited most favourably, at -45° and $+45^\circ$, with instability excitation accomplished more easily in the sector containing negative flow angles. Figure 5.2 shows the threshold velocity values for varying flow angle and zero aspect angle for two different regimes. These are a fluid approximation (Robinson, 1998), formulated by perturbing the fluid equations obtained from the kinetic theory and hereafter referred to as the fluid approximation, and a fluid approximation obtained by first perturbing the kinetic equations and then deriving fluid equations from these perturbed kinetic equations (Dimant and Sudan, 1995a, 1995b and 1995c), hereafter called the kinetic approximation. The two approximations may be summarised by equations given in chapter 2, with the kinetic case corresponding to equations (2.13)-(2.16), and the fluid case described by equations (2.17)-(2.20). At altitudes around 120 km, the fluid and kinetic approximations agree very well, with both giving similar results for the values of the threshold velocity. Also, positive and negative flow angles whose magnitudes are equal have the same limiting threshold velocity values, equal to $C_s \sec \theta$, where θ is the flow angle and C_s is the sound speed. Concentrating upon the fluid regime first, it is clear that the threshold velocity values depend on the sign of the flow angle, for a given flow angle magnitude. This figure shows that the threshold velocity at altitudes around 80-85 km in the negative sector is lower than that in the positive sector, thus demonstrating that the instability will be excited in the negative sector more easily. The instability is excited most favourably for $\theta = -45^\circ$, which corresponds to the lowest threshold velocity values at altitudes below 90 km. The situation is more complex for the kinetic

FBI growth rate values

Fluid theory regime

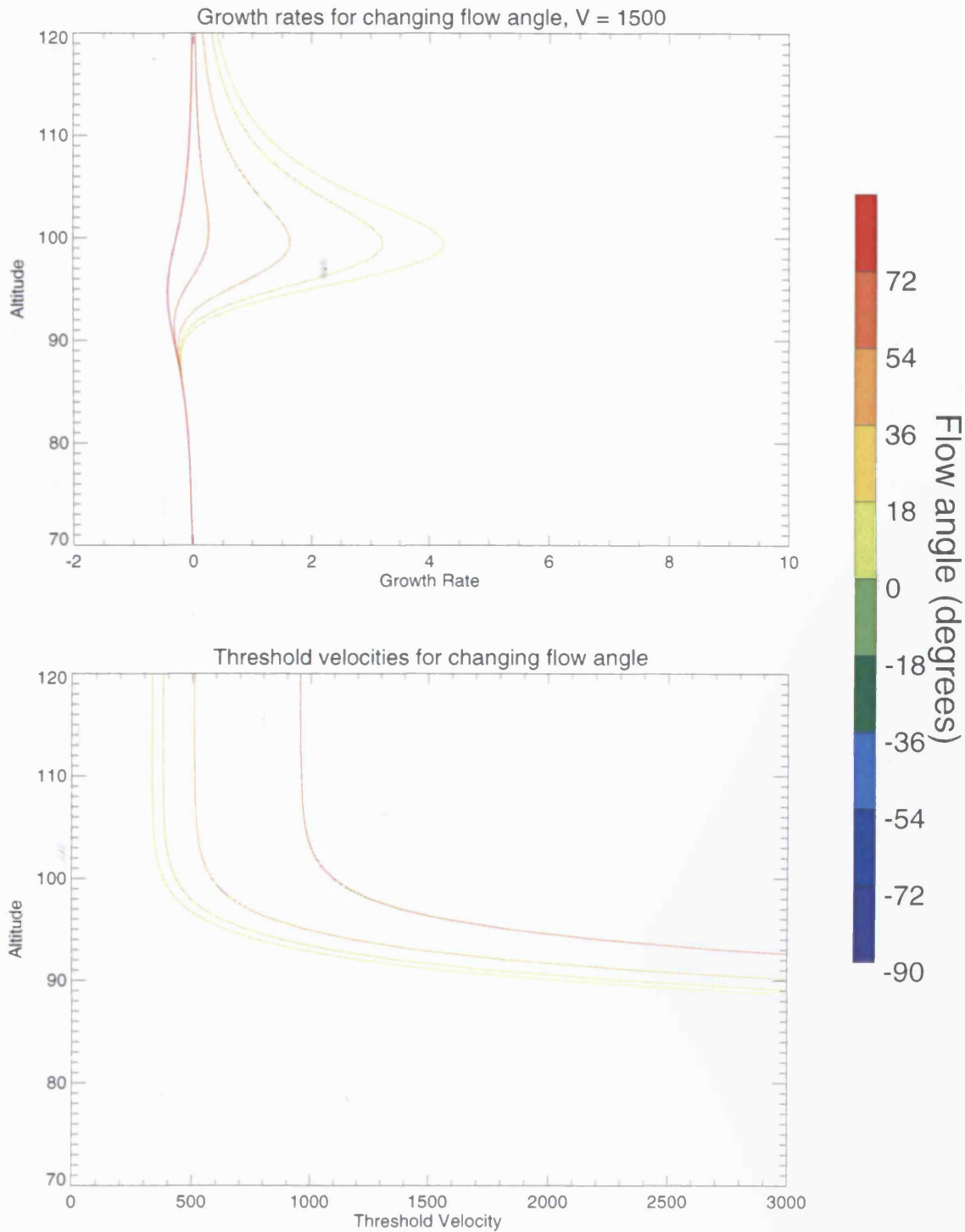


Figure 5.1: The growth rates and threshold velocities for the FBI. A drift velocity of 1500 m s⁻¹ has been used together with 20 m waves.

EPCI threshold velocity values

Fluid and kinetic regimes

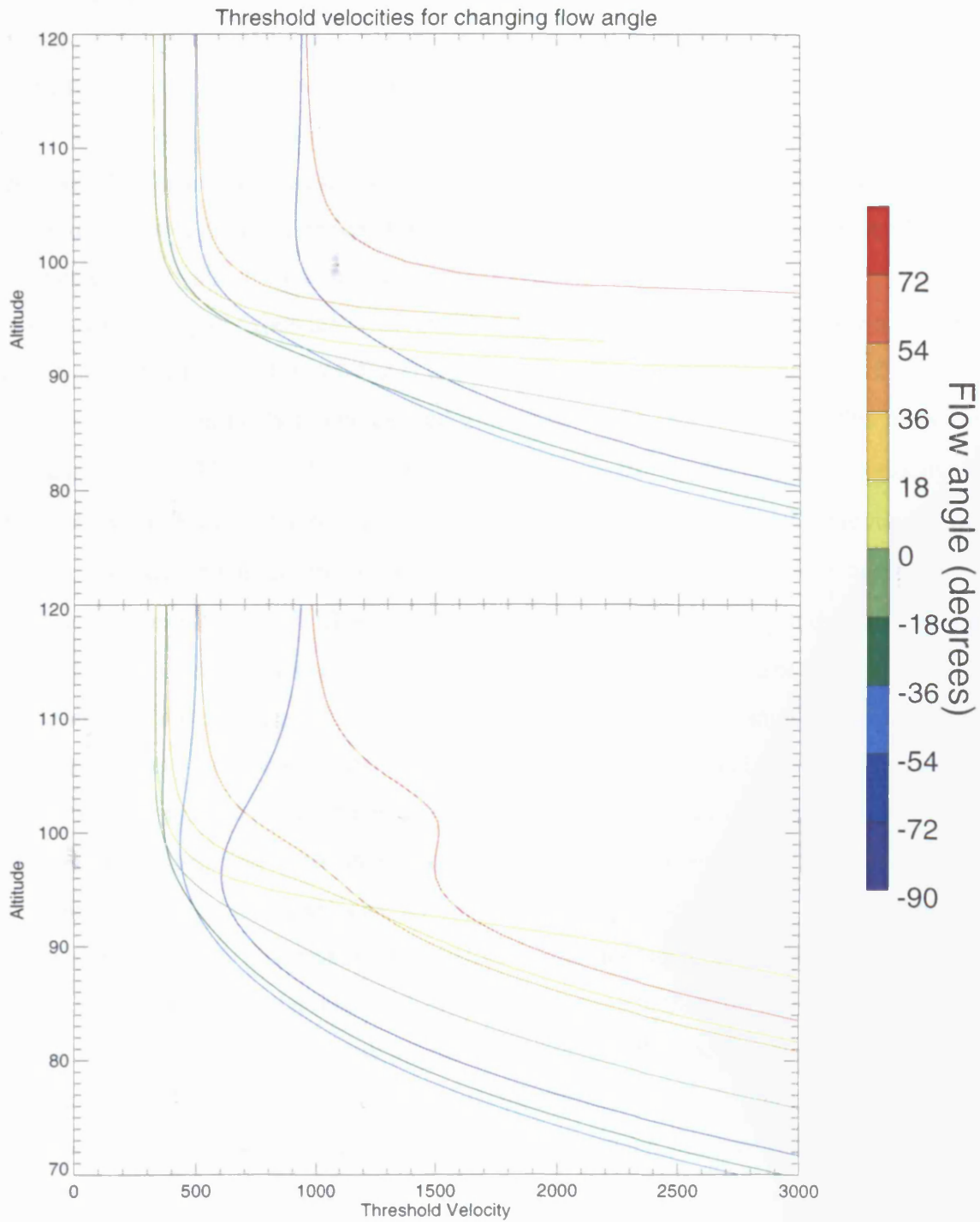


Figure 5.2: The threshold velocities for varying flow angle and zero aspect angle obtained for the fluid and kinetic approximations.

regime. The same limiting threshold velocity values are obtained at altitudes around 120 km. At flow angles around $+70^\circ$, there is an increase in altitude while the threshold velocity varies a little around 1500 m s^{-1} . There is a part of the figure where the curves for flow angles of $+10^\circ$, $+20^\circ$ and $+30^\circ$ almost converge at a point. This is at around 93 km with a threshold velocity value of around 1250 m s^{-1} . Also the overall profile of the threshold velocity curves varies significantly for the positive and negative sectors. The instability is again excited most favourably in the negative sector. The flow angle variation of the growth rate for the two regimes is similar for lower altitudes, with the same overall form and the differences between the fluid and kinetic regimes disappear for higher altitudes. At D-region altitudes the kinetic regime gives a lower value for the threshold velocity.

The aspect angle dependence of the threshold velocities has been shown for the kinetic and fluid regimes in figures 5.3(a) and 5.3(b), respectively. This range includes the angles where the instability should be excited most favourably, -45° and $+45^\circ$. The plots are for flow angle from -75° to $+75^\circ$. There is a local maximum in the threshold velocity at altitudes between 103 km and 109 km. As the flow angle increases from -75° , the maximum descends in altitude and is absent for flow angles of -15° and $+15^\circ$, before again being present at a flow angle of $+75^\circ$. This maximum in the threshold velocity indicates that the instability is more difficult to excite. This maximum was present for aspect angles higher than those shown but its value simply increases. For negative flow angles, the threshold velocity is lower than for positive flow angles, indicating that the instability may be excited more easily in the negative sector. Generally, the instability becomes more difficult to excite for higher aspect angles. The situation is more complex for a flow angle of $+75^\circ$, where there is a maximum in the threshold velocity for zero aspect angle, occurring at 103 km. As the aspect angle is increased, this maximum disappears and another maximum appears at 109 km. For positive flow angles, the threshold velocity values are higher for at D-region altitudes than for the negative sector. The overall profile of the threshold velocities is similar to that in the negative sector. The fluid regime predictions, shown in figure 5.3(b) are similar to those made by the kinetic regime for negative flow angles, although the threshold velocities are higher for a given aspect angle and altitude in the fluid regime. For positive flow angles, the fluid regime predicts that the instability effectively cannot be excited at lower altitudes, since the threshold velocities are very for altitudes below 95 km. This is a marked difference from the prediction made by the kinetic regime.

EPCI aspect angle dependence

Kinetic theory regime threshold velocities

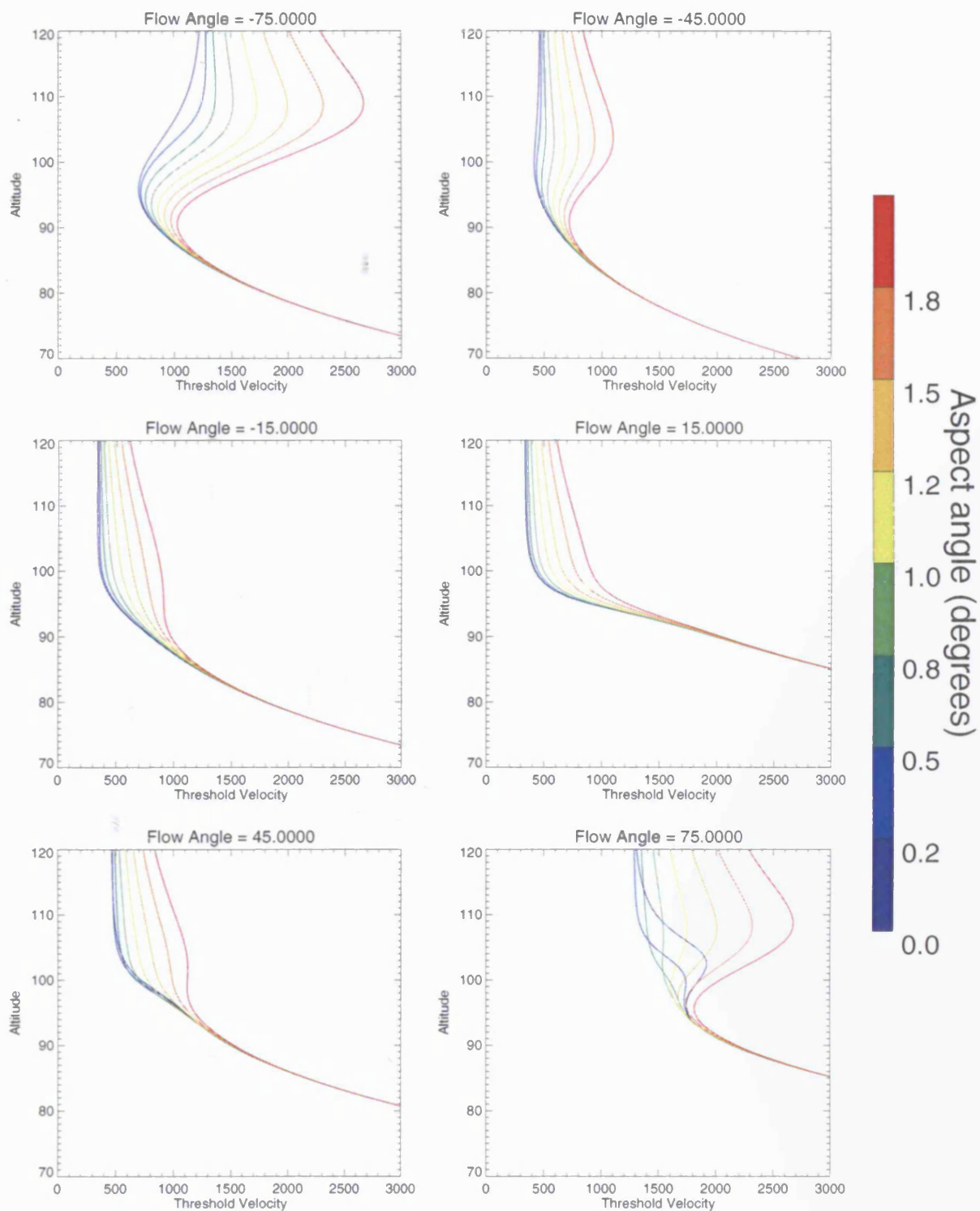


Figure 5.3(a): The kinetic theory aspect angle dependence of the threshold velocity for 6 different flow angles. The threshold is lowest for a flow angle of -45° .

EPCI aspect angle dependence

Fluid theory regime threshold velocities

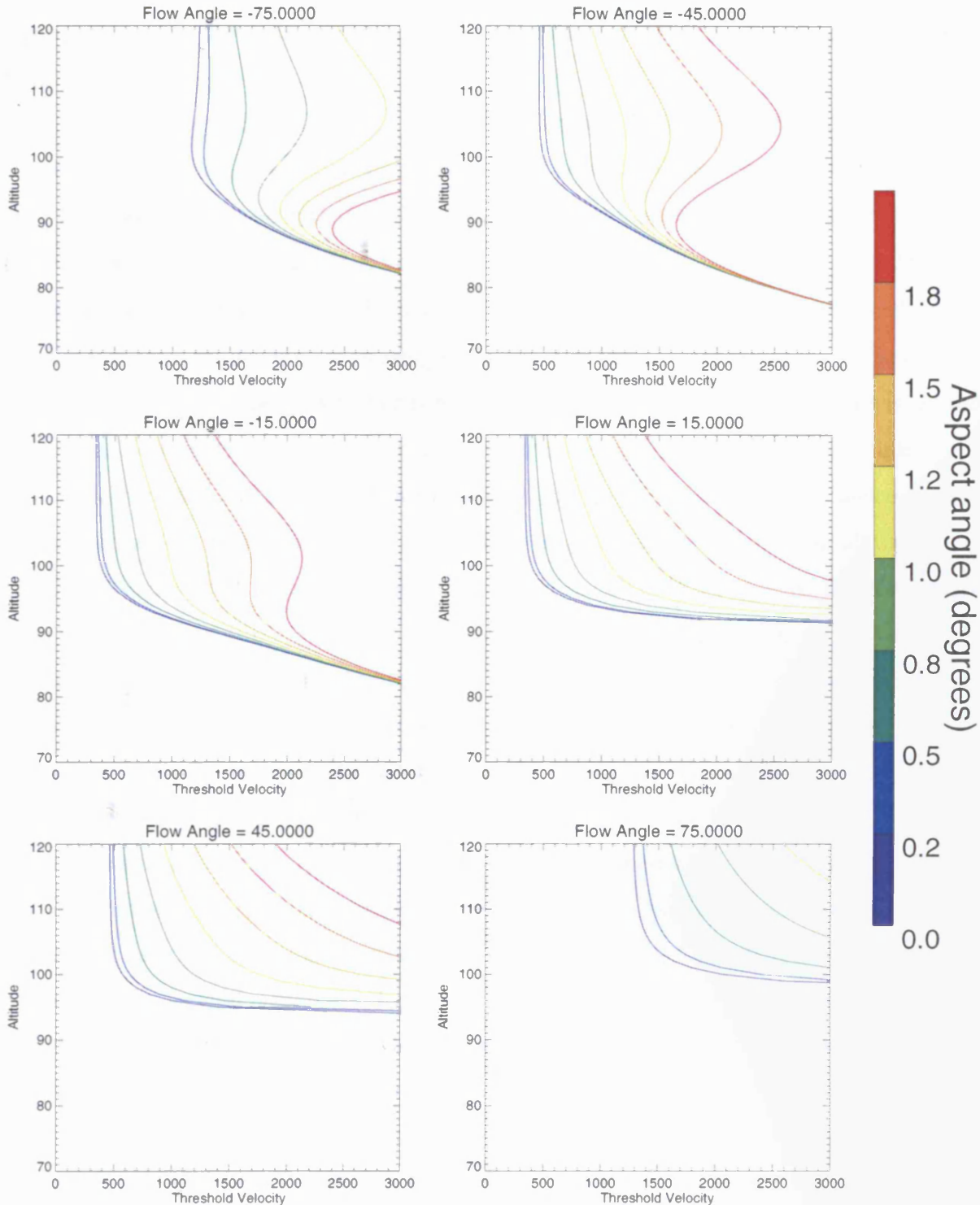


Figure 5.3(b): The fluid theory aspect angle dependence of the threshold velocity for 6 different flow angles. The threshold again is lowest for a flow angle of -45° and cannot be excited easily for positive flow angles.

5.2.2 Growth Rate Predictions

Figures 5.4(a)-(c) show the growth rates calculated for three relative electron-ion drift speeds of 500, 1000 and 1500 m s⁻¹, for a wavelength of 20 m and aspect angle of 0°. The upper panel in each figure corresponds to the fluid regime and the lower panel corresponds to the kinetic regime.

For a drift speed of 500 m s⁻¹, as shown in figure 5.4(a), the different altitude regions where the growth rates is positive and negative may be seen clearly. For flow angles close to -90°, the instability is damped for all altitudes, with the strongest damping occurring at around 93 km. As the flow angle increases to around 0°, the altitude at which most damping occurs decreases to around 91 km. Increasing the flow angle further towards +90° leads to the altitude of maximum damping increasing to 94 km. For flow angles between -50° and +50°, there is a region where the growth rate is positive. The altitude at which this occurs is around 100 km for flow angles close to 0°, but this altitude increases slightly as the magnitude of the flow angle increases. The variation in the growth rate profiles is more pronounced for the kinetic regime. The most damping occurs for flow angles around +45° with an altitude of 93 km. The altitude where most damping occurs varies from 90-95 km for the full flow angle range from -90° to +90°. For positive growth rates, the altitude of most growth varies between 96 and 102 km. The fluid interpretation reproduces most of the results given by the kinetic treatment, although the form of the growth rate is slightly different for the two regimes, in particular the damping rate is larger for the kinetic regime. The major difference between the predictions of the two regimes is for negative flow angles around -45°. The fluid regime gives negative growth rates for these flow angles whereas the kinetic regime predicts a positive growth rate. For flow angles closer to -70°, the damping predicted by the fluid regime was stronger than that predicted by the kinetic regime. The predictions of the two regimes are in general agreement for lower altitudes. At higher altitudes, the curves for positive and flow angles with the same magnitude converge to the same value for each regime, and the fluid and kinetic regimes agree very well at altitudes around 120 km.

Figure 5.4(b) shows the case where a drift speed of 1000 m s⁻¹ was used, the maximum calculated growth rate was, as expected, higher than for the lower drift speed. For the fluid regime, the negative flow angle case yields a maximum growth rate at a lower altitude than the corresponding positive flow angle case where the two angles have the same magnitude. The maximum growth rate occurs for flow angles around 0° and the altitude at which this occurs is 100 km. The strongest damping occurs for flow angles around +70° at an

EPCI growth rate values

Fluid and kinetic regimes

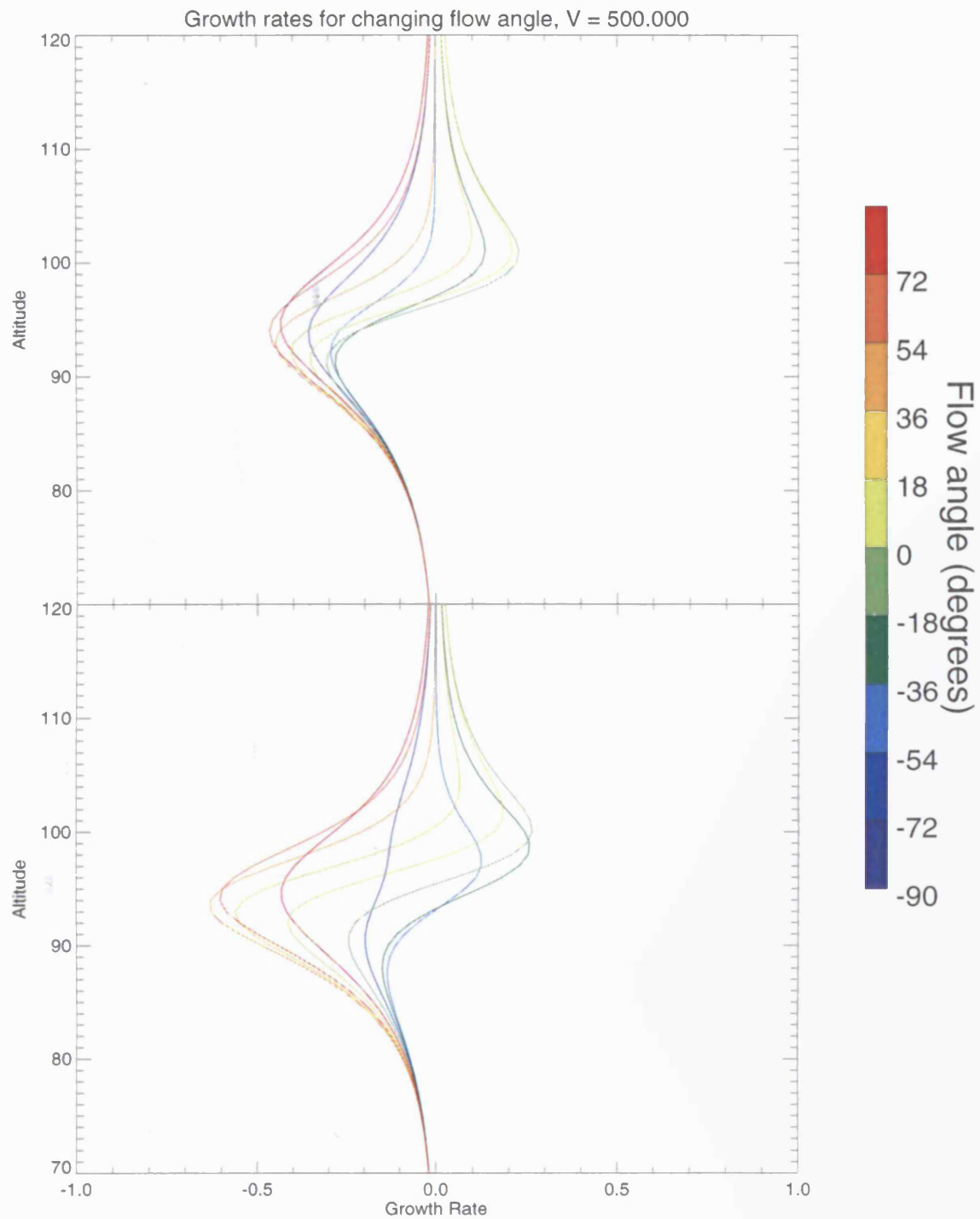


Figure 5.4(a): The growth rate for varying flow angle for a drift speed of 500 m s^{-1} and 20 m waves. The aspect angle is zero and results from both the fluid and kinetic regime have been shown.

EPCI growth rate values

Fluid and kinetic regimes

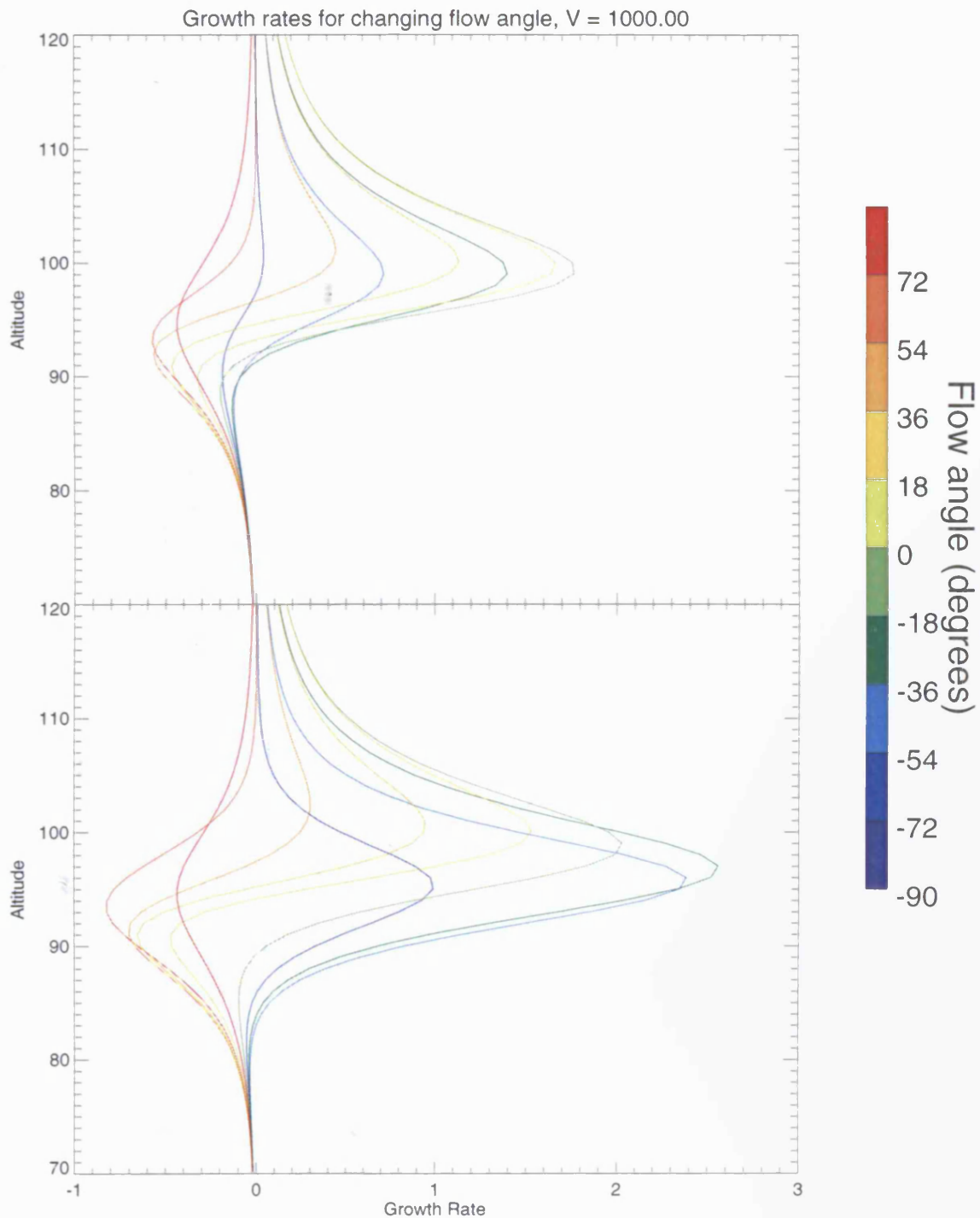


Figure 5.4(b): The growth rate for varying flow angle for a drift speed of 1000 m s^{-1} and 20 m waves. The aspect angle is zero and results from both the fluid and kinetic regime have been shown. The growth rate given by the kinetic regime is larger and more altitude dependent than the growth rate given by the fluid regime.

EPCI growth rate values

Fluid and kinetic regimes

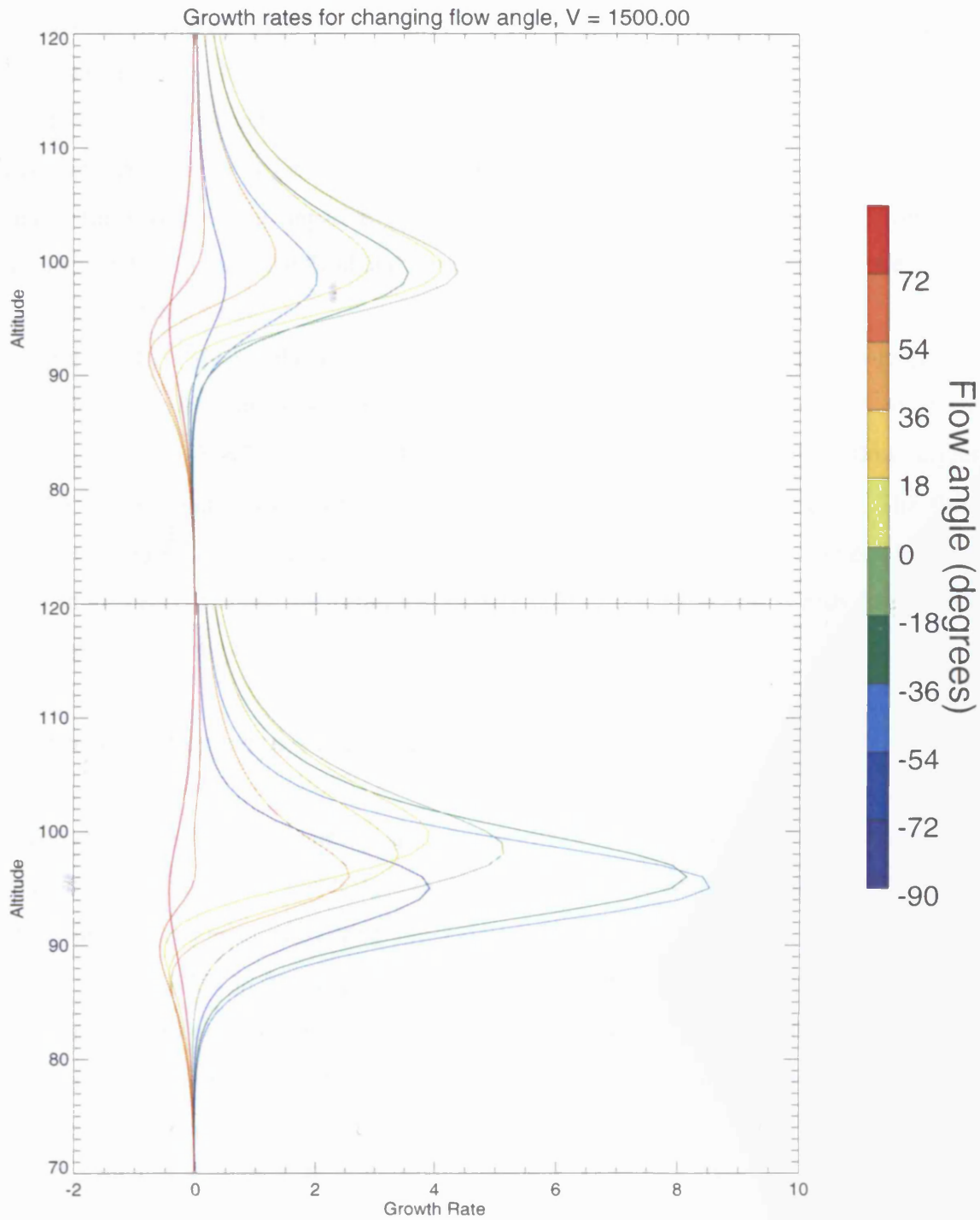


Figure 5.4(c): The growth rate for varying flow angle for a drift speed of 1500 m s^{-1} and 20 m waves. The aspect angle is zero and results from both the fluid and kinetic regime have been shown. Again, the growth rate given by the kinetic regime is larger and more altitude dependent than the growth rate given by the fluid regime.

altitude of 93 km. For the kinetic regime, the strongest growth rate occurs for flow angles around -30° at an altitude of 97 km. For a given flow angle magnitude, the negative sector flow angle gives a higher growth rate at a lower altitude and this is similar to the prediction made by the fluid regime. The most damping occurs for flow angles around $+70^\circ$ at an altitude of 93 km. The altitude dependence of the maximum growth is again most apparent for the kinetic regime. Comparing the fluid and kinetic regimes, the growth rate is higher for the kinetic regime at flow angles around -70° . As for a drift speed of 500 m s^{-1} , the growth rate curves for positive and negative flow angles with the same magnitude converge at altitudes around 120 km and the fluid and kinetic regimes predict the same growth rate values at altitudes around this value.

Figure 5.4(c) shows the case for a flow speed of 1500 m s^{-1} . The growth rate properties change further for the kinetic regime. The highest growth rate now occurs at 95 km for flow angles around -45° , with the altitude dependence now revealing that flow angles around $+10^\circ$ correspond to the highest altitude at which the instability is excited. The fluid approximation again gives similar results to the kinetic theory regime for higher altitudes. Finally, it should be noted that for zero aspect angle and for the three drift speeds considered, the maximum growth rate occurs for altitudes that range from 93-100 km.

5.2.3 Aspect Angle Dependence of the Growth Rate

The aspect angle dependence of the growth rate was investigated for the two regimes described above and the same wavelength of 20 m was used for the modelling. Figures 5.5(a) and 5.5(b) show the effects of varying the aspect angle, by up to 2° , for flow angles that varied from -75° to $+75^\circ$ in 30° steps. Three drift speeds of 500, 1000 and 1500 m s^{-1} were used and results were obtained for both regimes. The altitude range was extended to 130 km for these figures in order to highlight the altitude at which the growth rate was highest. These figures have been generated from equations (2.13) and (2.20) in chapter 2 by varying the orientation of the wave vector \mathbf{k} , thus increasing k_{\parallel} whilst keeping k fixed.

Figure 5.5(a) shows the results for the fluid regime for a drift speed of 500 m s^{-1} . Generally, for increasing aspect angle, the instability is damped as the growth rate becomes negative. For flow angles of -15° and $+15^\circ$, there is an altitude range of 100-120 km where the growth rate is positive. The maximum occurs at 115 km for an aspect angle of around 1° . The damping for higher aspect angles occurs at around the same altitude. For example, for a flow angle of $+45^\circ$, the growth rate becomes negative at around 114 km. The instability is

EPCI aspect angle dependence

Fluid theory regime growth rates

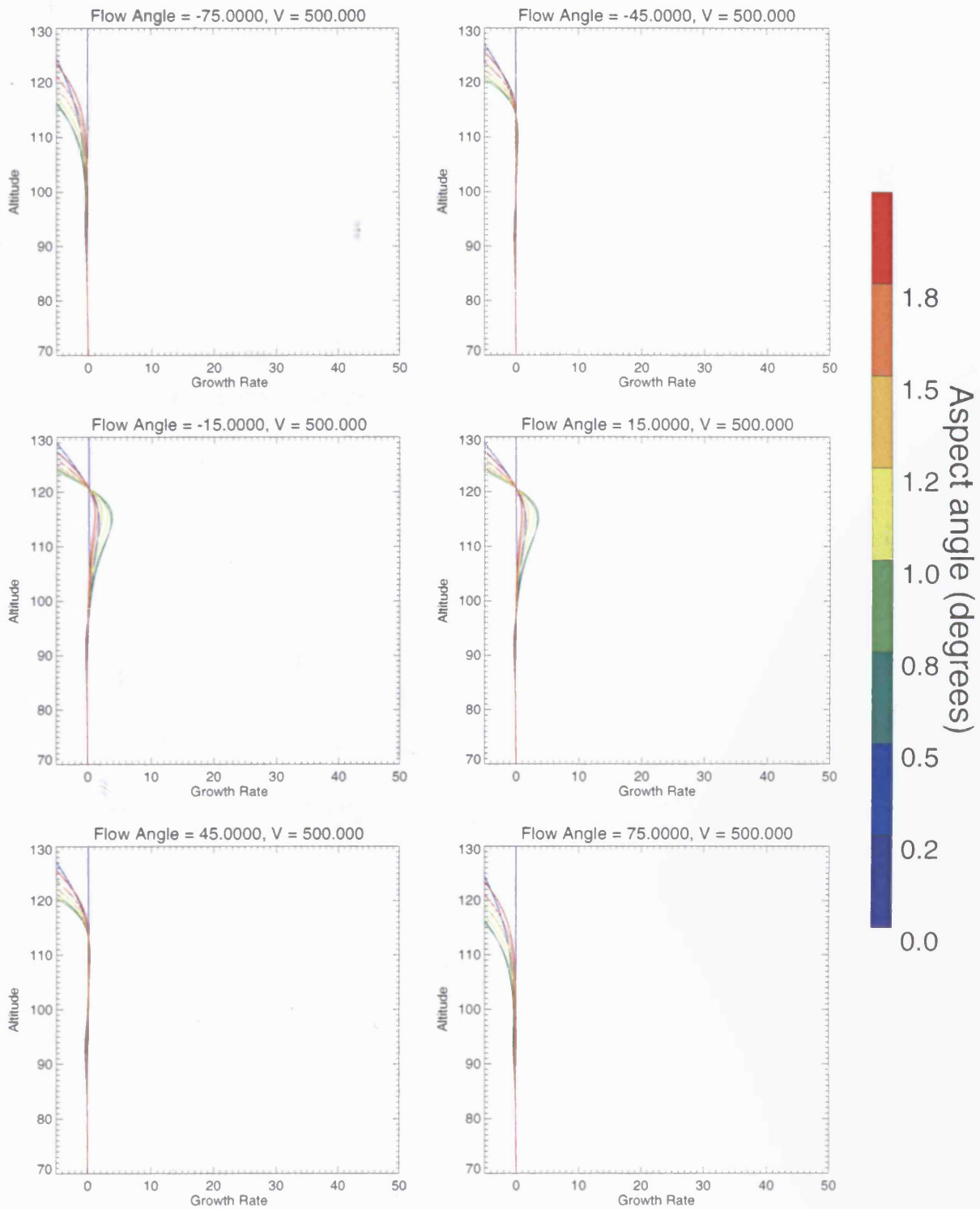


Figure 5.5(a): The fluid theory aspect angle dependence of the growth rate for 6 flow angles and a drift speed of 500 m s^{-1} and 20 m waves. The growth rate is positive only for flow angles close to zero.

EPCI aspect angle dependence

Kinetic theory regime growth rates

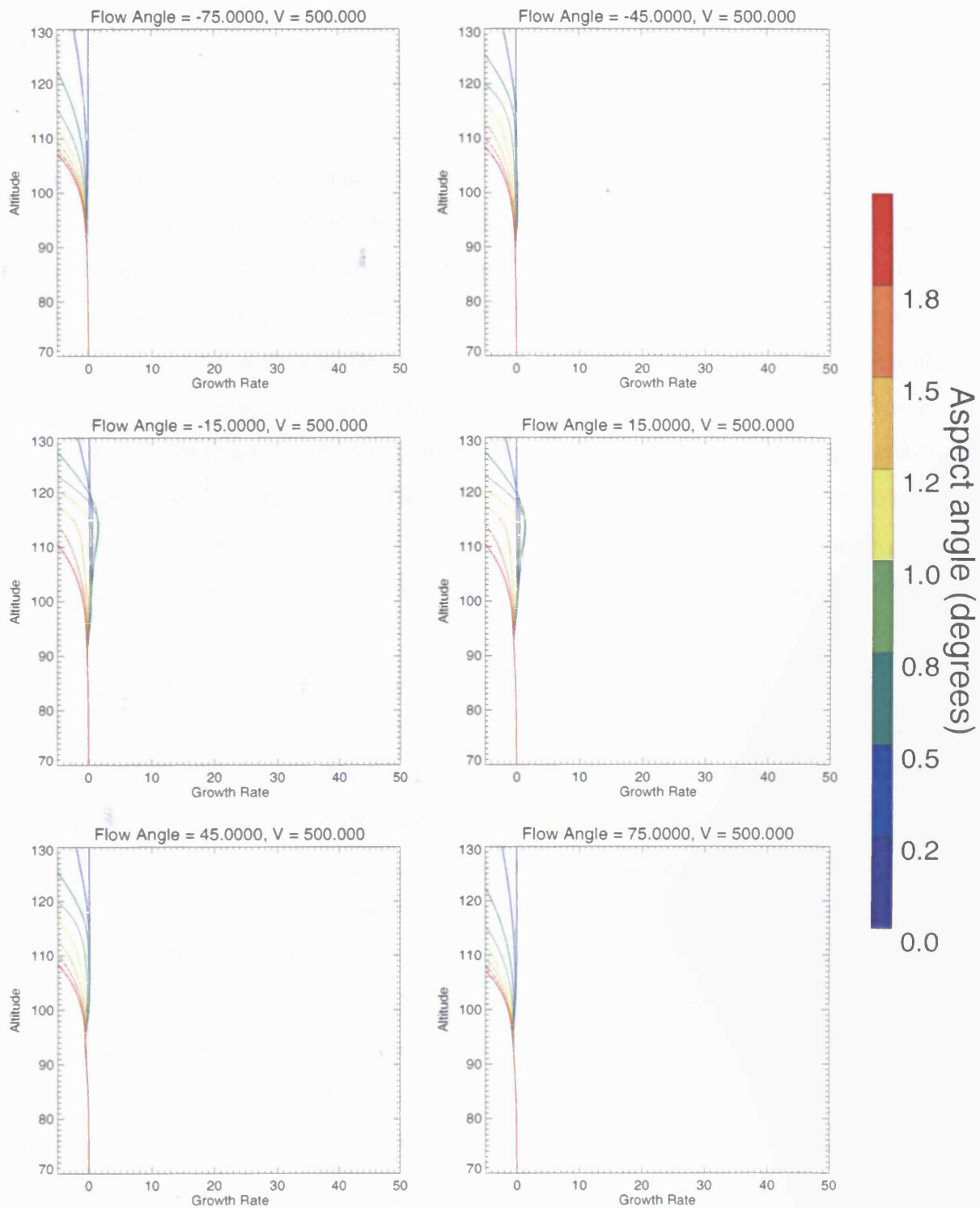


Figure 5.5(b): The kinetic theory aspect angle dependence of the growth rate for 6 flow angles and a drift speed of 500 m s^{-1} and 20 m waves. The growth rate is again positive only for flow angles close to zero.

damped at D-region altitudes for this flow speed. Figure 5.5(b) shows the results obtained for the kinetic regime where the same flow speed of 500 m s^{-1} was used. The damping is more pronounced for higher aspect angles at higher altitudes. The same positive growth rate region is seen to occur at around 115 km for flow angles of -15° and $+15^\circ$. There is no major effect at lower altitudes.

Figures 5.6(a) and 5.6(b) show the results obtained for the two regimes for a drift speed of 1000 m s^{-1} . For the fluid regime shown in figure 5.6(a), the damping is present for flow angles of -75° and $+75^\circ$ and there is no region where the growth rate is positive. For flow angles between these values, there is a region where the growth rate is positive and the maximum occurs at around 117 km. This happens for an aspect angle of around 1° . There is also a maximum in the growth rate at around 97 km. The kinetic regime, shown in figure 5.6(b), shows that for a flow angle of -45° where the instability in the D-region should be excited most favourably, a two-layer structure can be seen. This occurs where the growth rate is a maximum. There are two maxima, one at around 95 km for zero aspect angle and one at 116 km for an aspect angle of 1.2° . The higher altitude maximum is present for flow angles of -15° and $+15^\circ$, but the growth rate for non-zero aspect angles is almost equal to that for zero aspect angle. For both regimes, the maximum growth rate at 116 km is higher for flow angles close to 0° .

Figures 5.7(a) and 5.7(b) show the growth rates for a flow speed of 1500 m s^{-1} . For the fluid regime shown in figure 5.7(a), the altitude at which the maximum growth rate occurs is slightly higher for higher aspect angle. The maximum growth rate is higher for flow angles closer to 0° . The maximum again occurs for an aspect angle of around 1° . At lower altitudes, there is a maximum for zero aspect angle, but the value of the growth rate is similar for the higher aspect angles. The results for the kinetic theory are shown in figure 5.7(b). The maximum growth rate at around 117 km is highest for flow angles tending to 0° . The altitude of this maximum remains fixed for the kinetic regime. This prediction is different to that made by the fluid regime. For a flow angle of -75° , there is a maximum in the growth rate at 95 km. For a flow angle of -45° , the two-layer structure is again apparent, with the maximum growth rate occurring at 95 km for zero aspect angle and a maximum at 117 km for an aspect angle of 1.2° . Increasing the aspect angle for the lower altitude maximum leads to a decrease in the altitude at which the maximum growth rate occurs, thus showing that the instability may be excited at lower altitudes although not as efficiently. For a flow angle of $+45^\circ$,

EPCI aspect angle dependence

Fluid theory regime growth rates

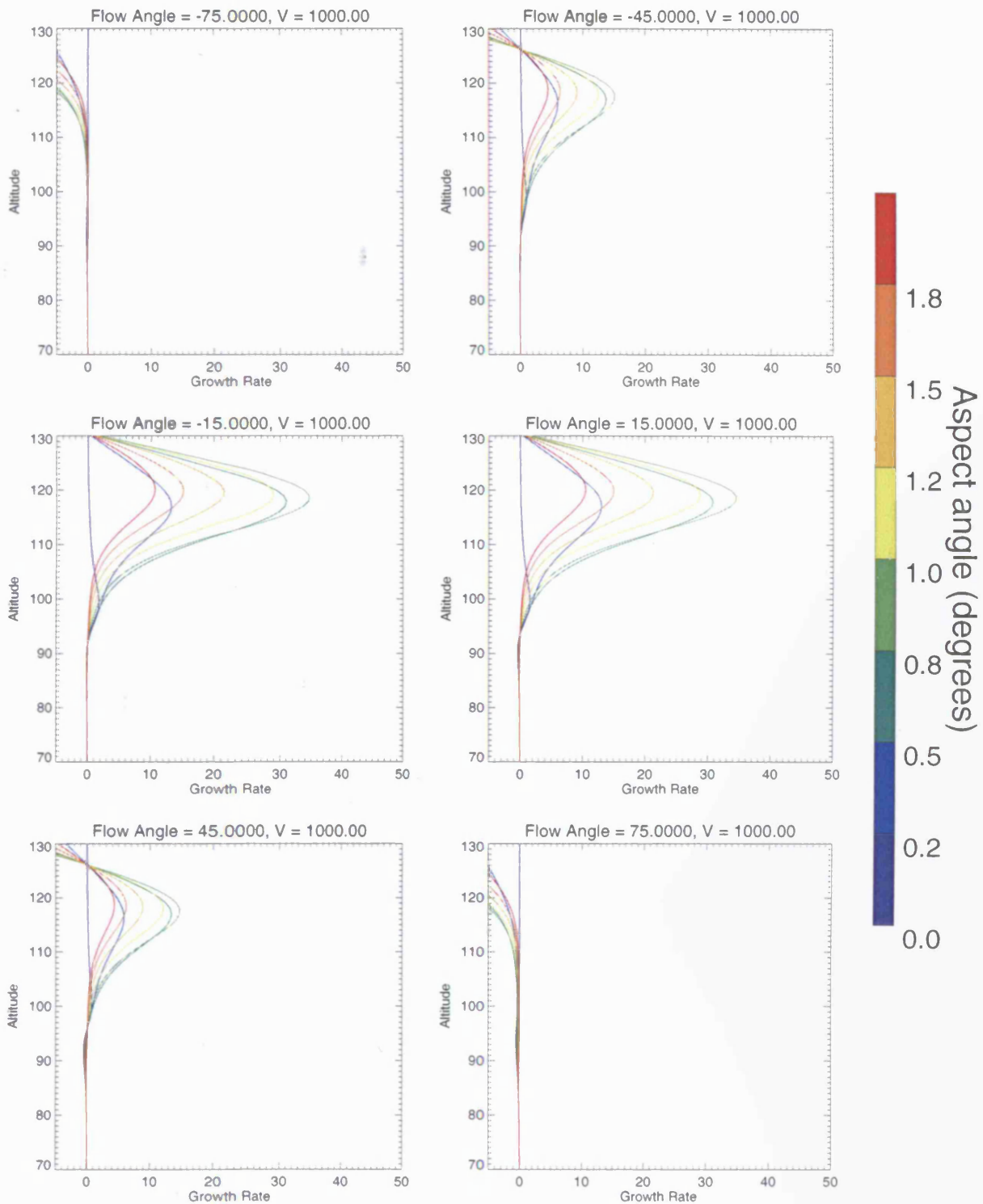


Figure 5.6(a): The fluid theory aspect angle dependence of the growth rate for 6 flow angles and a drift speed of 1000 m s^{-1} and 20 m waves. The growth rate is now positive for flow angles with magnitudes of over 45° .

EPCI aspect angle dependence

Kinetic theory regime growth rates

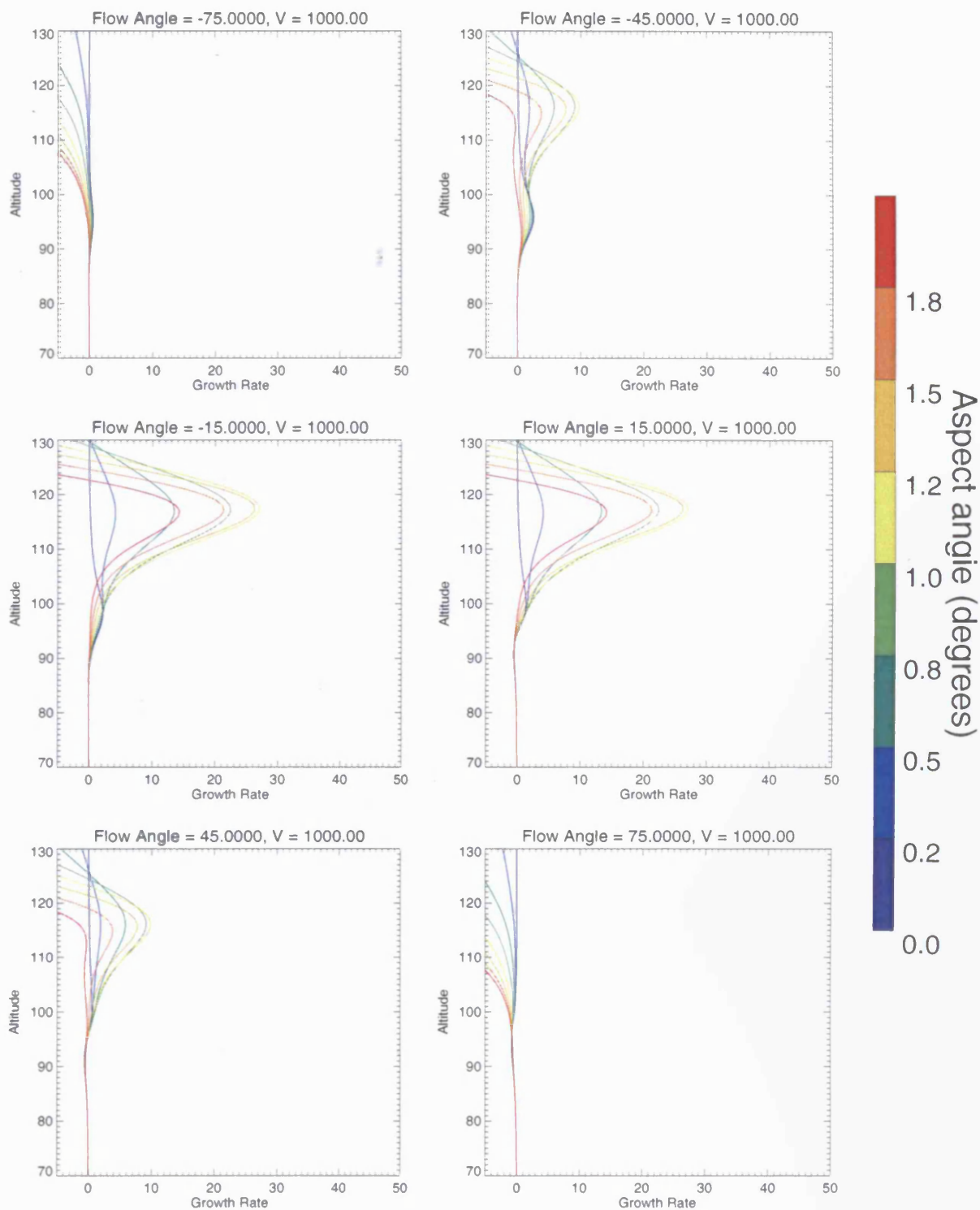


Figure 5.6(b): The kinetic theory aspect angle dependence of the growth rate for 6 flow angles and a drift speed of 1000 m s^{-1} and 20 m waves. Evidence now exists for a two-layer structure for a flow angle of -45° .

EPCI aspect angle dependence

Fluid theory regime growth rates

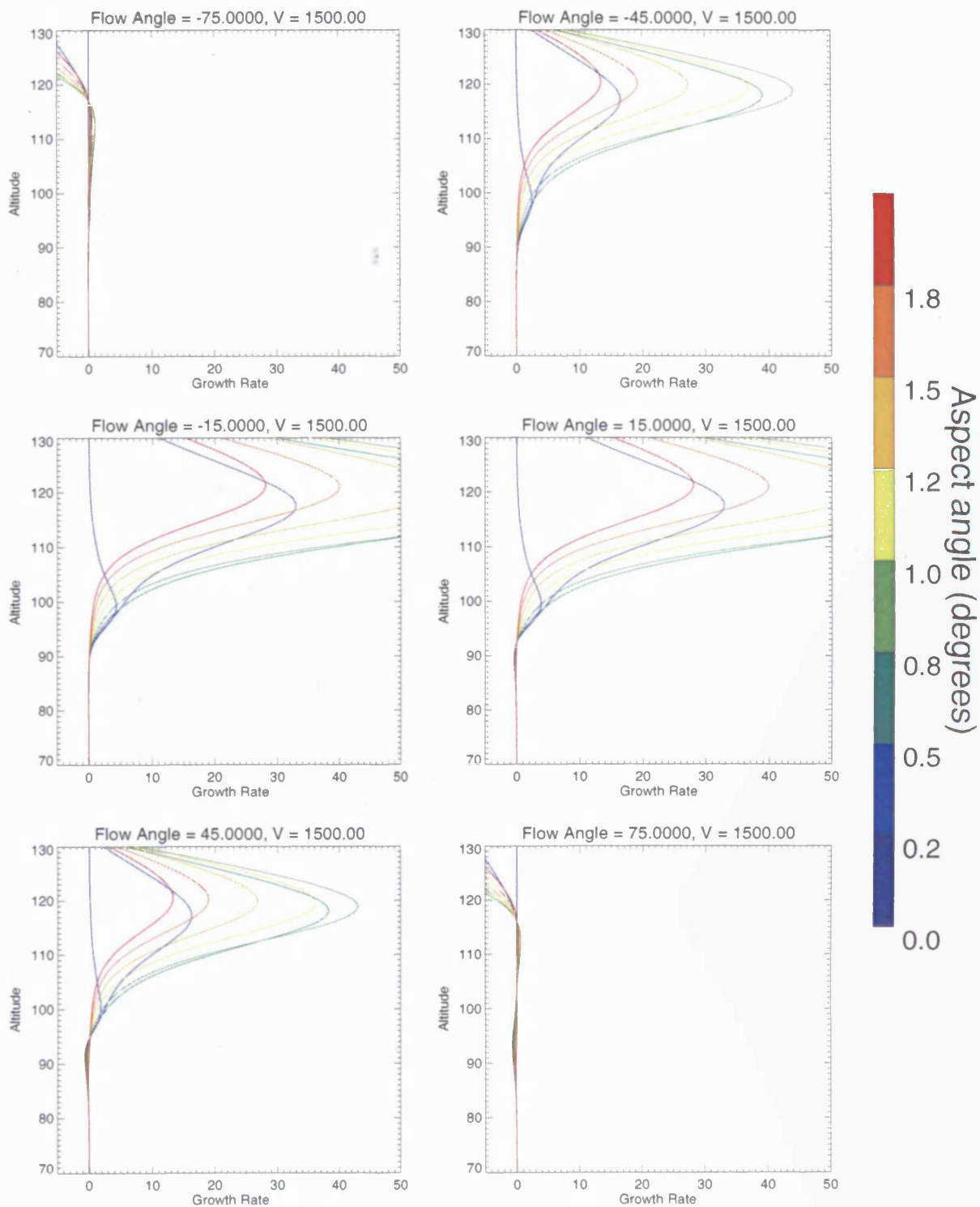


Figure 5.7(a): The fluid theory aspect angle dependence of the growth rate for 6 flow angles and a drift speed of 1500 m s^{-1} and 20 m waves. There is evidence for a two-layer structure.

EPCI aspect angle dependence

Kinetic theory regime growth rates

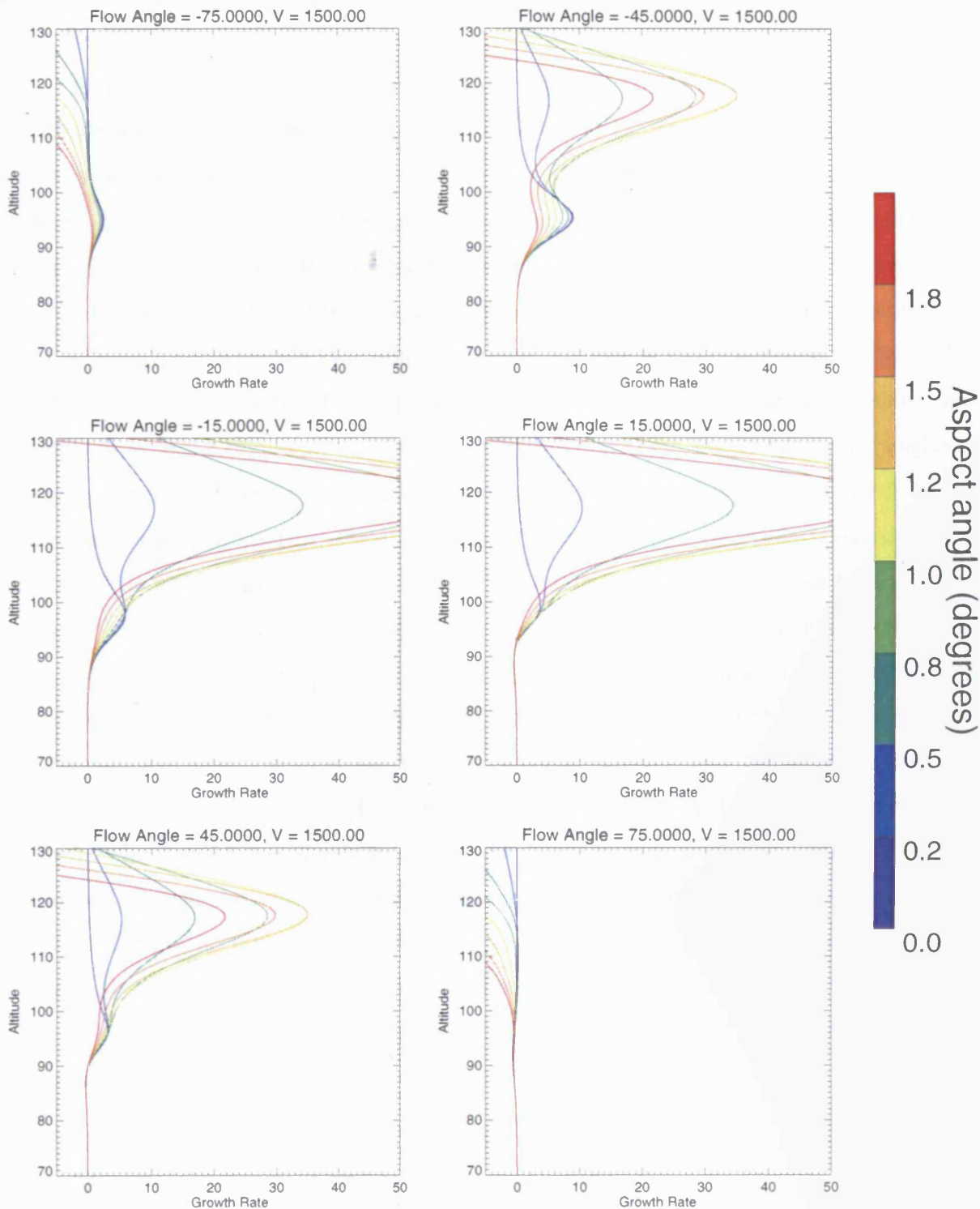


Figure 5.7(b): The fluid theory aspect angle dependence of the growth rate for 6 flow angles and a drift speed of 1500 m s^{-1} and 20 m waves. For a flow angle of -45° , there is now strong evidence for a two-layer structure, with the EPCI maximum growth rate for zero aspect angle and the FBI maximum growth rate for an aspect angle of 1° .

increasing the aspect angle leads to a decrease in the value of the growth rate such that the maximum growth rate at lower altitudes gradually disappears.

5.2.4 Comparison between Theoretical Predictions

It should be noted that the theory proposed by Dimant and Sudan, whose characteristics may be summarised by equations (2.13)-(2.16), appears to agree with the generally well-accepted theory of FBI irregularities, which predict an enhancement in the FBI at aspect angles of around 1° . The growth rates are largest at two different altitudes, thus forming two layers at which the instability is excited. Figures 5.6(a), 5.6(b), 5.7(a) and 5.7(b) show that, at small magnitude flow angles, the maximum growth rate at E-region altitudes is much higher than that for the D-region, i.e. the growth rate is swamped by FBI effects. The largest growth rates in the lower-altitude layer occur for aspect angles around zero, corresponding to the region where the EPCI should be excited. For larger aspect angles of around 1° , the growth rate again reaches a maximum value and this occurs in the E-region, thus corresponding to the FBI. The theory therefore predicts that two echo layers should be seen in the data, one corresponding to the EPCI for zero aspect angle and one corresponding to the FBI for a non-zero aspect angle. Radar data consistent with this prediction of two layers will be presented in chapter 6. The damping of the instability at lower flow speeds is in general agreement with the FBI theory. Finally, as a matter of note, it should be pointed out that for the EPCI, the drift is the electron drift associated with the heating term that characterises the instability. The drift corresponding to the FBI is the true relative electron-ion drift, whose magnitude tends to zero as the altitude increases, since the ions become magnetised. For the theoretical predictions presented in this chapter, the relative electron-ion drift was used for all altitudes. Although this is strictly inaccurate for lower altitudes where the EPCI should occur, in reality it does not affect the results noticeably since the ion drift in the D-region is practically zero and the ion motion is heavily damped through collisions with neutral particles.

5.3 Chaotic Diffusion in the E-region

5.3.1 Wave-induced Collision Processes

Many parts of the FBI theory regarding excitation of waves, wave-particle interactions and the enhancement of the E-region collision frequency remain unclear. This enhancement occurs when strong electric fields of magnetospheric origin are present and the purpose of this section is to describe a mechanism that may provide a partial explanation for the anomalous collision frequency.

A process by which FBI drift waves may affect the motion of particles is now considered. The drift waves, together with the magnetic field, give rise to an $\mathbf{E} \times \mathbf{B}$ drift of the particles. It is the potential of the varying electric field that causes the anomalous drifts, which then lead to the onset of chaos, in turn giving rise to particle diffusion.

One of the aims of this study on wave-induced collision processes was to determine the characteristics of particle motion under the influence of electrostatic waves. To do this satisfactorily, it was necessary to describe the waves and how they interact with the particles. The approach described here utilises the concept of the Hamiltonian to describe this interaction. The argument used is based on that described by Kleva and Drake (1984).

Consider a plasma in a homogeneous magnetic field, which is parallel to the z direction. An electrostatic wave, standing in the x direction and propagating in the y direction, generates the resultant $\mathbf{E} \times \mathbf{B}$ drift. The velocity may be resolved into the x and y directions, meaning that the motion need only be considered in the x - y plane.

The potential associated with the electrostatic wave is of the form

$$\phi(x, y - V_{p1}t) = \phi_{01} \cos(k_1 x) \cos[k_1(y - V_{p1}t)] \quad (5.1)$$

V_{p1} is the propagation phase speed in the y direction and k_1 is the wavenumber of the wave. The particle response to this wave, the $\mathbf{E} \times \mathbf{B}$ drift, can be written as

$$\mathbf{V}_d = \frac{-\nabla \phi \times \hat{\mathbf{z}}}{B} \quad (5.2)$$

After splitting this into x and y components, the following pair of equations is obtained

$$\frac{dx}{dt} = -\frac{1}{B} \frac{\partial \phi}{\partial y} \quad (5.3)$$

$$\frac{dy}{dt} = \frac{1}{B} \frac{\partial \phi}{\partial x} \quad (5.4)$$

These equations have Hamiltonian form and a Hamiltonian, $H \equiv -\phi/B$, may be defined. By transforming to the frame that travels with the wave, the explicit time-dependence of the Hamiltonian is removed. By definition, a Hamiltonian is not time-dependent if it is not explicitly time-dependent. This means that ϕ/B is a time-independent constant of the motion, a conserved quantity. Since B may be taken to be fixed for the ionosphere, it follows that ϕ also is fixed. Consequently, the particle trajectories are constrained to lie on curves of constant ϕ .

The two-wave case is a more complex situation. The second wave may be taken to travel at a different phase speed to the first wave. After transforming to the moving frame of the first wave, the following expressions for the velocity components result

$$\frac{dx}{dt} = \frac{1}{B} [k_1 \phi_1 \cos(k_1 x) \sin(k_1 y) + k_2 \phi_2 \cos(k_2 x + \theta) \sin(k_2 y - \omega t)] \quad (5.5)$$

$$\frac{dy}{dt} = -V_{p1} - \frac{1}{B} [k_1 \phi_1 \sin(k_1 x) \cos(k_1 y) + k_2 \phi_2 \sin(k_2 x + \theta) \cos(k_2 y - \omega t)] \quad (5.6)$$

This expression has a time-dependent part that is present irrespective of the transformation. This means that the Hamiltonian is now a function of time and hence there is no longer a constant of the motion. For the case of the single wave, the particles were constrained to lie on surfaces of constant ϕ . This is no longer the case and the new conditions modify the particle trajectories significantly.

The particles are no longer confined to particular regions of space, and are free to enter regions that would otherwise be forbidden and hence diffuse. The diffusion is calculated using a statistical technique. The displacement in the x direction of a particle from its initial position is given by

$$\delta x_i(t) \equiv x_i(t) - x_i(0) \quad (5.7)$$

The covariance over all particles is then given by

$$C(t) \equiv \langle\langle [\delta x_i(t)]^2 \rangle\rangle \equiv \frac{1}{N} \sum_{i=1}^N [\delta x_i(t)]^2 - \left(\frac{1}{N} \sum_{i=1}^N \delta x_i(t) \right)^2 \quad (5.8)$$

where N is the number of particles. The diffusion coefficient, $D(\tau)$, satisfies

$$C(t) = 2D(\tau)t \quad (5.9)$$

An ideal diffusion coefficient is given in the limit of τ tending to infinity, but a practical value may be obtained by choosing a suitably large value of τ . This diffusion may cause the enhancement of the anomalous collision frequency.

5.3.2 Covariance and Diffusion Results

The results of simulating particle motion given by equations (5.1)-(5.9) are presented. Hamiltonian dynamical techniques were used to calculate the particle trajectories and diffusion coefficients associated with two propagating electrostatic waves present in the E-region. The amplitude of the waves was defined as $k\phi/B$, where k is the wavenumber and ϕ is the electrostatic potential of a wave. This expression corresponds to E/B , the magnitude of the $\mathbf{E} \times \mathbf{B}$ drift velocity. In the simulation, this value was chosen to be 1000 m s^{-1} , since this is typical of the relative electron-ion drift speed in the E-region. It also exceeds the drift speed necessary to excite the Farley-Buneman instability. B was chosen to be $5 \times 10^{-5} \text{ T}$, which is the value of the field strength at the Earth's surface. It was found that setting $k_1 = k_2$, and therefore $\phi_1 = \phi_2$, for both waves gave diffusion coefficients that were smaller than the case when $k_1 \neq k_2$. Therefore, to ensure that k_1 was not equal to k_2 , the conditions $k_1 = 2k_2$ and $\phi_2 = 2\phi_1$ were chosen such that the wave amplitudes were equal. The simulation was performed for 200 particles whose initial positions were distributed randomly throughout the truncated x - y plane. This value was chosen because it provided enough particles for a reliable calculation of the covariance, given by equation (5.9), without taking too long computationally. The use of more particles, 2000 say, led to smoother covariance curves but did not result in a significant improvement in the calculation of the covariance, since the linear relationship between the covariance and the diffusion coefficient was not seen more clearly. The diffusion coefficient was calculated by following the particle trajectories. The modelling of the particle trajectories was carried out by a FORTRAN program, called GTRAJ, supplied by S. Chapman of the University of Warwick.

Figures 5.8 and 5.9, presented below, show snapshots of the motion characterised by Poincaré sections through the phase-space in which the particle trajectories corresponding to equations (5.5) and (5.6). The Poincaré section is composed of points sampled at time intervals of 2π seconds, thus allowing the evolution of the trajectory to be investigated. This form of plot is preferable to taking the continuous trajectory because at time periods of 2π , the equations have the same instantaneous form and the points generated by this sampling that give the Poincaré section may be compared directly. The two-dimensional space has been limited by mapping into the interval $-\pi < x \leq \pi$, where any trajectory passing outside this interval is mapped back into it. A similar interval is used in the y direction in which the electrostatic waves are taken to propagate. The upper panel of figure 5.8 shows the case of the particle response to one wave when the potential well of the wave does not confine the

PARTICLE MOTION FOR ONE WAVE

Poincare sections for non-confining and partially confining potential wells

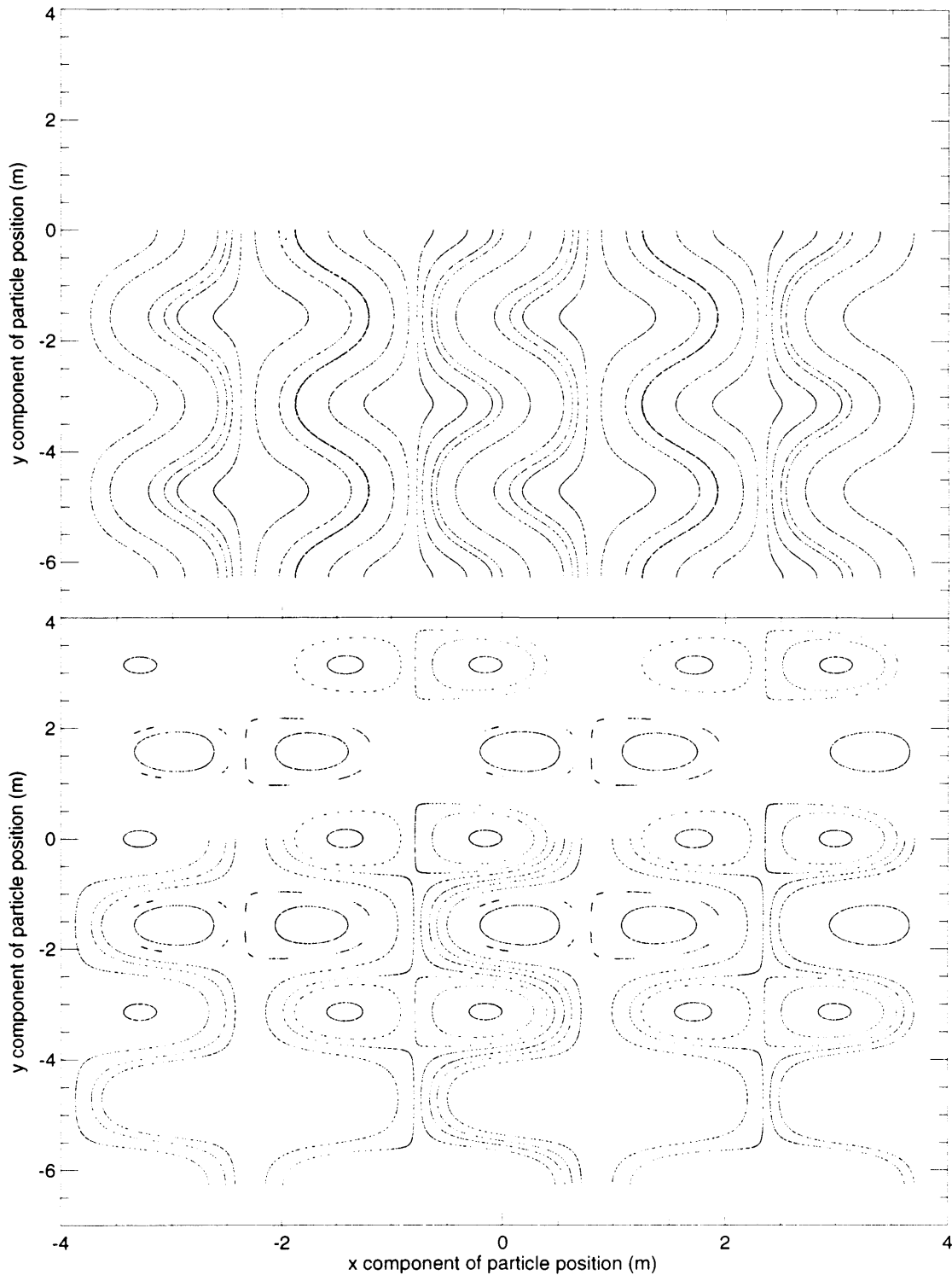


Figure 5.8: A single electrostatic wave affecting particle trajectories. The upper panel shows the x and y components of the motion for the case where the potential well of the wave is unable to confine the particles. The lower panel shows the particle trajectories that result when the potential well of the wave is able to confine some of the particles.

PARTICLE MOTION FOR TWO WAVES

Poincare sections for significantly different and equal wave amplitudes

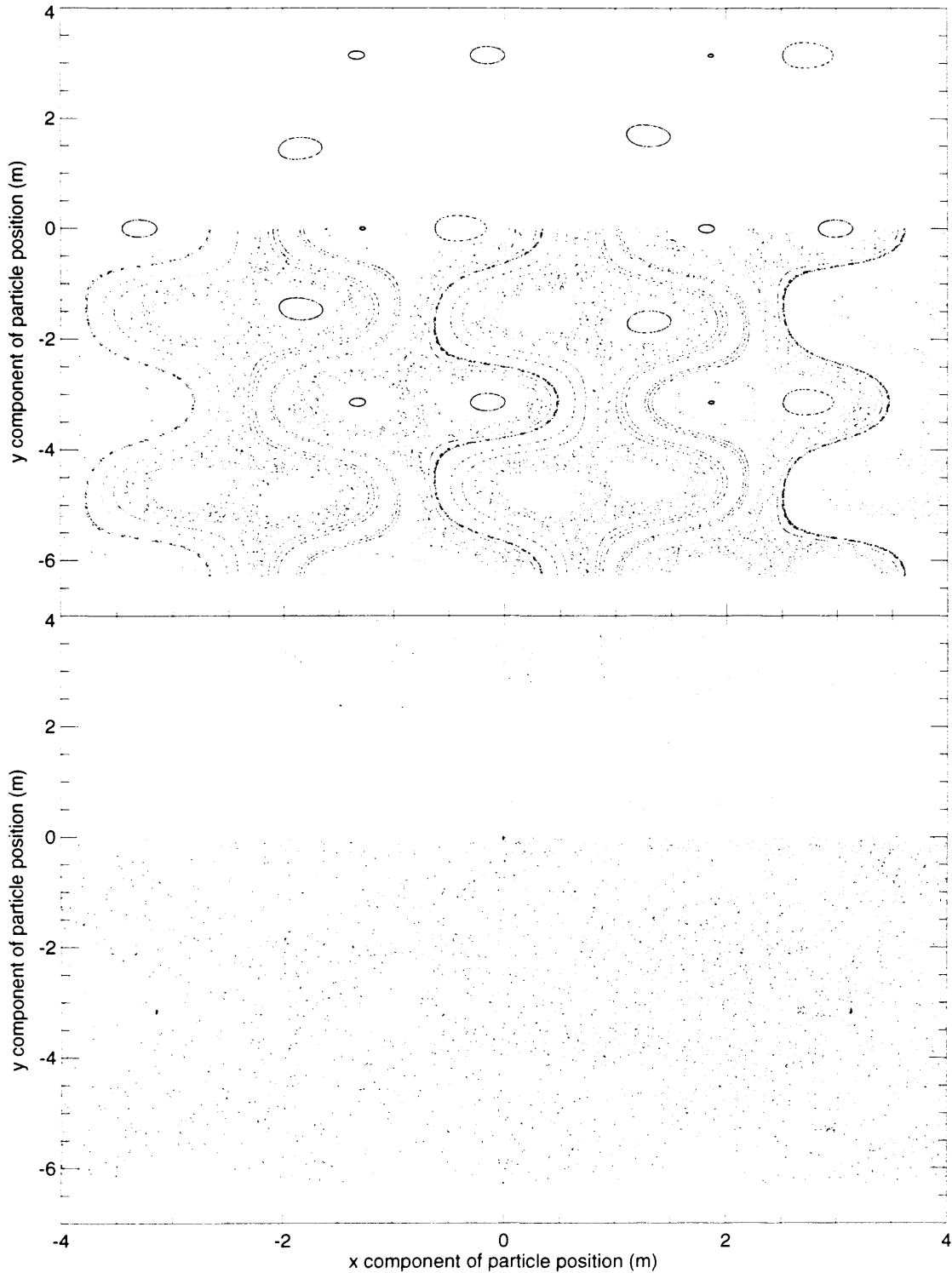


Figure 5.9: The two-wave case where the amplitudes of the waves are unequal, shown in the upper panel, and equal, shown in the lower panel. In the upper panel, there is partial confinement of the particles as non-traversable boundaries exist that prohibit diffusion in the x direction. The lower panel shows the case where particles are free to diffuse since they are no longer confined.

particles. The particles oscillate but are confined to distinct trajectories within a certain region. The lower panel of figure 5.8 shows the case when the potential well is able to confine the particles partially. Some of the particles are trapped in the potential well of the wave. However, they still have definite trajectories that are confined to certain localised regions, as before.

The case for two waves is illustrated in figure 5.9. The effects of the second wave become apparent when the amplitude of the second wave is a suitable fraction of that of the first, as shown in the upper panel of figure 5.9, where the amplitude of the second wave was one-fifth that of the first wave. The particles may be trapped in a well, but they are no longer confined to definite trajectories and are free to describe trajectories that vary in time. However, there is no resultant diffusion from this type of motion. This is because there are certain periodic boundaries that the particles cannot cross, i.e. they are still confined to distinct two-dimensional regions whereas for the single-wave case the trajectories are curvilinear and therefore one-dimensional. The lower panel of figure 5.9 shows the case for two waves that have equal amplitudes. The particle motion here is truly chaotic and the particle trajectories are not confined spatially. The absence of confinement means that the particles are free to enter regions from which they were previously forbidden. Unlike the previous case, no boundaries exist that the particles cannot traverse and the particles are free to diffuse.

The particle trajectories were calculated for different values of ω , the frequency of the second wave given by equations (5.5) and (5.6). In order to obtain reliable values for the covariance, the simulation was performed for 1000 seconds, corresponding to nearly 160 time intervals of period 2π seconds, thus allowing the overall linear relationship between the covariance and the time to become apparent. The covariance values are shown in figures 5.10(a) and 5.10(b) and correspond to values of ω of 10, 20, 30 and 40 rad s^{-1} . Values of ω lower than 10, say 1 or 2, produced similar results to those obtained for $\omega = 10$, and so these are not shown. The definition of the diffusion coefficient, given by equation (5.9), demonstrates that the covariance is proportional to the diffusion coefficient. In the figures, the x -axis corresponds to time in seconds and y -axis gives the covariance in units of m^2 , thus resulting in the usual units for a diffusion coefficient, $\text{m}^2 \text{s}^{-1}$. The values of the diffusion coefficient obtained from the covariance for the four values of ω were 0.55, 0.65, 0.35 and $0.15 \text{ m}^2 \text{ s}^{-1}$, i.e. the diffusion coefficient was lower for higher values of ω . These are all of the order of $1 \text{ m}^2 \text{ s}^{-1}$. Equations (2.21) and (2.22) in chapter 2 defined the anomalous electron collision frequency. The collision frequency may be related to a diffusion coefficient by

DIFFUSION CHARACTERISTICS

Covariances for second-wave frequencies of 10 and 20 rad/s

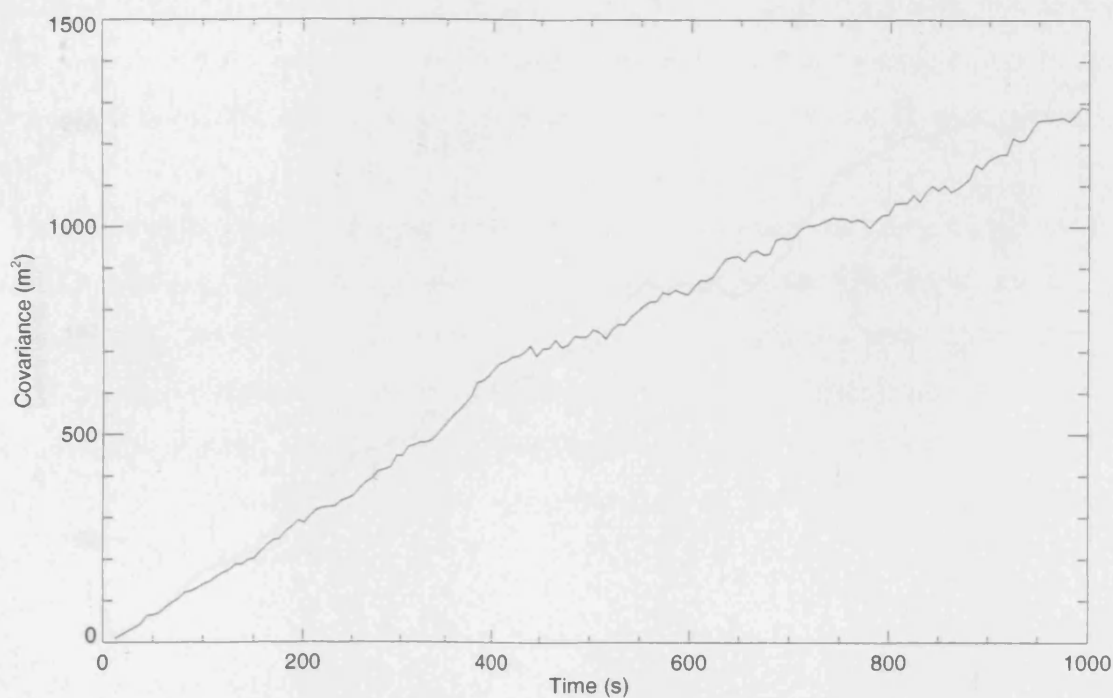
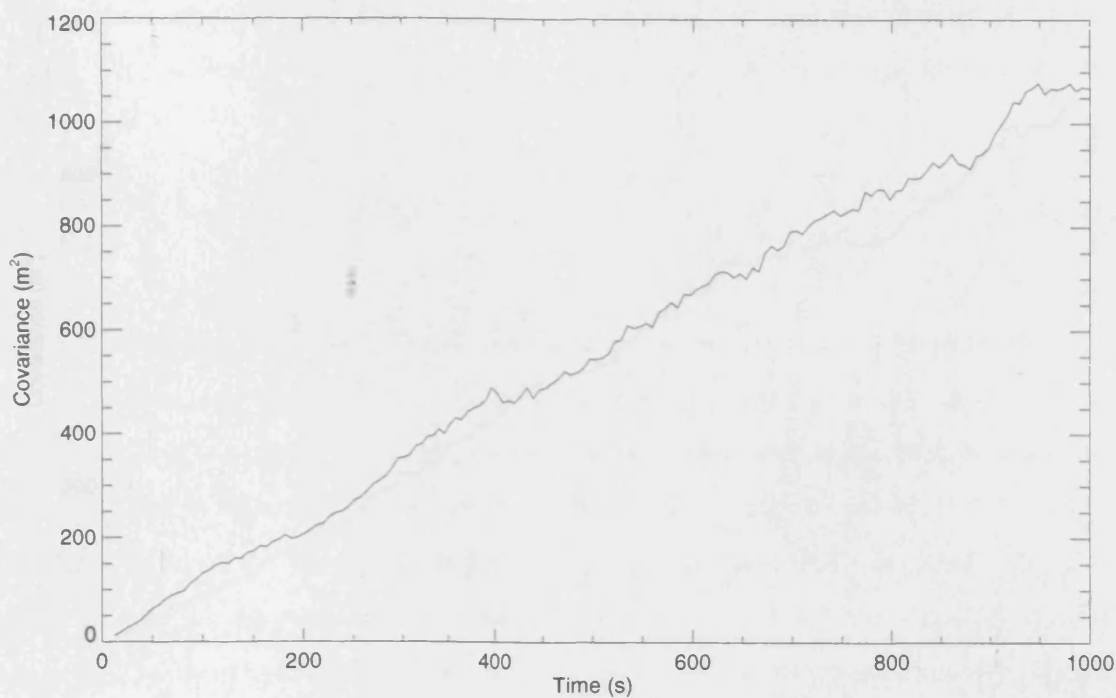


Figure 5.10(a): The covariance values, from which a diffusion coefficient may be calculated, obtained for frequencies values of $\omega = 10$ and $\omega = 20 \text{ rad s}^{-1}$.

DIFFUSION CHARACTERISTICS

Covariances for second-wave frequencies of 30 and 40 rad/s

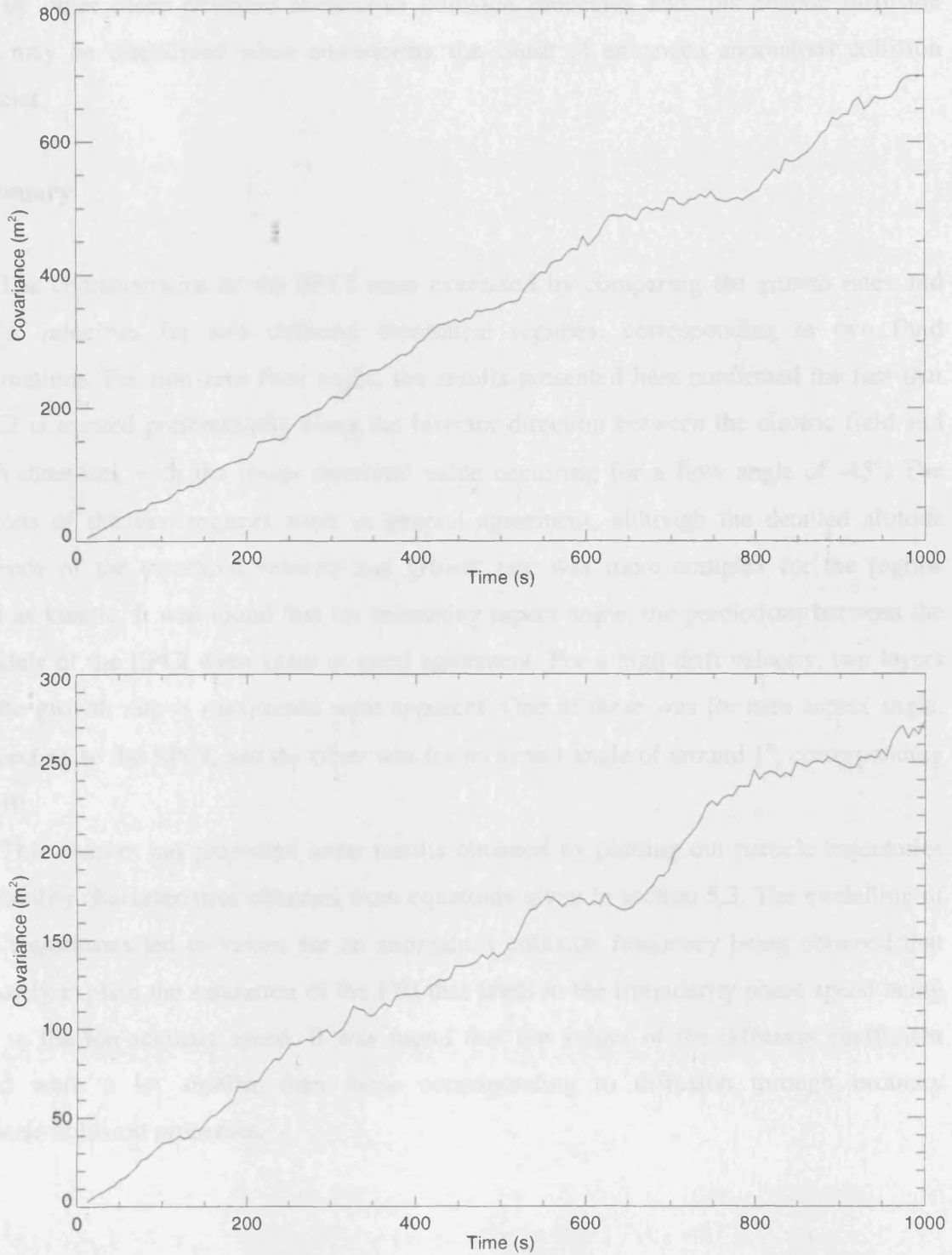


Figure 5.10(b): The covariance values, from which a diffusion coefficient may be calculated, obtained for frequencies values of $\omega = 30$ and $\omega = 40$ rad s⁻¹.

applying an argument involving the mean free path. However, the value of the diffusion coefficient obtained for this two-wave particle diffusion case is much smaller than the diffusion coefficient for ordinary ionospheric temperature-driven collision processes. Therefore, diffusion caused by this mechanism would be insignificant when compared to that caused by other more effective anomalous collision processes and this chaotic diffusion process may be discounted when considering the cause of enhanced anomalous collision frequencies.

5.4 Summary

The characteristics of the EPCI were examined by comparing the growth rates and threshold velocities for two different theoretical regimes, corresponding to two fluid approximations. For non-zero flow angle, the results presented here confirmed the fact that the EPCI is excited preferentially along the bisector direction between the electric field and the drift direction, with the lower threshold value occurring for a flow angle of -45° . The predictions of the two regimes were in general agreement, although the detailed altitude dependence of the threshold velocity and growth rate was more complex for the regime labelled as kinetic. It was found that for increasing aspect angle, the predictions between the two models of the EPCI were again in good agreement. For a high drift velocity, two layers where the growth rate is maximised were apparent. One of these was for zero aspect angle, corresponding to the EPCI, and the other was for an aspect angle of around 1° , corresponding to the FBI.

This chapter has presented some results obtained by plotting out particle trajectories and instability characteristics obtained from equations given in section 5.3. The modelling of particle trajectories led to values for an anomalous collision frequency being obtained that could partly explain the saturation of the FBI that leads to the irregularity phase speed being limited to the ion-acoustic speed. It was found that the values of the diffusion coefficient obtained were a lot smaller than those corresponding to diffusion through ordinary ionospheric collision processes.

Chapter 6

Observations of Naturally Occurring Irregularities in the Lower Ionosphere

6.1 Introduction

This chapter describes observations of D-region and E-region radar echoes and provides a classification of the low-altitude FAIs as observed mainly by the CUTLASS system. STARE data are also presented for two specific case studies. The earlier sections of chapter 2 gave an overview of the theory behind the Electron Pedersen Conductivity Instability (EPCI) and its relationship to the Farley-Buneman Instability (FBI). Chapter 5 presented theoretical calculations of the growth rates and threshold velocities for the EPCI.

The CUTLASS data presented in this chapter were collected when the myopic scan mode was in operation. The myopic scan mode is intended to give a higher spatial resolution for closer features. The radar field of view consists of sixteen beams with range gates 15 km in length. The range to the first gate is 180 km and the maximum range is 1290 km. The myopic scan mode was chosen because it allowed the detailed examination of backscatter emanating from D-region and E-region altitudes. Normal scan data were also examined, but no clear signature was seen and the data were of a lower range resolution since this mode uses 45 km range gates. CUTLASS observed at 10.2-10.6 MHz during the myopic campaign. Previous studies conducted using the myopic scan mode include those performed by Milan and Lester (2001). This study provided a comprehensive look into the characteristics of the myopic campaign data set. Occurrence statistics were obtained for both electrojets and the results obtained, including the echo types observed, are of great relevance to this study.

6.2 Physical Processes Responsible for Natural Irregularities in the Lower Ionosphere

Possible natural mechanisms responsible for creating E-region and D-region backscatter targets include the FBI, the gradient drift instability, meteor trails that create ionisation, a mechanism involving auroral forms and the EPCI. The FBI is excited in the E-region when the relative electron-ion flow speed exceeds the threshold velocity for excitation and FAIs are created preferentially in the direction along the electrojet. Because of non-linear effects that lead to stabilisation; the phase speed of the irregularities saturates at the ion-

acoustic speed leading to Type I echoes that are characterised by Doppler velocities of around the ion-acoustic speed and spectral widths of around 50 m s^{-1} . Hence, Type I echoes may be identified directly with the FBI. The primary FBI waves have associated density gradients and in the E-region these gradients lead to excitation of the gradient drift instability and the creation of secondary gradient drift waves. The secondary waves occur at oblique angles to the direction of the electrojet flow and the resulting echoes have a high spectral width. These are Type II echoes and may be identified with the gradient drift instability. Primary gradient drift waves are possible but are rare in the E-region. Type II echoes have small Doppler shifts and spectral widths of around $200\text{-}400 \text{ m s}^{-1}$. These standard definitions of echo types will be applied to the data in this chapter:

In the D-region, low spectral width echoes may be associated with meteor scatter, a mechanism involving optical auroral forms and the EPCI. Backscatter from meteor trails is characterised by low spectral width values that are dependent on the altitude of the scatter and the observing wavelength of the radar. Hall et al. (1997) described the diffusion-dominated density structures that comprise meteor trails. The spectral width of backscatter from such structures ranges from $0\text{-}20 \text{ m s}^{-1}$ for a wavelength of 10.5 MHz. Milan et al. (2001) identified a further mechanism by which low spectral width backscatter could be produced at altitudes from 80-100 km. It was suggested that these low spectral width values were caused by a non-coherent scattering process from density irregularities created in the lower ionosphere by pulsating auroral forms. The spectral widths associated with this form of backscatter range from $0\text{-}25 \text{ m s}^{-1}$. In this chapter, data with spectral widths ranging from $0\text{-}25 \text{ m s}^{-1}$ and low Doppler velocities will be designated as LW1 data. As described in chapter 2, the Farley-Buneman and gradient drift instabilities may be described by a combined theory that was extended to include the EPCI by Dimant and Sudan (1997). There is another backscatter population that occurs in the D-region, characterised by low Doppler velocities and spectral widths of around 100 m s^{-1} and designated as LW2 data in this chapter, and it is suggested that the presence of this population is a consequence of the EPCI.

6.3 The Myopic Campaign Data Set

Table 6.1 shows the time intervals during which the myopic campaign was run on the Iceland radar. The Finland radar was often running another mode during these times. For the 24th-26th February 1997 and the 3rd, 9th and 10th October 1997, the dwell time was 7 seconds, whereas it was 3 seconds for the other intervals.

Myopic Scan Interval	Scheduled Dates for Myopic Scan Mode
00-24 UT	February 1997: 24, 25, 26; February 1998: 5, 13, 14
15-24 UT	October 1997: 3, 9
00-06 UT, 15-24 UT	October 1997: 10; November 1997: 20, 21, 22, 23, 24, 25
00-06 UT, 18-24 UT	March 1998: 9, 10, 11, 30

Table 6.1: Intervals when the myopic scan was running on CUTLASS Iceland

Figures 6.1(a)-(c) show the backscatter obtained in the D and E-regions for the 378 hours of data taken during the myopic scan mode. Each panel in the figures shows the data obtained for a continuous run of the myopic scan mode and the panels, from left to right and then down the page, correspond to chronological order. The frequency of occurrence is plotted on the vertical axis. The red bars denote scatter from the E-region and the green bars denote scatter from the D-region. The width of each bar corresponds to an interval of 15 minutes. The boundary altitude separating the D-region from the E-region was chosen as 95 km, with the D-region occurrence plotted from 70-95 km and the E-region occurrence plotted from 95-120 km. The value of 95 km was chosen because it was sufficiently below the electrojet to exclude most Farley-Buneman echoes and associated gradient drift echoes. As predicted by the theoretical description given in chapter 2, when there is a high occurrence of D-region scatter, then the occurrence in the E-region is also high, since the threshold drift velocity is higher for the D-region than the E-region. Also, numerous E-region echoes may be detected without there being a high occurrence of backscatter in the D-region, and this is also consistent with values of the threshold drift velocity. The threshold velocity for the EPCI is approximately 1000 m s^{-1} in the D-region for negative flow angles.

There are a number of intervals during which a high frequency of backscatter occurrence was observed. The intervals of high D-region backscatter cover a large range of magnetic local times and include observations corresponding to both the eastward and westward electrojets. Because of the location of the CUTLASS radars, magnetic local time (MLT) and universal time (UT) are very similar. The Iceland data covers the full range of MLT, whereas the Finland data range from around 15-06 MLT, i.e. magnetic latitude coverage of 225° , mostly on the night side including the evening and post midnight sectors. All data obtained during the myopic campaign were examined in order to determine the nature of the scatter in the D-region. The D-region scatter present was consistent with both LW1 and LW2 echoes. As a point of note, Milan and Lester (2001) obtained most observations in the period from 18 to 06 UT.

SUPERDARN PARAMETER PLOT

E-region and D-region Backscatter Occurrence

Figure 6.1(a): Frequency of occurrence, for backscatter echoes from 95-120 km (shown in red) and 70-95 km (shown in green) from the myopic campaign.

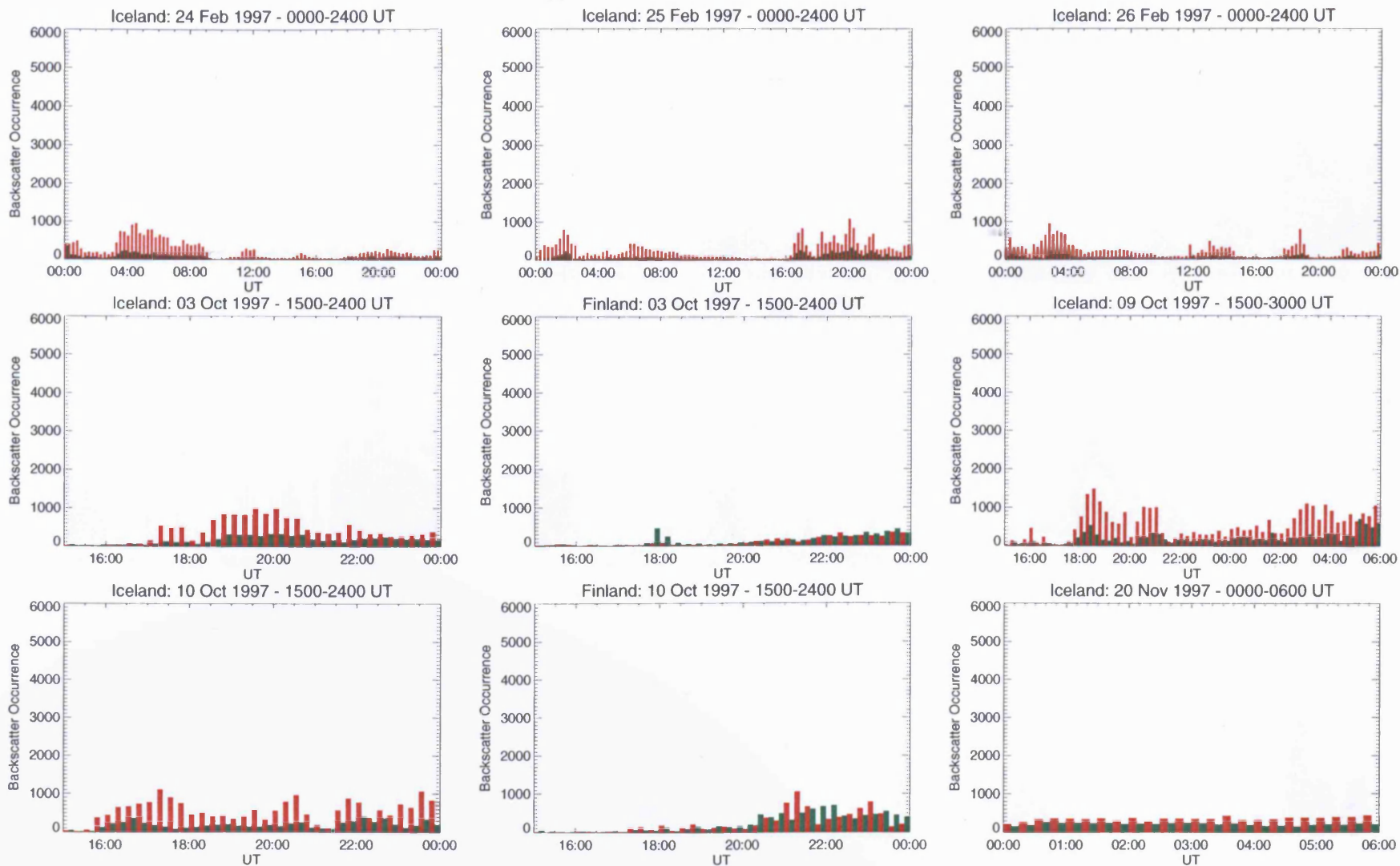


Figure 6.1(b): Frequency occurrence for echoes in the E-region and D-region during the myopic campaign.

SUPERDARN PARAMETER PLOT

E-region and D-region Backscatter Occurrence

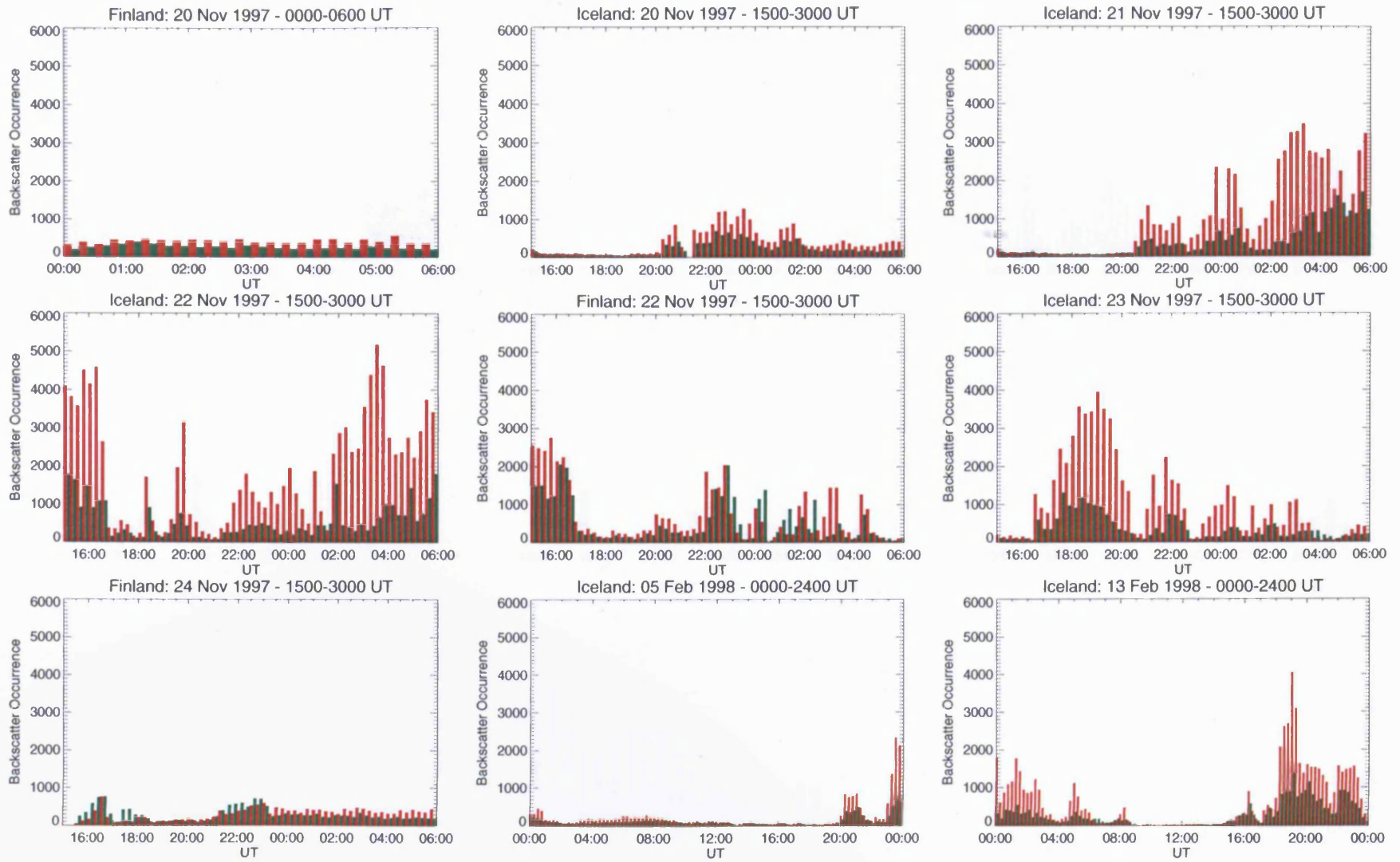
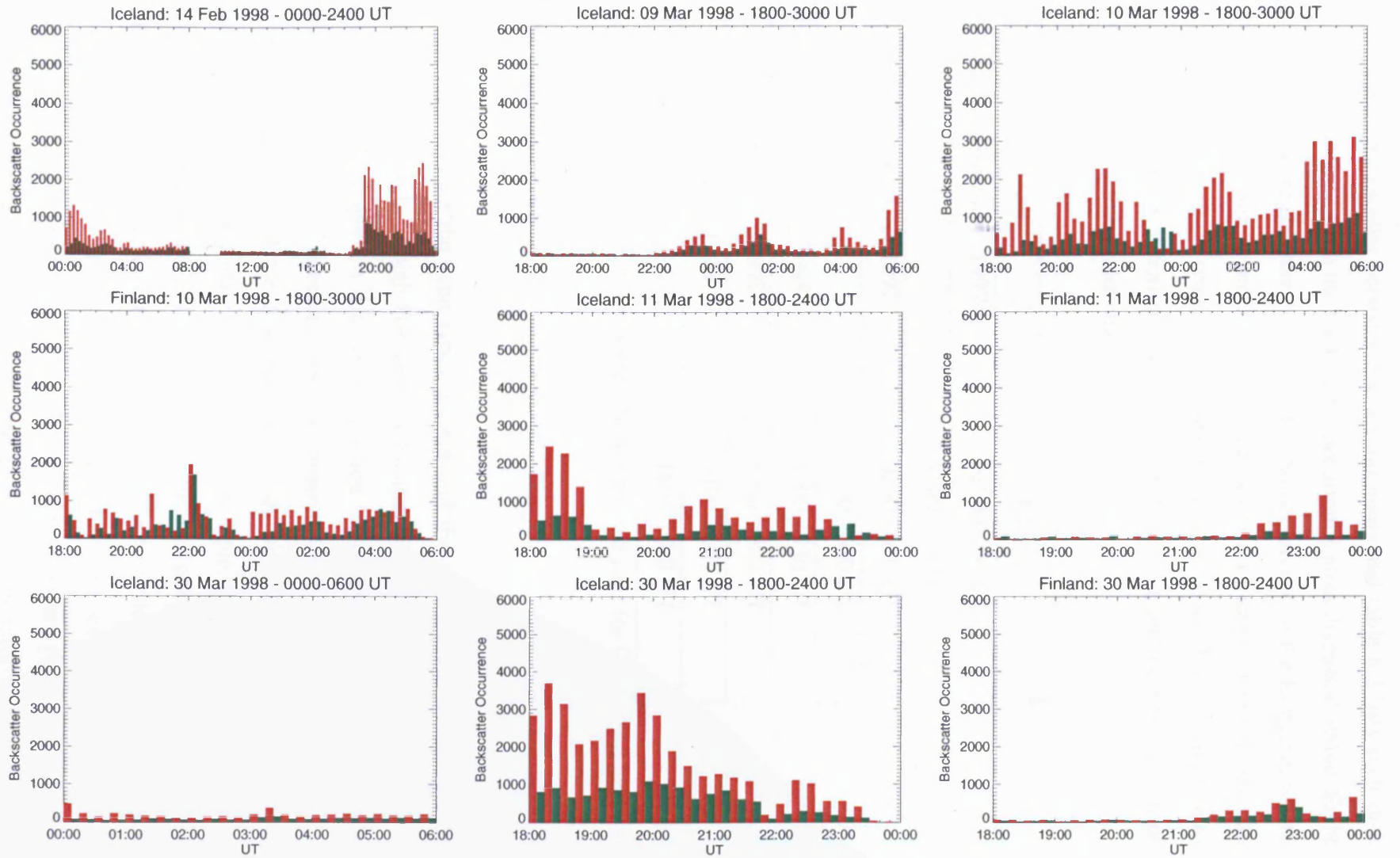


Figure 6.1(c): Frequency occurrence for echoes in the E-region and D-region during the myopic campaign.

SUPERDARN PARAMETER PLOT

E-region and D-region Backscatter Occurrence



Intervals of high backscatter persisted for several hours and table 6.2 lists such data intervals for CUTLASS Iceland from the backscatter occurrence plots discussed above. Eight intervals were found that were characterised by high echo occurrence in the E-region, where the effective criterion was chosen as more than 2500 echoes in a 15-minute interval, because the EPCI was more likely to be seen when the backscatter occurrence was high. In addition to the myopic scan data, 830 hours of normal scan data were examined, but there was a lack of D and E-region scatter during these intervals.

Date	Interval
22 nd November 1997	0200-0400 UT
	1500-1630 UT
23 rd November 1997	0200-0600 UT
	1800-2000 UT
13 th February 1998	1900-1930 UT
14 th February 1998	1900-2100 UT
11 th March 1998	0400-0600 UT
30 th March 1998	1800-2000 UT

Table 6.2: Intervals where strong scatter was seen during myopic runs for CUTLASS Iceland

6.4 Radar Echo Characteristics

In order to demonstrate the echo types present and the altitude dependence of the scatter, two 15-minute intervals of high D-region backscatter from 23rd November 1997 are now described to highlight important data characteristics. Two case studies showing data from 22nd November 1997 and 13th February 1998 are shown in the next section.

The altitude dependence of the echo populations shown below has been presented using five panels and figure 6.2(a) may be taken as an example. From left to right, these panels show the altitude in km plotted against the backscatter power in dB, the spectral width in m s^{-1} , the line-of-sight Doppler velocity in m s^{-1} , the range from the radar in km and the radar beam that made the measurement. The echoes detected were collected by all radar beams and fractional values for each radar beam in the fifth panel are proportional to the range gate in which the target lay. Each echo collected during the time interval is shown as a point.

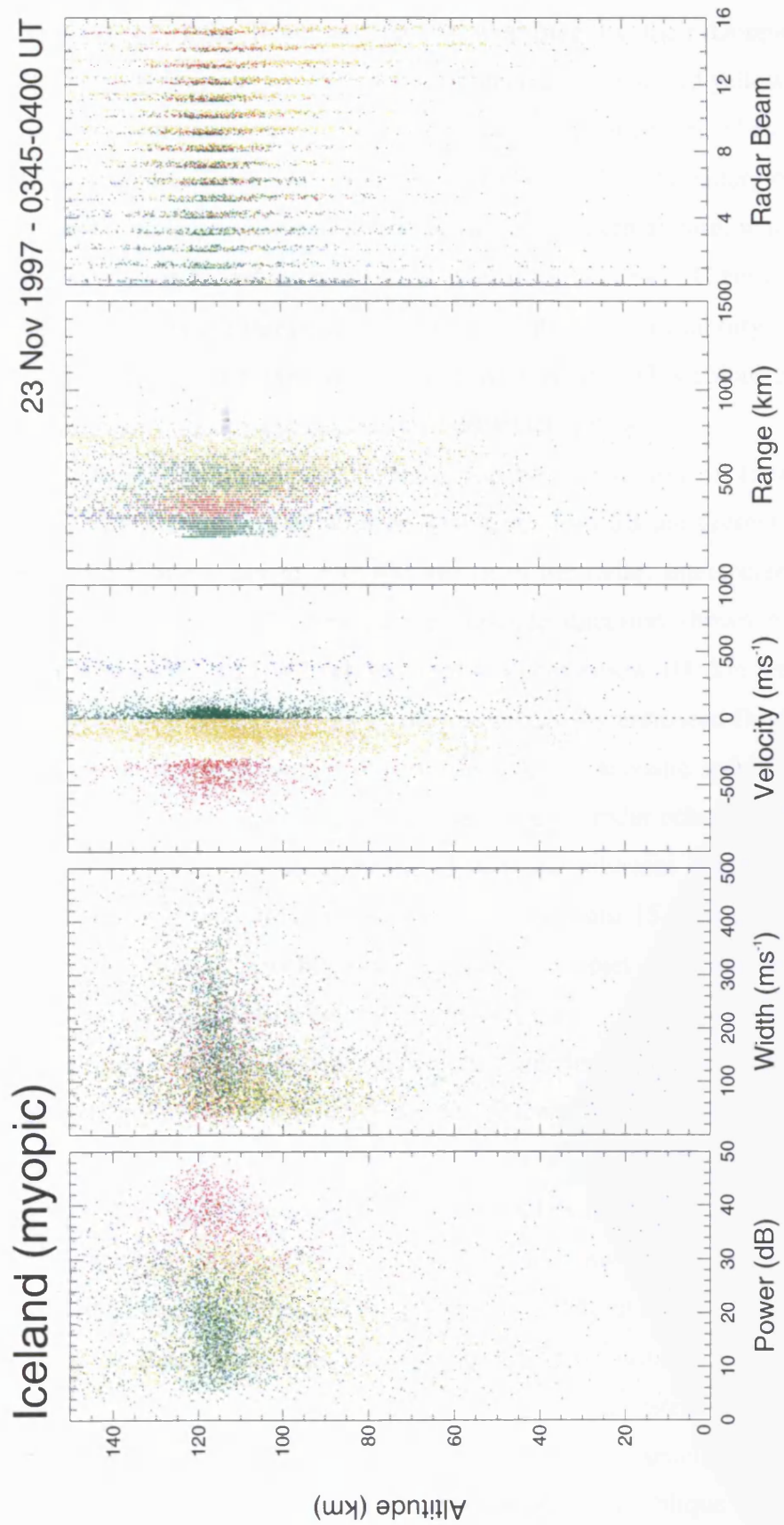


Figure 6.2(a): The altitude of backscatter echoes, shown against other backscatter parameters for the interval 0345-0400 UT on 23rd November 1997. Red = Doppler velocities from -1000 to -300 m s^{-1} , yellow = -300 to 0 m s^{-1} , green = 0 to $+300$ and blue = $+300$ to $+1000 \text{ m s}^{-1}$.

The main discriminator between different echo types was taken to be the Doppler velocity, since Type I and Type II echoes can be identified by their Doppler velocity. Velocities ranging from -1000 m s^{-1} to -300 m s^{-1} are denoted by red and yellow is used for velocities lying between -300 and 0 m s^{-1} . Green is used for the range 0 m s^{-1} to $+300 \text{ m s}^{-1}$, and blue is used for velocities from $+300 \text{ m s}^{-1}$ to $+1000 \text{ m s}^{-1}$. The boundary of 300 m s^{-1} was chosen because the ion-acoustic speed at 200 K for the isothermal case, which has been assumed in the modelling conducted in chapter 5, was around 340 m s^{-1} . Therefore, for cases where the flow speed exceeds the threshold for the Farley-Buneman instability, it should be possible to differentiate Type I and Type II echoes in the E-region. This colour code is used in subsequent figures describing altitude dependence presented below.

Figure 6.2(a) shows the altitude dependence for the period from 0345-0400 UT on 23rd November 1997. Type I red echoes with powers around 40 dB are present at altitudes from around 100-120 km and occur at 300-400 km from the radar. Interspersed with this scatter are Type II echoes with velocities in the opposite direction shown as the green population. It is suggested that the LW2 echoes from altitudes below 100 km are associated with the EPCI. The speeds of around 500 m s^{-1} may be caused by enhanced flow that would raise the plasma temperature, which would in turn raise the ion-acoustic speed at which the instability saturates, possibly corresponding to cases of Type IV radar echoes as described in chapter 3. The red population is seen in beam 15 and the adjacent beams. The yellow population is seen in most beams, although preferentially in beam 15. The echo population shown here is consistent with a possibly fast westward electrojet flow that would excite secondary gradient drift waves that correspond to Type II echoes.

Figure 6.2(b) shows the altitude dependence of scatter for the period from 1830-1845 UT on 23rd November 1997. There is E-region scatter described by the blue population and this extends into the D-region as well as to altitudes of 150 km. As for the interval described above, the E-region scatter again contains three echo populations. There is the Type I blue population and also the green and yellow populations with positive and negative Doppler velocities. The range dependence of the echoes is also similar to that of the previous interval. The blue population is present in beams 11-15 at E-region altitudes, and the yellow population is present in beams 0-10. These echo signatures are consistent with an electrojet flow that is optimally observed by beams 14 and 15. The creation of secondary gradient-drift waves would then lead to Type II echoes that occur at angles more oblique to the electrojet direction. The blue population extends up to altitudes above the Hall current region and echoes caused by the Farley-Buneman instability should not be detected from these altitudes.

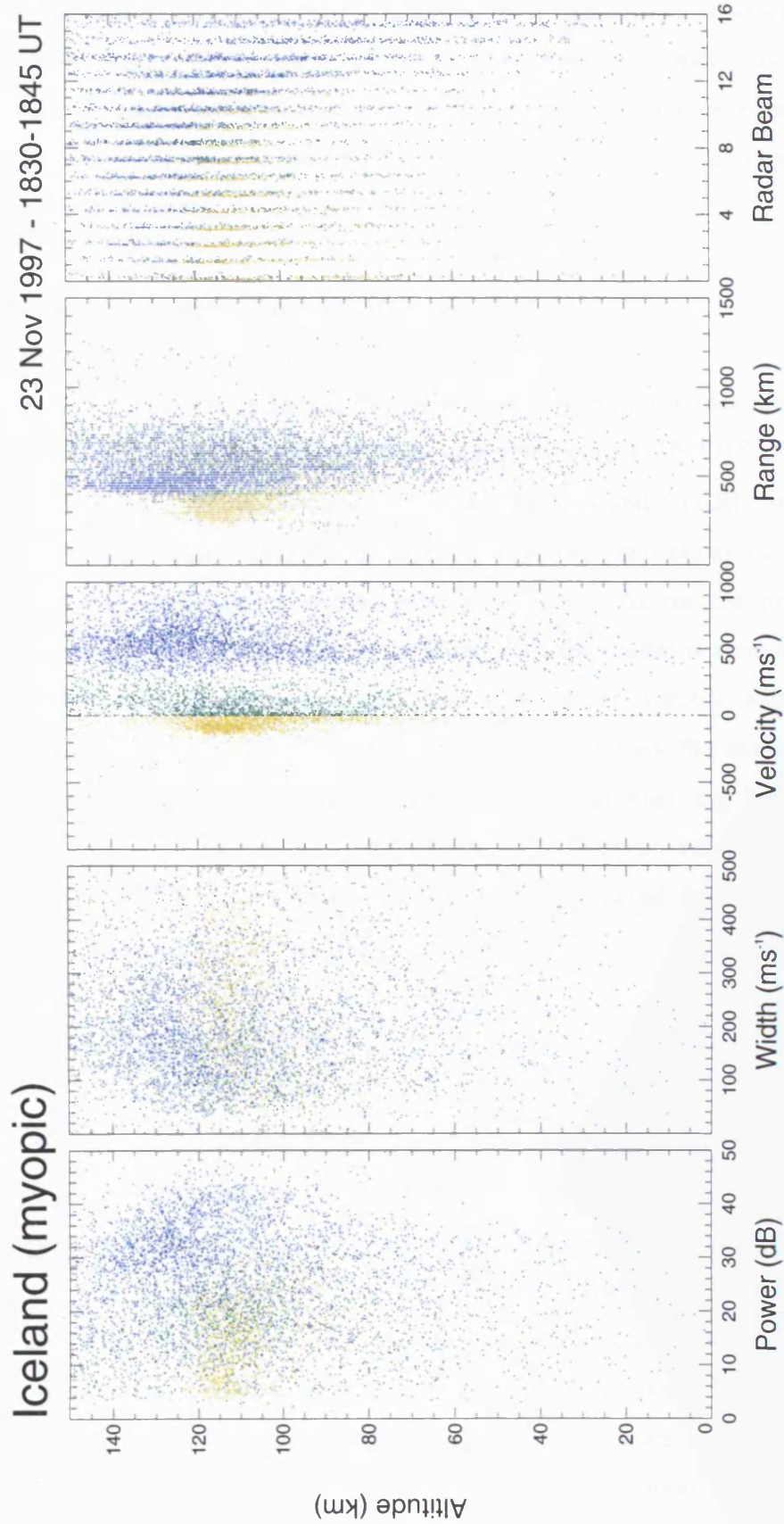


Figure 6.2(b): Another interval on 23rd November 1997, 1830-1845 UT, for which the altitude variation of the backscatter parameters has been shown. The same colour code has been used as for the previous figure and all subsequent figures of this type adopt the same colour code.

These higher altitude echoes may result from refraction of the radio waves, thus giving a false higher altitude from which the echoes originate. This interval demonstrates how the interferometer may at times provide suspect results, as the blue population extends quite a long way down into the D-region and beyond and values of the Doppler velocity around the ion-acoustic speed would not be seen at such a low altitude.

6.5 Two Case Studies of D-region Echo Occurrence

High backscatter occurrence in the D-region was observed for two intervals: 22nd November 1997 from 1500-1715 UT and 13th February 1998 from 1730-2045 UT. The echo occurrence during these intervals is discussed, using CUTLASS and STARE data, together with the evolution of a D-region backscatter layer. The growth and decay of the layer is examined, together with associated E-region echo populations. As for the previous data intervals that have been described, the altitude dependence of the scatter is shown by plotting the altitude of the echoes against, in turn, the backscatter power, spectral width, Doppler velocity, range from the radar and, finally, the radar beam that took the measurement. In addition, backscatter parameters have been plotted against one another, e.g. the backscatter power and spectral width plotted against the line-of-sight Doppler velocity. As for the previous intervals shown, 15-minute time intervals were considered because geophysical conditions will not vary very much during this time.

6.5.1 Case Study 1: 22nd November 1997

Figure 6.3(a) shows the altitude dependence of the backscatter for the Iceland radar for 1500-1515 UT. Dividing the returns into a set of altitude layers allows examination of the different echo types that were observed. Considering the altitude range from around 130-140 km first, there are two easily identified echo populations. The green population has a backscatter power around 10 dB, a spectral width that varies from 100-400 m s⁻¹ and a low Doppler velocity. It occurs at a range from the radar of around 600 km and is seen in all radar beams. This population has the characteristics of Type II echoes, as defined above, corresponding to secondary gradient drift waves. The blue population has a backscatter power of around 40 dB, spectral width values of around 50 m s⁻¹ usually, a Doppler velocity around the ion-acoustic speed, a range from the radar of around 400 km and is also seen in all beams. This population has the characteristics of Type I echoes.

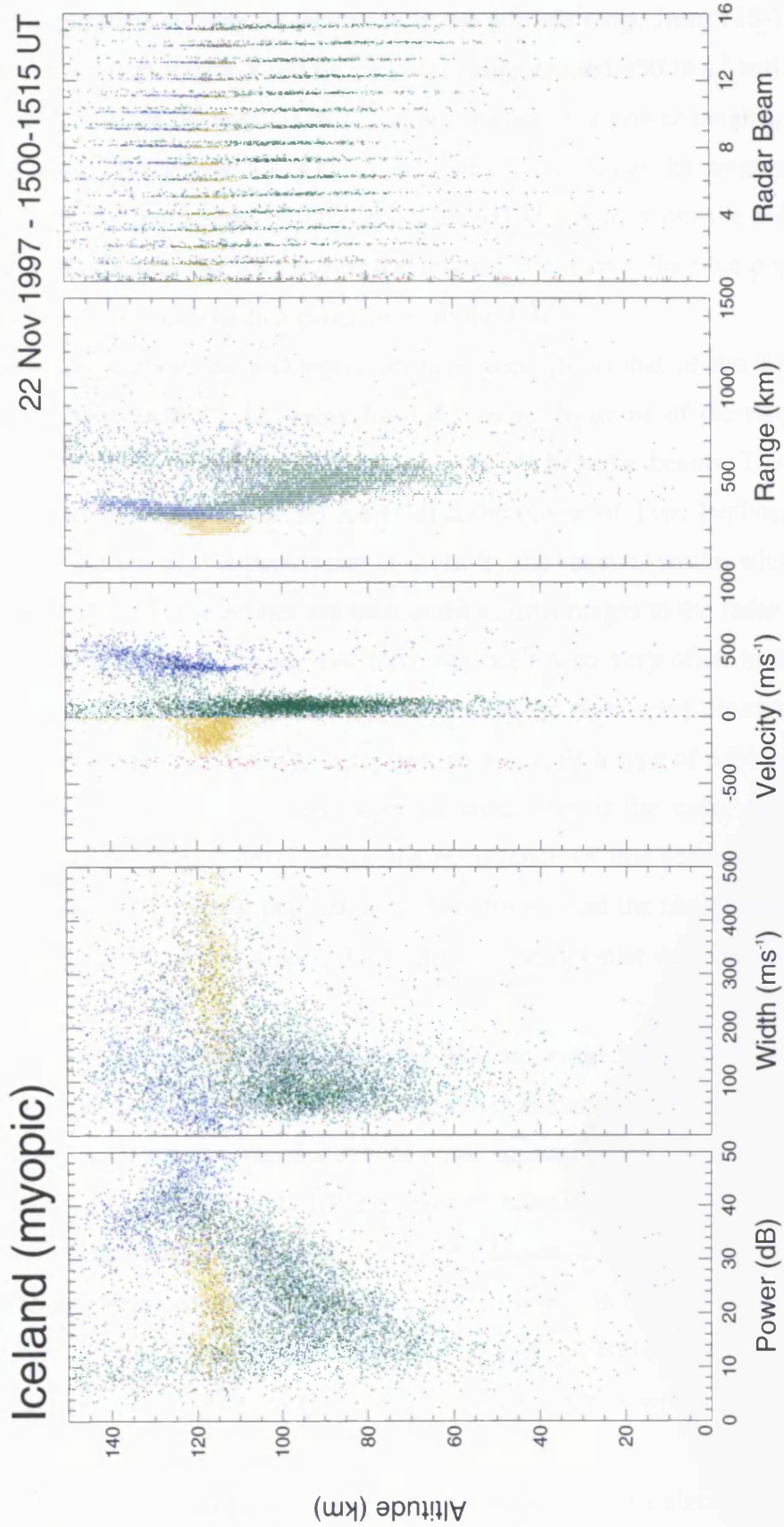


Figure 6.3(a): 1500-1515 UT for the first case study. Strong Type I echoes are present in the E-region, together with Type II echoes. There is a population present in the D-region, denoted by the colour green.

Three echo populations may be identified in the altitude range from 115-125 km. The blue population echoes occurred at a narrow velocity range around 350 m s^{-1} and the spectral width of this population was around 20 m s^{-1} , with a backscatter power ranging from 40-50 dB, especially at an altitude around 120 km. In the panel that indicates the range of the scatter from the radar, the blue population is seen to occur 300 km away from the radar and was again seen in all radar beams. As for the altitudes considered above, the blue population has the characteristics of Type I echoes that correspond to the FBI.

The yellow population has a Doppler velocity opposite to that of the Type I echoes and ranges from -300 to 0 m s^{-1} , i.e. away from the radar. In terms of the range from the radar, this population is the closest and appears in most of the radar beams. The backscatter power of the echoes is typically 15-20 dB lower than the power of Type I echoes. However, the most distinctive feature of this population is given by the spectral width, which ranges in value from 100 - 500 m s^{-1} . These echoes are seen at the closest ranges to the radar and possess the defining features of Type II echoes, but have not been seen very often in SuperDARN data (St. Maurice, private communication). However, these echoes were observed by Milan and Lester (2001) who identified them as belonging to a new fifth type of echo population. It has been suggested that this scatter may originate from behind the radar (Milan, private communication), and this would also explain the occurrence of this scatter in the smallest ranges close to the radar. The green population at this altitude had the characteristics of Type II echoes. The backscatter power is around 35-40 dB and the Doppler velocity ranges from 0 - 200 m s^{-1} .

The green population that occurred at the altitude range of 85-105 km has a low Doppler velocity value, is situated furthest from the radar and extends down to about 65 km. The echoes have a backscatter power that ranges from approximately 10-35 dB. The values of the spectral width are consistent with LW2 echoes, thus making meteor scatter an unlikely explanation for this population. Referring back to chapter 5, the results of theoretical predictions of the growth rate predicted that two layers should be formed where the growth rate was maximised, an EPCI layer for zero aspect angle and an FBI layer for aspect angles of around 1° . These layers correspond very well with the altitudes at which Type I and LW2 echoes are seen.

The data presented in this case study are consistent with an electrojet flow whose velocity exceeds that at which the EPCI is excited. The blue Type I echoes correspond to the Farley-Buneman instability and the D-region green echoes correspond to the EPCI. The high altitude blue and green populations again may be an effect of refraction. The maximum

backscatter power of the green population decreases with altitude, from 40 dB at 110 km down to 10 dB at 60 km. This is consistent with the decreasing value of the density perturbation because of the ionospheric profile. The backscatter power is proportional to ΔN^2 , the square of the irregularity density perturbation. In the E-region, the electron density is 10 times as high as in the D-region and hence the backscatter power may be 20 dB higher in the E-region than in the D-region for a corresponding density perturbation. In addition, the Type II E-region green population corresponds to secondary gradient drift waves.

The temporal evolution of the backscatter population is shown in figures 6.3(b)-(e). These figures show the backscatter population for 4 more 15-minute intervals up to 1715 UT, two hours after the first time interval. In figure 6.3(b) that shows the interval from 1530-1545 UT, the blue population with Type I Farley-Buneman characteristics has a lower Doppler velocity, around 300 m s^{-1} as opposed to 350 m s^{-1} in the previous figure. The other characteristics are mostly unchanged for this population, apart from a slight change in the range of the backscatter, which appears to originate from slightly further away than for the first time interval from 1500-1515 UT. The yellow population has the same characteristics in this plot, with the backscatter parameters almost identical to the previous interval and this is also true for the E-region green population. There are fewer echoes for the lower altitude green population, although the spectral width and backscatter powers have similar values to those shown in figure 6.3(a). The red population echoes are almost as numerous.

For the time interval 1600-1615 UT shown in figure 6.3(c), the Type I population Doppler velocity has now decreased below 300 m s^{-1} . The occurrence of the green population in the E-region has dropped in frequency. The yellow population Doppler velocity now ranges from about $100\text{-}250 \text{ m s}^{-1}$ and there is a slight gap between this and the population around 0 m s^{-1} . The echo occurrence of the lower altitude green population has now decreased significantly.

For figure 6.3(d), which shows the time interval 1630-1645 UT, the Type I population has now all but disappeared. The altitudinal extent of the yellow population has increased markedly since the previous interval, now extending down into the D-region. Finally, for the last interval, 1700-1715 UT shown in figure 6.3(e), the backscatter occurrence has dropped for all populations.

The data shown in figures 6.3(a)-(e) are consistent with an electrojet flow where the flow velocity decreases over time. As the velocity drops below the threshold velocity for the EPCI, the occurrence of the D-region green scatter decreases. As the velocity decreases further, the threshold velocity for the FBI is no longer exceeded and the scatter corresponding

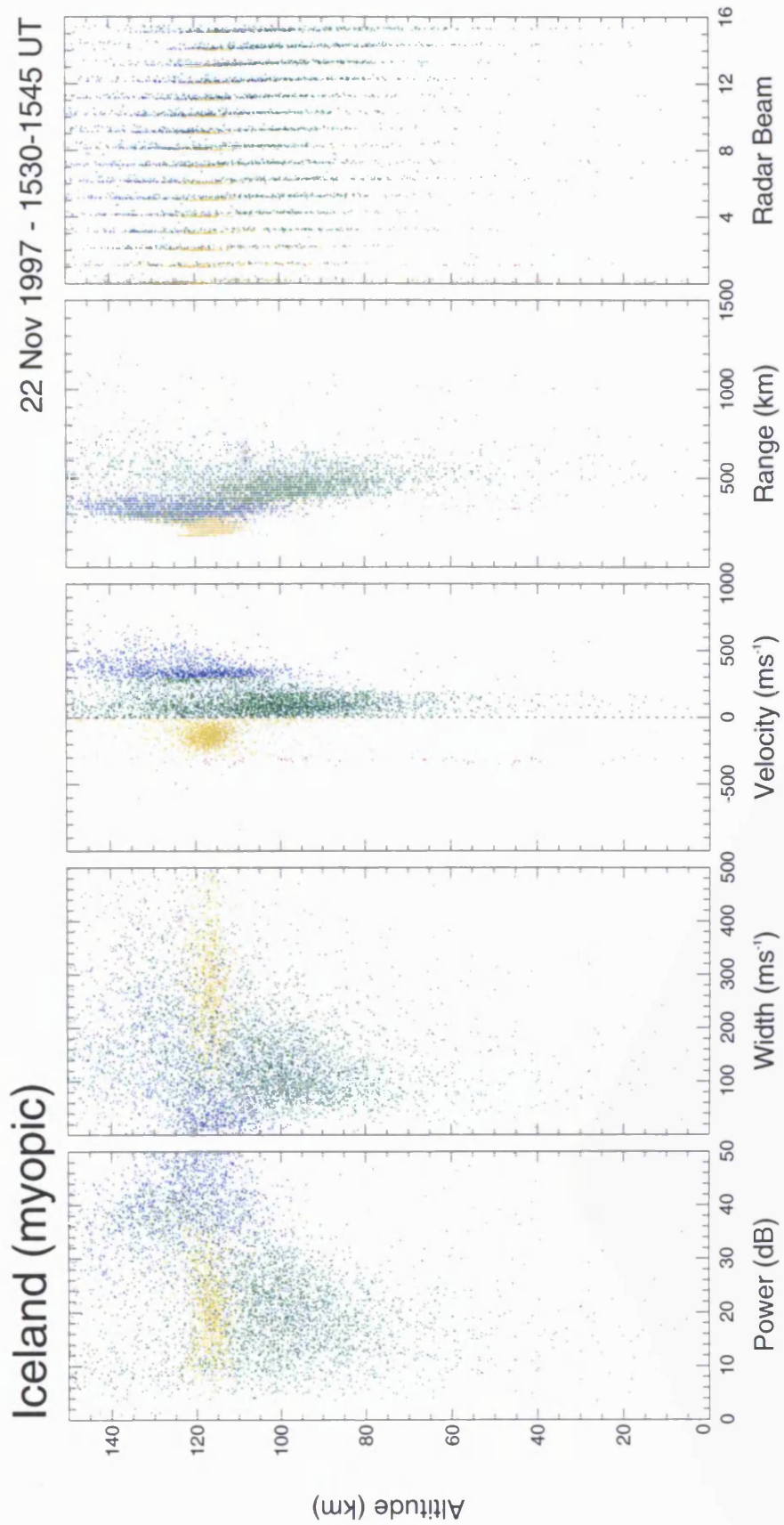


Figure 6.3(b): The interval from 1530-1545 UT is shown in this figure. The Doppler velocity of the Type I echoes has fallen and the backscatter occurrence in the D-region has also lessened.

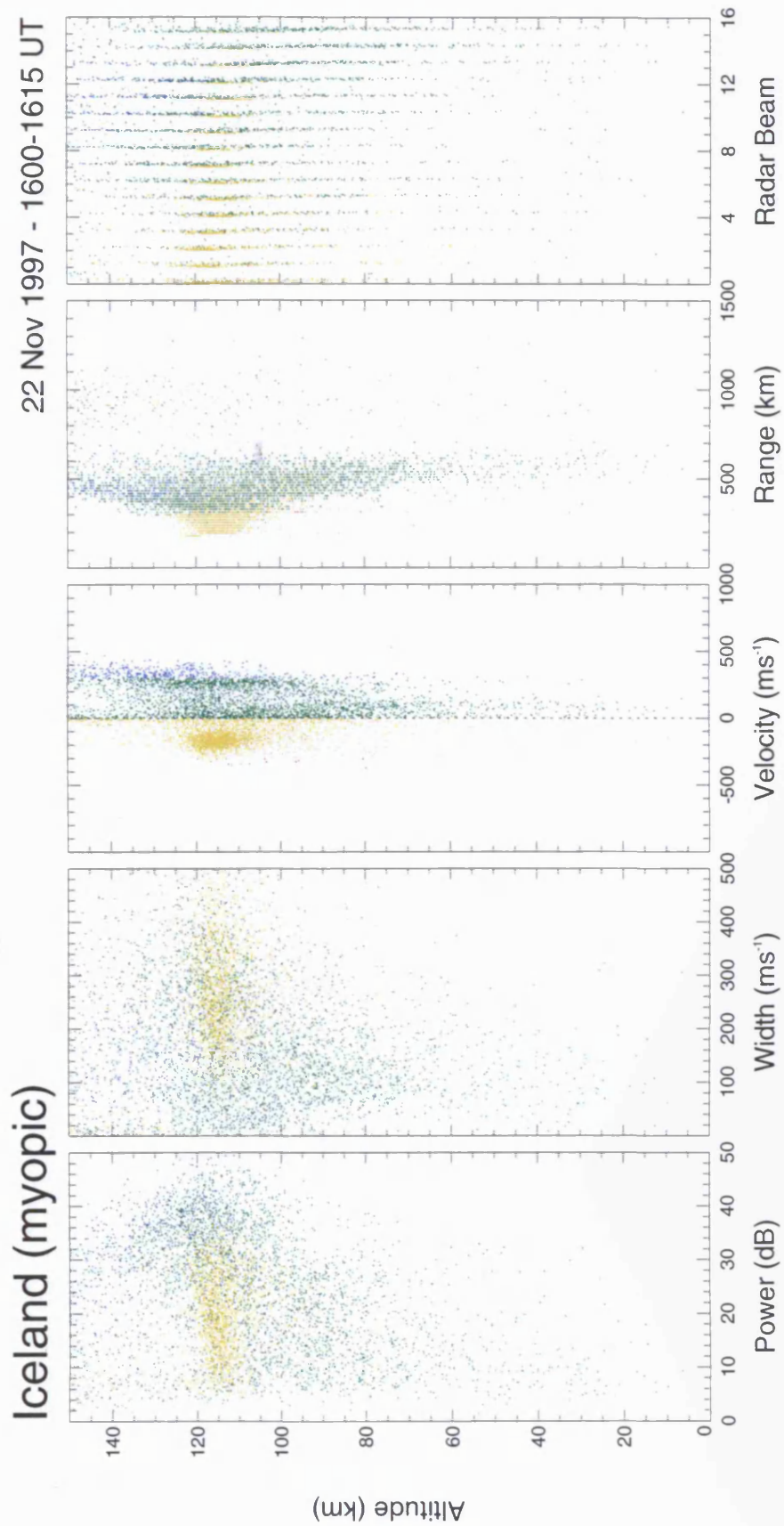


Figure 6.3(c): The interval 1600-1615 UT is shown in this figure. The Doppler velocity of the Type I echoes decreases further and the E-region Type II echoes occur over a higher altitude range. The D-region echo occurrence has decreased significantly.

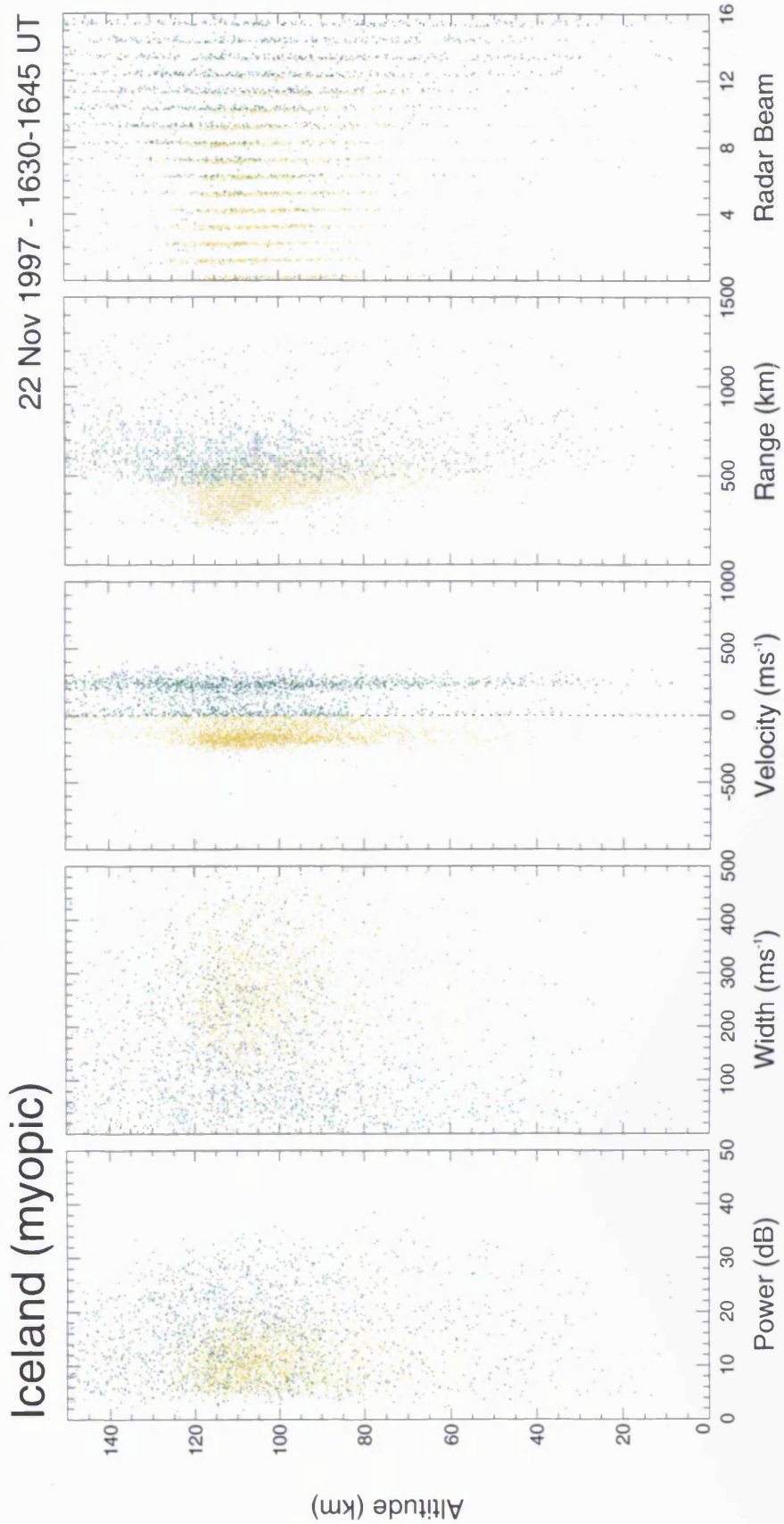


Figure 6.3(d): The interval 1630-1645 UT is shown in this figure. The Type II echoes previously confined to the E-region are now present over an altitude range 80-120 km.

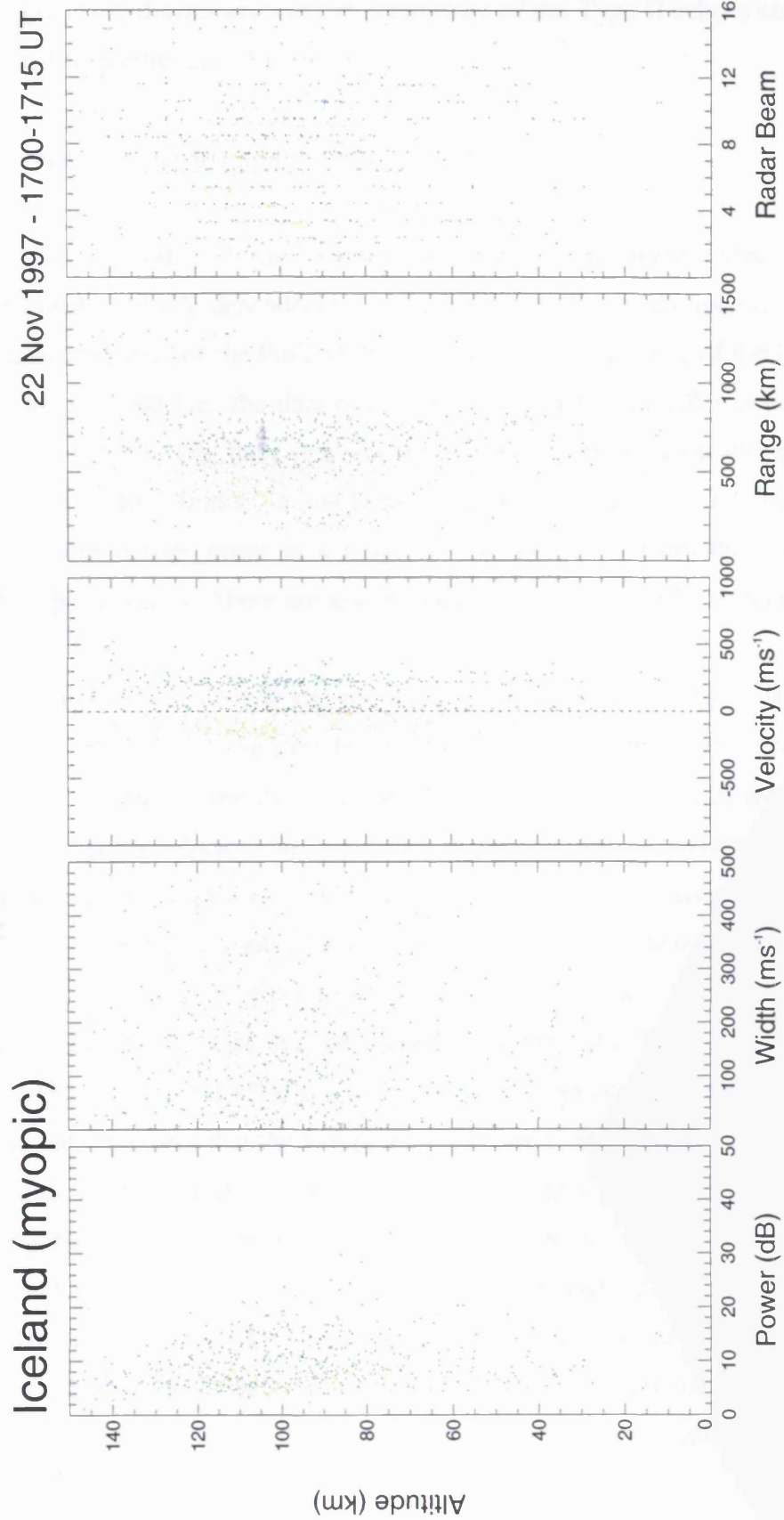


Figure 6.3(e): The interval 1700-1715 UT is shown in this figure. The backscatter occurrence for all echo populations has now fallen significantly.

to these echoes gradually disappears and the occurrence of the Type II echoes corresponding to the gradient drift instability also decreases.

6.5.2 Simultaneously Collected Finland Data

For this data interval, both the Iceland and Finland radars were collecting data and figure 6.4(a) shows the altitude dependence for the Finland radar for the interval from 1500-1515 UT. The characteristics of the Finland data are different from those of the Iceland data. For altitudes from 130-140 km, the data have the characteristics of LW1 echoes. For the altitude range from 120-130 km, there is a single population with a backscatter power of 40 dB, a spectral width of 40-100 m s⁻¹, a low Doppler velocity in directions towards and away from the radar. These echoes occur at a range of 250 km away from the radar and are consistent with Type II echoes. There are also echoes at a range of 1000 km and are seen in all radar beams.

For the altitude range 105-120 km, the backscatter power ranges from 20-40 dB, the spectral width is around 40 m s⁻¹, the Doppler velocity is again low, the scatter occurs slightly further away at 300 km and is seen in all beams. Positive Doppler velocities are observed in beams 6-15 and negative velocities are observed in beams 0-5. Concentrating on the E-region, Type II echoes with velocities close to zero are seen. This echo signature persisted to lower altitudes, i.e. there was a continuous region of scatter that extended over an altitude range of about 50 km. The range of the scatter gradually moves away from the radar as the altitude decreases. Two layers may still be identified in the data. The spectral widths are consistent with LW2 data and the velocities are negative over an altitude range of 80-120 km. The range of the data indicates that the E-region returns are closer than the D-region returns and this is similar to that which is seen in the Iceland data. The altitude gap between backscatter populations is again evident and may be related to the absence of scatter in CUTLASS Iceland for this region, i.e. if the FBI is not strongly excited within a certain altitude range then the secondary gradient drift instability will also not be strongly excited.

From 75-105 km, the Doppler velocities are again low, and the spectral width is characteristic of LW2 echoes. The scatter is seen in all beams and the range of the radar is further away.

The echo populations shown here are consistent with radar echoes observed at directions perpendicular to the auroral electrojet. Again, the decrease in the backscatter power

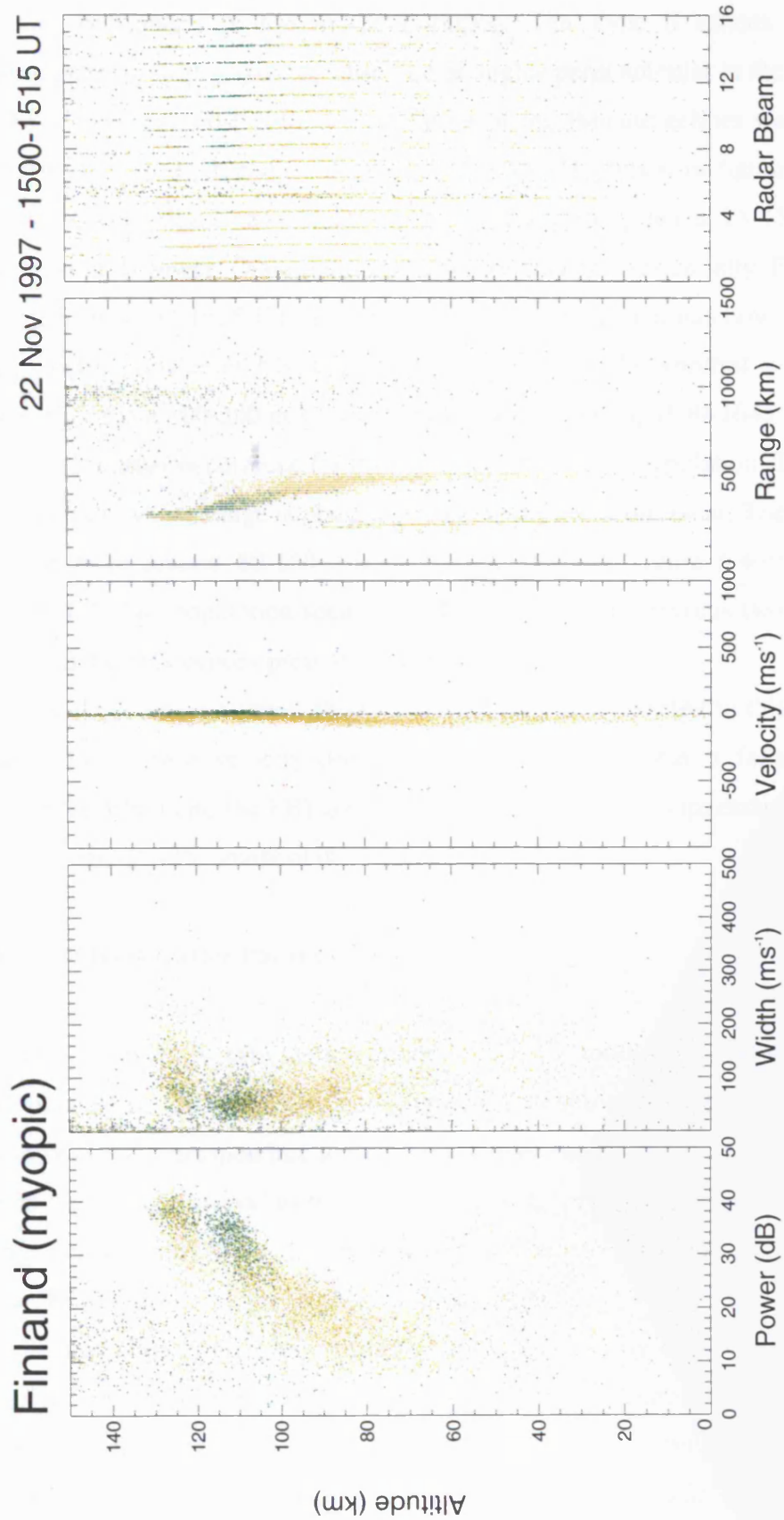


Figure 6.4(a): The interval from 1500-1515 UT for the CUTLASS Finland radar is shown in this figure. The backscatter occurrence is dominated by Type II echoes. There is a high echo occurrence in the D-region.

corresponds to the ionospheric profile in the D-region. The Type II echoes are present because secondary gradient drift waves are observed at angles perpendicular to the electrojet.

As for the Iceland data, the temporal evolution of the Finland echoes was examined by looking at figure 6.4(b)-(e). For the interval 1530-1545 UT shown in figure 6.4(b), the population at 120-130 km altitude has a higher range of backscatter powers, 25-45 dB, and its spectral widths are slightly lower. Other parameters do not change substantially. Figure 6.4(c) shows the interval from 1600-1615 UT. The population above 120 km has now disappeared and the D-region echo population has Type II characteristics. The spectral width of this population now ranges from 100-300 m s^{-1} . For figure 6.4(d) showing 1630-1645 UT, there is a reduction in the backscatter occurrence for the extended altitudinal population. There is also an additional population whose range is about 1200 km away from the radar. These are LW1 echoes and extend from around 80-150 km in altitude. Finally, figure 6.4(e) shows the interval 1700-1715 UT. The population seen in the D-region in the previous two figures has now disappeared and the only echoes present are LW1 echoes.

As for the Iceland data discussed above, the Finland data presented in this section are consistent with a flow whose velocity decreases over time such that it falls below the threshold at which the EPCI and the FBI are excited, leading to the disappearance of scatter from irregularities created by the gradient drift instability.

6.5.3 Comparison of Backscatter Parameters

The figures discussed in this section relate to the 15-minute interval of data from 1500-1515 UT collected by CUTLASS Iceland. Figure 6.5(a) shows a scatter plot of spectral width against the velocity, corresponding to the two altitudes ranges of 70-95 km and 95-120 km. The different colours correspond to the different radar beams, with colours from blue to red representing beams from 0 to 15. Examining the echoes carefully, a number of populations may be discerned at the higher altitude range. The Type I Farley-Buneman echoes may be distinguished by their low spectral widths and velocity values around the ion-acoustic speed. The colours of the data points indicate that most echoes of this type were observed by beam 15, although beam 0 also observed Type I echoes but these were not as numerous. This is consistent with an eddy in the flow since ion-acoustic speed echoes are present in beams from opposite sides of the radar. The central beams were observing echoes where the spectral width ranged from 50-150 m s^{-1} . All radar beams made measurements corresponding to zero velocity, although different beams highlighted different regions of

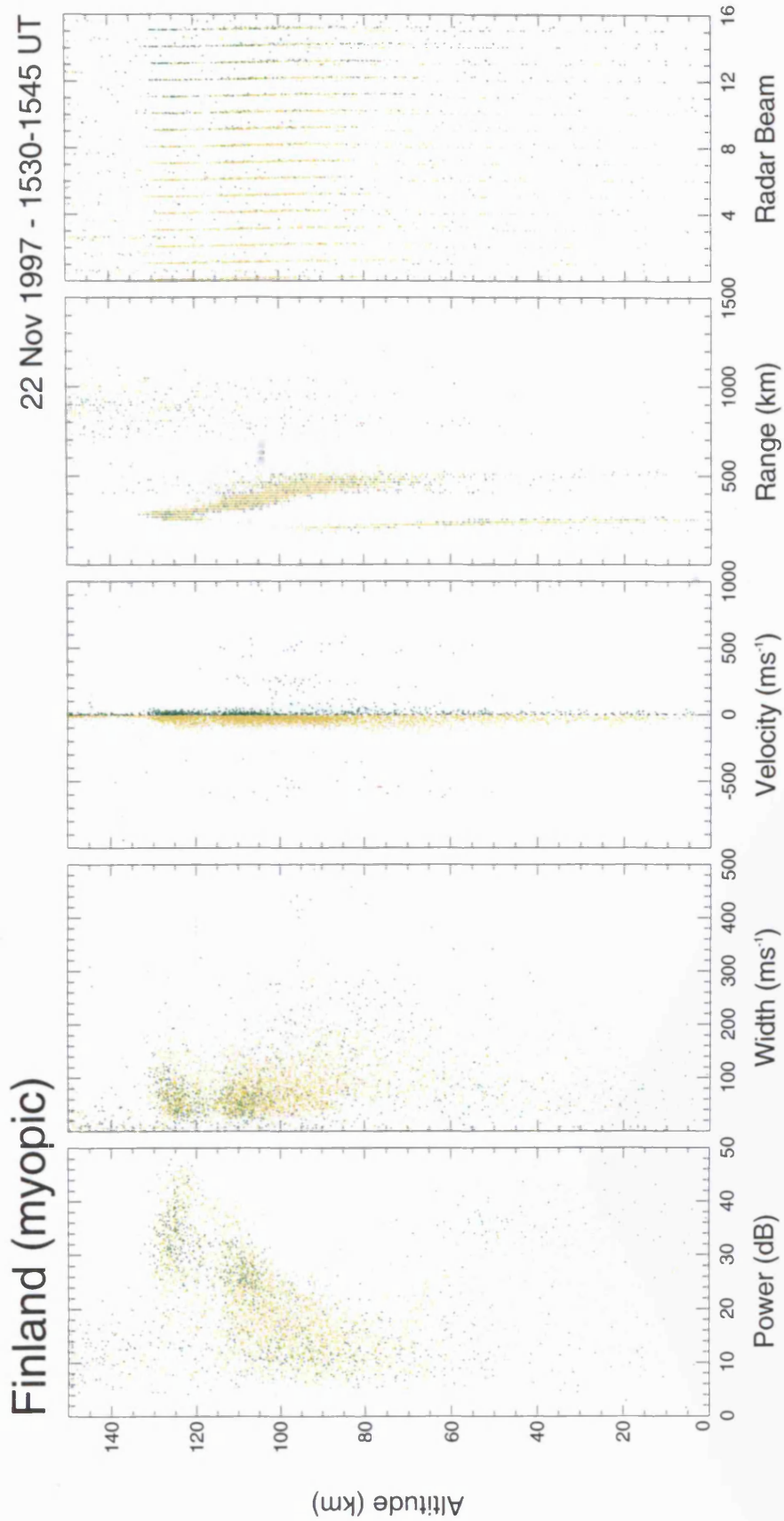


Figure 6.4(b): The interval from 1530-1545 UT is shown in this figure. The morphology of scatter in the D-region resembles that for the same interval corresponding to the CUTLASS Iceland radar, especially for the backscatter power.

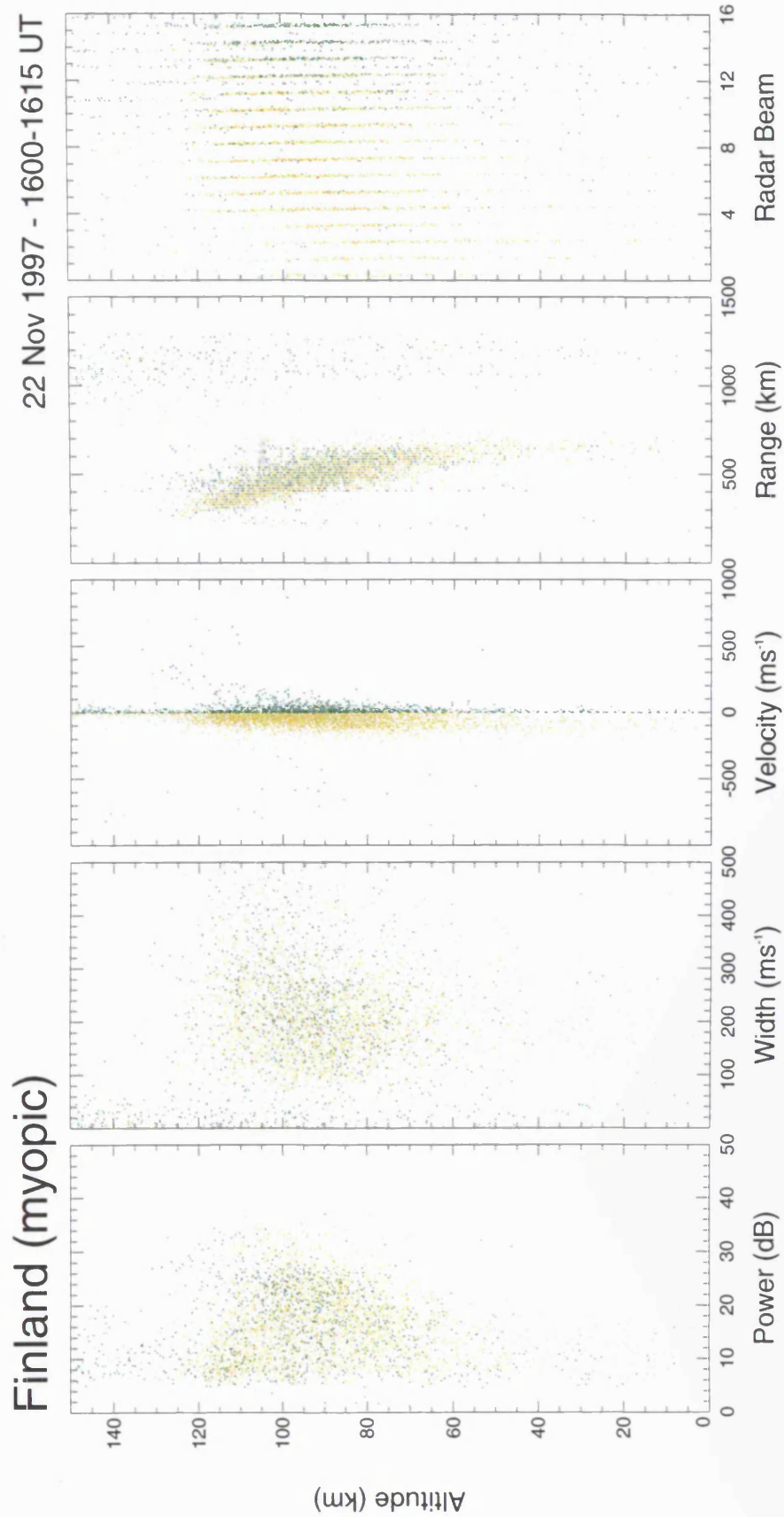


Figure 6.4(c): The interval 1600-1615 UT is shown in this figure. The altitude dependence of the scatter for the period from 1500-1515 UT is obtained by the CUTLASS Finland radar.

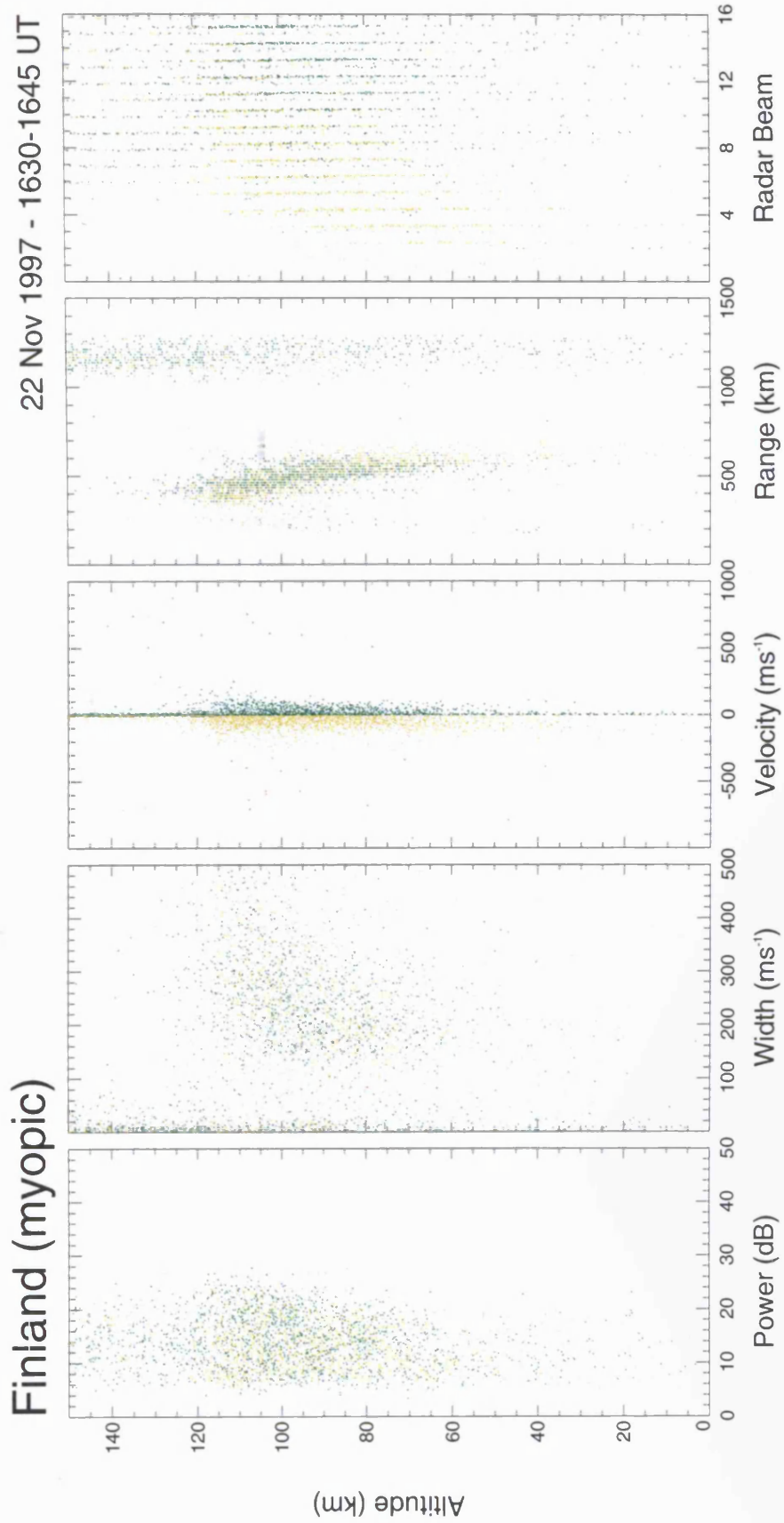


Figure 6.4(d): The interval 1630-1645 UT is shown in this figure. The backscatter occurrence in the D-region and E-region has lessened.

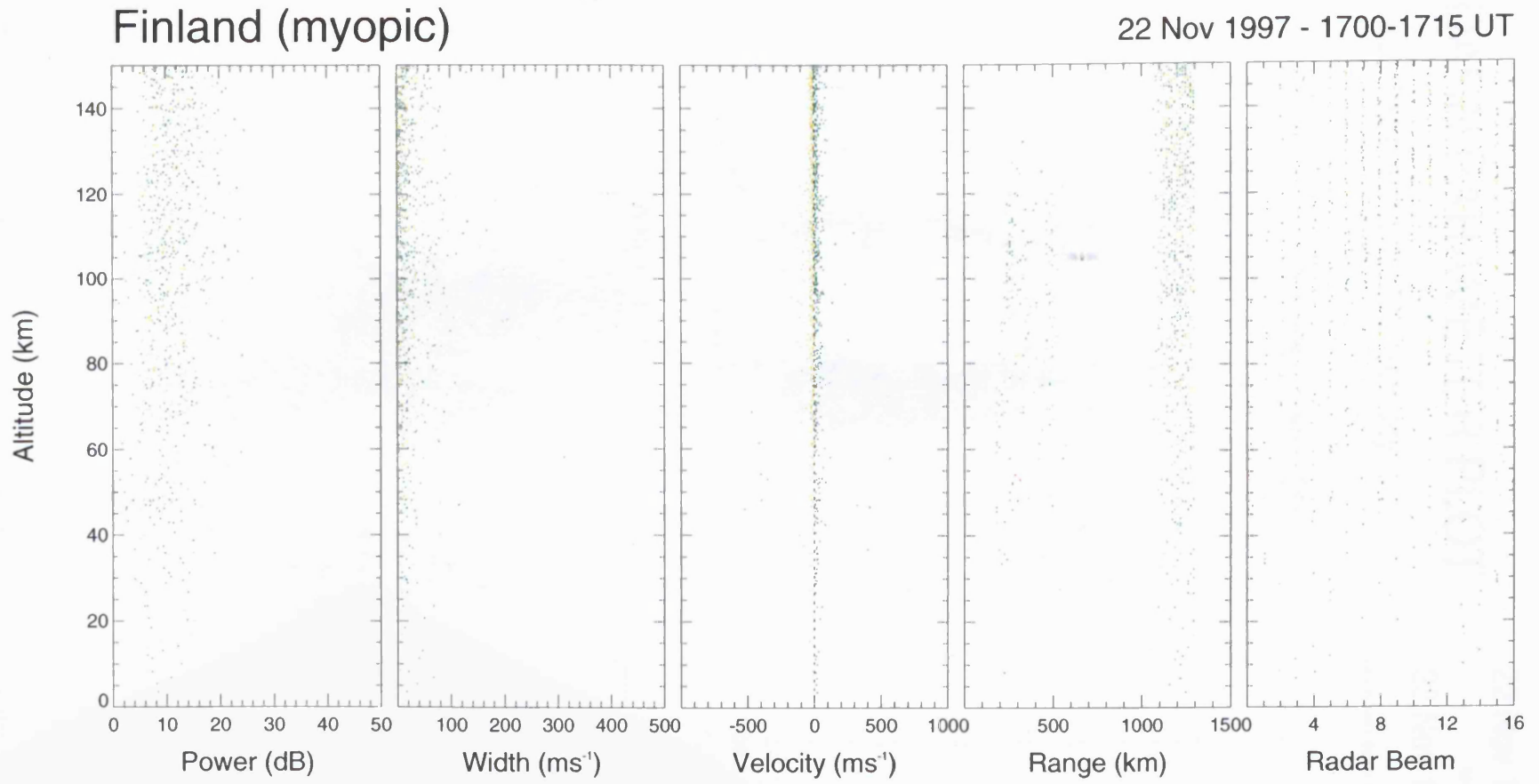


Figure 6.4(e): The interval from 1700-1715 UT is shown in this figure. There is now little backscatter present.

SUPERDARN PARAMETER PLOT

Iceland Spectral Width against LOS Velocity

22 Nov 1997⁽³²⁶⁾

to

23 Nov 1997⁽³²⁷⁾

unknown scan mode (-6312)

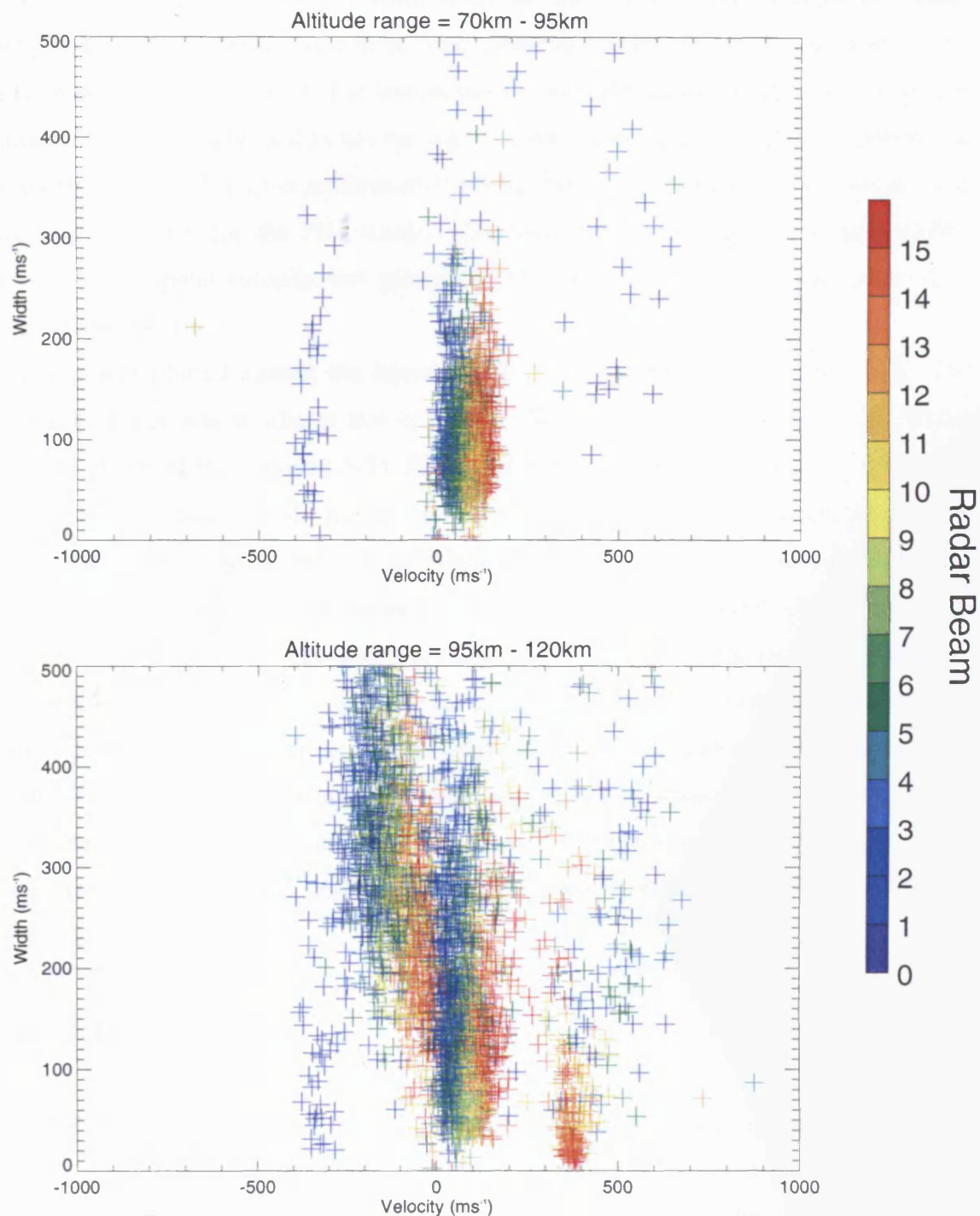


Figure 6.5(a): The spectral width plotted against the line-of-sight velocity for two altitude ranges in the D-region and the E-region.

scatter. The Type II echoes, apparent in the figure 6.3(a), had high spectral widths values and were observed by all beams, although mainly by beams around beam 0.

For the lower altitude range, the velocities ranged from around 20-150 m s⁻¹ and the spectral widths varied from 30-180 m s⁻¹ and most of the echoes were concentrated in a patch. The observing beam ranged from 0-15 as the line-of-sight velocity increased, indicating that higher Doppler velocities were observed along the flow direction of the electrojet. A small amount of scatter at around the ion-acoustic speed was also seen. E-region FBI echoes may be characterised as having high Doppler velocity and backscatter power and narrow spectra. Type II E-region gradient drift echoes have low Doppler velocity and a lower backscatter power than for the FBI echoes. They also have wide spectra. D-region EPCI echoes have low Doppler velocity, low spectral width, but not as low as that for FBI echoes, and have narrow spectra.

The power plotted against the line-of-sight velocity is shown in figure 6.5(b). The spread of echo types was similar to that in figure 6.5(a) for the lower altitude range. There was a spread in power from around 5-35 dB for the Type II echoes with negative velocities. The small amount of scatter at the ion-acoustic speed is seen to have the highest backscatter power. For the higher altitude range, Type I echoes were confirmed as those that have the strongest backscatter power. The power plotted against the spectral width is shown in figure 6.5(c). The D-region altitude range shows a concentrated patch of backscatter with spectral widths around 100 ms⁻¹ and a backscatter power of 20 dB. This may be contrasted with the E-region altitude range, where there is a large spread in both backscatter power and spectral width. The Type I echoes are apparent in the top-left hand region of the plot, with low spectral widths and high backscatter powers. The rest of the scatter displayed in the figure comprises mainly Type II echoes. Eglitis (1994) used a similar technique to identify different irregularity populations.

6.5.4 STARE Data Intervals

STARE data are presented for the case study discussed above, i.e. the period from 1500-1715 UT on 22nd November 1997. The upper two panels of figure 6.6(a) shows RTI plots of the backscatter power and velocity obtained for beam 3 of the Trondheim radar, which observes in the electrojet direction. There is strong backscatter observed in range gates 0-20, especially for 1500-1540 UT. The Doppler velocity for the same interval is fairly uniform, ranging from 200-400 m s⁻¹ and is consistent with Type I echoes. This high

SUPERDARN PARAMETER PLOT

Iceland Power against LOS Velocity

22 Nov 1997 ⁽³²⁶⁾

to

23 Nov 1997 ⁽³²⁷⁾

unknown scan mode (-6312)

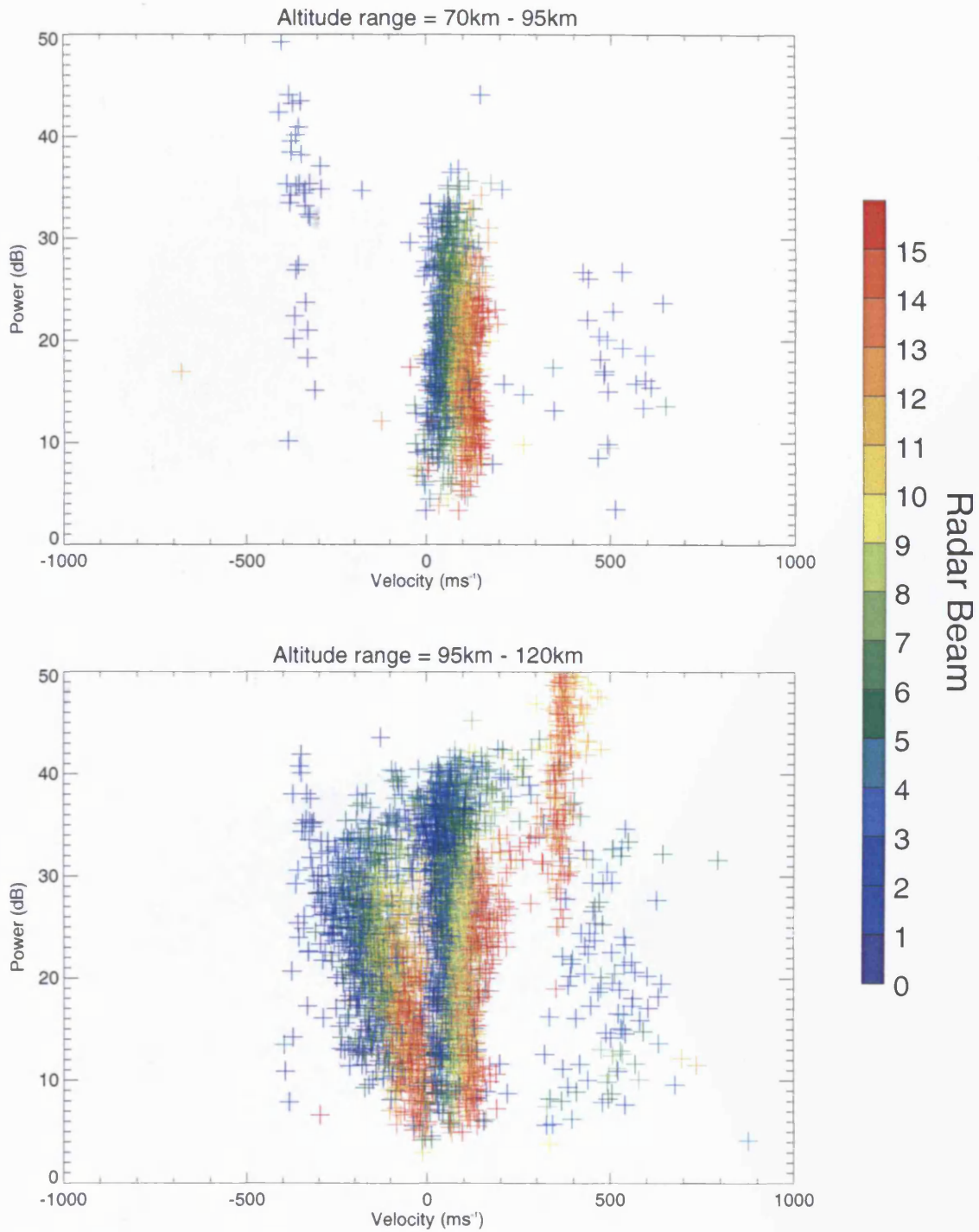


Figure 6.5(b): The backscatter power plotted against the line-of-sight velocity for two altitude ranges in the D-region and the E-region.

SUPERDARN PARAMETER PLOT

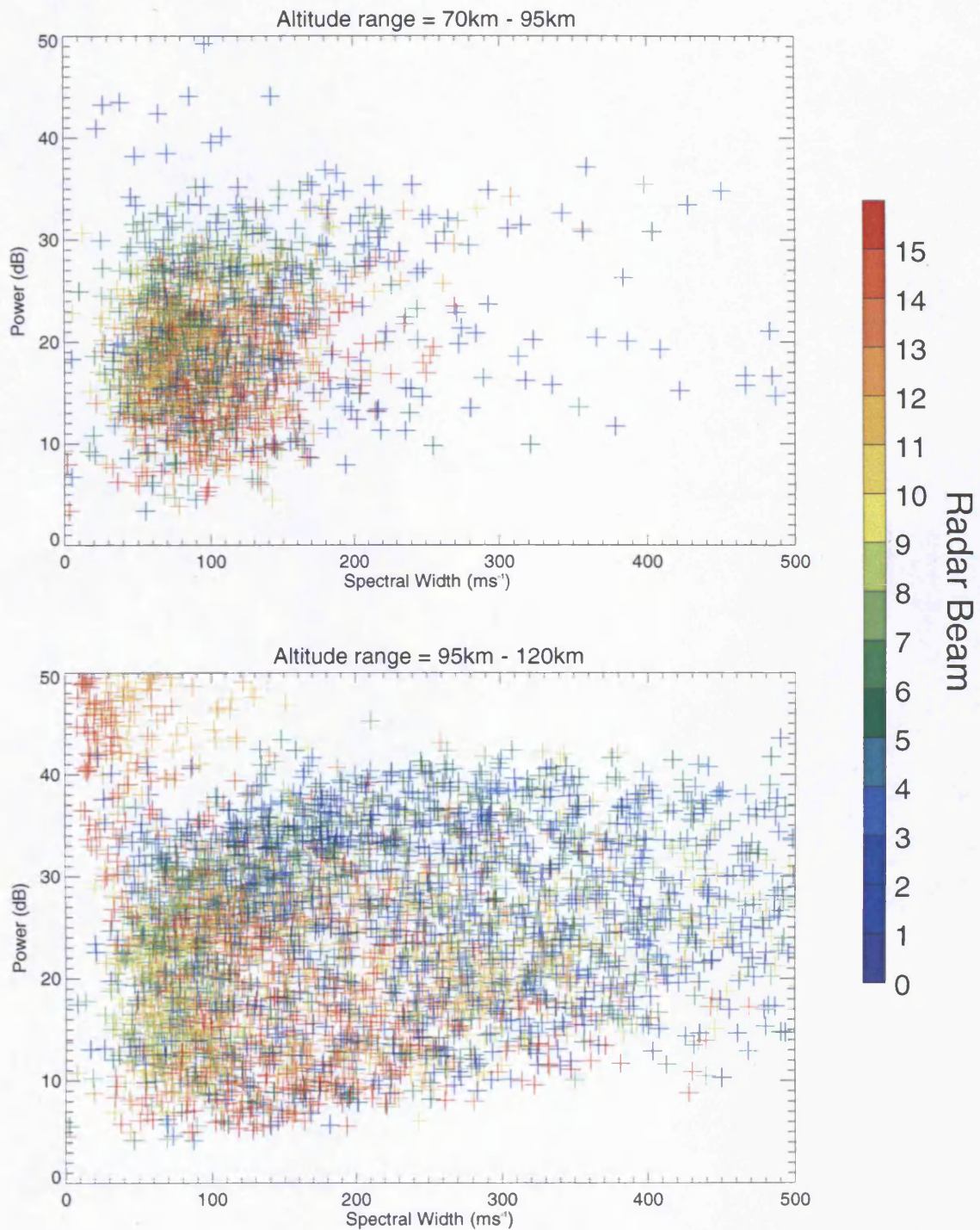
Iceland Power against Spectral Width

22 Nov 1997⁽³²⁶⁾

to

23 Nov 1997⁽³²⁷⁾

unknown scan mode (-6312)



6.5(c): The backscatter power plotted against the spectral width for two altitude ranges in the D-region and the E-region.

STARE AND CUTLASS DATA

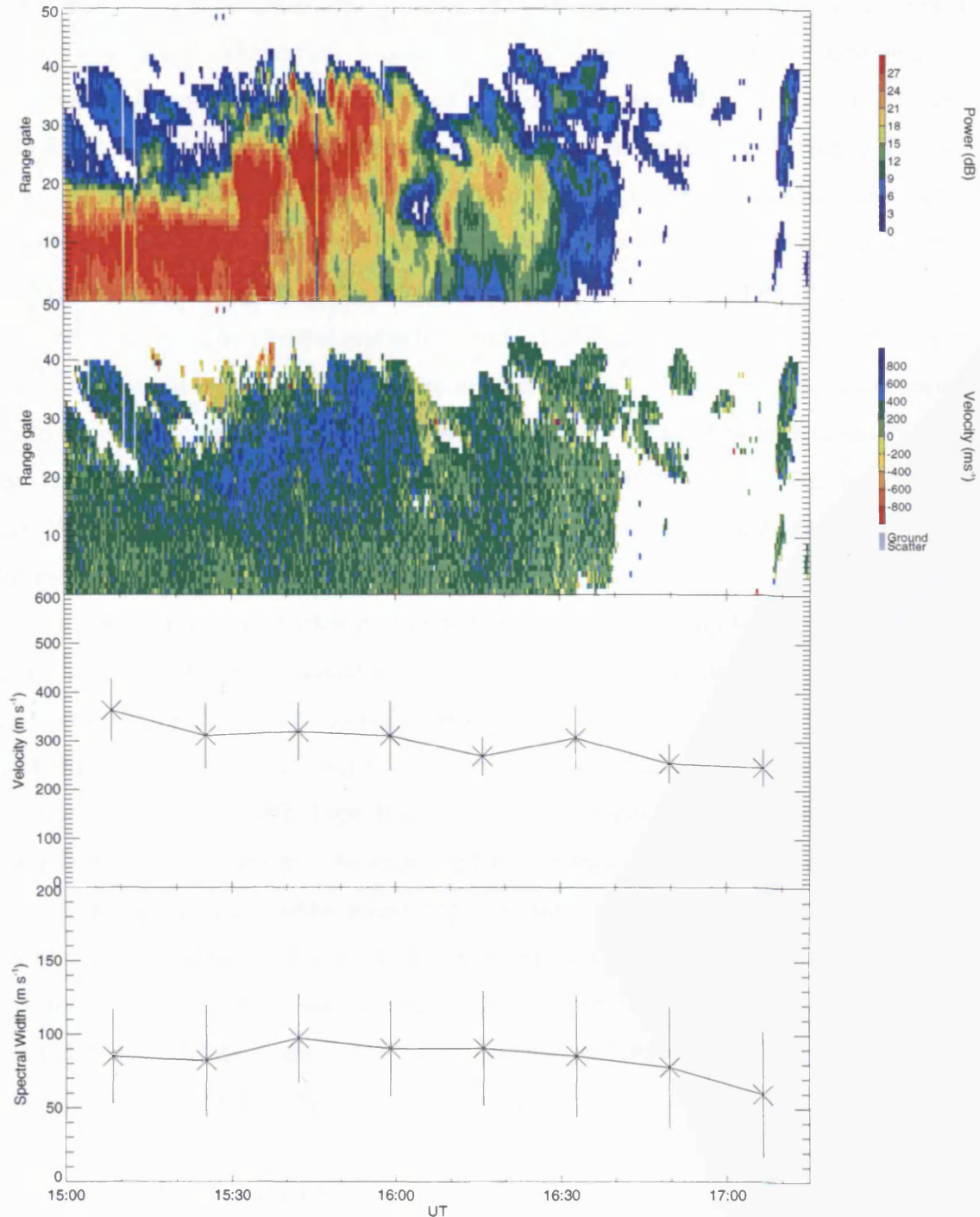
Pwr and vel with E-region Type I vel and D-region width

22 Nov 1997⁽³²⁶⁾

to

23 Nov 1997⁽³²⁷⁾

unknown scan mode (0)



6.6(a): Data from beam 3 of the STARE Norway radar, together with E-region Type I echo velocity and D-region spectral width measured by CUTLASS, for the interval 1500-1715 UT corresponding to the first case study. The lowering of the CUTLASS D-region spectral width corresponds with the disappearance in backscatter observed by STARE.

backscatter power is consistent with an electrojet flow whose velocity exceeds that at which the FBI is excited. The scatter seen in range gates 0-20 became less intense after 1600 UT. By 1630 UT, the scatter became scarce and this corresponds to the absence of scatter in the CUTLASS data, corresponding to a fall in the electrojet velocity that fell below the threshold for the FBI. The third panel from the top shows the Doppler velocity of E-region Type I scatter with the highest occurrence, together with associated error bars, determined by considering all backscatter that occurred in each 15-minute interval, corresponding to the CUTLASS Iceland altitude plots presented above. The Doppler velocity falls from 360 m s^{-1} to 250 m s^{-1} at just after 1650 UT. This corresponds to the time where the STARE backscatter disappears. The lowest panel of figure 6.6(a) shows the highest occurrence D-region spectral width corresponding to the green LW2 echo population that was discussed in the altitude dependence plots above. The spectral width has values around 100 m s^{-1} until just after 1630 UT, at which time it falls gradually to values of around 60 m s^{-1} . This is again consistent with a falling electrojet velocity value. The phase velocity of the irregularities falls gradually and when the velocity falls below the threshold value for the FBI, the STARE backscatter disappears. When the velocity threshold for the EPCI is no longer exceeded, the LW2 echoes in the D-region are not as numerous.

Figure 6.6(b) shows the backscatter power and Doppler velocity for the same interval observed by beam 3 of the Hankasalmi radar, which observes across the electrojet. The backscatter power is weaker for the same interval, although the maximum scatter occurs for range gates from about three to 15. Also, the Doppler velocity mainly lies between -200 - 200 m s^{-1} and this is consistent with Type II echoes. The differences between the backscatter powers and Doppler velocities may be explained by considering the look-directions of the radars. The Hankasalmi radar looks across the electrojet, mostly, whereas the Trondheim radar observes along it. Therefore, periods where the electrojet flow is enhanced will lead to the production of Type I echoes and this is consistent with the data. When the FBI is no longer excited, the secondary gradient drift waves are also no longer excited and this explains the fall off in the scatter observed by the Hankasalmi radar.

6.6 Case Study 2: 13th February 1998

For case study one discussed above, the radar started running the myopic mode at 1500 UT, and the lower altitude population was already present at this time. This case study considers a similar event, but the growth as well as the decay of the population is shown.

STARE PARAMETER PLOT

22 Nov 97 ⁽³²⁶⁾

Hankasalmi (STARE): vel

unknown scan mode (0)

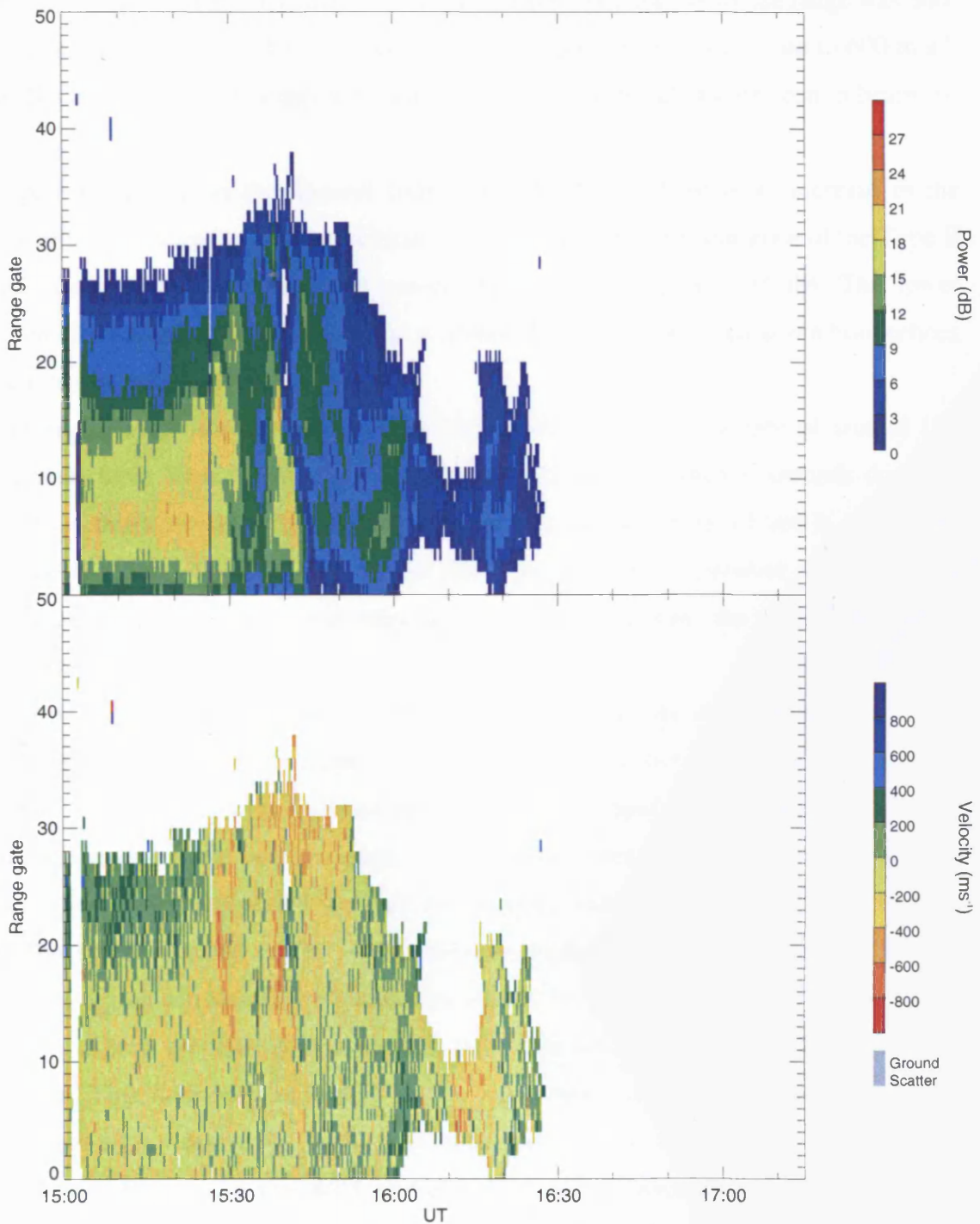


Figure 6.6(b): Data from beam 3 of the STARE Finland radar for the interval 1500-1715 UT corresponding to the first case study. The lack of backscatter later in the interval corresponds approximately to the absence in for STARE Norway.

Only data from CUTLASS Iceland are presented since only this radar was running the myopic campaign at the time. Figures 6.7(a)-(g) show the temporal evolution of the backscatter populations. Figure 6.7(a) shows the 15-minute interval from 1730-1745 UT. From about 60-130 km in altitude, there was a Type II echo population whose range was 600-700 km away from the radar. There are echoes with Doppler velocity values up to 600 m s^{-1} . The Type II scatter is seen in beams 0-5, and the higher velocity echoes are seen in beams 6-12.

Figure 6.7(b) shows the interval from 1800-1815 UT. There is an increase in the population with higher value Doppler velocities and the backscatter occurrence of the Type II echoes has decreased. The backscatter powers have values around 5-35 dB. The lower Doppler velocity echoes, $0-300 \text{ m s}^{-1}$, occur at around 500 km range whereas the blue echoes occur at a range of 500-700 km.

Figure 6.7(c) shows the interval from 1830-1845 UT. At an altitude of around 130 km, the echoes have Type I characteristics, although the blue population extends down to altitudes below those at which backscatter occurrence is usually observed and is seen in all beams in the E-region. There is a growth in the Type II yellow population and as for the previous case study, this occurs at a range of around 300 km from the radar. The yellow population is seen in beams 0-9.

Figure 6.7(d) shows the interval from 1900-1915 UT. Its characteristics are very similar to the interval shown in figure 6.3(a). Again dividing the population into altitude layers allows the characteristics to be examined. The blue population extends to a slightly higher altitude than for the previous case study and the green population occurs with the yellow population in the D-region because the Doppler velocities are negative as well as positive. The spectral width profile of this lower-altitude scatter is consistent with LW2 echoes. The E-region echoes show a population around 500 m s^{-1} with spectral widths rising to 100 m s^{-1} . There are also echoes around zero. The D-region echoes display Type II characteristics. This interval is consistent with a flow whose velocity increases beyond the threshold required to excite the EPCI and then falls below this threshold. The green population is observed in beams 8-15 preferentially, with echoes observed by beams 15 originating from the lowest altitude. This is consistent with flow along the electrojet.

Figure 6.7(e) shows the interval from 1930-1945 UT. The Type I echoes have a much lower occurrence and the occurrence in the D-region has decreased also. Figures 6.7(f) and 6.7(g) then show the populations for 2000-2015 and 2030-2045 UT, respectively. There is an increase in the blue population in the E-region.

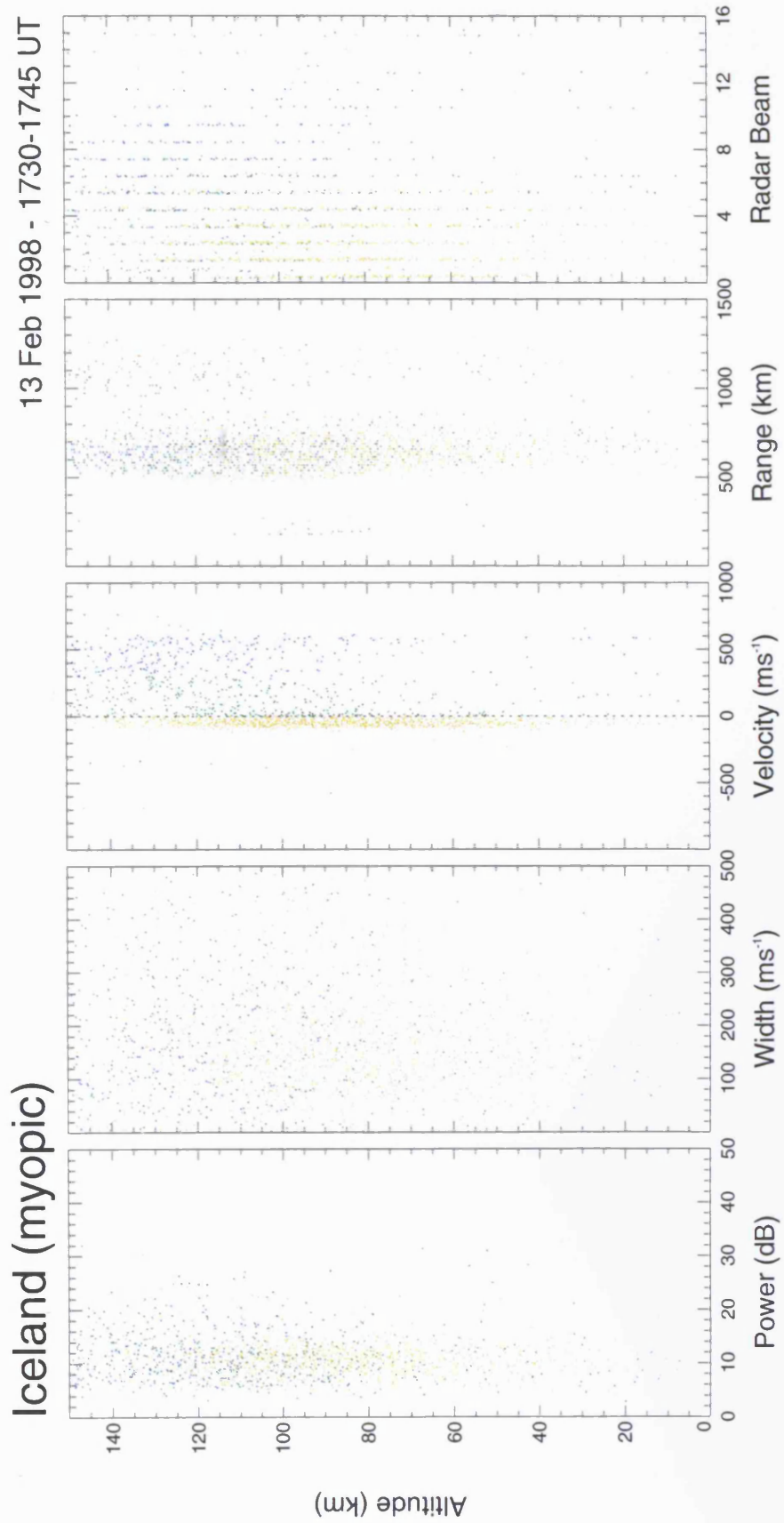
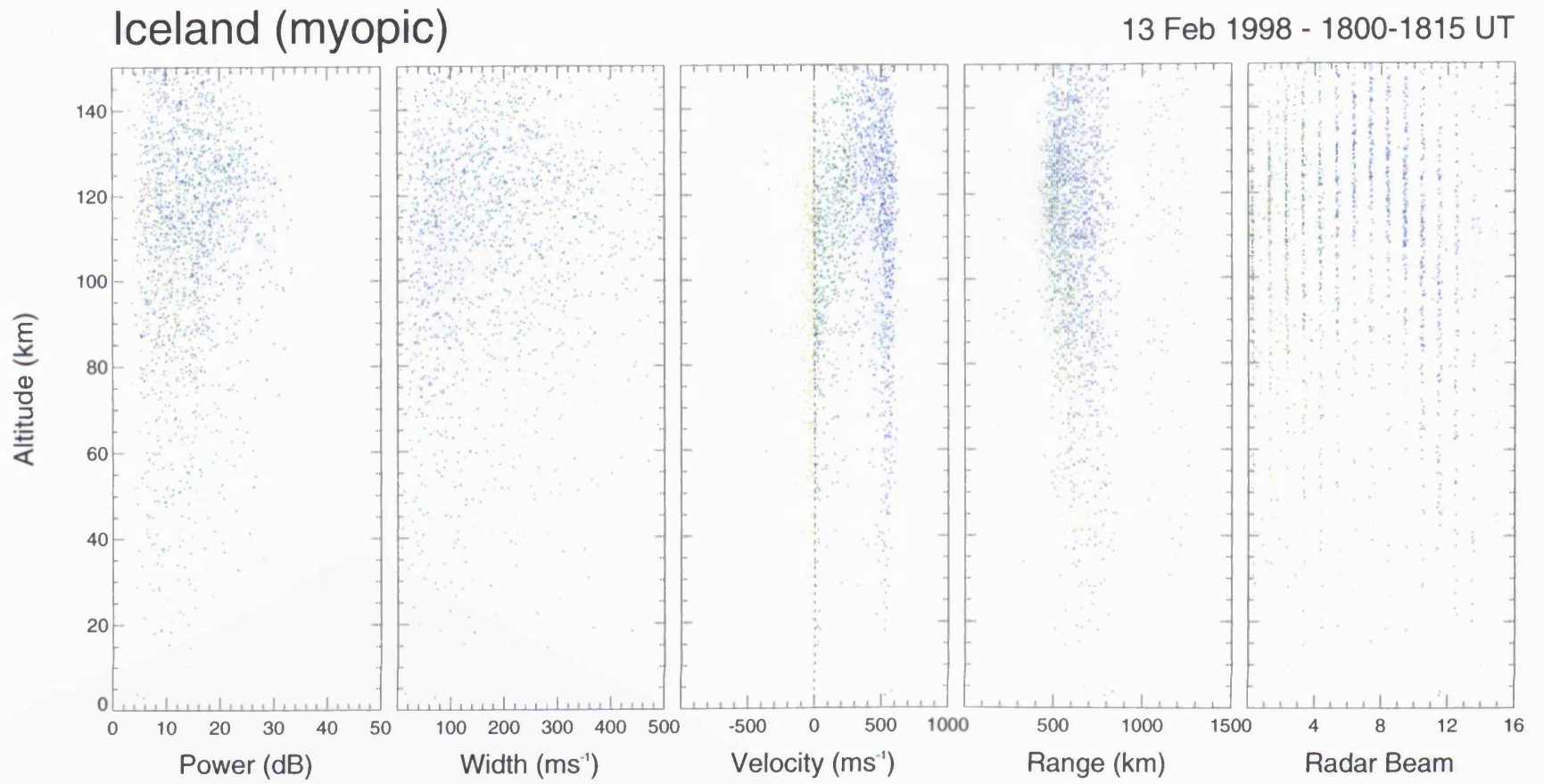


Figure 6.7(a): This and the following six figures show the evolution of a D-region echo layer. There is a lack of scatter for this interval.

Figure 6.7(b): Type II echoes are present for this interval, 1800-1815 UT.



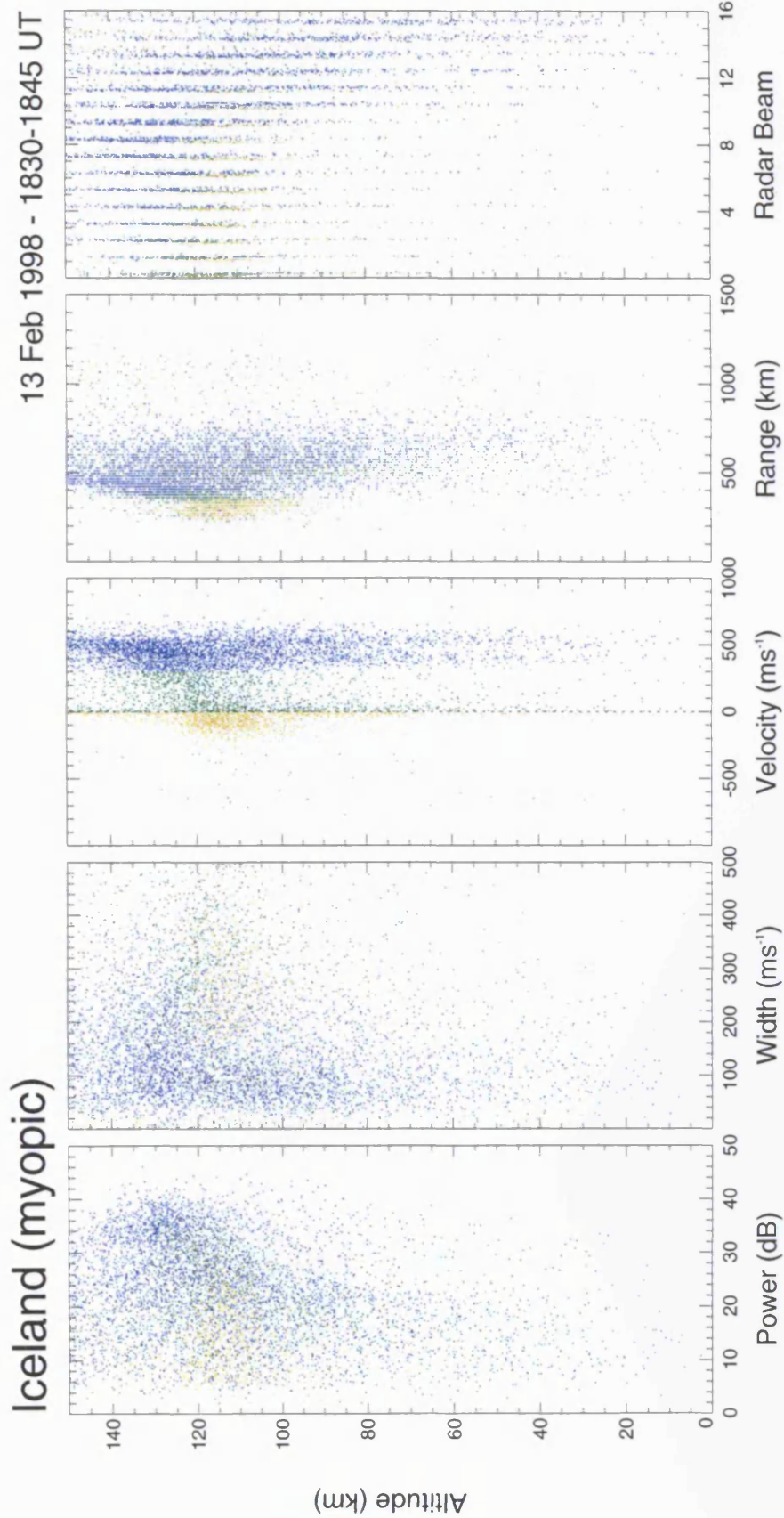


Figure 6.7(c): The interval 1830-1845 UT. There is now scatter present in the E-region corresponding to Type I and Type II echoes.

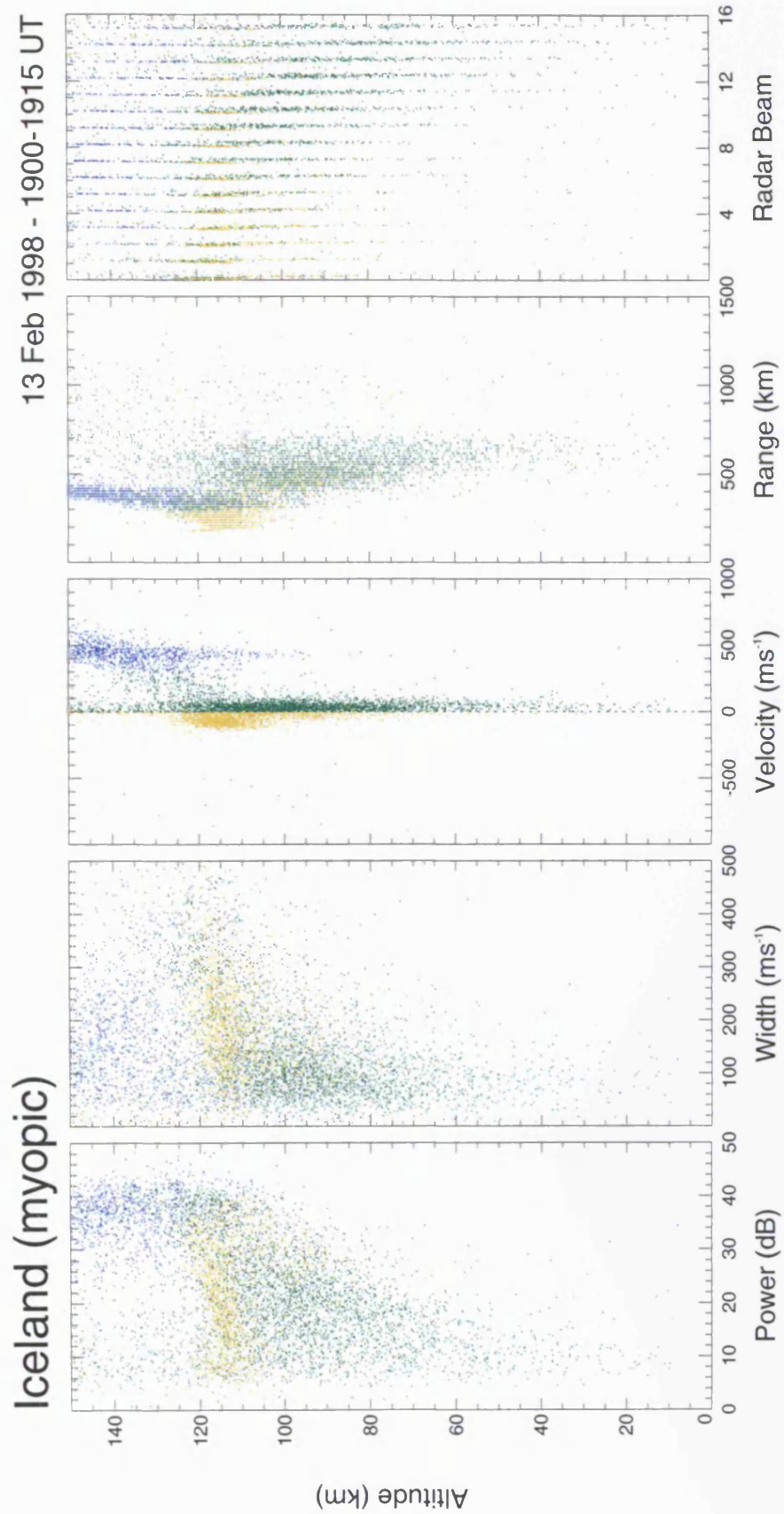


Figure 6.7(d): This interval, 1900-1915 UT, is very similar to that shown in figure 6.3(a), with Type I and Type II echoes present in the E-region, together with D-region scatter.

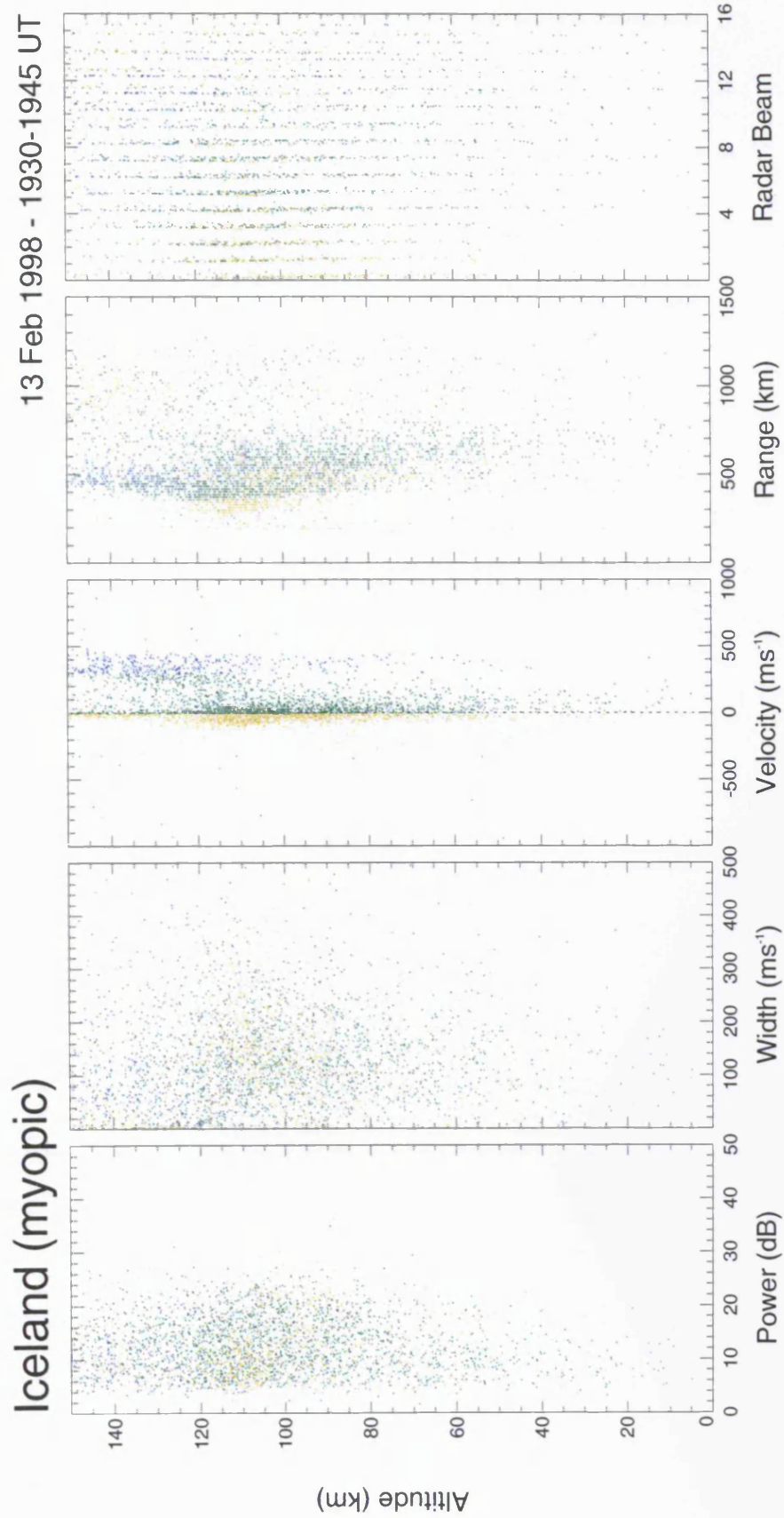


Figure 6.7(e): The interval from 1930-1945 UT is shown in this figure. There is a lower backscatter occurrence in the D-region and the Type I echo velocity has dropped.

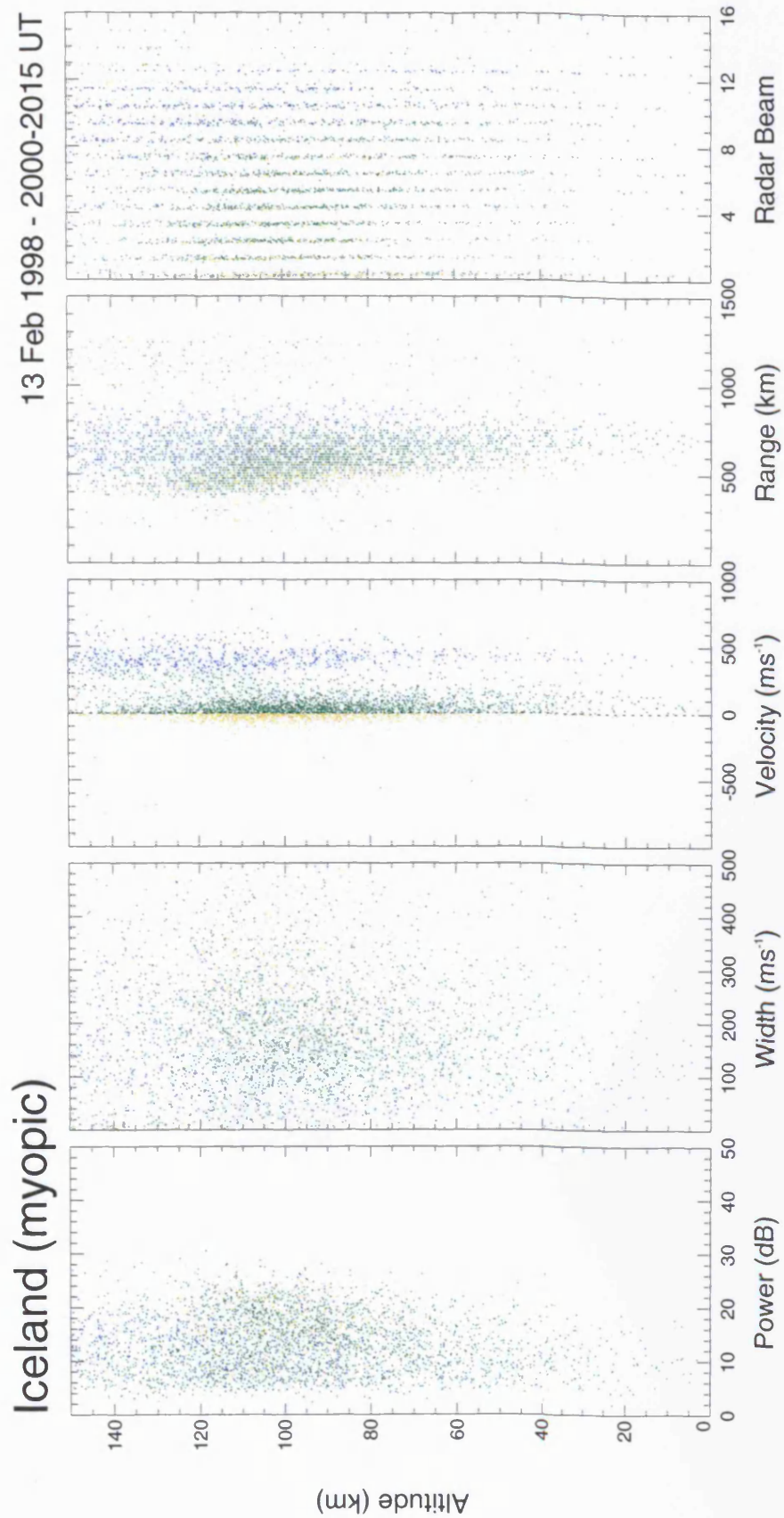


Figure 6.7(f): For the interval shown here, 2000-2015 UT, the backscatter occurrence in the E-region has increased since the previous interval.

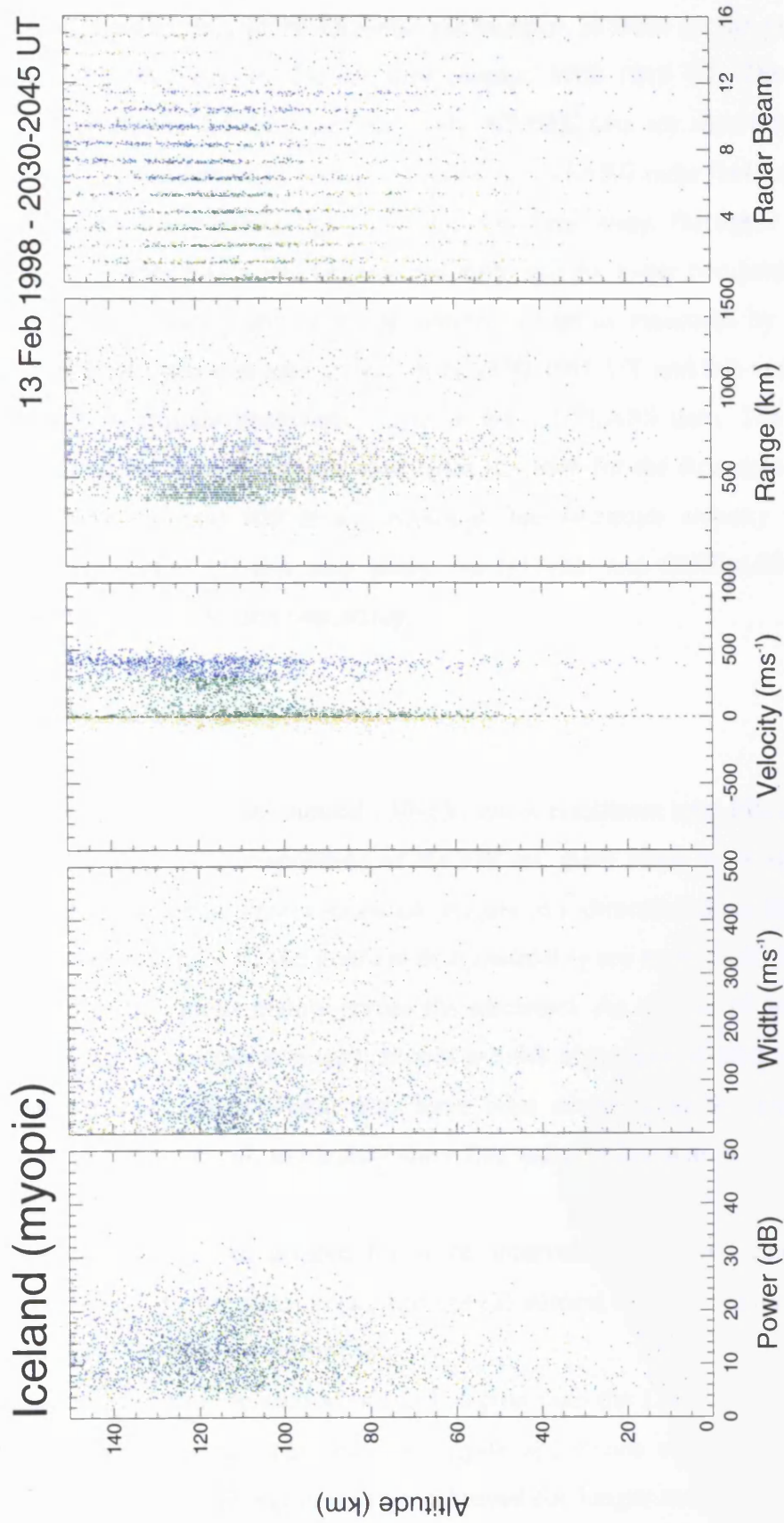


Figure 6.7(g): The interval shown here, 2030-2045 UT, once again shows an increase in the backscatter occurrence in the E-region with Type I echoes again present.

The backscatter parameters plotted against one another, as done for the previous case study, are shown in figures 6.8(a)-(c) for the time interval 1900-1915 UT. These have the same overall characteristics as for the first case study. STARE data are shown in figure 6.9 for beam 3 of STARE Trondheim only, since it was the only STARE radar that was operating at the time. As for the corresponding figure for the first case study, the upper two panels show the STARE backscatter power and Doppler velocity, and the lower two panels show the E-region Type I Doppler velocity and D-region spectral width as measured by CUTLASS. The scatter becomes most intense at near ranges from 1850-1910 UT and this corresponds to the presence of the low altitude backscatter layer in the CUTLASS data. The CUTLASS velocity and spectral width values vary less systematically than for the first case study, with the velocity value being around 400 m s^{-1} . Although the electrojet velocity value again provides the best explanation for this case study, the STARE and CUTLASS data taken together are not as clear as for the first case study.

6.7 Summary of the Case Studies

The backscatter from altitudes around 110-130 km is consistent with FBI and gradient drift instability effects. Echoes corresponding to the FBI are more likely to be seen with the CUTLASS Iceland radar since its observations are mainly in a direction along the electrojet. Additionally, radar echoes caused by the gradient drift instability are more likely to be seen in the Finland radar, since this looks mainly across the electrojet. As a point of note, Type III echoes corresponding to ion-cyclotron waves, should provide signatures around 120 m s^{-1} for CUTLASS measuring at 10 MHz. These may have been observed in the data, but their signatures would have been difficult to identify since this velocity lies within the range given by Type II echoes.

The D-region LW1 echoes present for some intervals may have been caused by meteor scatter (Hall, 1997) or processes related to optical auroral forms (Milan et al., 2001). LW2 echoes seem to be consistent with the EPCI.

Radio waves suffer more refraction in the E-region than the D-region because of the quantity of plasma through which they must propagate and hence orthogonality with the terrestrial magnetic field in the D-region will be achieved for longer ranges from the radar. Therefore, echoes corresponding to the EPCI should also be observed at longer ranges from the radar and this is in agreement with the data. D-region echoes are often seen by beams 14 and 15, which observe in roughly an L-shell aligned direction.

SUPERDARN PARAMETER PLOT

13 Feb 1998⁽⁴⁴⁾

Iceland Spectral Width against LOS Velocity

unknown scan mode (-6313)

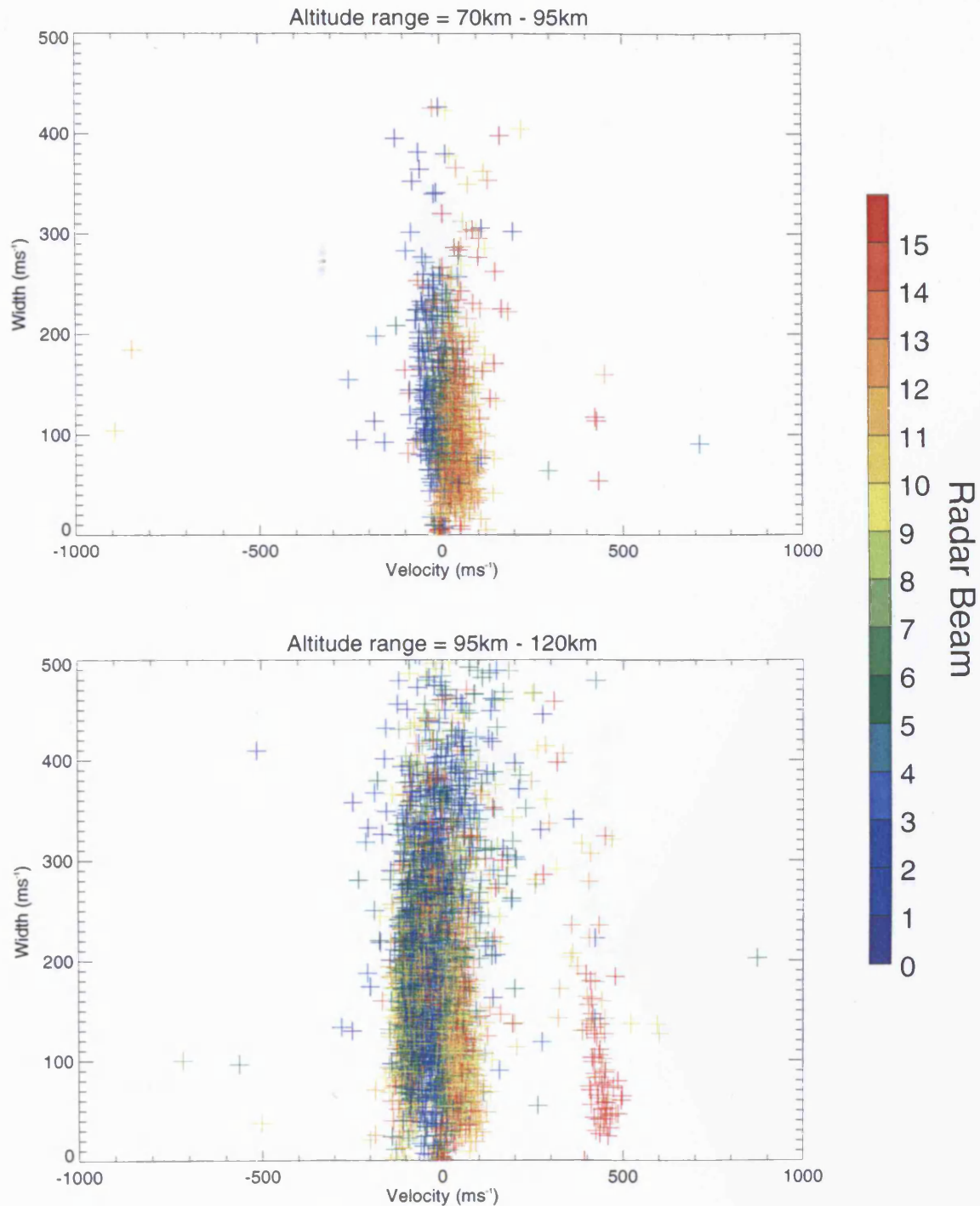


Figure 6.8(a): The spectral width plotted against the line-of-sight velocity for two altitude ranges in the D-region and the E-region. This is for the second case study, 1900-1915 UT.

SUPERDARN PARAMETER PLOT

13 Feb 1998 ⁽⁴⁴⁾

Iceland Power against LOS Velocity

unknown scan mode (-6313)

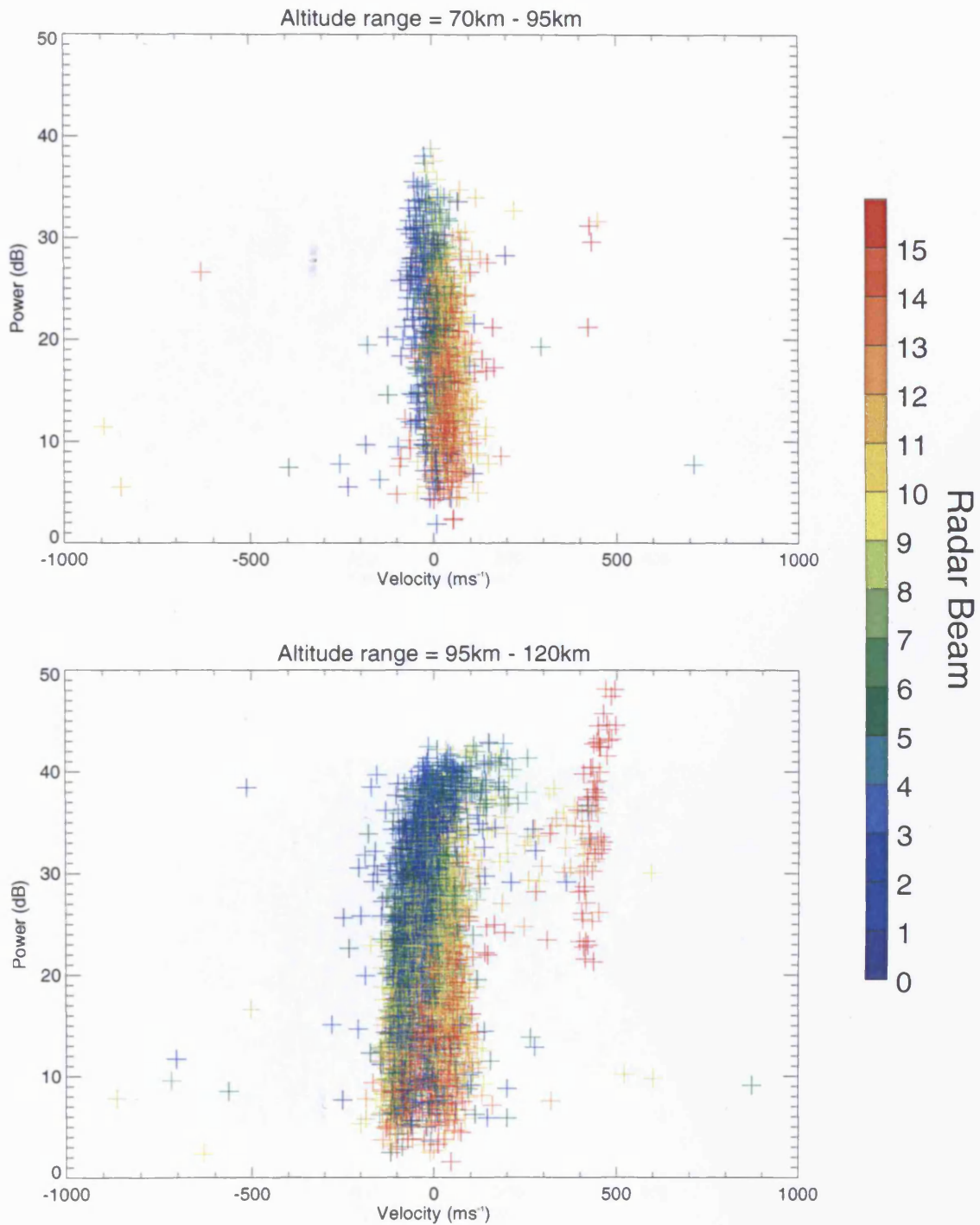


Figure 6.8(b): The power plotted against the line-of-sight velocity for two altitude ranges in the D-region and the E-region. This is for the second case study, 1900-1915 UT.

SUPERDARN PARAMETER PLOT

13 Feb 1998⁽⁴⁴⁾

Iceland Power against Spectral Width

unknown scan mode (-6313)

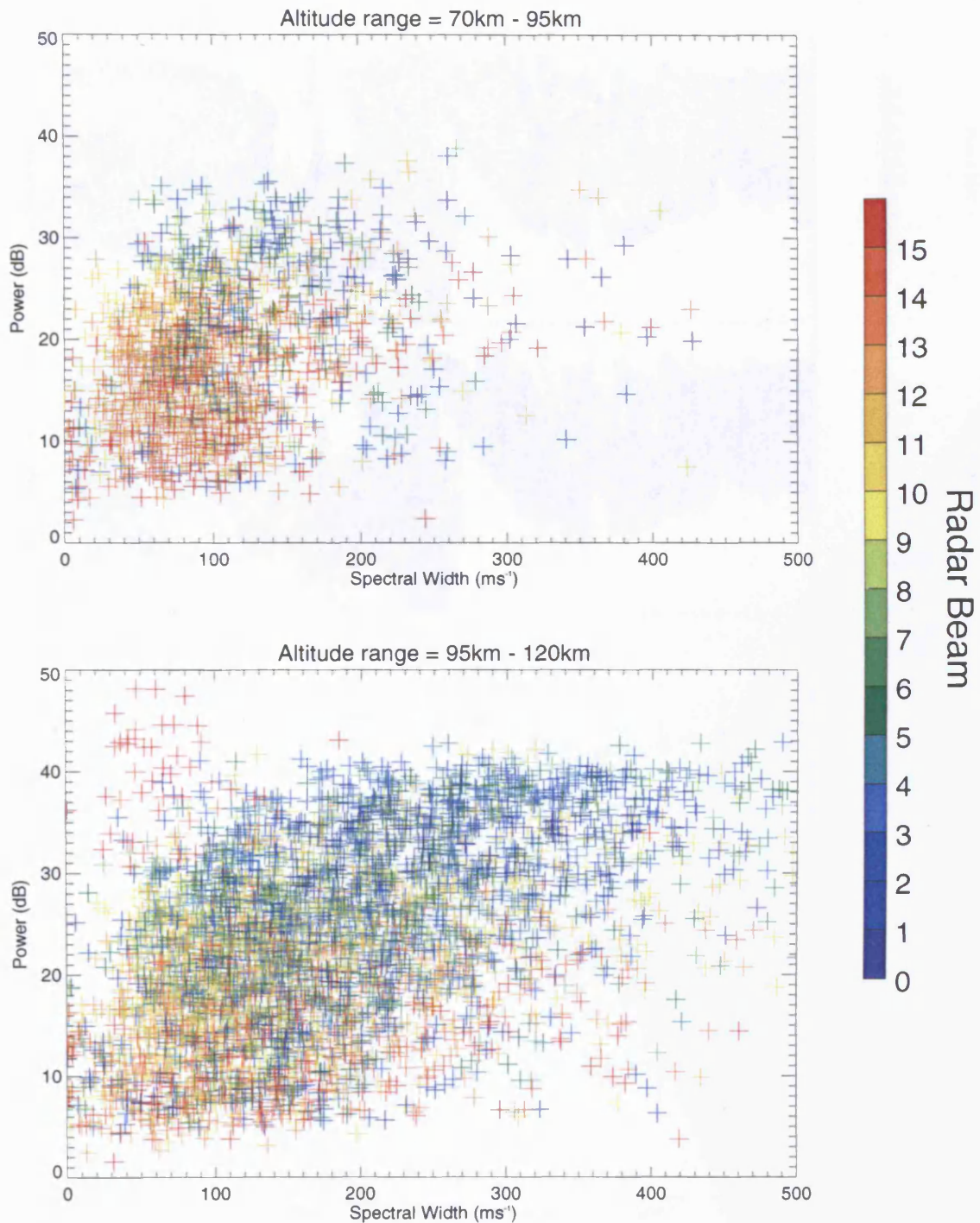


Figure 6.8(c): The power against the spectral width for two altitude ranges in the D-region and the E-region. This is for the second case study, 1900-1915 UT.

STARE AND CUTLASS DATA

13 Feb 1998⁽⁴⁴⁾

to

14 Feb 1998⁽⁴⁵⁾

Pwr and vel with E-region Type I vel and D-region width

unknown scan mode (0)

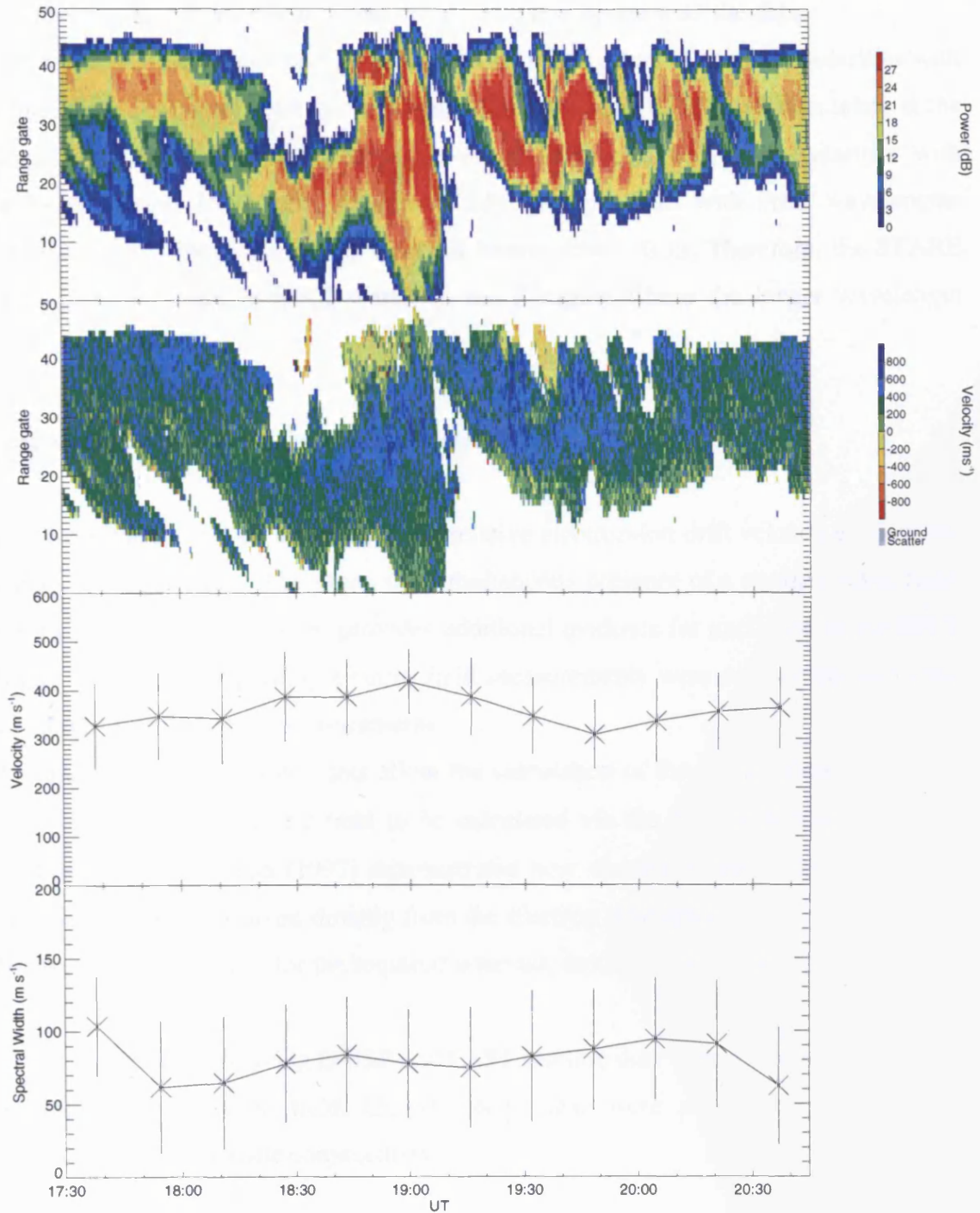


Figure 6.9: STARE and CUTLASS data obtained for the second case study. The relationship between STARE data and E-region Doppler velocity and D-region spectral widths is not as clear for this case. For the period from 1900-1915 UT, STARE backscatter is present over more range gates.

Another indicator, applying for the first case study, is provided by considering the returns from the two CUTLASS radars taken together. Since the EPCI irregularities should be excited preferentially at angles close to the $E-E \times B$ bisector direction, there should be a line-of-sight velocity component present for both radars, but the obliquity of the propagation direction should give velocities with lower values, and this agrees with the data.

Since the STARE radars operate at around 140 MHz, they observe irregularities with wavelengths of approximately one metre. Comparing this to the CUTLASS data taken at the same time, the radar was operating at just over 10 MHz, resulting in irregularities with wavelengths of around 15 m being observed. EPCI irregularities with these wavelengths should be excited and there should be a cut-off below about 10 m. Therefore, the STARE radio waves will not observe EPCI scatter in the D-region where the longer wavelength irregularities exist.

6.8 Attempts to Measure the Convection Electric Field

EPCI excitation will be achieved if the relative electron-ion drift velocity exceeds the characteristic threshold value. Therefore, the simultaneous presence of a strong electric field, together with LW2 D-region echoes, provides additional evidence for excitation of the EPCI. A number of approaches regarding electric field measurements were considered, including the use of EISCAT and satellite measurements.

Tristatic EISCAT measurements allow the calculation of the plasma flow velocity in the F-region, allowing the electric field to be calculated via the $E = -v \times B$ relationship. In addition, Davies and Robinson (1997) demonstrated how electron turbulent heating allows the electric field to be determined directly from the electron temperature. Unfortunately, due to the absence of EISCAT data for the required intervals, neither of these techniques could be used.

Other approaches involving DMSP and FAST satellite data were attempted in order to obtain values for the electric field. Unfortunately these were unsuccessful because of unreliable data and unfavourable conjunctions.

6.9 Summary

This chapter has described CUTLASS observations from two case studies that are consistent with excitation of the EPCI. STARE data were presented that confirmed the

geophysical conditions measured by CUTLASS. The FBI and gradient drift instabilities were observed in the E-region, together with associated Type I and Type II echoes. Irregularities with low Doppler velocities and spectral width values of around 100 m s^{-1} were observed in the D-region. The altitudes at which the echoes occurred agreed with the theoretical predictions presented in chapter 5.

Chapter 7

Radar Backscatter from Artificially Generated FAIs

7.1 Introduction

The thermal oscillating two-stream instability and its relevance to artificially generated FAIs, via the transmission of high-power radio waves, was described in chapter 2 and previous observations of artificially generated irregularities were described in chapter 3. The configuration and operation of the heater, together with radar systems that can measure the effects of modification, have been described in chapter 4. This chapter describes and presents data taken during the experimental campaigns conducted in October 1998 and October 1999.

Experiments conducted during the October 1998 campaign included examining the effects of seeding the ionosphere and spatial sweeping. The spatial sweeping experiments utilised the capability of the heater to change its pointing direction instantaneously. The power was kept constant and the direction, controlled by the phased antenna array, was varied. This allowed the effects of varying the illumination time of a particular heated patch of the ionosphere to be studied.

The October 1999 campaign was the first time that CUTLASS was run using a new longer-lag mode, where the radar pulse separation time was changed. This study was conducted to compare the irregularity backscatter decay and ACF decorrelation time constants. An additional goal was to determine parameters relating to the artificially generated irregularity distribution. The study was motivated by the fact that artificial FAIs, as observed by CUTLASS, have low small spectral width values, typically less than 10 m s^{-1} . The small spectral width values are derived from ACFs that do not decorrelate, and these ACFs are due to fairly static irregularity distributions. The latter part of this chapter presents turbulence characteristics obtained by treating the ionospheric plasma as a turbulent fluid.

The CUTLASS data shown in this chapter were obtained by the Finland radar, as the heater and EISCAT fall within the field-of-view of beam 5 of CUTLASS Finland. For the heating experiments discussed, CUTLASS was running a special heating mode where the radar only collected 1-second resolution data from beam 5. The heated patch normally fell within range gates 20-40.

7.2 Use of CUTLASS and EISCAT

The basic effects of heating, including raised electron temperatures, are well documented (e.g. Honary et al., 1993; Robinson, 1989; Robinson et al., 1996) and have been observed by EISCAT (Rishbeth and Williams, 1985). EISCAT provides details of background parameters, including the ion temperature and electron density and the height at which the ion-line overshoot occurs. The data presented in this chapter were mainly taken by CUTLASS, although EISCAT data were also obtained using the long pulse that observes F-region properties, which utilised range gates of 22 km and an integration time of usually 10 s.

CUTLASS detected backscatter within a second of heater switch-on and CUTLASS backscatter persisted throughout the period when the heater was operating. Irregularities grow and decay throughout the duration of the heater-on and over the entire heated patch, and result in a continuous irregularity signature in the CUTLASS data. When the heater was switched off, the backscatter power typically fell away to zero within a time of the order of 15 seconds.

For certain experiments conducted on 5th and 6th October 1998, heating was carried out at frequencies close to a harmonic of the electron gyrofrequency and the generation of FAIs was inhibited (e.g. Mjølhus, 1993; Huang and Kuo, 1994). Observations of associated effects have been made (Honary et al., 1995, Robinson et al., 1996), but this case will not be described further because the backscatter amplitude in the CUTLASS data was very low.

7.3 Overview of Spatial Sweeping Experiments

An important aim of the October 1998 campaign was to obtain data relating to the effects of ionospheric modification for varying intervals of excitation and thus determine how the amount of time that passed between instances of heater-on affected the power needed to excite and maintain the irregularities.

The 1998 campaign consisted of various on-off heating experiments with a constant heater power during heater on and also experiments where power stepping was conducted. A different type of experiment involved spatially sweeping the heater beam. The transmitted power of the heater was kept constant whilst the pointing direction of the beam was steadily altered, e.g. 30° North to 30° South in a period of a minute. The change was made by maintaining a constant value for the rate of change of the angle that the heater beam made with the vertical. Since the direction was controlled by the phases of the individual

transmitter beams, it was possible to control precisely the pointing direction and change it in a very short period of time. As an example of this, the fastest spatial sweep consisted of a direction change from 30° North to 30° South in one second. Immediately after the termination of this interval, the beam would sweep from North to South again. This form of experiment allowed the study of the response of the ionosphere to differing periods of illumination and hence different levels of incident power.

7.3.1 Spatial Sweeping

Figures 7.1(a)-(c) show the backscatter decay profile for a vertical heater beam. As for other figures presented below, the vertical red lines in the figure indicate the times at which the heater was turned on and off. For the intervals from 1506-1512 UT and 1602-1608 UT shown in figures 7.1(a) and 7.1(b), the heater was operating at 6.2 MHz, with a transmitter power of 75 kW. All transmitters of array 2 were in operation and O-mode radiation was transmitted. The decay times of the backscatter may be discerned from the fall in backscatter power that occurs after the heater is turned off. The backscatter decay time was 30 seconds for these intervals. Figure 7.1(c) shows the interval from 1646-1652 UT. The heater was operating at 4.54 MHz using a transmitter power of 75 kW with transmitters 3-8 of array 2 in operation and O-mode radiation was being transmitted. The decay time of the backscatter for this interval was also 30 seconds, and this establishes a characteristic decay time for backscatter during this part of the day.

Figure 7.2(a) shows three sets of spatial sweeping experiments conducted during 6th October and the spatial variation of the CUTLASS backscatter is clear. Each panel contains data from 10-minute intervals. During all three intervals, the heater was transmitting O-mode polarised radiation at a frequency of 4.54 MHz. All 12 transmitters of array 2 were in operation and the heater power was 75 kW. The first panel shows data from the interval 1430-1440 UT and the data form a series of slanting stripes, indicating that the direction of the heater beam was changing from North, with higher range gates, to South, with lower range gates. The backscatter for the entire sweeping range covers 13 range gates, corresponding to a horizontal extent of around 200 km. Examining the backscatter power more closely, it is clear that the signal persisted for longer at about range gate 28 and the power did not decay as much as for the edges of the beam.

The period from 1442-1452 UT contained two 40-second scan intervals followed by 10-second scan intervals. The vertical red line in figure 7.2(a), at around 1444 UT, indicates

SUPERDARN PARAMETER PLOT

6 Oct 1998⁽²⁷⁹⁾

Hankasalmi: pwr_l

normal (ccw) scan mode (150)

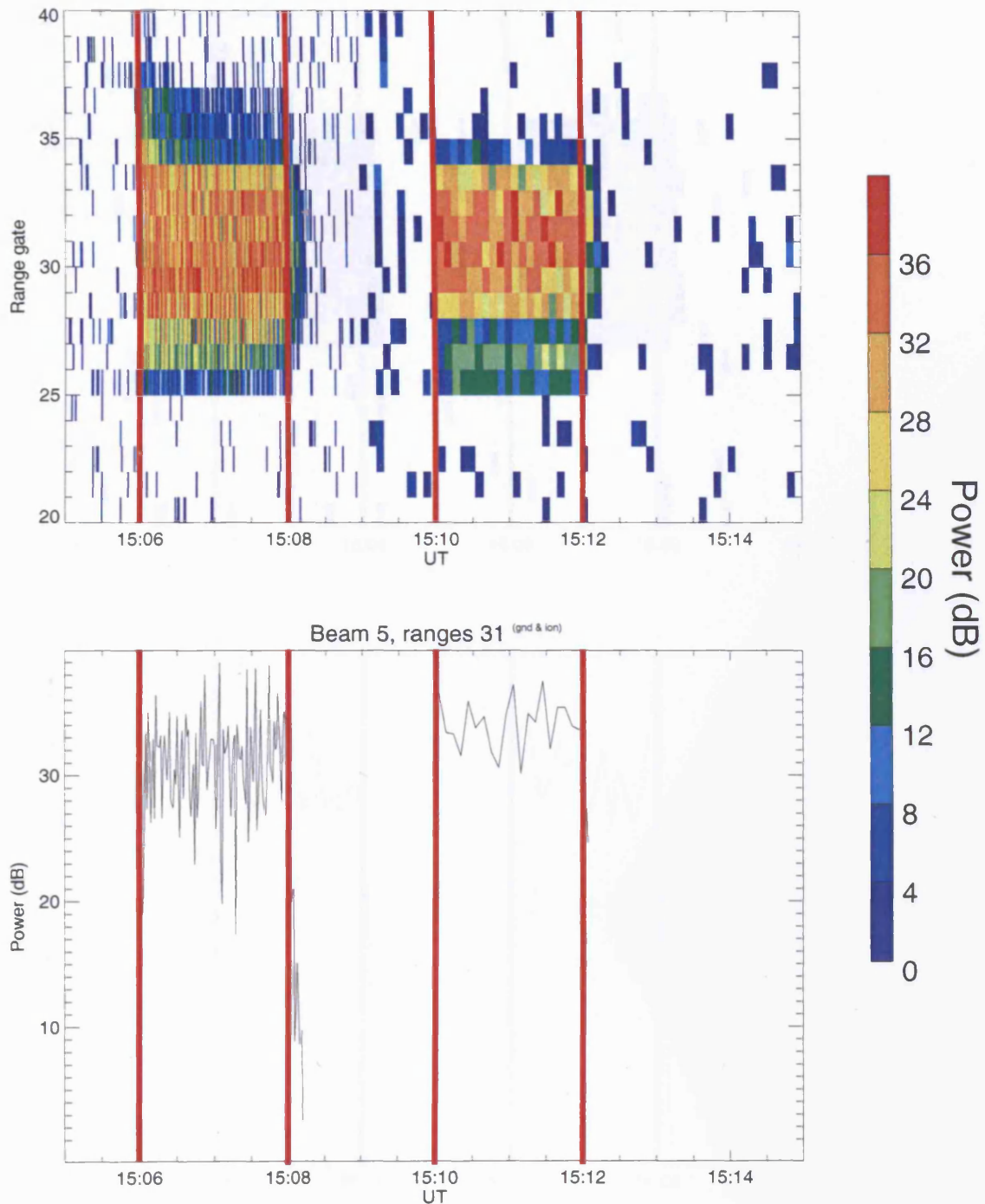


Figure 7.1(a): Two intervals of 2-minute-on/2-minute-off for the interval 1506-1512 UT. The backscatter power took 30 seconds to decay. As for subsequent figures, the vertical red lines indicate times when the heater was turned on or off.

SUPERDARN PARAMETER PLOT

6 Oct 1998⁽²⁷⁹⁾

Hankasalmi: pwr_l

normal (ccw) scan mode (150)

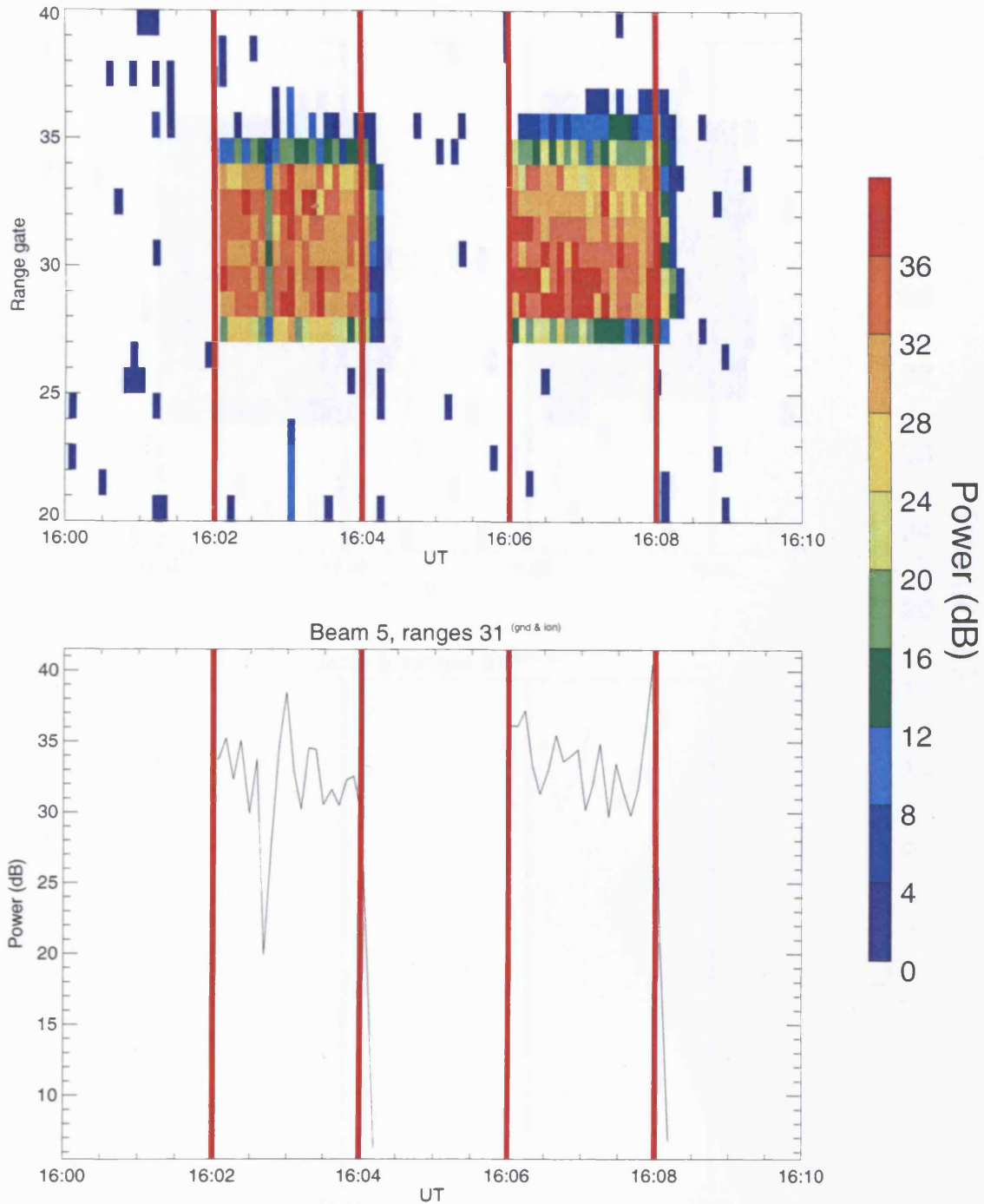


Figure 7.1(b): Two further periods of 2-minute-on/2-minute-off. The backscatter power again decayed in 30 seconds.

SUPERDARN PARAMETER PLOT

6 Oct 1998⁽²⁷⁹⁾

Hankasalmi: pwr_l

normal (ccw) scan mode (150)

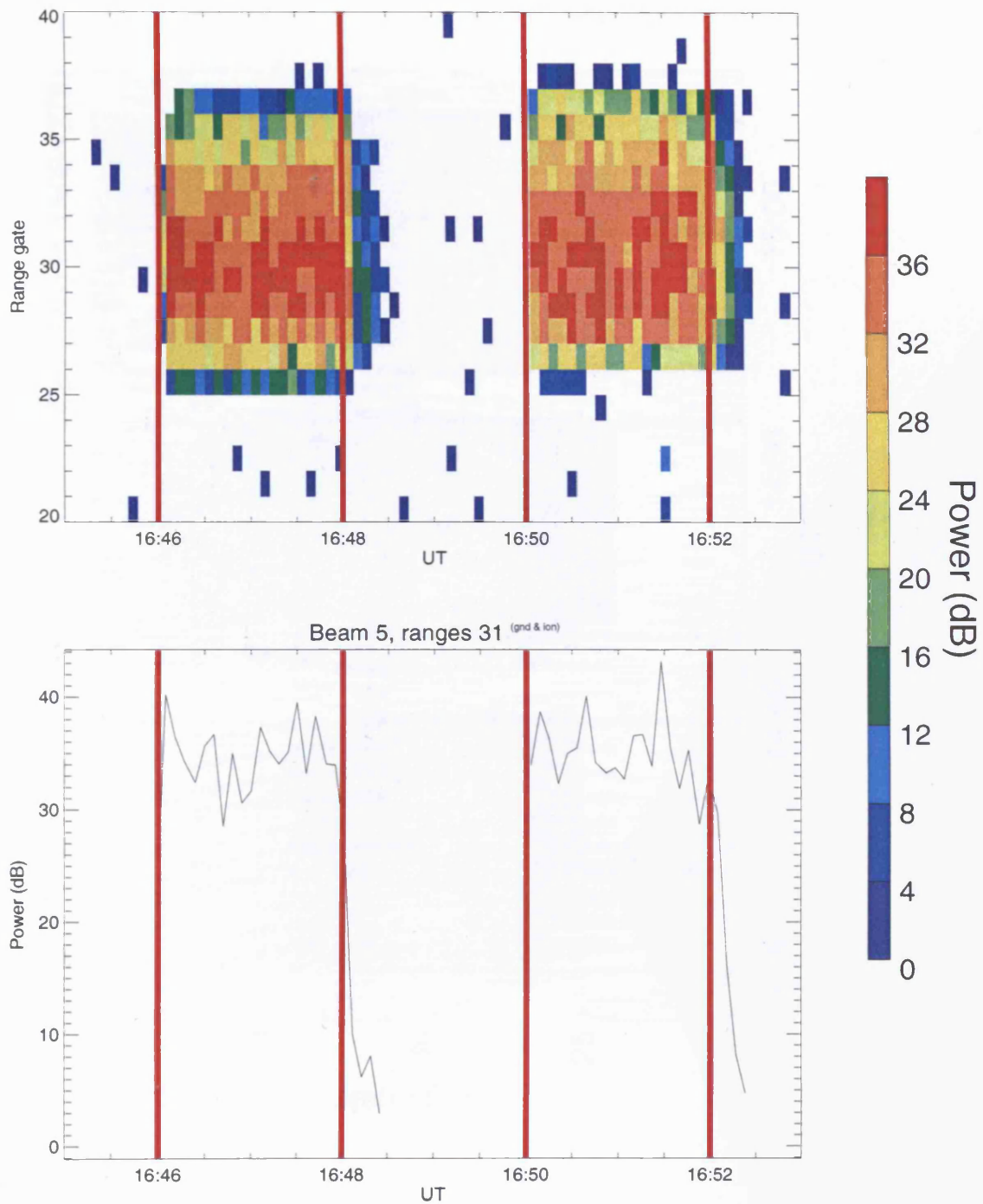


Figure 7.1(c): As for the previous figures, another two periods of 2-minute-on/2-minute-off have been shown. The backscatter power again decayed in 30 seconds.

SUPERDARN PARAMETER PLOT

Hankasalmi: pwr_1

6 Oct 1998⁽²⁷⁹⁾

normal (ccw) scan mode (150)

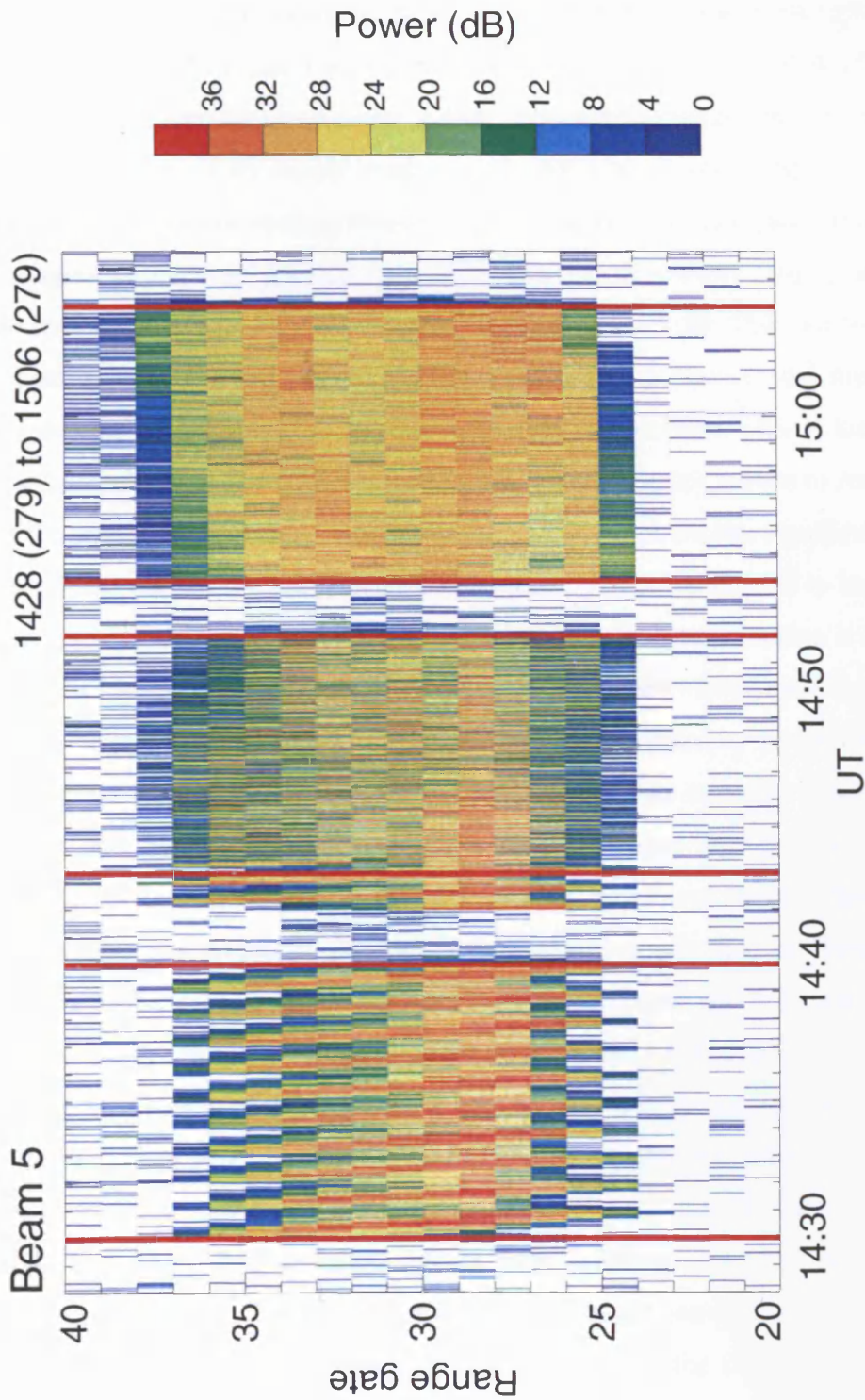


Figure 7.2(a): Three intervals when spatial sweeping experiments were conducted. The first panel corresponds to 1-minute sweeps. The other two panels correspond to 10 second and 1 second sweeps. The vertical red line at around 1444 UT indicates where the heater changed from 40 second sweeps to 10 second sweeps.

where this change in sweeping period occurred. The interval from 1454-1504 UT contained 1-second scan intervals. Since the resolution of the CUTLASS mode is also 1 second, the return signal appears to be continuous for the entire interval. The central and rightmost panels of figure 7.2(a) show the data from the two intervals, 1442-1452 UT and 1454-1504 UT.

Figure 7.2(b) shows the backscatter power, measured at range gate 26 corresponding to the southernmost edge of the heater beam, for the intervals shown in figure 7.2(a) and the panels in figure 7.2(b) correspond to those in figure 7.2(a). The maximum observed power for the 1-minute scans was greater than that for the 10-second and 1-second scans. Considering first the 1-minute sweeps, the power was around 35 dB. This fell to about 25 dB for the 1-second sweeps. For the 1-minute sweeps, there was an interval of 1 minute between the commencements of excitation of the same patch of ionosphere. This is longer than the characteristic backscatter decay time, thus allowing the backscatter power to reach the noise level before the excitation resumes. Also, since the heater beam excites a particular area for a comparatively longer time, the backscatter power recorded by CUTLASS is higher. For the case of 10-second sweeps, the characteristic time between commencements is less than the time taken for the backscatter to decay. Therefore, the irregularity amplitude has not fallen to the noise level before the excitation resumes. Also, the backscatter power level is lower because a particular area of the ionosphere is being excited less strongly. Finally, for the 1-second sweeps, the irregularities do not have time to decay significantly. The overall backscatter power is initially around 25 dB, but increases to around 30 dB. This corresponds to a possible change in ionospheric conditions. It is also possible that the threshold electric field for the excitation of the instability is only just exceeded for this scan period, thus leading to a slow growth in the backscatter power observed by CUTLASS.

Further confirmation of heating effects may be obtained by considering EISCAT data, shown in figure 7.2(c), from the same interval. This shows the effects of ionospheric modification as an increase in the value of the electron temperature. The three panels that are shown contain data that were collected during three heating runs. The first heating run consisted of the three spatial sweeps that have been described above. The other two heating runs consisted of similar spatial sweeping cycles. Considering the first heating run: for the period of 1-minute spatial sweeping, the electron temperature is higher than that for the 10-second and 1 second spatial sweeps. It is lowest for the 1-second sweeps. The electron temperature lies between 2260 and 2400 K for the 1-minute sweep and between 1560 and 1840 K for the 10 second and 1 second sweeps. This is broadly the case in the latter cycles, although for the second cycle, the temperatures corresponding to the 1-second sweeps are

SUPERDARN PARAMETER PLOT

Hankasalmi: pwr_l

6 Oct 1998 (279)
normal (ccw) scan mode (150)

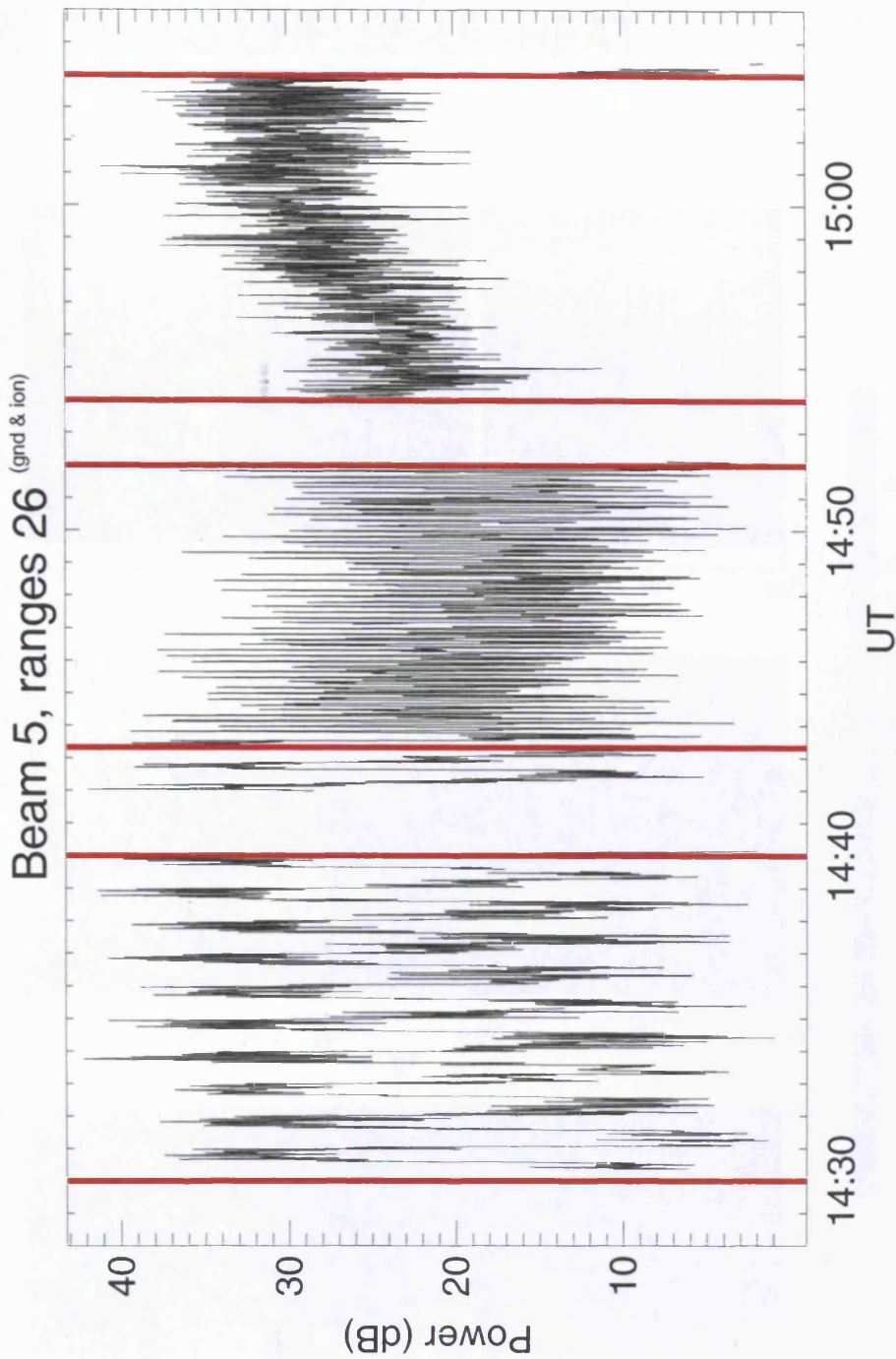


Figure 7.2(b): The backscatter power observed at range gate 26 for the three intervals presented in figure 7.2(a). The irregularities backscatter power does not have time to decay for the 10 second and 1 seconds sweeps. The vertical red line at around 1444 UT indicates where the heater changed from 40 second to 10 second sweeps.

EISCAT Tromso UHF: SP-UK-HEAT

Az: 359.9 El: 90.0

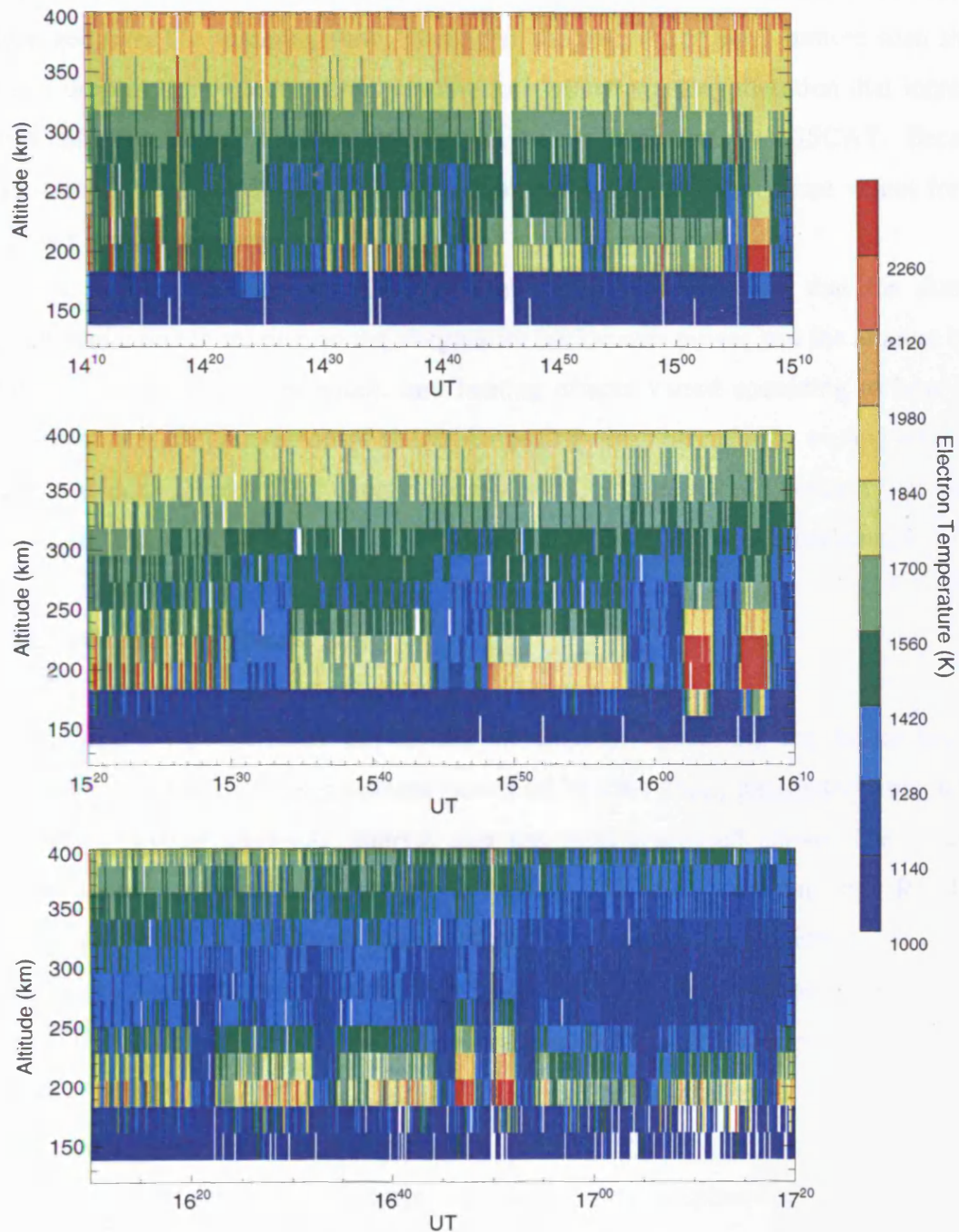


Figure 7.2(c): EISCAT data showing the electron temperature increase for the intervals presented above, together with subsequent intervals when sweeping was again conducted. It was expected that the temperature increase ought to be less for a lower sweeping period.

higher than those corresponding to the 10-second sweeps. This is unexpected as the excitation occurs for a shorter duration and the rise in temperature ought not to be as high. The strongest heating occurs for the periods where the pointing direction of the heater beam was not varied during the period of heater-on, as for the two 2-minute-on intervals that occurred between 1600 and 1610 UT. The heater parameters were the same as for the spatial sweeping periods. It is worth bearing in mind that the EISCAT data are taken at a resolution of 10 seconds and are averaged over the scanning time. Therefore, the results for the 1-minute scan show that there is a drop in temperature corresponding to a heater pointing direction that increases the electron temperature in a patch that is not being observed by EISCAT. Because the integration was 10 seconds, this resulted in a smearing in the temperature values for the 10-second and 1-second sweeps.

The results obtained by EISCAT and CUTLASS indicated that the duration of excitation had a direct bearing on the irregularity backscatter power and the amount by which the electron temperature was raised, and heating effects varied according to how long the heater excited a particular region of space. An analogy may be made to waving a hand over a flame. If it is done quickly, less energy is transferred to the hand and hence it will not absorb as much heat. Conversely, slower motion will result in the transfer of more heat.

7.3.2 Modelling of the Heater Beam

Figures 7.3(a)-(d) show the results obtained by modelling the heater beam for a frequency of 4.54 MHz and a transmitter power of 75 kW. These parameters obtained during the 10-minute spatial sweeping interval that has been discussed above. The figures were produced using a modelling program, called EZNEC, written by R. Lewallen (w7el@eznec.com). This program uses a FORTRAN calculating engine called NEC-2 and determines the beam pattern from the size, position, design and orientation of the antennae. Figures 7.3(a)-(d) correspond to the heater beam with off-zenith angles of 0°, 10°, 20° and 30°. Table 7.1 shows the effective radiated power (ERP) and electric field, calculated from the expression given in chapter 4, at an altitude of 200 km. As the off-zenith angle is increased, the ERP falls and the range to a particular ionospheric altitude increases, thus reducing the power incident in the ionosphere and the associated electric field falls.

Heater (zenith, real gnd)

EZNEC-M 2.5

09-13-2001 11:25:16
Freq = 4.54 MHz

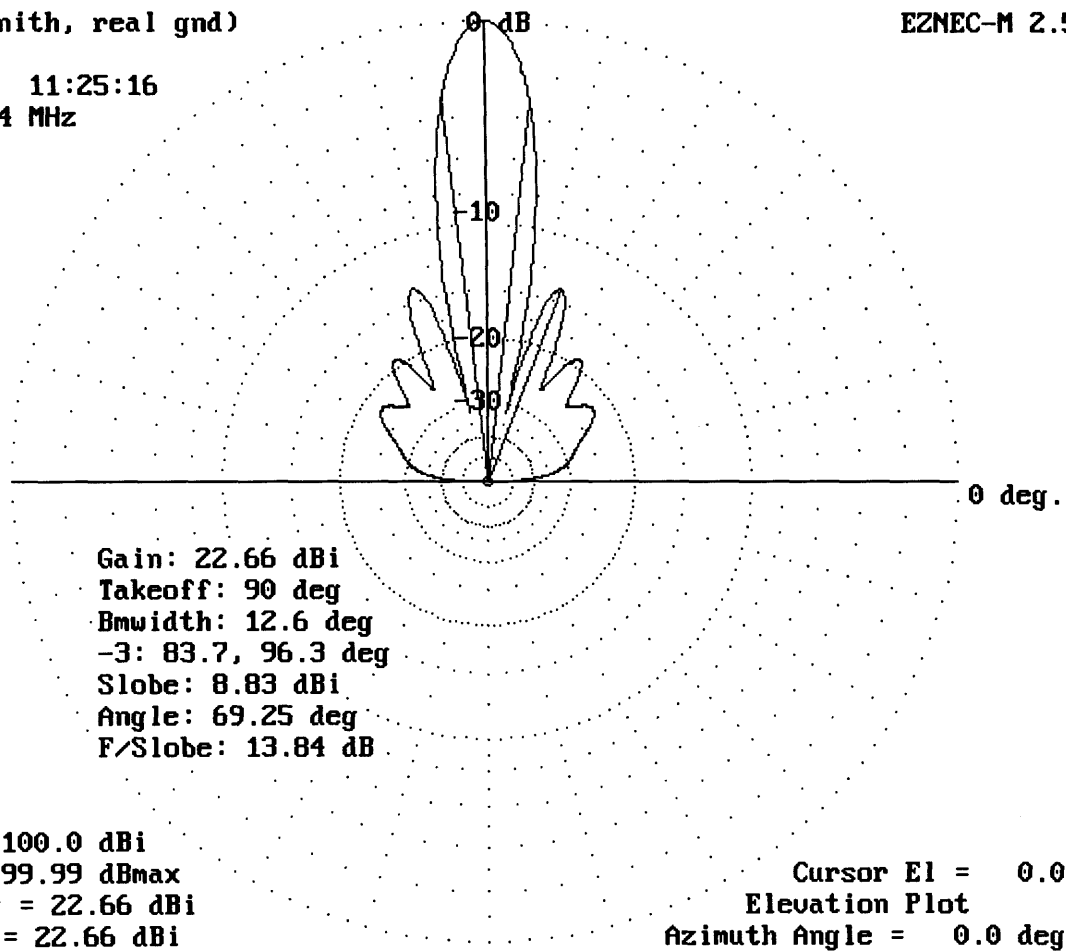


Figure 7.3(a): The modelled heater beam for a frequency of 4.54 MHz and a transmitter power of 75 kW. This is the case for a vertical heater beam. The side lobes are arranged symmetrically around the beam.

Heater (10deg, real gnd)

EZNEC-M 2.5

09-13-2001 14:47:53
Freq = 4.54 MHz

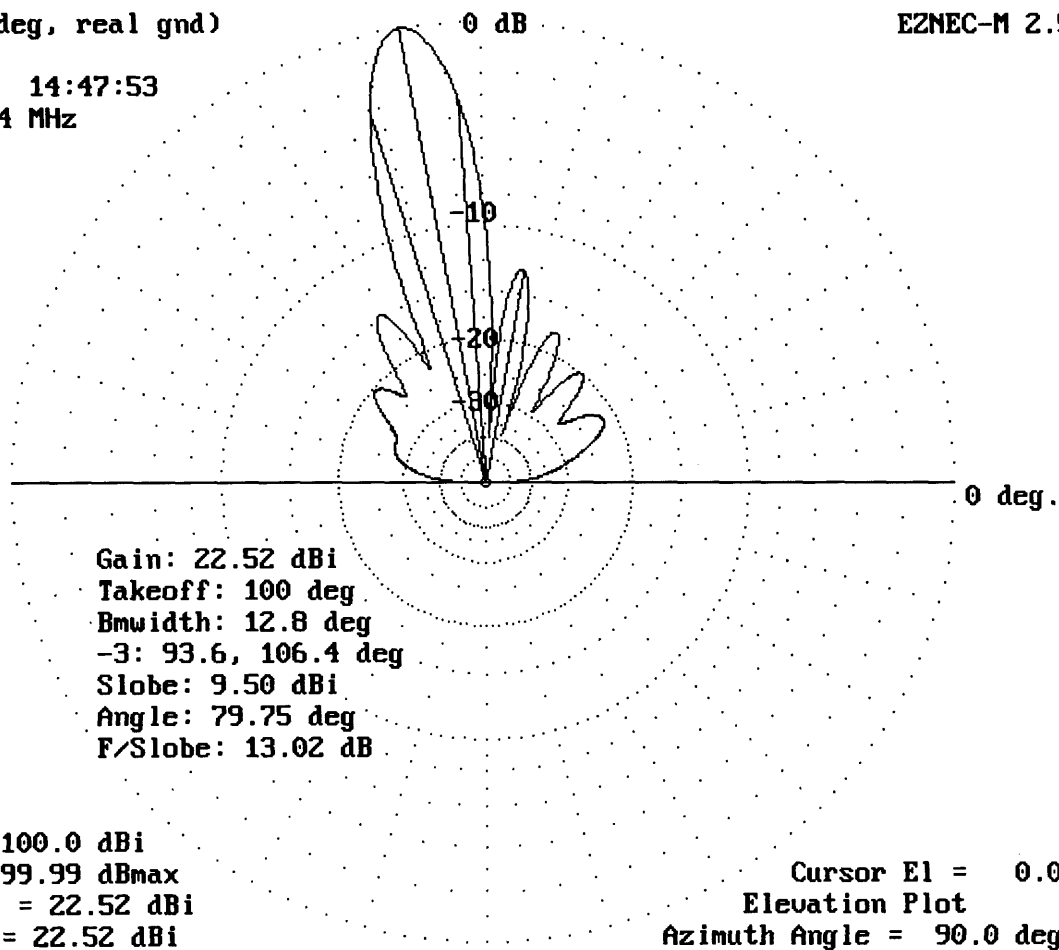


Figure 7.3(b): The modelled heater beam for a tilt of 10°. The side lobe amplitude increases for the closest side lobe to the main beam in a direction opposite to the tilt.

Heater (20deg, real gnd)

0 dB

EZNEC-M 2.5

09-13-2001 15:28:56

Freq = 4.54 MHz

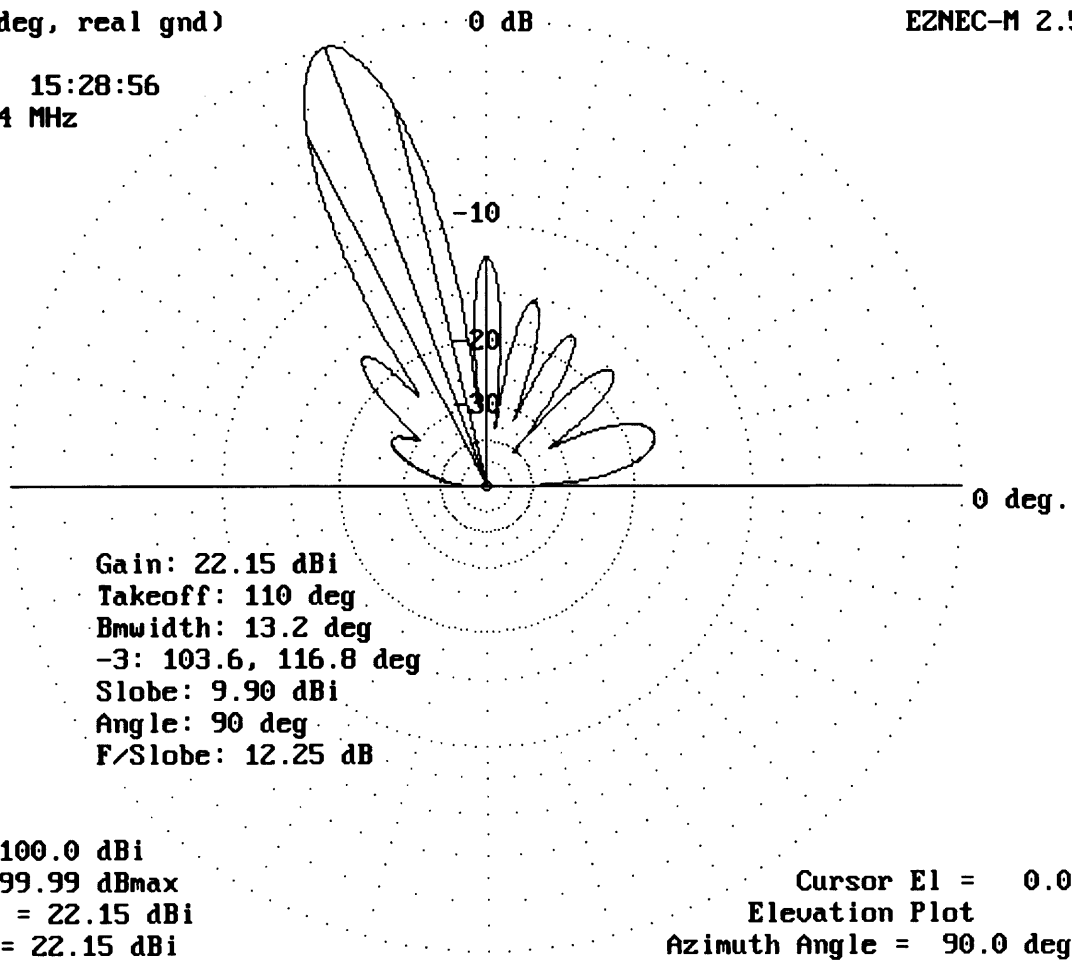


Figure 7.3(c): The modelled heater beam for a tilt of 20°. The vertical side lobe is the most prominent one.

Heater (30deg, real gnd)

0 dB

EZNEC-M 2.5

09-13-2001 16:10:30

Freq = 4.54 MHz

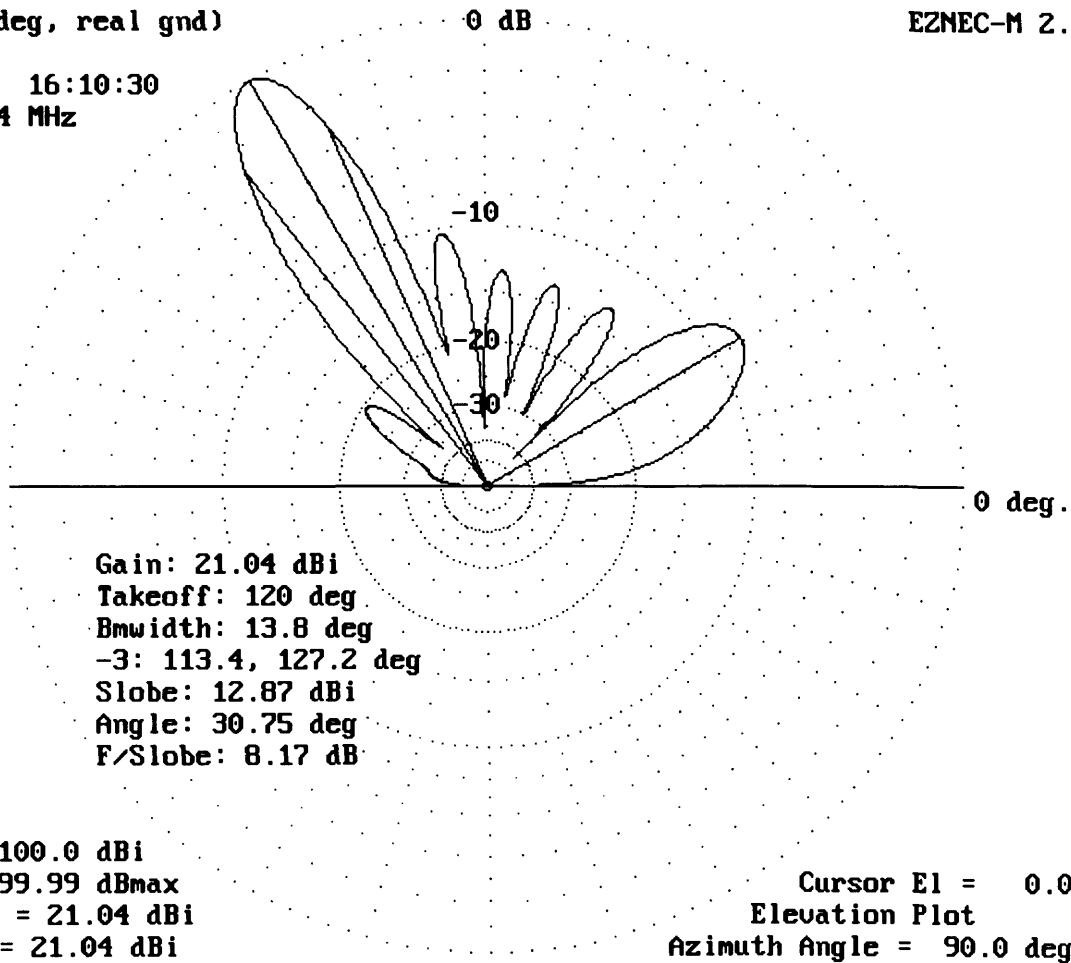


Figure 7.3(d): The modelled heater beam for a tilt of 30°. The highest power side lobe now occurs at a direction of 60° opposite to that of the tilt, but this may be discounted. The most important side lobe effect occurs for the side lobe at 10° in the direction of the tilt.

Off-zenith Angle, degrees	ERP, MW	E, mV m ⁻¹
0°	166	509
10°	161	494
20°	148	451
30°	114	366

Table 7.1: ERP and electric field for the heater at 4.54 MHz and varying off-zenith angle

Figure 7.3(a) shows the vertical heater beam case. There are side lobes present with angles of 20°, 35° and 55°, with powers of 13, 18 and 22 dB below the maximum power and these occur symmetrically around the heater beam. Figure 7.3(b) shows the case for a 10° tilt. The side lobes grow in the direction opposite to that of the tilt. The highest power side lobe occurs at 10° in the opposite direction at a power of 13 dB below the maximum power. Figure 7.3(c) shows the case for a 20° tilt. The most powerful side lobe is now vertical and has a power 13 dB below the maximum. For the case of a 30° tilt, the highest side lobe occurs at 59° in the direction opposite to the tilt. However, this is unimportant, since scatter will not be present for this side lobe. More important than this is the side lobe that occurs at 10° in the same direction as the tilt. This side lobe has a power 10 dB below the maximum power and theoretically has an observable effect.

At an altitude of 200 km, the maximum horizontal extent of the mapping of the heater beam is 200 km for an off-zenith angle of 30°. This corresponds very well with the range gate extent of the CUTLASS backscatter seen in the data. For a lower ERP, the electric field would exceed the threshold by less and this would result in lower-power backscatter.

7.3.3 CUTLASS Range Gate Profiles of the Heater Beam

This section presents some profiles of the CUTLASS backscatter over the heater beam for the spatial sweeping periods that were shown in the previous section. The figures correspond to the 1-minute spatial sweeps.

Figures 7.4(a)-(d) show the averaged backscatter power for the intervals when the heater beam was pointing in the directions corresponding to those assumed in the modelling that was described above. These data correspond to the relevant parts of the spatial sweep for the particular pointing direction. The average was performed for the 10 sweeps that occurred during the period 1430-1440 UT. Figure 7.4(a) shows the case for a vertical heater beam.

SUPERDARN PARAMETER PLOT

Heater Beam Direction Dependence of Backscatter Power

6 Oct 1998 (279)

normal (ccw) scan mode (150)

Beam Direction = Vertical

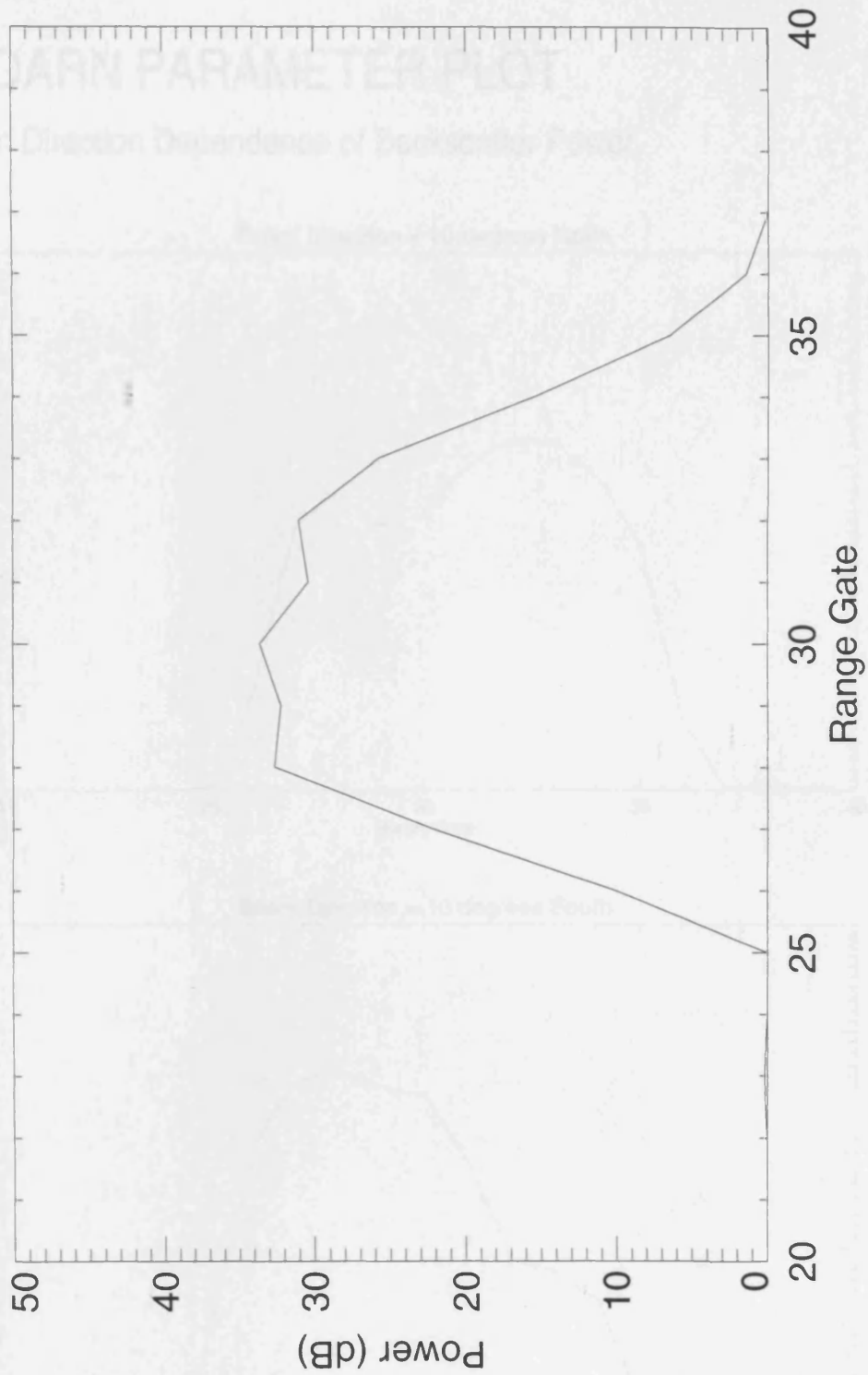


Figure 7.4(a): The averaged backscatter power over the range gates corresponding to the heated patch for a vertical heater beam. The highest power backscatter occurs for the vertical direction, as expected.

SUPERDARN PARAMETER PLOT

Heater Beam Direction Dependence of Backscatter Power

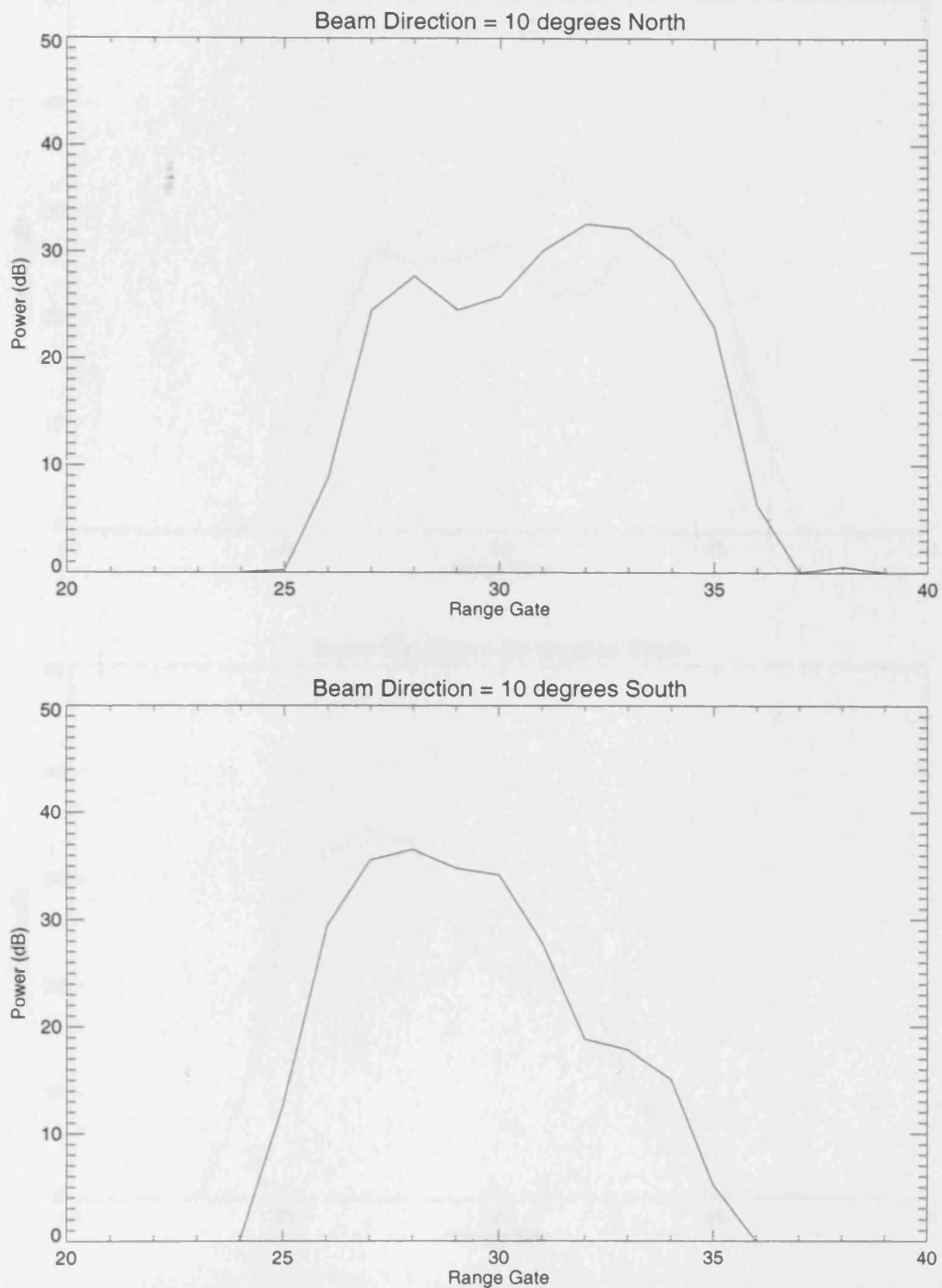


Figure 7.4(b): The averaged backscatter power for tilt directions of 10° North and 10° South. There are maxima with lower amplitudes that occur in addition to the maximum corresponding to the pointing direction.

SUPERDARN PARAMETER PLOT

Heater Beam Direction Dependence of Backscatter Power

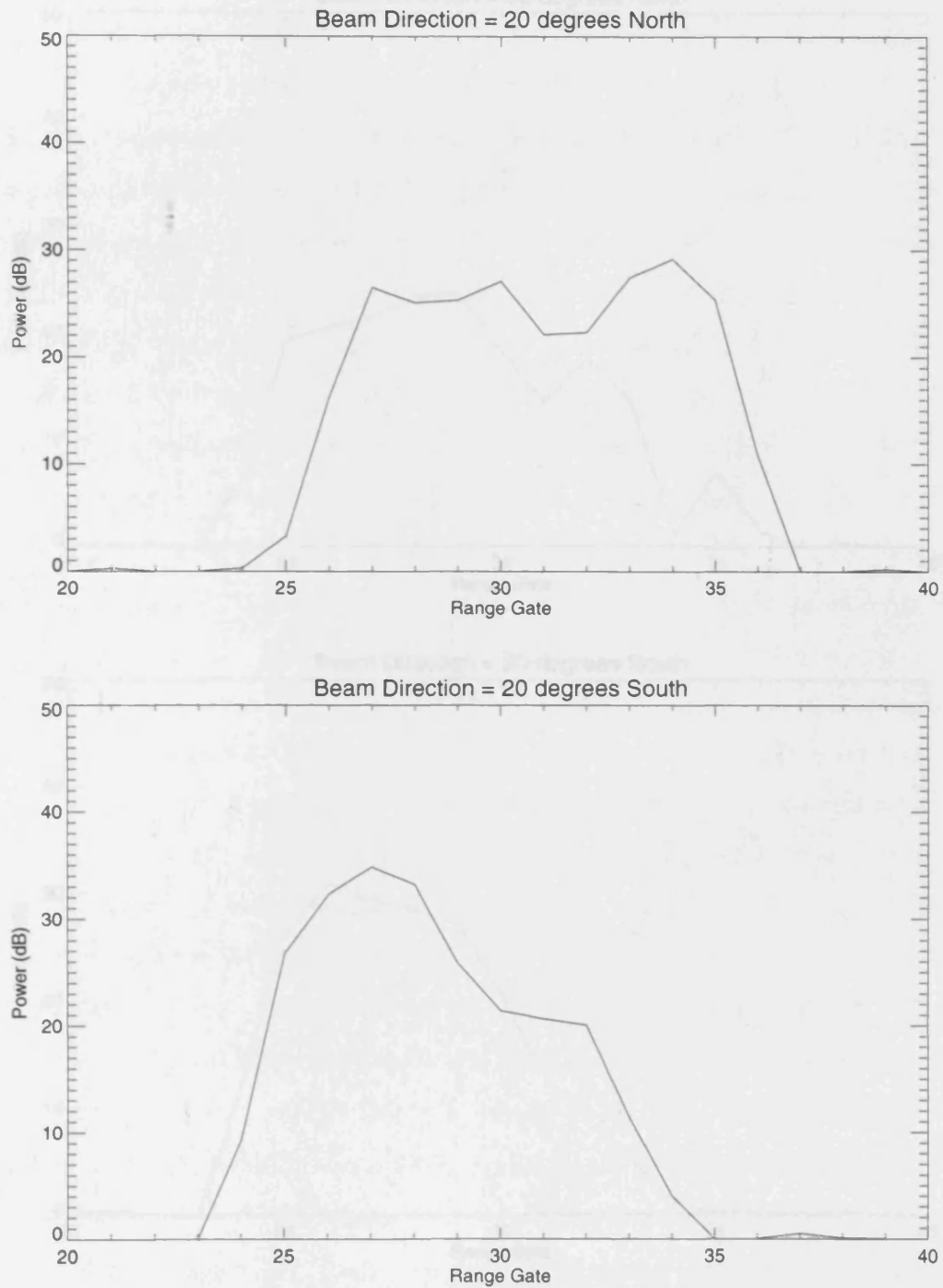


Figure 7.4(c): The averaged backscatter power for tilt directions of 20° North and 20° South. Again, there are maxima with lower amplitudes that occur in addition to the maximum corresponding to the pointing direction.

SUPERDARN PARAMETER PLOT

Heater Beam Direction Dependence of Backscatter Power

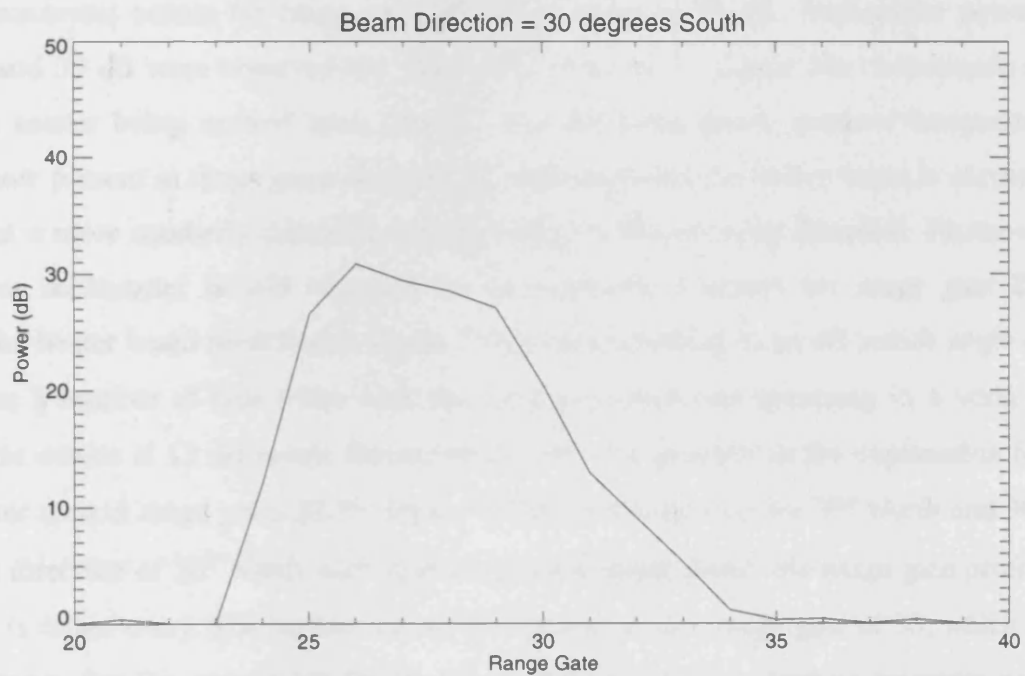
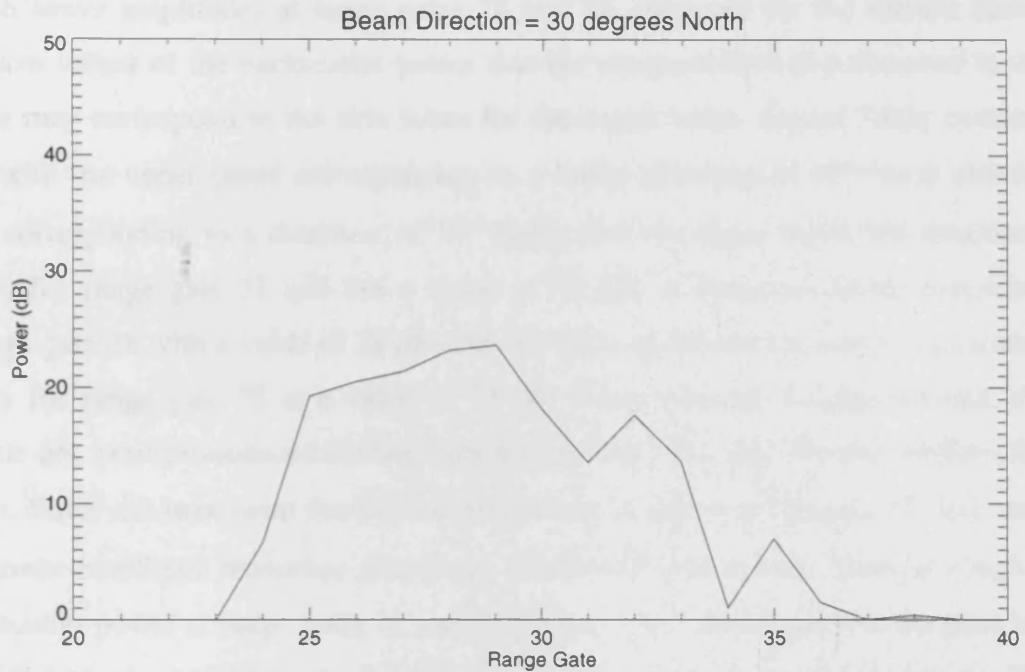


Figure 7.4(d): The averaged backscatter power for tilt directions of 30° North and 30° South. The data corresponding to the southerly direction show the pointing direction effect more clearly.

This corresponds directly with the modelled result and with the conclusions of Bond et al. (1997), who showed that the spatial profile of the CUTLASS backscatter power over the heated patch generally had a Gaussian shape, with the highest power in the centre of the patch. The maximum backscatter power occurs at the centre of the heater beam. The two maxima, with lower amplitudes at range gates 28 and 32, observed for the vertical heater beam case have values of the backscatter power that are comparable to that observed in the centre. These may correspond to the side lobes for the heater beam. Figure 7.4(b) contains two panels, with the upper panel corresponding to a heater direction of 10° North and the lower panel corresponding to a direction of 10° South. For the upper panel, the maximum power occurs for range gate 32 and has a value of 33 dB. A lower-amplitude maximum occurs at range gate 28 with a value of 28 dB. For the lower panel, the maximum backscatter power occurs for range gate 28 at a value of 38 dB. From theoretical considerations, the heating effects are most pronounced for the field-aligned direction and this may explain the higher power. Since the maximum for the 10° South case occurs at range gate 27, this may explain the lower-amplitude maximum that occurs for the 10° North case. There is a region of high backscatter power at range gates 32 and 33. Figure 7.4(c) shows the case for pointing directions of 20° North and 20° South. For the upper panel corresponding to the case for 20° North, the maximum occurs for range gate 34 with a value of 30 dB. Backscatter powers between 25 and 30 dB were observed for range gates down to 27. Again this corresponds to field-aligned scatter being excited most strongly. For the lower panel, positive backscatter powers are now present in range gates down to 25, indicating that the heater beam is exciting backscatter in a more southerly direction, corresponding to the pointing direction. However, the maximum backscatter is still observed in the southerly direction for range gate 27. Examining the heater beam modelled in figure 7.3(c) corresponding to an off-zenith angle of 20° , there are a number of side lobes with the most important one occurring in a vertical direction. This occurs at 12 dB below the maximum and may provide an the explanation for the backscatter seen at range gates 30-33. Figure 7.4(d) shows the case for 30° North and 30° South. For a direction of 30° North, corresponding to the upper panel, the range gate profile of the return is rather noisy. The highest backscatter power is for a range gate of 30, which is the vertical beam. For the case of 30° South, the backscatter power is highest for range gate 26. There is not much correlation between the data shown here and the corresponding heater modelling case, shown in figure 7.3(d).

7.3.4 Persistent Backscatter Observed at the Centre of the Beam

Figure 7.5(a) shows the backscatter power for three range gates: 26, 29 and 33 for the interval 1430-1440 UT. Range gates 26 and 33 collected data from close to the southernmost and northernmost extents of the heater beam as it was swept. Range gate 29 was slightly to the south of the centre of the beam. Figure 7.5(a) shows how the CUTLASS backscatter, for range gate 26, decayed away from about 40 dB to about 10 dB when the illumination ceased briefly. For range gate 29, however, the backscatter fell to between 20 and 30 dB. There are two possible explanations for this: that the central part of the heater beam was more intense, and this has been shown for the modelling of the heater beam in figure 7.3(a), and that the heater beam was wide, resulting in the continuous illumination of a particular patch of the ionosphere, even when the beam was swept. Although the central part of the heater beam should transfer most power to the F-region, it is clear that the spatial profile of the backscatter was asymmetric. This is because of preferential heating in the field-aligned direction, as described above. Table 7.2 shows the mean and standard deviation of the backscatter powers for the 10 1-minute sweeps.

Range gate	Minimum power, dB	Maximum power, dB
26	9.5 ± 3.6	32.4 ± 4.1
29	20.9 ± 3.6	31.4 ± 4.0
33	9.8 ± 3.8	30.0 ± 3.2

Table 7.2: Range gate variation of maximum and minimum power during sweeps

Therefore, for range gates 26 and 33, the minimum backscatter power during the sweeps was approximately 20 dB below the maximum power. However, for range gate 29, which was the range gate where the highest backscatter power was observed, the minimum power was approximately 10 dB below the maximum power. This confirms the observation of a central backscatter region where the backscatter power remained high. The sequence of spatial sweeping experiments, consisting of 1-minute, 10-second and 1-second sweeps, was repeated twice and figure 7.5(b) shows the backscatter power for range gates 30 and 31, corresponding to the centre of the beam for the intervals 1520-1530 UT and 1610-1620 UT. For the interval 1520-1530 UT, the minimum and maximum powers are 16.8 ± 2.9 dB and 28.0 ± 2.0 dB, respectively. The corresponding values for the interval 1610-1620 UT are 19.8 ± 3.9 dB and 34.2 ± 3.3 dB. Returning to figures 7.2(a)-(c), the backscatter covered a range

SUPERDARN PARAMETER PLOT

Hankasalmi: pwr_1

6 Oct 1998 (279)

normal (ccw) scan mode (150)

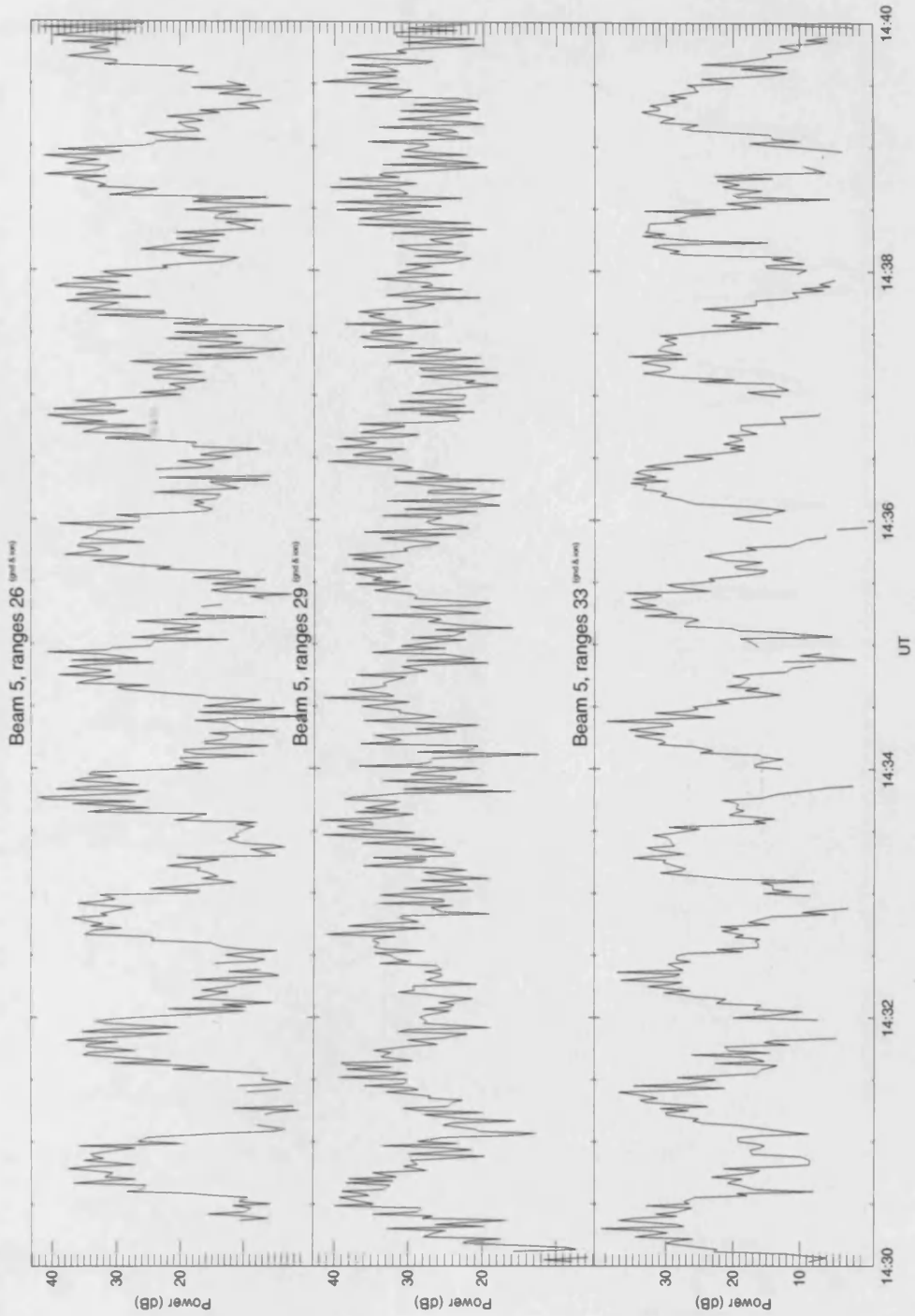


Figure 7.5(a): The backscatter power for range gates 26, 29 and 33. The backscatter powers obtained from range gate 29 do not fall as much as for range gates 26 and 29 during the sweep.

SUPERDARN PARAMETER PLOT

Hankasalmi: pwr_j

6 Oct 1998 (279)

normal (ccw) scan mode (150)

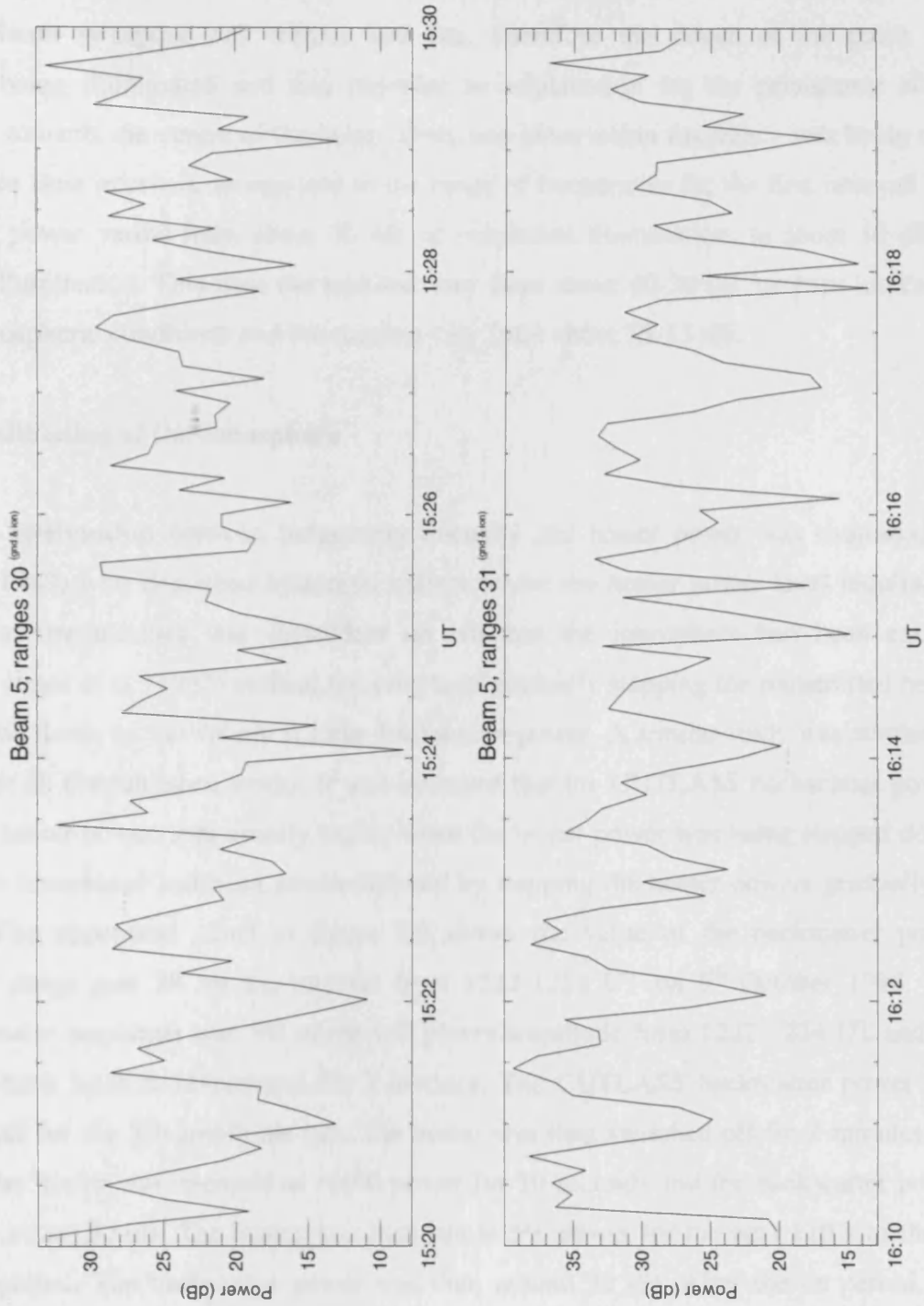


Figure 7.5(b): Data for the central part of the heater beam for two further periods when spatial sweeping was conducted. The backscatter powers again do not fall to zero during the sweep.

of around 160 km for a vertical heater beam. The maximum extent of the heated patch for North to South sweeping was around 200 km. Therefore the centre of the patch was constantly being illuminated and this provides an explanation for the persistence of the backscatter towards the centre of the beam. Only one observation frequency was being used for these two time intervals, as opposed to the range of frequencies for the first interval. The backscatter power varied from about 30 dB, at maximum illumination, to about 10 dB, at minimum illumination. This time the maxima vary from about 40-30 dB, perhaps indicating varying ionospheric conditions and the minima vary from about 25-15 dB.

7.4 Preconditioning of the Ionosphere

The relationship between irregularity intensity and heater power was examined by Robinson (1989) who described hysteresis effects where the heater power level required to maintain the irregularities was dependent on whether the ionosphere had been excited previously. Jones et al. (1983) studied the effects of gradually stepping the transmitted heater power up and down on the values of radar backscatter power. A similar study was conducted by Wright et al. (unpublished work). It was observed that the CUTLASS backscatter power, for a given heater power, was usually higher when the heater power was being stepped down, i.e. after the ionosphere had been preconditioned by stepping the heater powers gradually up to 100%. The uppermost panel in figure 7.6 shows the value of the backscatter power obtained at range gate 28 for the interval from 1222-1252 UT on 5th October 1998. The operating heater amplitude was 5% of the full-power amplitude from 1222-1224 UT and the heater had been inactive beforehand for 3 minutes. The CUTLASS backscatter power was around 10 dB for the 5%-amplitude run. The heater was then switched off for 2 minutes. At 1226 UT, the heater was operated at 100% power for 10 seconds and the backscatter power rose to just under 30 dB. The heater was then run at 5% power for the next 110 s of the 2-minute on period. The backscatter power was then around 22 dB. After the on period, the heater was left off for 2 minutes once more and then operated at 5% amplitude from 1230-1232 UT. The average power was then down to around 15 dB. After the next 2-minute off period, the heater was operated at 100% amplitude for 5 seconds. The heater was then run at 5% for the remainder of the 2-minute on period. This procedure was repeated but the seeding interval was reduced to 2 seconds, and then to 1 second for the last run in the 30-minute interval. A 2.5% amplitude was utilised during one of the subsequent 30-minute intervals that were run to demonstrate the effects of preconditioning the ionosphere and these are shown in

SUPERDARN PARAMETER PLOT

5 Oct 1998 ⁽²⁷⁸⁾

Hankasalmi: pwr_l

unknown scan mode (-6312)

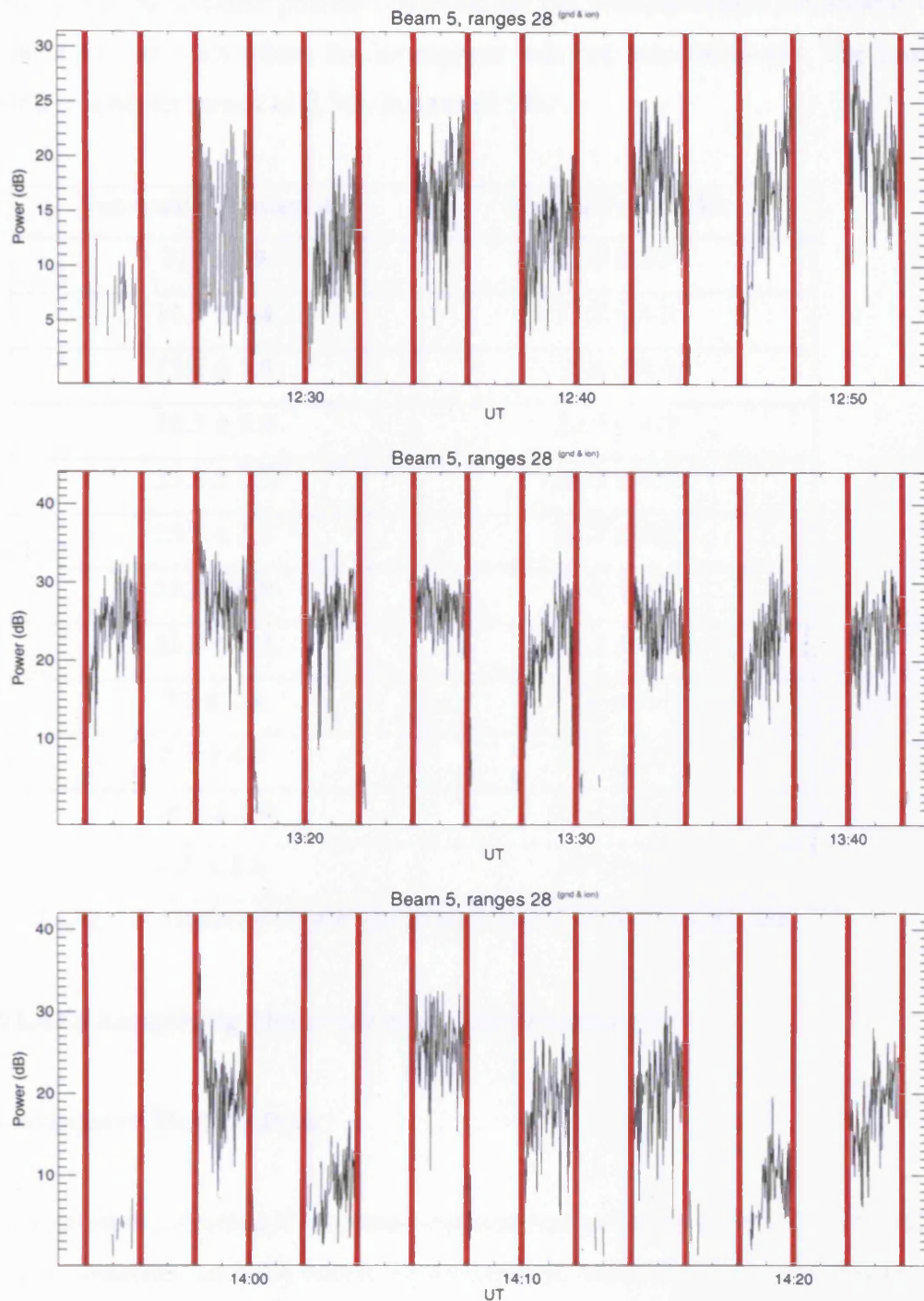


Figure 7.6: The backscatter power corresponding to periods when a seeding experiment was conducted. The backscatter powers after seeding were higher than those when seeding had not been carried out, for the same heater power.

the lower two panels of figure 7.6. The preconditioning occurred at the same duration into the interval as for the previous cycle. The results obtained for these preconditioning experiments are shown in table 7.3 where the mean powers in dB, along with the standard deviation are shown. Generally, the backscatter powers observed for the preconditioned ionosphere were higher than those for intervals where the ionosphere was not preconditioned. The lower 4 rows correspond to a heater power of 2.5%, instead of 5%.

Non-seeded Power, dB	Seeded Power, dB
7.3 ± 2.9	13.5 ± 5.9
11.2 ± 4.4	17.2 ± 4.3
12.6 ± 3.9	17.6 ± 4.0
16.3 ± 5.8	20.3 ± 4.7
23.8 ± 5.5	26.5 ± 4.0
25.1 ± 5.7	26.7 ± 3.0
21.7 ± 6.0	24.2 ± 3.8
21.8 ± 6.2	24.3 ± 4.2
3.9 ± 2.1	19.6 ± 4.3
8.3 ± 4.0	25.7 ± 4.2
18.2 ± 5.6	21.2 ± 4.8
8.5 ± 3.8	18.7 ± 4.6

Table 7.3: Backscatter powers unseeded and seeded ionosphere

7.5 The CUTLASS Longer-lag Mode and Associated Parameters

7.5.1 Characteristics of Heating Data

Backscatter return obtained from heater-induced scatter has low spectral width values, less than 10 m s^{-1} whereas naturally occurring ionospheric backscatter associated with, say, magnetospheric convection, has spectral width values of the order of a few hundred m s^{-1} . These spectral width values, as mentioned above, are derived from the decorrelation rate of the ACF, where a higher spectral width value corresponds to a higher value of the ACF decorrelation rate. Conversely, a lower value for the spectral width is associated with an ACF

that does not decorrelate as quickly. The properties of ACFs have been described in previous work (e.g. Villain et al., 1987; Baker et al., 1995).

For naturally occurring radar backscatter, the ACF decorrelates quickly. Within 20 lags or 4800 μs , the ACF power has fallen substantially so that it is a small fraction of the lag-0 maximum amplitude, as illustrated in figure 7.7. The irregularity distribution, corresponding to naturally occurring irregularities in the F-region, changes sufficiently quickly during the sampling interval to allow the ACF to decorrelate.

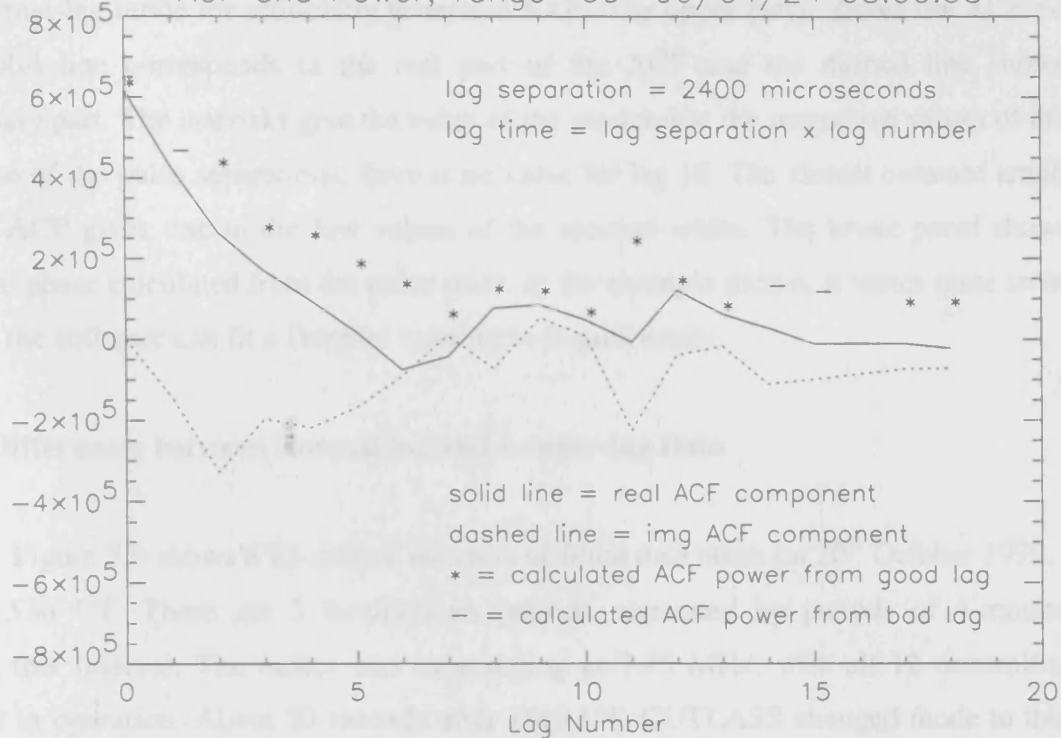
7.5.2 The CUTLASS Longer-lag Mode

The effects associated with the spectral width and the characteristics of irregularity distributions were examined during the campaign run in October 1999. This campaign utilised a new longer-lag mode where the lag separations were 12000 and 24000 μs instead of the usual 2400 μs . The longer lag separations were used in order to provide a longer sampling time, thus providing an opportunity to examine whether the irregularity distribution remained static for the longer sampling time. Basically, the pulse sequence was spread out so that it was 5 or 10 times as long as the sequence that is transmitted most commonly, thus leading to a 5 or 10 second data resolution and integration time, rather than the usual 1 second resolution. The operation of CUTLASS, and the extraction of information from the ACF, was explained in chapter 4. The value of the spectral width, the Fourier transform of the ACF, is an indicator of the level of turbulent diffusion in the plasma. This diffusion acts to alter the irregularity distribution as detected by the radar. Heater scatter obtained from the 2400 μs CUTLASS scan mode has a characteristically small spectral width, indicating that the irregularity distribution during the sampling period remains fairly constant for artificial FAIs. This feature often differentiates artificial backscatter from natural backscatter.

SuperDARN data are usually considered in terms of the fitted parameters, e.g. backscatter power and Doppler velocity and this is entirely adequate for most purposes, e.g. the construction of convection maps relating to magnetospheric plasma flow. The fitted parameters are obtained from the ACF by the fitting software, using similar signal processing techniques to those described in chapter 4.

The power is taken as the lag-0 power, the spectral width comes from the decorrelation rate, the decay profile, of the ACF and the Doppler velocity is calculated by performing a linear fit to the residual phase calculated from the pulse pairs. Because of the relatively static irregularity distribution, the software has difficulty fitting a decay profile,

ACF and Power, range 60 99/04/24 08:00:38



Range: 60 Residual Phase 99/04/24 08:00:38

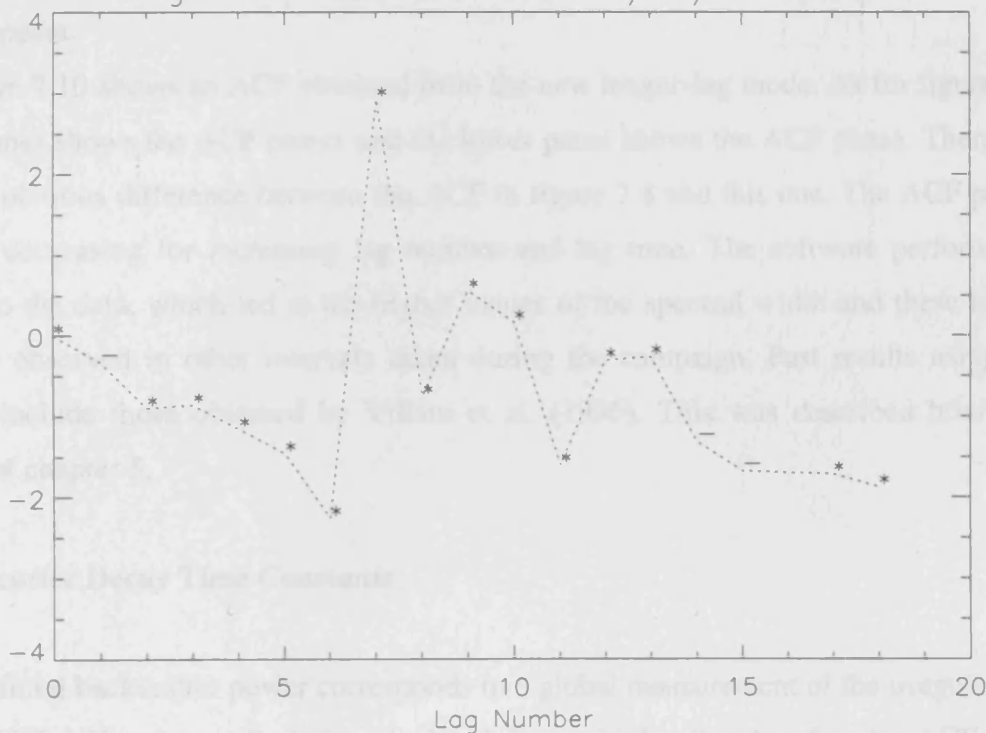


Figure 7.7: An ACF corresponding to natural irregularities in the F-region. The ACF decorrelates during the sampling interval indicating that the irregularity distribution is not static.

either Gaussian or exponential, to the ACF. Figure 7.8 shows a typical ACF obtained from the normal-lag mode for artificially generated FAIs. The upper panel shows the ACF power. The solid line corresponds to the real part of the ACF and the dashed line shows the imaginary part. The asterisks give the value of the modulus at the respective values of the lag. Because of the pulse separations, there is no value for lag 16. The almost constant amplitude of the ACF gives rise to the low values of the spectral width. The lower panel shows the residual phase calculated from the pulse pairs. In the example shown, it varies quite smoothly and so the software can fit a Doppler velocity to it quite easily.

7.5.3 Differences between Normal-lag and Longer-lag Data

Figure 7.9 shows a 25-minute duration of fitted data taken on 20th October 1999, from 1505-1530 UT. There are 3 4-minute-on periods, separated by periods of 4-minute-off, during this interval. The heater was transmitting at 7.95 MHz, with all 12 transmitters of array 3 in operation. About 30 seconds after 1516 UT, CUTLASS changed mode to the new longer-lag mode, described above. The transition to the new mode is clear as the noise and clutter disappears.

Figure 7.10 shows an ACF obtained from the new longer-lag mode. As for figure 7.8, the upper panel shows the ACF power and the lower panel shows the ACF phase. There is a distinct and obvious difference between the ACF in figure 7.8 and this one. The ACF power was clearly decreasing for increasing lag number and lag time. The software performed a reliable fit to the data, which led to the higher values of the spectral width and these higher values were observed in other intervals taken during the campaign. Past results using the normal lag include those obtained by Villain et al. (1996). This was described briefly in section 3.5 of chapter 5.

7.5.4 Backscatter Decay Time Constants

The fitted backscatter power corresponds to a global measurement of the irregularities within a CUTLASS range cell. It is calculated from the lag-0 value for the ACF. The fluctuations in the global decay of the irregularities ought to be of the same type as the microscopic decay, from the irregularity dissipation theorem. Therefore, the macroscopic decay should follow the same profile as that of the microscopic decay, i.e. the decay time for the irregularity backscatter power, should be the same as the ACF decorrelation time, within

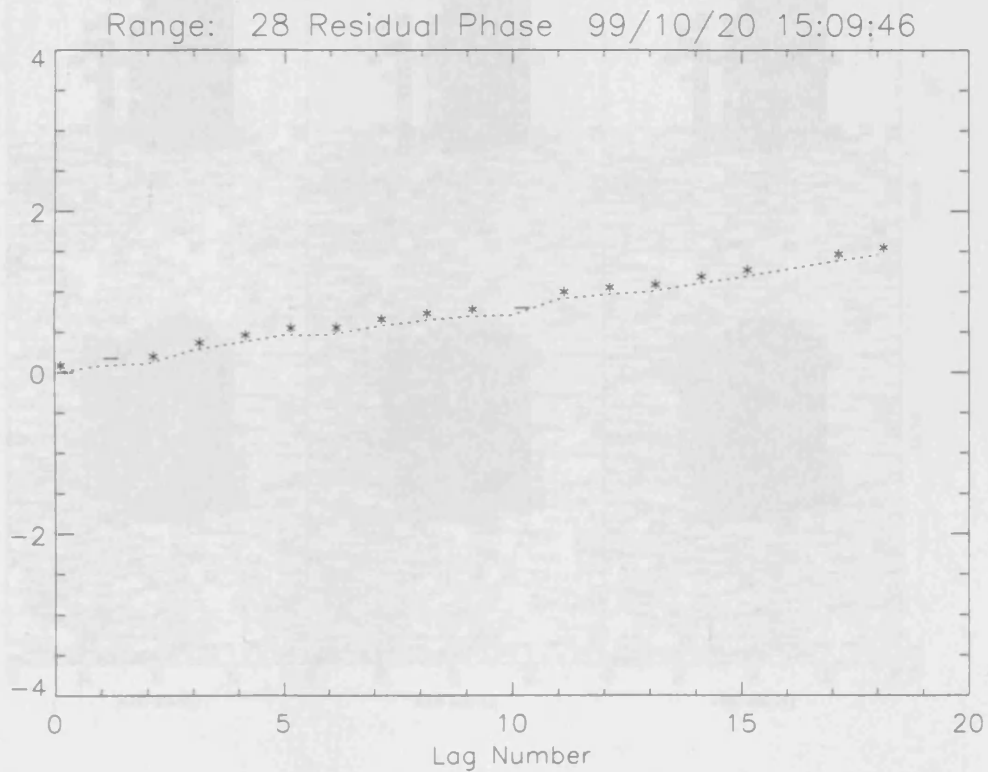
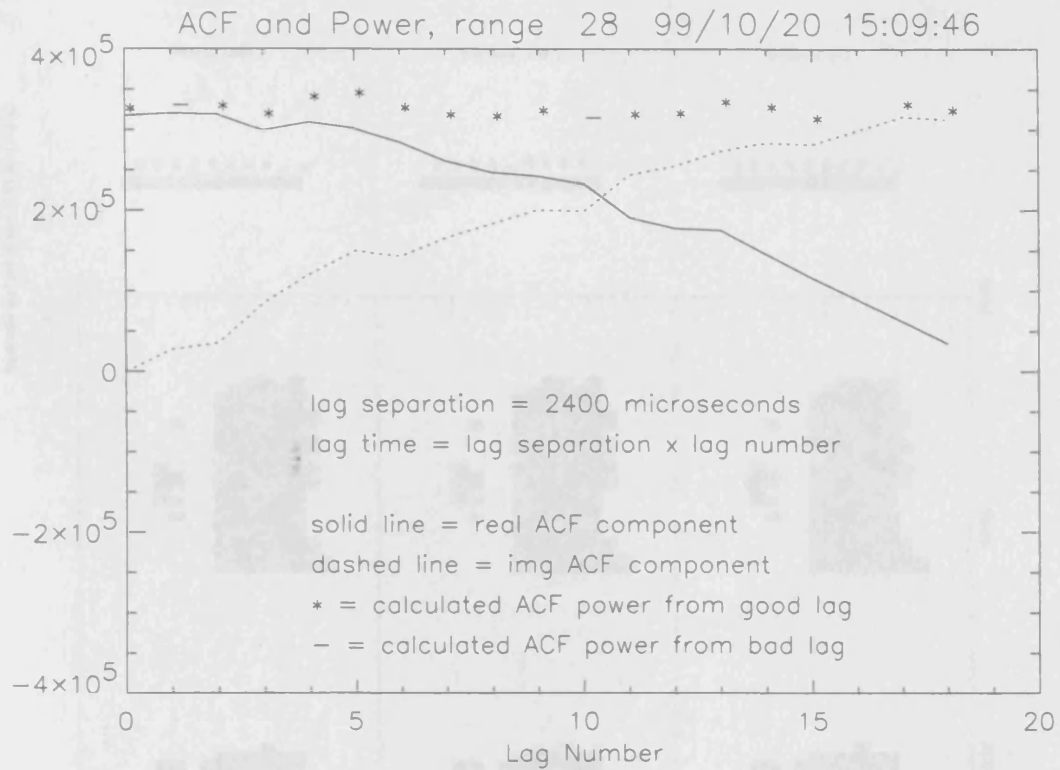


Figure 7.8: A typical ACF taken during the normal-lag mode. The power of the ACF, shown in the upper panel, is seen to remain steady with increasing lag time. This indicates the presence of a static irregularity distribution.

SUPERDARN PARAMETER PLOT

20 Oct 1999 (293)

normal (ccw) scan mode (150)

Hankasalmi: width_1

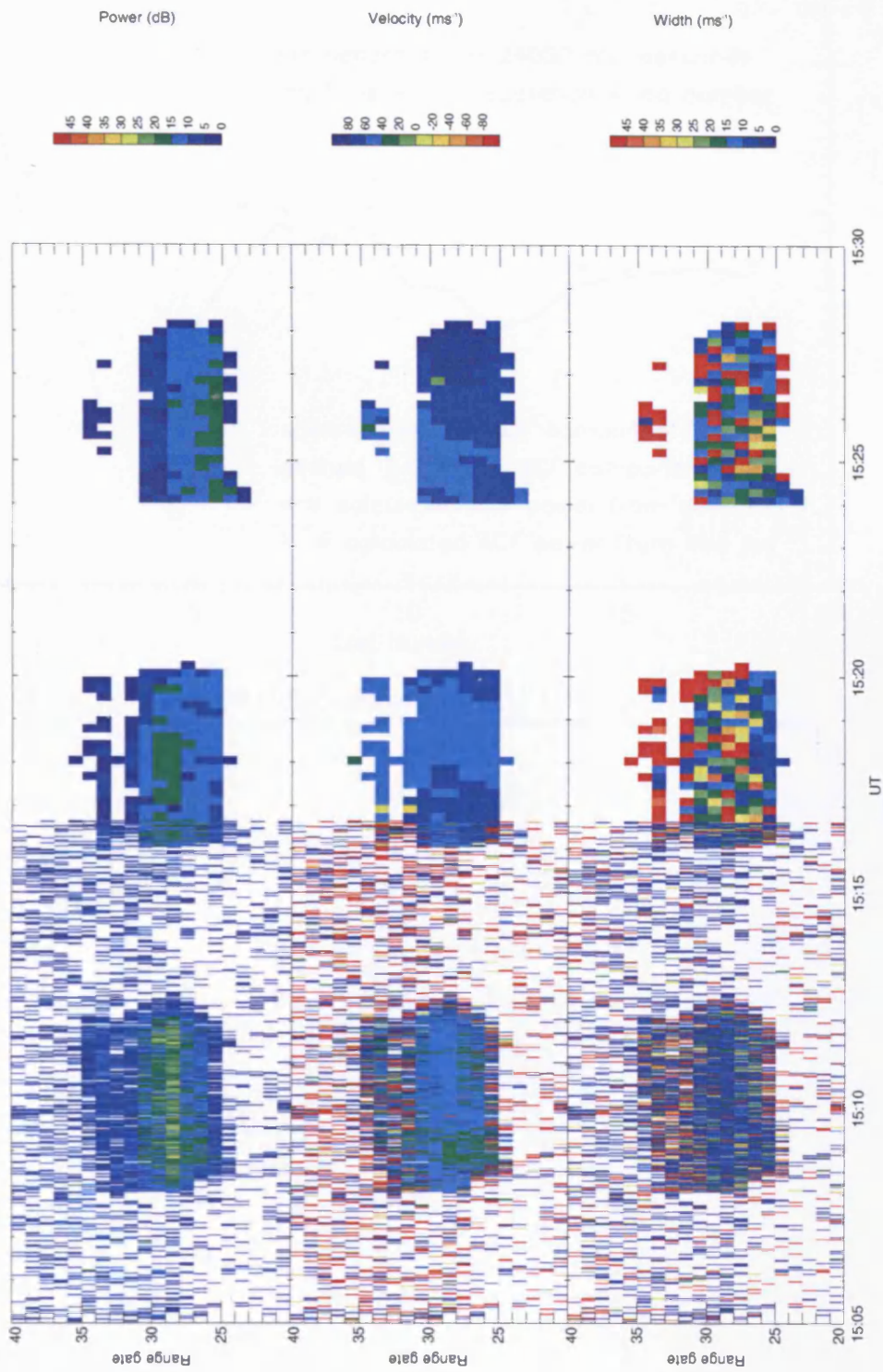


Figure 7.9: A 25-minute interval of data, when CUTLASS changed mode from the normal-lag to the longer-lag mode. This occurred at just after 1516 UT.

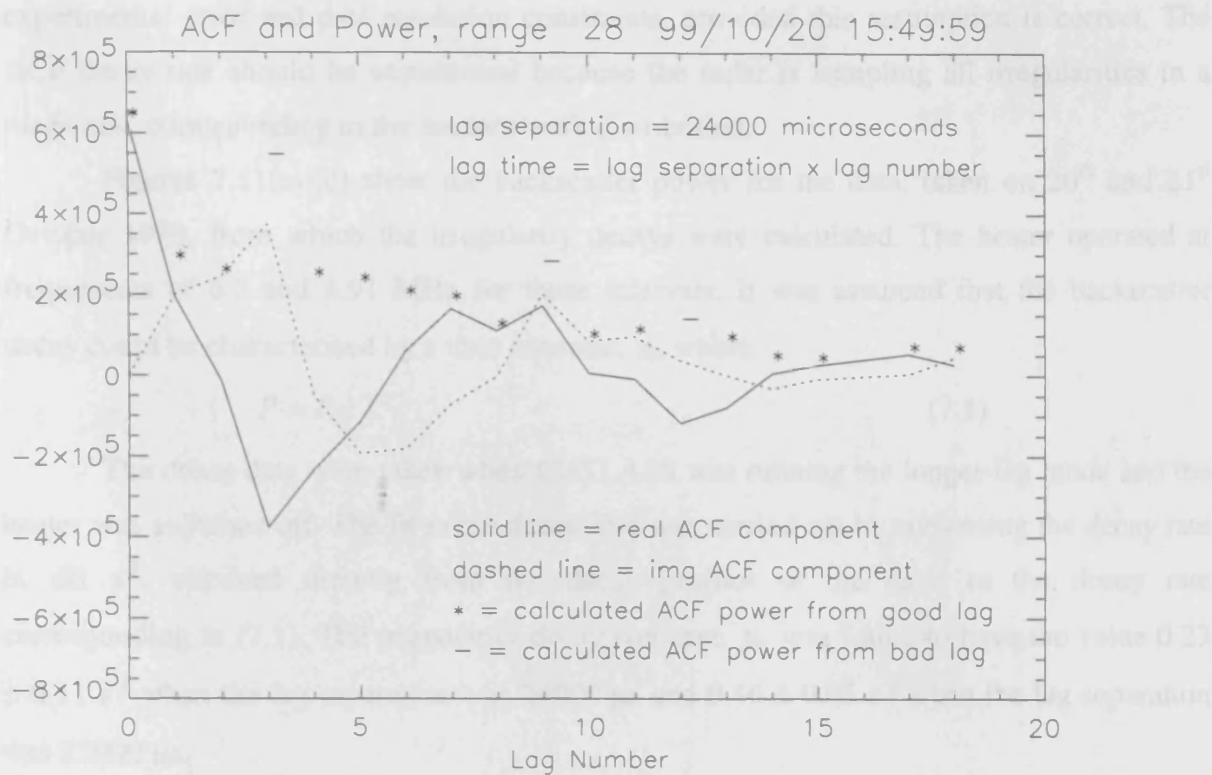


Figure 7.10: An ACF obtained during the longer lag mode. As for the ACF corresponding to natural irregularities shown above, this ACF now decorrelates indicating an irregularity distribution that is not static for the longer sampling time.

experimental error and data resolution constraints, provided this assumption is correct. The ACF decay rate should be exponential because the radar is sampling all irregularities in a range cell, corresponding to the random walk distribution.

Figures 7.11(a)-(c) show the backscatter power for the data, taken on 20th and 21st October 1999, from which the irregularity decays were calculated. The heater operated at frequencies of 6.2 and 4.91 MHz for these intervals. It was assumed that the backscatter decay could be characterised by a time constant, γ_b , where

$$P = P_0 e^{-\gamma_b t} \quad (7.1)$$

The decay data were taken when CUTLASS was running the longer-lag mode and the heater was switched off. The fit to the decay data was carried out by converting the decay rate in dB s⁻¹, obtained directly from the decay profiles of the data, to the decay rate corresponding to (7.1). The irregularity decay constant, γ_b , was found to have the value 0.23 ± 0.11 s⁻¹ when the lag separation was 24000 μ s and 0.46 ± 0.05 s⁻¹ when the lag separation was 12000 μ s.

7.5.5 ACF Decorrelation Time Constants

The ACFs were obtained for the data that have been described in the previous section. It should be noted that the ACF for each case was obtained by averaging the individual ACFs for the 4-minute-on period, and then smoothing to remove the effects of known bad lags. Bad lags are values of the lag time that correspond to erroneous ACF values. When an averaged ACF is constructed, the effects of the bad lags are easily seen, and may then be removed. In averaging, it was assumed that the same conditions obtained in the ionosphere for the 4-minute-on period. Some of these averaged ACFs are shown in figure 7.12. For the case of the ACF data, two fits were carried out after the logarithm of them had been taken. One of these fits was linear and the other was quadratic. The linear fit corresponds to an exponential decorrelation and the quadratic fit corresponds to a Gaussian decorrelation. These two correlation decay profiles correspond to

$$P = P_0 e^{-\gamma_b t} \quad (7.2)$$

and

$$P = P_0 e^{-\sigma_k^2 t^2} \quad (7.3)$$

SUPERDARN PARAMETER PLOT

20 Oct 1999 ⁽²⁹³⁾

Hankasalmi: pwr_l

normal (ccw) scan mode (150)

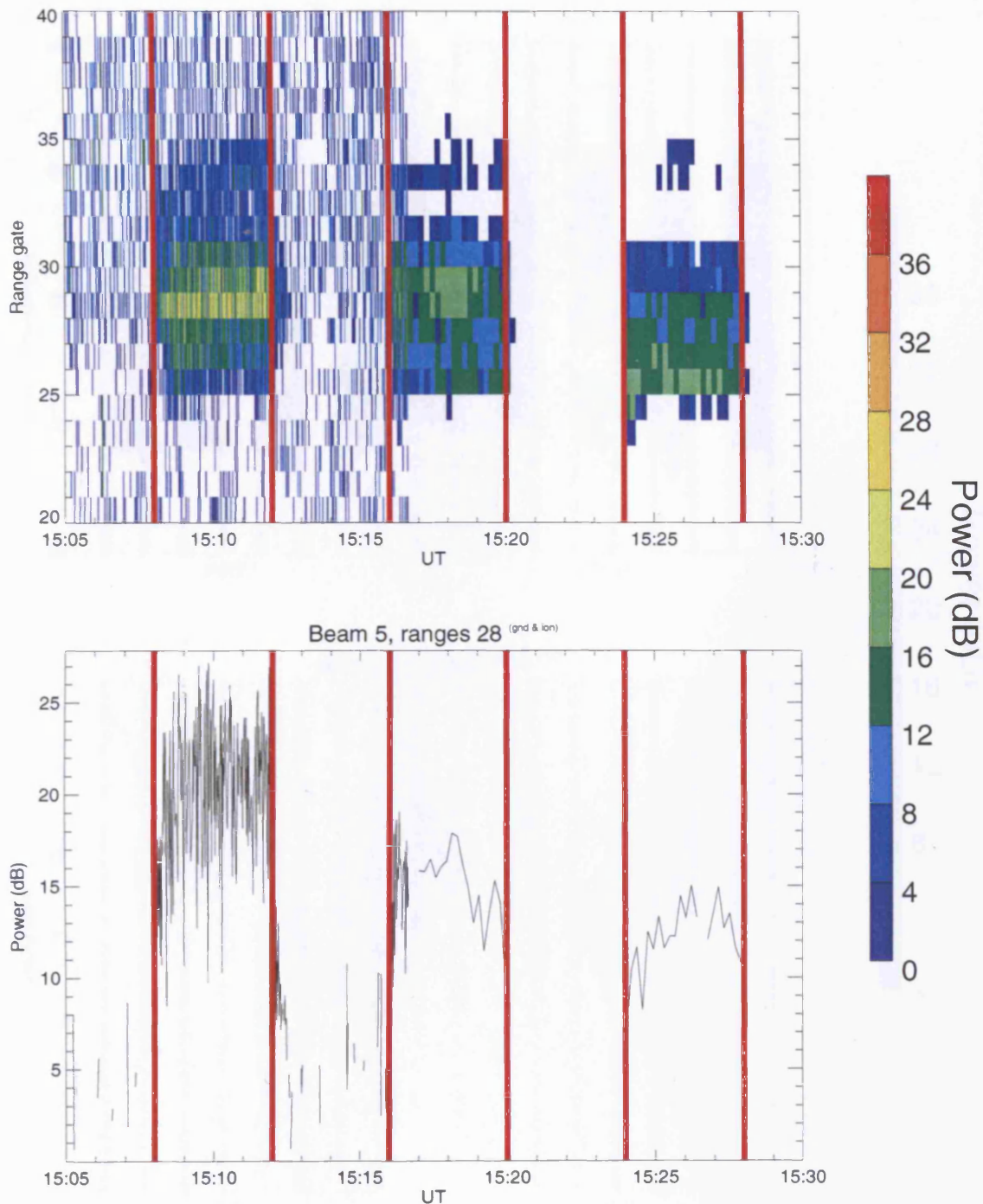


Figure 7.11(a): This figure and the next two figures show data intervals from which the backscatter power decays and ACF decorrelations were taken.

SUPERDARN PARAMETER PLOT

20 Oct 1999 ⁽²⁹³⁾

Hankasalmi: pwr_l

normal (ccw) scan mode (150)

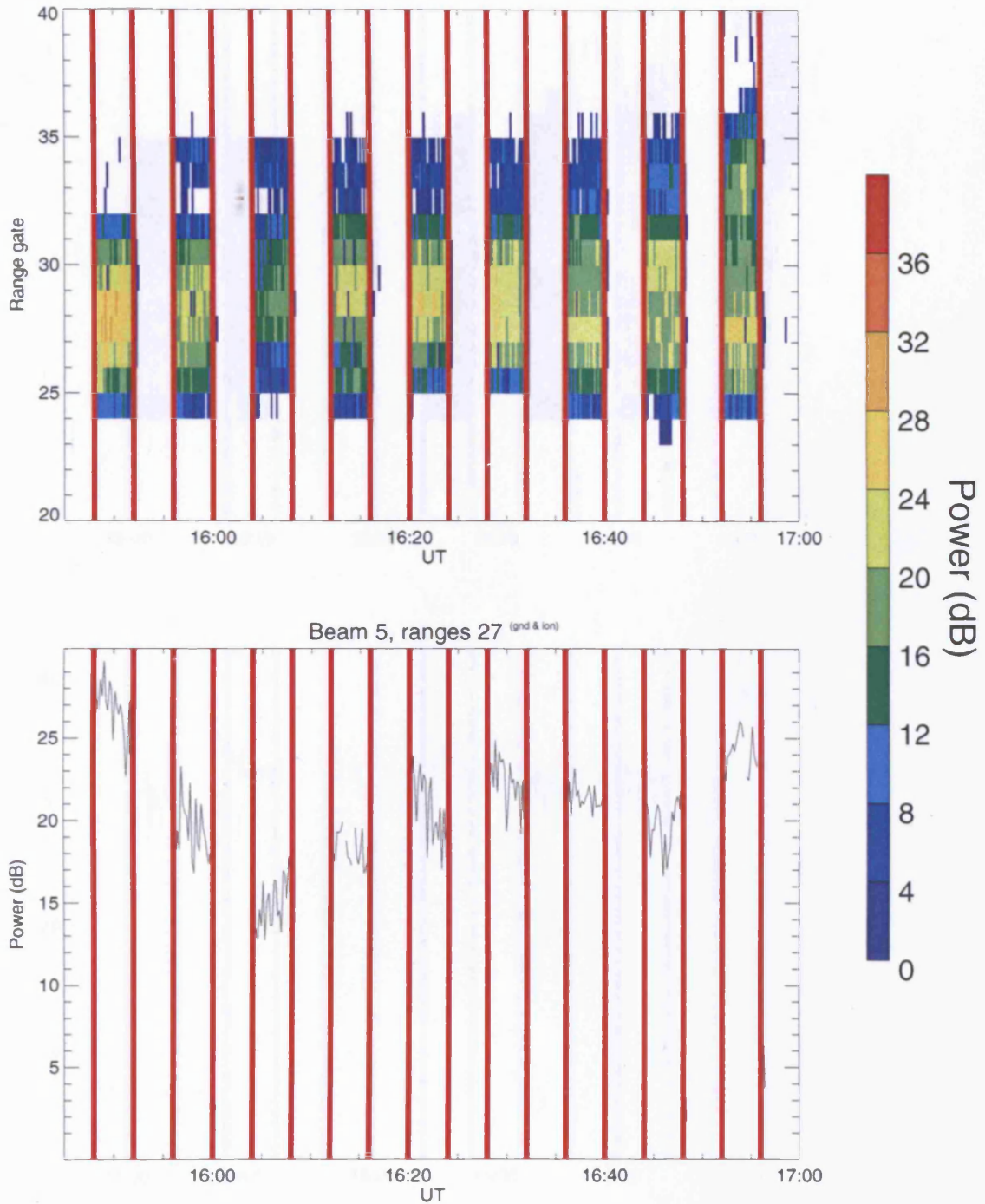


Figure 7.11(b): A data interval from which the backscatter power decays and ACF decorrelations were taken.

SUPERDARN PARAMETER PLOT

21 Oct 1999 ⁽²⁹⁴⁾

Hankasalmi: pwr_l

unknown scan mode (-6318)

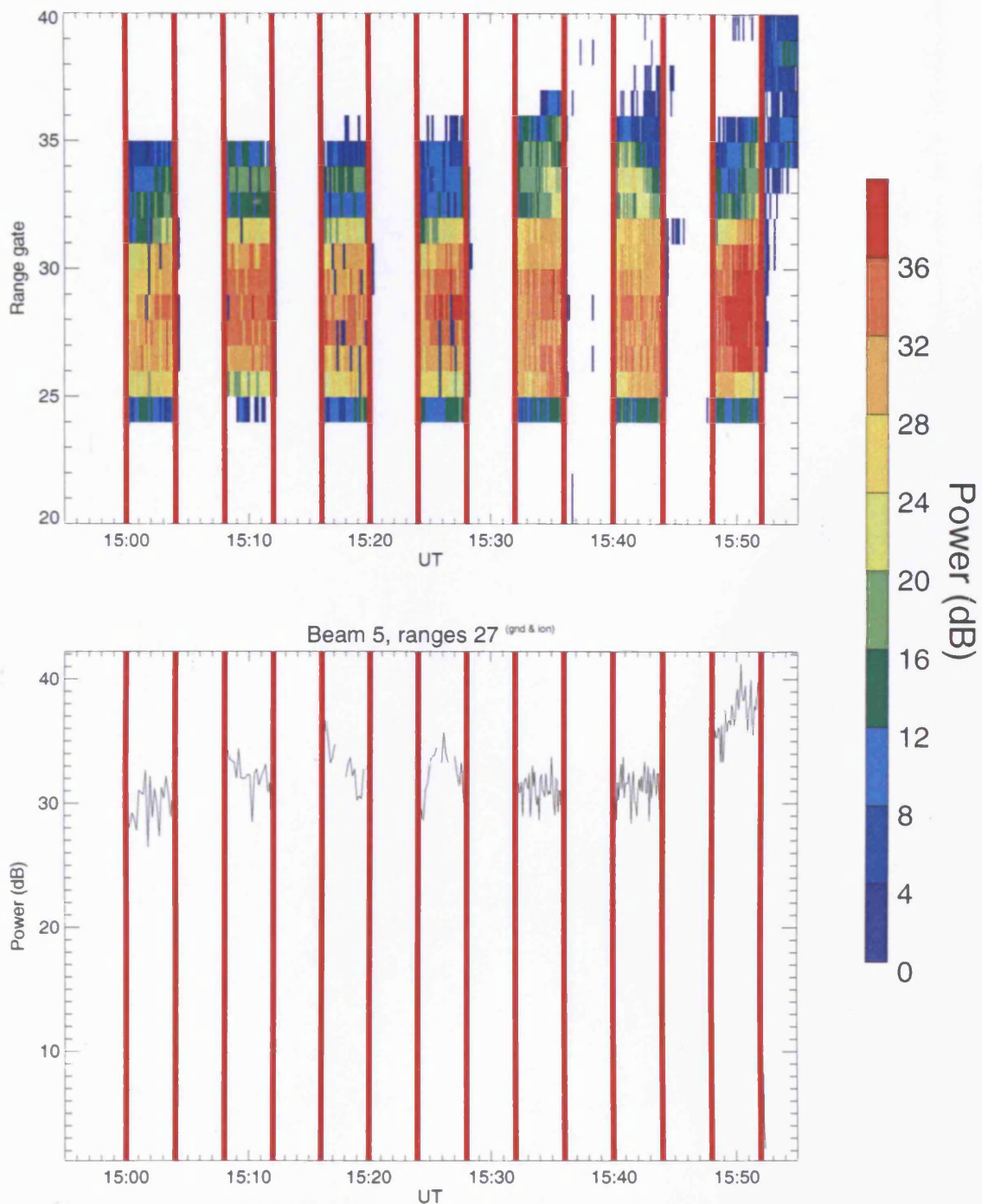


Figure 7.11(c): A data interval from which the backscatter power decays and ACF decorrelations were taken.

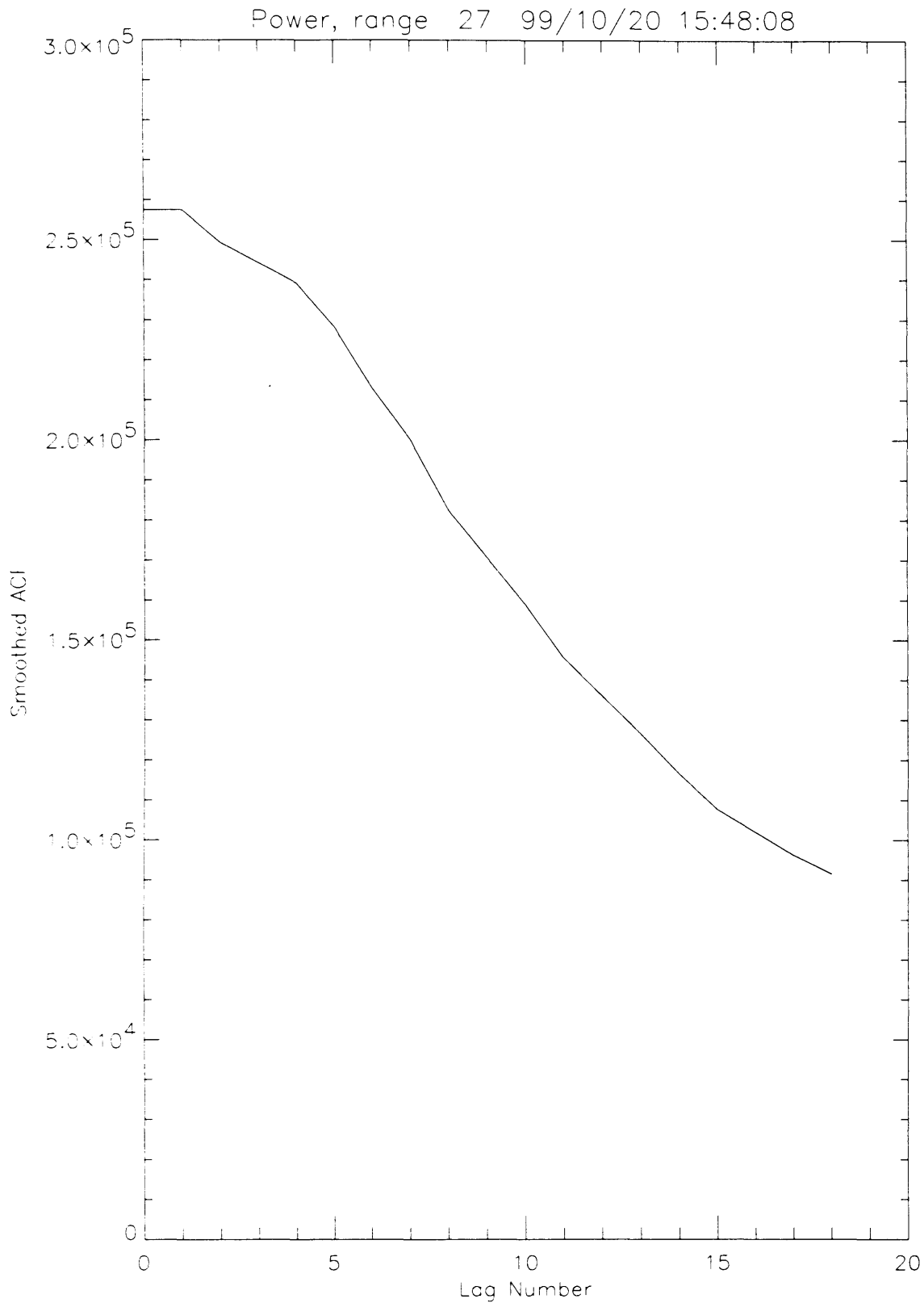


Figure 7.12(a): This and the following two figures show example averaged ACF moduli that were used to calculate the ACF decorrelation times. A lag time of 24000 μ s was used for this calculation.

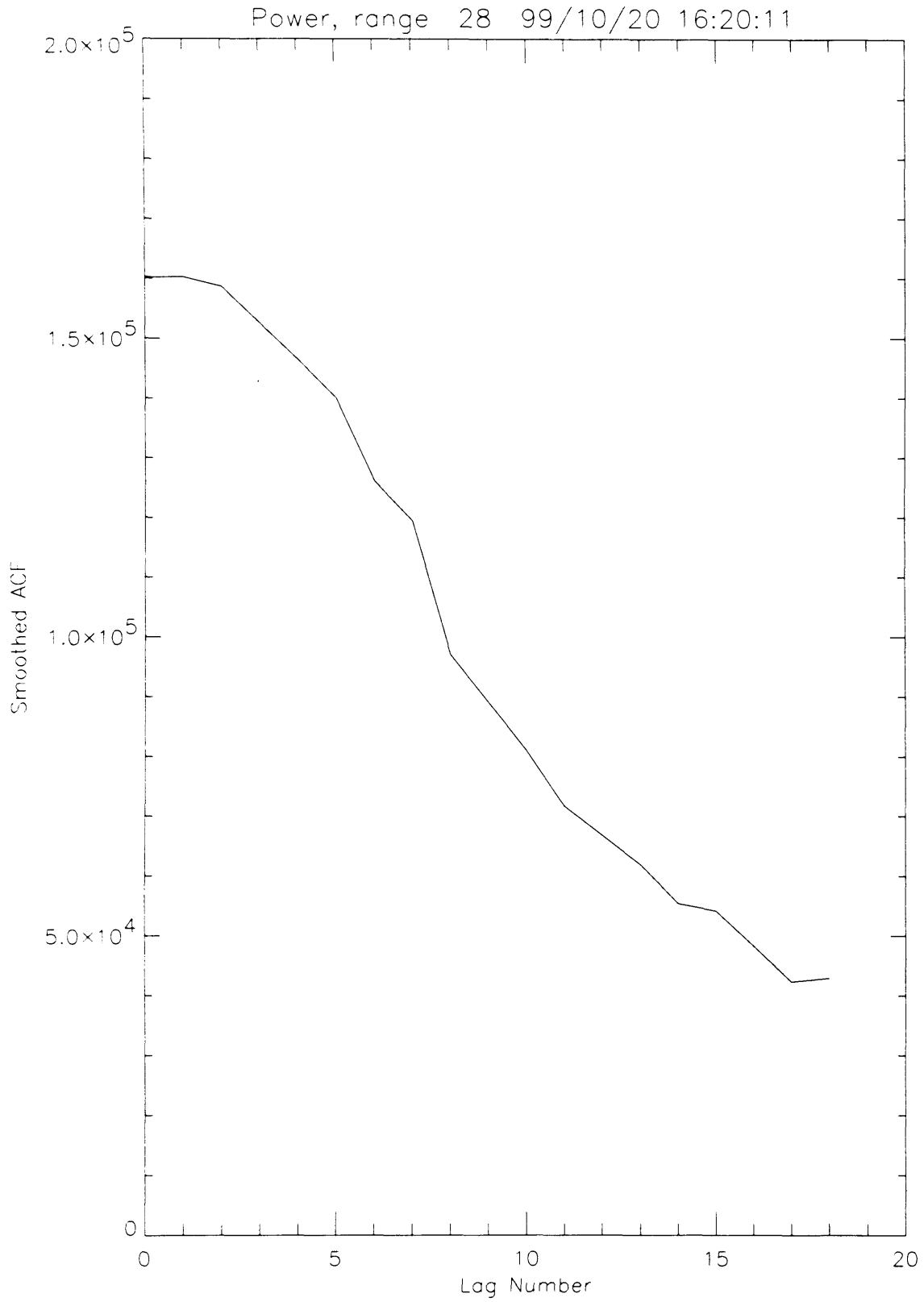


Figure 7.12(b): An example of an averaged ACF modulus that was used to calculate the ACF decorrelation times. A lag time of 24000 μs was used for this calculation.

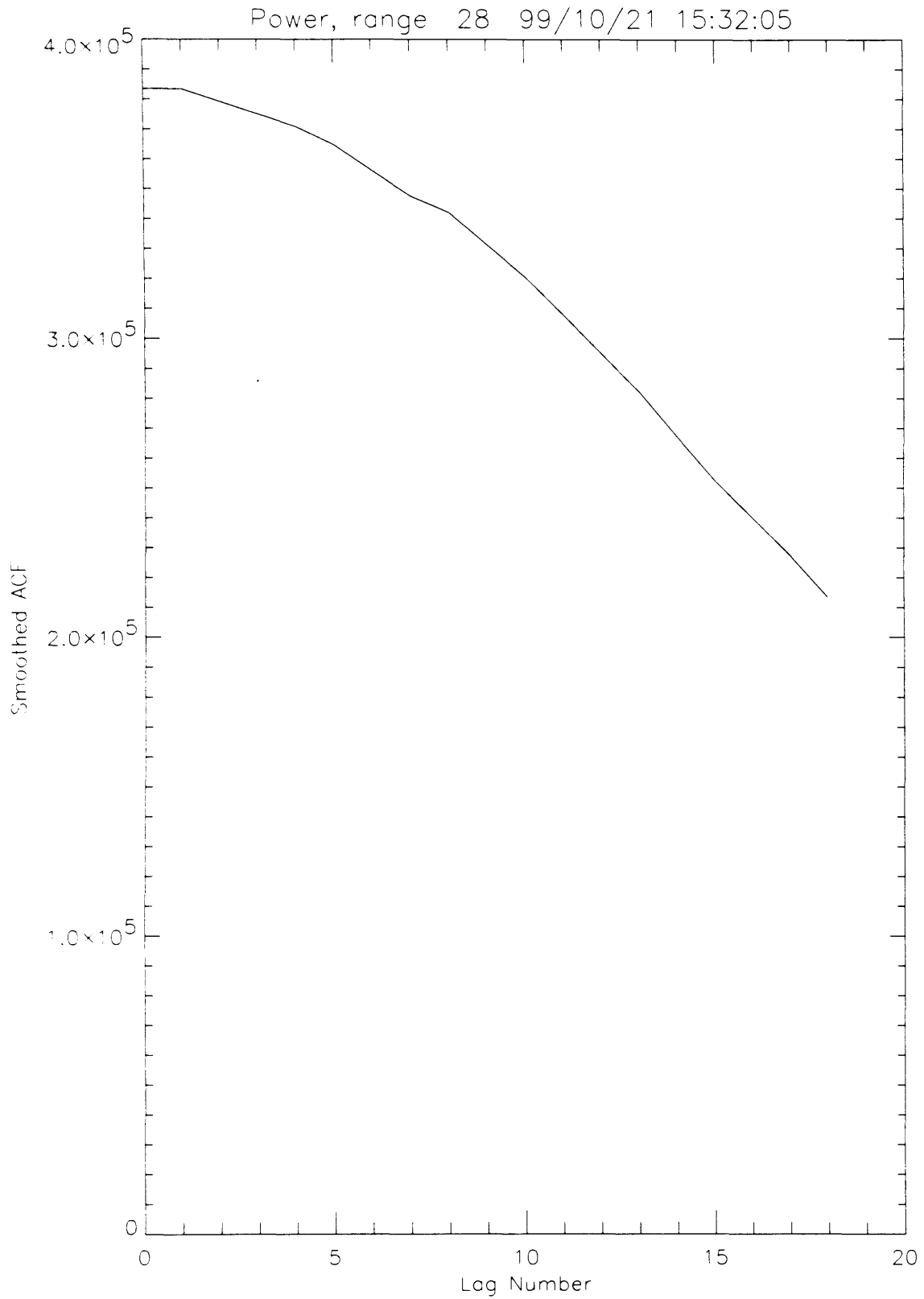


Figure 7.12(c): An example of an averaged ACF modulus that was used to calculate the ACF decorrelation times. A lag time of 12000 μ s was used in the calculation.

Therefore, this procedure replicated the action of the fitting software. The results of the fitting are shown in table 7.4. Mode A refers to a 12000 μs lag separation and mode B refers to a 24000 μs lag separation.

Decay Constant Type	Mode A constant, s^{-1}	Mode B constant, s^{-1}
γ_e	3.25 ± 0.63	2.51 ± 0.59
σ_g	3.76 ± 0.22	2.29 ± 0.30

Table 7.4: ACF decorrelation time constants for the longer lag heater mode

Using the data from the October 1999 campaign, the ACF decorrelation times for the longer-lag mode were compared to the irregularity backscatter decay times after heater switch-off. There are two reasons why the sampled distribution may change: some physical process may occur that alters the wavelength of the set of irregularities, thus making them invisible and causing others to become visible, or there may be little eddies in the velocity field that cause the positions to change. These two cases are indistinguishable from one another and both cause a decorrelation of the ACF. Figure 7.13 shows the time constants obtained from all the instances where the longer-lag mode was run. The irregularity decay constant, γ_b , was plotted against the time constants corresponding to the Gaussian ACF decorrelation, σ_g , and the exponential ACF decorrelation, γ_e . The discrepancy in values may in part be explained by considering the resolution of the data: the ACF lag time has units of the order of 10000 μs , i.e. 10 ms, which is a much higher resolution than that of the backscatter decay. In summary, the values of the ACF decorrelation and backscatter decay time constants differed by a factor of 10.

7.5.6 F-Region Plasma Treated as a Turbulent Fluid

The theoretical background to turbulent fluid flow was provided in section 2.9 of chapter 2, where the significance of the ACF in the calculation of turbulence characteristics was described. As reported by Villain et al. (1996), ACFs may usually be divided into three categories: those with an exponential decay profile, those with a Gaussian decay profile and a composite type that is a mixture of the two. The exponential type corresponds to the case where the observation wavelength of the radar is much larger than the correlation length of the turbulent motion. This is similar to a random walk distribution. The Gaussian type corresponds to the wavelength being very small compared to the correlation length. In this

SUPERDARN PARAMETER PLOT

Characteristic decay constants

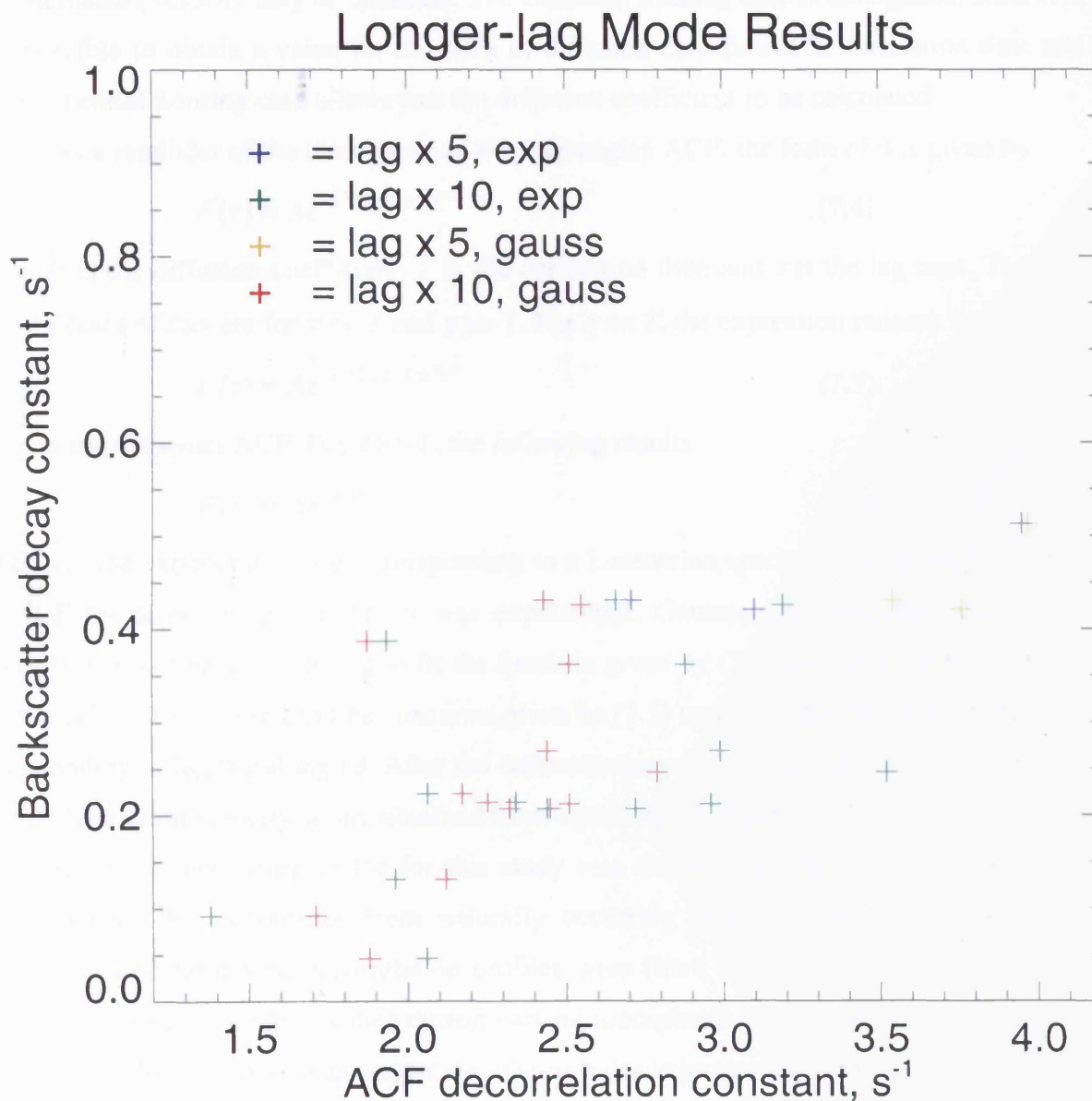


Figure 7.13: The backscatter decay and ACF decorrelation time constants obtained for the data where the longer-lag mode was running.

case the velocity distribution of the plasma is being sampled. The third, and most useful, case corresponds to the situation where the observation wavelength is of the order of the correlation length.

Figure 7.14 shows an example of a composite ACF: at first with a Gaussian decay profile, passing through a transition time and then having an exponential profile. Fitting a Lagrangian ACF, as described in chapter 2, to the decay profile would allow the immediate determination of a diffusion coefficient and correlation time. From these a correlation length and fluctuation velocity may be obtained. The Gaussian limiting case is ambiguous, since it is only possible to obtain a value for the ratio of diffusion coefficient to correlation time and the exponential limiting case allows just the diffusion coefficient to be calculated.

As a reminder of the theory behind the Lagrangian ACF, the form of it is given by

$$F(\tau) = Ae^{-k^2DT(\tau/T + e^{-\tau/T} - 1)} \quad (7.4)$$

where D is the diffusion coefficient, T is the correlation time and τ is the lag time. The two limiting cases of this are for $\tau \ll T$ and $\tau \gg T$. For $\tau \ll T$, the expression reduces to

$$F(\tau) = Ae^{-(1/2)(D/T)k^2\tau^2} \quad (7.5)$$

which is the Gaussian ACF. For $\tau \gg T$, the following results

$$F(\tau) = Ae^{-k^2D\tau} \quad (7.6)$$

and this is the exponential case corresponding to a Lorentzian spectrum. An attempt to fit to the ACF by determining whether it was exponential, Gaussian or composite was made. However, it was found that trying to fit the function given by (7.4) proved to be too difficult and it was better to fit the limiting functions given by (7.5) and (7.6), for the parts of the ACF corresponding to lag 0 and lag 18. After the determination of D and T , the correlation time, L , and the fluctuation velocity, u , are obtained from equations (2.76) and (2.77).

A strong motivating factor for this study was the work conducted by Villain et al. (1996), where the backscatter from naturally occurring FAIs was examined. Gaussian, exponential and composite decorrelation profiles were fitted to nearly 9000 ACFs obtained for naturally occurring irregularities during varying ionospheric conditions. It was hoped that this study would also provide an insight into the turbulence properties of the ionosphere.

Figures 7.15(a) and 7.15(b) show the results of fitting turbulence parameters for the data. Figure 7.15(a) shows the diffusion coefficient and correlation time. The vertical line in the upper plot corresponds to the study by Villain et al. The vertical line in the lower plot shows the maximum correlation time in the Villain study. This is a tenth of that in this study and arises because the SHERPA radar from which the results were taken ran a mode with the

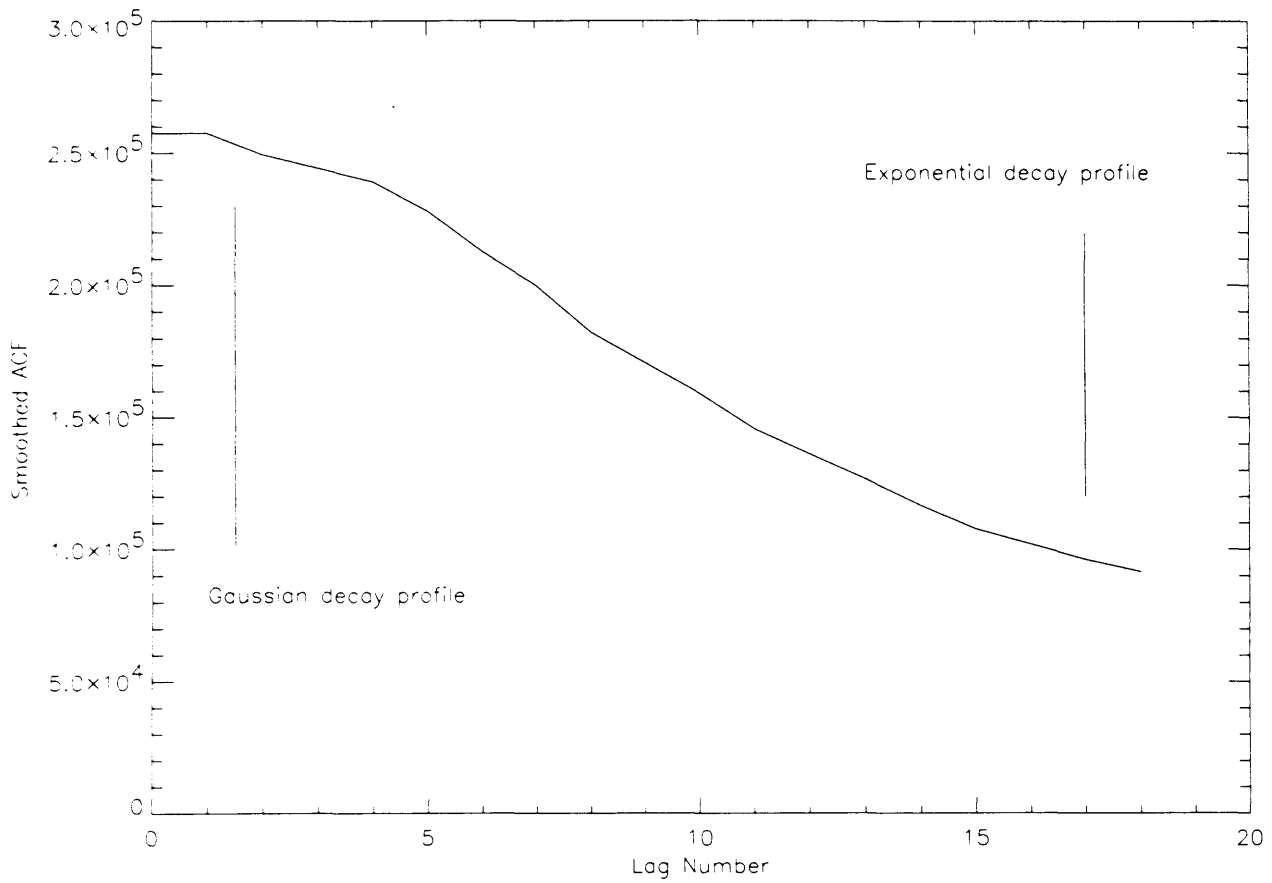


Figure 7.14: The type of composite ACF, first considered by Villain et al. (1996), from which turbulence characteristics were calculated. The change in decay profile occurs because the size of the sampling volume increases and the radar no longer samples a correlated fluctuation, but instead samples many irregularities, thus leading to a random walk distribution.

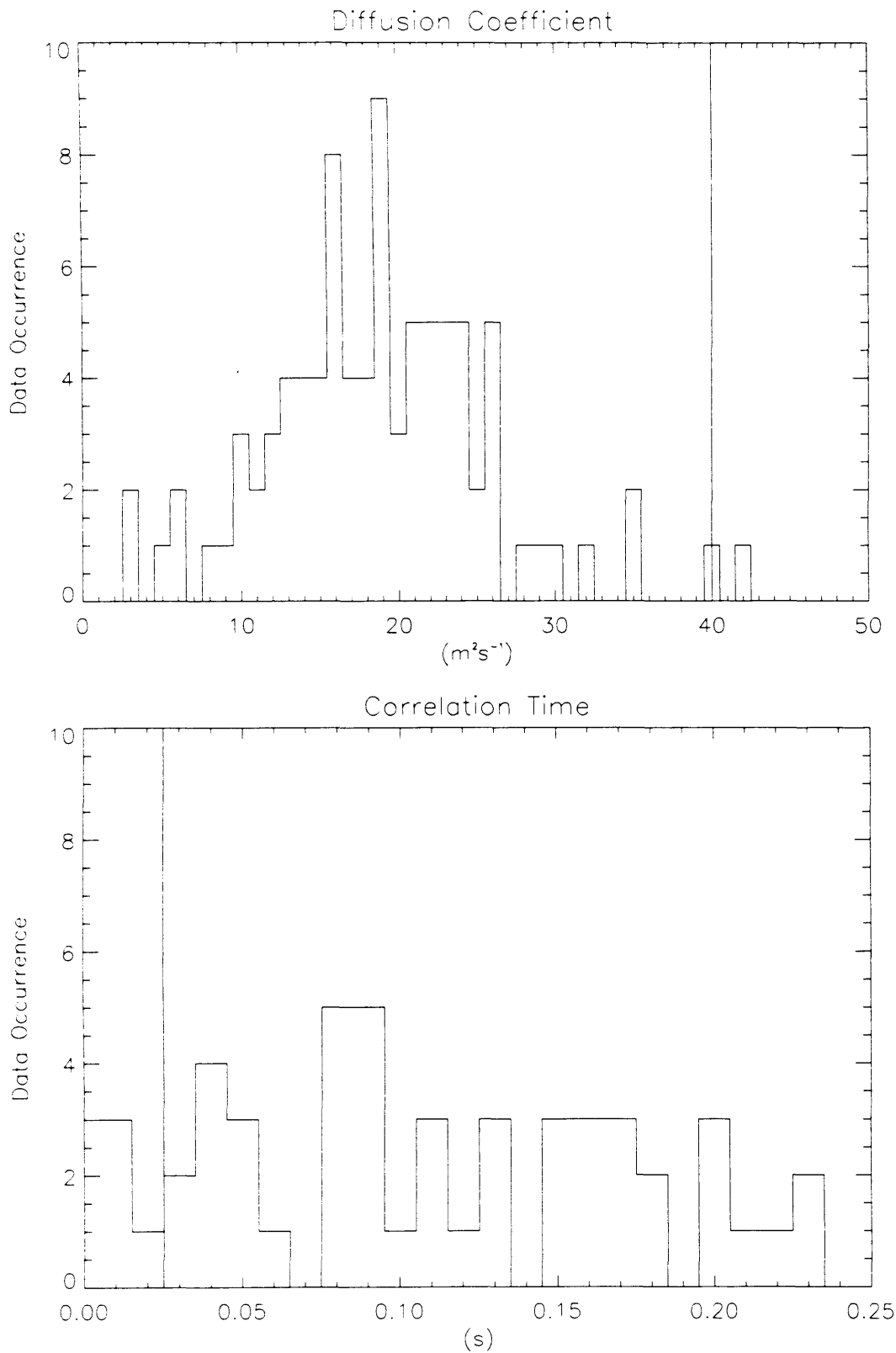


Figure 7.15(a): The diffusion coefficient and correlation time for the artificial irregularity distribution. The vertical lines are comparison with the study performed by Villain (1996). This distribution was obtained for all data where the heater was operating using the longer lag times, i.e. both 12000 and 24000 μ s lag times.

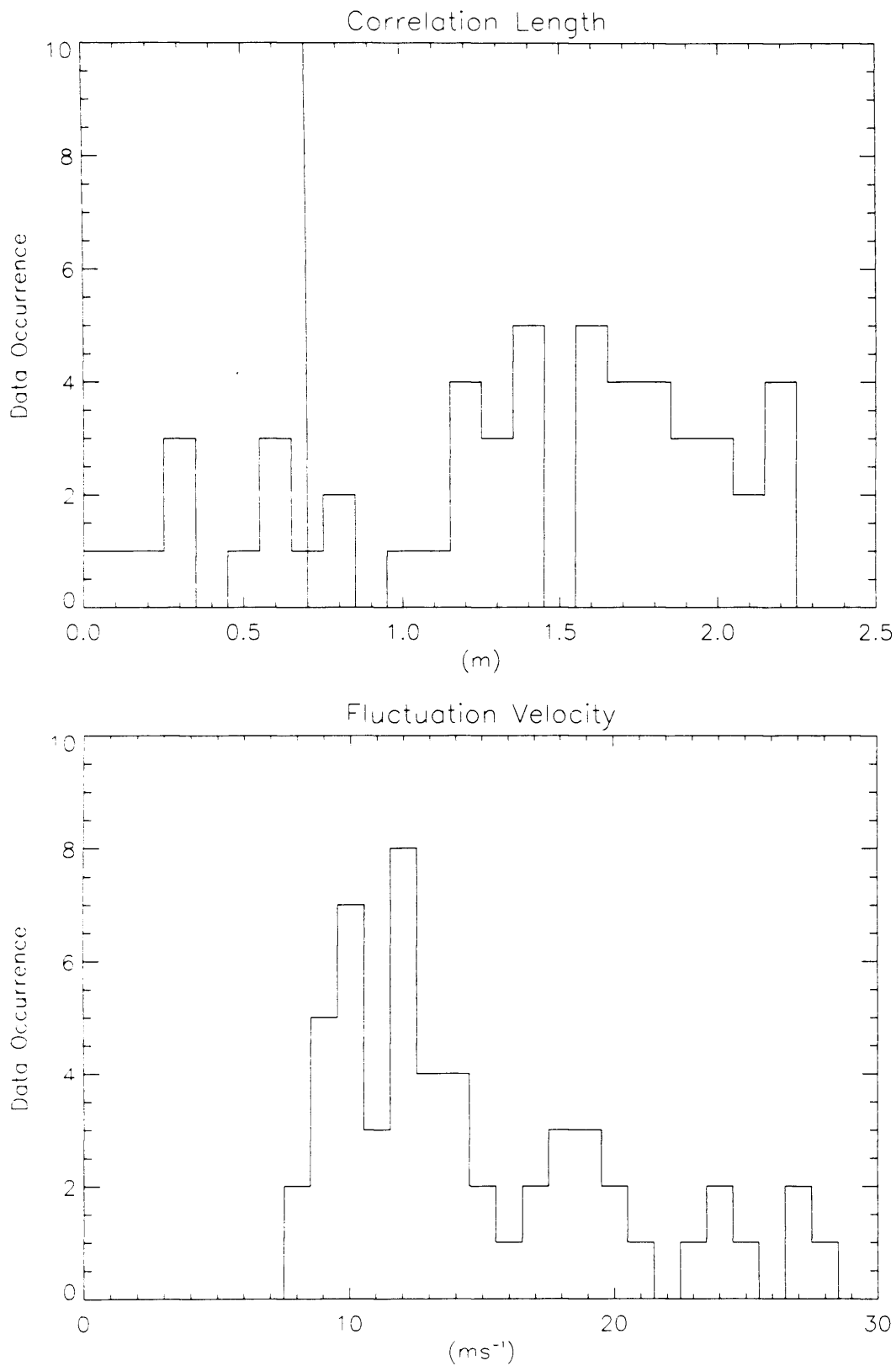


Figure 7.15(b): The correlation length and fluctuation velocity for the artificial irregularity distribution. The vertical line present for the correlation time is again a comparison with the study performed by Villain (1996). This distribution was obtained for all data where the heater was operating using the longer lag times, i.e. both 12000 and 24000 μs lag times.

same lag separation as CUTLASS. Figure 7.15(b) shows the correlation length and turbulence fluctuation velocity. The vertical line is again a comparison with the study by Villain. The data were obtained from averaged ACFs for all the range gates in which backscatter from artificially generated backscatter was detected. The most data were obtained for the diffusion coefficient, since a value for this could be obtained for the composite and exponential cases. If a composite ACF could be fitted, then the correlation time could be obtained. Therefore, the amount of data for the correlation time, correlation length and fluctuation velocity, where these latter two quantities could be calculated from the correlation time, was the same.

The upper panel of figure 7.15(a) shows the diffusion coefficient. It has the overall form of a Gaussian distribution with a mean of $18 \text{ m}^2 \text{ s}^{-1}$. The correlation time, shown in the lower panel of the same figure, is more evenly distributed over the time range for which it was calculated. The correlation length, shown in the upper panel of figure 7.16(b), has more of an even distribution, as for the correlation time. The fluctuation velocity, shown in the lower panel of figure 7.15(b), has a maximum of around 11 m s^{-1} .

The values for the turbulence characteristics for artificially generated backscatter, shown in figures 7.15(a) and 7.15(b), were distinctively different to those corresponding to naturally occurring backscatter, calculated by Villain et al. The diffusion coefficient was smaller and the correlation length was longer. These factors point towards the irregularity distribution for artificially generated backscatter diffusing less quickly than the distribution corresponding to naturally occurring backscatter. The higher value for the correlation length suggests that artificially generated FAIs are more spatially correlated, i.e. the region where the plasma velocity variations are similar is larger. Also, the correlation time spanned a greater range for the longer lag mode. It should also be noted that the study by Villain et al. took into account a wide variety of ACFs in both the E-region and the F-region. This is in contrast to this study, which only included F-region backscatter ACFs from artificially generated irregularities recorded by CUTLASS Finland when the longer-lag mode was running.

7.6 Summary

Effects associated with the observation of artificial FAIs were presented in this chapter. The first section covered spatial sweeping and its effects. This demonstrated that the duration of the excitation of a particular area is closely related to the backscatter power that is

observed. The effects of seeding the ionosphere were also considered, and it was found that the amplitude of the backscatter power after seeding had been done were higher than for the cases without seeding.

The latter part described a new longer-lag heating mode. This was used to compare ACF decorrelation times to irregularity decay times. Also, turbulence characteristics corresponding to artificially generated FAIs were obtained. It was found that the characteristics for artificially generated instabilities were consistent with a more static irregularity distribution.

Chapter 8

Conclusions and Future Work

8.1 Introduction

Observations of radar backscatter from different types of irregularity population have been examined. Backscatter from the near ranges of CUTLASS, from which D-region and E-region irregularities acted as targets, were classified in order to determine whether observations of the EPCI, a relatively recently proposed instability mechanism that should create irregularities in the D-region, had been made. The entire myopic data set was examined and intervals of strong low-altitude scatter were highlighted and then examined to determine the backscatter characteristics, i.e. the backscatter power, the spectral width and the Doppler velocity. The altitude dependence of the scatter was obtained by the CUTLASS interferometer. The threshold velocities and growth rates for the EPCI were also investigated, together with a possible mechanism that could contribute to the anomalous electron collision frequency.

In addition to the low-altitude scatter, observations were made of backscatter from artificially generated FAIs in the F-region, created by ionospheric modification undertaken by the heating facility at Tromsø, Norway. The observations were made by the CUTLASS Finland radar as this was located closer to the target region than CUTLASS Iceland. Data from three experimental campaigns were examined, with the decay profiles of the backscatter power having the most prominence. Properties associated with ACFs obtained when the ionosphere was being modified were also examined and turbulence characteristics relating to treating the F-region plasma as a turbulent fluid were obtained.

8.2 Present Work Undertaken in this Thesis

8.2.1 Modelling Instability Characteristics and Anomalous Diffusion

Dimant and Sudan (1995a, 1995b, 1995c, 1997) proposed the existence of a new D-region instability mechanism associated with the electron Pedersen conductivity and the instability was termed the electron Pedersen conductivity instability (EPCI) by Robinson (1998). This instability was presented as an augmented form of the generally accepted theory

of irregularity generation in the E-region and was postulated to create long-wavelength irregularities in the D-region that are excited most favourably in the bisector direction between the convection electric field and the relative electron-ion drift velocity direction.

The work presented in chapter 5 included a study of the growth rates and threshold velocities of the EPCI. These instability characteristics were investigated for a fluid regime and a kinetic regime, and for different flow velocities, flow angles and aspect angles. The EPCI is proposed to be excited most easily for flow angles of -45° , and this was confirmed by the modelling that was undertaken.

Also considered in chapter 5 were the electron diffusion characteristics resulting from the interaction between electrostatic waves. The case for two waves led to modelled particle trajectories that led to diffusion of the electrons. This diffusion was then related to an anomalous electron collision frequency, but the calculated value was much smaller than that which corresponds to observations of E-region irregularities whose phase velocities saturate at the ion-acoustic speed.

8.2.2 D-region Radar Echoes

The work in this thesis on near-range echoes consisted of comparing the E-region echo characteristics, whose properties are well known, to those of D-region echoes in order to determine similarities and differences between them. After suitable data intervals had been isolated and the associated echo types examined, two case studies were undertaken using the most promising intervals of data.

Type I and Type II echoes, associated with the Farley-Buneman and gradient-drift instabilities, were observed frequently in the E-region. These included echo types concentrated around a small velocity range that had spectral widths that were as large as 500 m s^{-1} . The D-region echoes had spectral widths around 100 m s^{-1} , although very low spectral widths were also observed and these were discounted as being caused by meteor scatter or a mechanism associated with optical auroral forms.

The data from the case studies, including the range from the radar of CUTLASS scatter, together with the line-of-sight velocity values, were consistent with the observation of the EPCI. Also, the presence of definite layers in altitude where echo signatures were localised presented further evidence that the EPCI had been observed. It was found that the altitudes at which scatter was observed most frequently agreed with those predicted by theory. STARE data were also examined in order to see how the radar echoes differed from

those measured by CUTLASS. The echoes disappeared when the E-region Type I echo velocity observed by CUTLASS fell substantially below the ion-acoustic speed. This is consistent with weakening electrojet flow such that the relative electron-ion drift speed falls below the threshold value for the EPCI and then the FBI. This signature was accompanied by the fall in spectral width from values around 100 m s^{-1} to values consistent with meteor scatter.

8.2.3 F-region Radar Echoes

The effects of varying the heater power incident on a particular region of the ionosphere were examined. The variation of the heater power was undertaken by spatially sweeping a beam of constant power, thus resulting in varying illumination times of the ionosphere, and also by maintaining a constant direction and altering the amount of power beamed into the ionosphere. EISCAT data were obtained in order to determine how the heating affected the electron temperatures measured in the F-region. It was found that, as expected, the different illumination times resulted in variations in the backscatter recorded by CUTLASS. The electron temperature was also seen to depend on the duration of illumination, a quickly swept beam was less effective at raising the temperature than a beam swept more slowly. The heater beam intensity for varying tilt angles was modelled and the backscatter power variation over ranges gates detected by CUTLASS was found to be consistent with the expected effects achieved by tilting the heater beam. The highest backscatter powers were found to occur in the field-aligned direction. The experiments involving changing the power beamed into the ionosphere confirmed that the heater power needed to maintain irregularities was lower if the ionosphere had been preconditioned by heating at 100% power beforehand.

The irregularity distribution that was sampled by CUTLASS during modification experiments was examined by comparing the results of the normal-lag mode that had been run previously for all heating experiments with a new longer-lag mode that was run during the October 1999 experimental campaign. It was found that the new longer-lag mode allowed the value of the spectral width, usually very low for heating data, to be calculated with more accuracy. The ACF decorrelation time constants, from which the spectral width values were obtained, were compared to the backscatter power decay time constants. By the irregularity dissipation theorem, these time constants should have been comparable, but it was found that they differed by about a factor of ten. Treating the F-region plasma as a turbulent fluid

allowed turbulence characteristics to be calculated from the decorrelation rate of the ACF. The diffusion coefficient obtained from this analysis was found to be about half the value of that obtained by Villain et al. (1996) in their study of the ACFs from naturally occurring irregularities. Also, the average value of the correlation length was found to be about twice that for the natural irregularities. These calculations were consistent with the distribution of the artificial irregularities remaining spatially correlated for time scales longer than the distribution of naturally occurring irregularities.

8.3 Future Work

8.3.1 Possible Observations of the EPCI

The study of lower-altitude radar echoes in order to determine whether the EPCI had been observed would have been augmented greatly if measurements of the convection electric field had been available. The threshold values of the relative electron-ion drift speed were given in chapter 2 and this drift, which is effectively the $E \times B$ drift in the E-region, is directly related to the electric field. Measuring the electric field would have determined whether it was sufficiently strong to excite the instability and, if so, would have given added weight to the assumption that the EPCI was operating. An important area in which future work may be conducted is the measurement of the electric field together with lower-altitude radar echoes. Although the FAST satellite collected electric field data, its observations were not coincident with the area that was being observed by CUTLASS. The DMSP satellites did pass through the correct area during the interval that formed the first case study, but because of the time of year the concentration of heavy ions was not high enough to allow the retarding potential analyser to obtain reliable results. Also, the EISCAT system, which is usually a valuable tool for providing details of the background ionospheric conditions, was inoperative when the myopic data were collected.

8.3.2 Artificially Generated FAIs

The ACFs obtained from artificial FAIs corresponded mainly to the regions contained well within the heated patch and hence were obtained from regions where instability excitation was most efficient. The extremities of the heated patch, where the corresponding backscatter power is lower, are regions where there may be a mixture of ACFs that

correspond to the more usually observed types from artificial irregularities together with types that may resemble more closely those that correspond to natural irregularities. Hence an examination of properties at the extremities of the heated patch would provide more information regarding the nature of the irregularities there.

The variable and increasing level of backscatter power observed for the 1-second sweeps may indicate a gradual onset of irregularities and this could be assessed by examining the backscatter power for repeated 1-second sweeps.

There is also scope for study regarding events that were not presented in this thesis. For example, observations exist where a region of natural backscatter migrated towards the heated patch and provided an interface between natural and artificial irregularities. The approach of the natural backscatter region definitely affected the heated patch. The identification of such interfaces between naturally occurring and artificially generated irregularities should provide an area where the plasma properties and irregularity distributions change from one type to the other and would provide an excellent opportunity to investigate the differences between natural and artificial irregularities.

References

- André D., G. J. Sofko, K. B. Baker and J. MacDougall**, SuperDARN interferometry: Meteor echoes and electron densities from groundscatter, *J. Geophys. Res.*, **103**, 7003, 1998
- André R., M. Pinnock and A. S. Rodger**, Identification of the low-altitude cusp by Super Dual Auroral Radar Network radars: A physical explanation for the empirically derived signature, *J. Geophys. Res.*, **105**, 27081, 2000
- Baker K. B., R. A. Greenwald, J.-P. Villain and S. Wing**, Spectral characteristics of high frequency (HF) backscatter from high latitude ionospheric irregularities: Preliminary analysis of statistical properties, Report to Rome Air Development Centre, EEP, Hanscomb AFB, 1986
- Baker K. B., J. R. Dudeney, R. A. Greenwald, M. Pinnock, P. T. Newell, A. S. Rodger. N. Mattin and C.-I. Meng**, HF radar signatures of the cusp and low-altitude boundary layer, *J. Geophys. Res.*, **100**, 7671, 1995
- Baumjohann W. and R. A. Treumann**, Basic Space Plasma Physics, Imperial College Press, 1997a
- Baumjohann W. and R. A. Treumann**, Advanced Space Plasma Physics, Imperial College Press, 1997b
- Belenov A. F., V. A. Bubnov, L. M. Erukhimov, Y. V. Kiselev, G. P. Komrakov, E. E. Mityakova, L. N. Rubstov, V. P. Uryadov, V. L. Frolov, Y. V. Chagnuov and B. V. Ykhmatov**, Parameters of artificial small-scale ionospheric irregularities, *Radiophys. Quantum Electron. Engl. Transl.*, **20**, 1240, 1977
- Bering E. A.**, Apparent electrostatic ion cyclotron waves in the diffuse aurora, *Geophys. Res. Lett.*, **10**, 647, 1983
- Bernhardt P. A., L. M. Duncan and C. A. Tepley**, Heater-induced cavities as optical tracers of plasma drifts, *J. Geophys. Res.*, **94**, 7003, 1989
- Blix T. A., E. V. Thrane and Ø. Andreassen**, In situ measurements of the fine-scale structure and turbulence in the mesosphere and lower thermosphere by means of electrostatic positive ion probes, *J. Geophys. Res.*, **95**, 5533, 1990
- Blix T. A., E. V. Thrane, S. Kirkwood, Y. S. Dimant and R. N. Sudan**, Experimental evidence for unstable waves in the lower E/upper D-region excited near the bisector between the electric field and the drift velocity, *Geophys. Res. Lett.*, **23**, 2137, 1996
- Bond G. E.**, The interaction of radio waves with the auroral ionosphere, PhD. Thesis, Univ. of Leicester, 1997

- Bond G. E., T. R. Robinson, P. Eglitis, D. M. Wright, A. J. Stocker, M. T. Rietveld and T. B. Jones**, Spatial observations by the CUTLASS coherent scatter radar of ionospheric modification by high power radio waves, *Ann. Geophys.*, **15**, 1412, 1997
- Booker H. G., C. W. Gartlein and B. Nichols**, Interpretation of radio reflections from the aurora, *J. Geophys. Res.*, **60**, 1, 1955
- Booker H. G.**, A theory of scattering by non-isotropic irregularities with application to radar reflections from the aurora, *J. Atmos. Terr. Phys.*, **8**, 204, 1956
- Bowles K. L., R. Cohen, G. R. Ochs and B. B. Balsley**, Radar echoes from field-aligned ionisation above the magnetic equator and their resemblance to auroral echoes, *J. Geophys. Res.*, **65**, 1853, 1960
- Bowles K. L., B. B. Balsley and R. Cohen**, Field aligned irregularities identified with acoustic plasma waves, *J. Geophys. Res.*, **68**, 2485, 1963
- Buneman O.**, Excitation of field aligned sound waves by electron streams, *Phys. Rev Lett.*, **10**, 285, 1963
- Cahill L. J. jr., R. A. Greenwald and E. Nielsen**, Auroral radar and rocket doubleprobe observations of electric fields across the Harang discontinuity, *Geophys. Res. Lett.*, **5**, 687, 1978
- Carpenter G. B.**, VHF and UHF bistatic observations of a region of the ionosphere modified by a high power radio transmitter, *Radio Science*, **9**, 965, 1974
- Chen F. F.**, *Introduction to Plasma Physics*, Plenum, 1974
- Cohen R. and J. D. Whitehead**, Radio-reflectivity detection of artificial modification of the ionospheric F layer, *J. Geophys. Res.*, **75**, 6439, 1970
- Coster A. J., F. T. Djuth, R. J. Jost and W. E. Gordon**, The temporal evolution of 3-m striations in the modified ionosphere, *J. Geophys. Res.*, **90**, 2807, 1985
- Cragin B. L. and J. A. Fejer**, Generation of large-scale field-aligned irregularities in ionospheric modification experiments, *Radio Science*, **9**, 1071, 1974
- Das A. C. and J. A. Fejer**, Resonance instability of small-scale field-aligned irregularities, *J. Geophys. Res.*, **84**, 6701, 1979
- Davies K.**, *Ionospheric Radio*, Pregrinus, 1990
- Davies J. A. and T. R. Robinson**, Heating of the high-latitude ionospheric plasma by electric fields, *Adv. Space Res.*, **20**, 1125, 1997
- Dimant Y. S. and R. N. Sudan**, Kinetic theory of low-frequency cross-field instability in a weakly ionised plasma I, *Phys. Plasmas*, **2**, 1157, 1995a

- Dimant Y. S. and R. N. Sudan**, Kinetic theory of low-frequency cross-field instability in a weakly ionised plasma II, *Phys. Plasmas*, **2**, 1169, 1995b
- Dimant Y. S. and R. N. Sudan**, Kinetic theory of the Farley-Buneman instability in the E-region of the ionosphere, *J. Geophys. Res.*, **100**, 14605, 1995c
- Dimant Y. S. and R. N. Sudan**, Physical nature of a new cross-field current-driven instability in the lower ionosphere, *J. Geophys. Res.*, **102**, 2551, 1997
- Djuth F. T., C. A. Gonzales and H. M. Ierikic**, Temporal evolution of the HF-enhanced plasma line in the Arecibo F-region, *J. Geophys. Res.*, **91**, 12089, 1986
- Duncan L. M. and J. P. Sheerin**, High-resolution studies of the HF ionospheric modification interaction region, *J. Geophys. Res.*, **90**, 8371, 1985
- Dungey J. W.**, Interplanetary magnetic fields and the auroral zones, *Phys. Rev. Lett.*, **6**, 47, 1961
- Dysthe K. B., E. Mjølhus, H. L. Pécseli and K. Rypdal**, A thermal oscillating two-stream instability, *Phys. Fluids*, **26**, 146, 1983
- Eglitis P.**, Radar studies of small-scale E-region plasma irregularities, PhD. Thesis, Univ. of Leicester, 1994
- Eglitis P., T. R. Robinson, M. T. Rietveld, D. M. Wright and G. E. Bond**, The phase speed of artificial field-aligned irregularities observed by CUTLASS during HF modification of the auroral ionosphere, *J. Geophys. Res.*, **103**, 2253, 1998
- Evans J.**, Theory and practice of ionosphere study by Thomson scatter radar, *Proc. IEEE* **57**, 496, 1969
- Farley D. T.**, A plasma instability resulting in field-aligned irregularities in the ionosphere, *J. Geophys. Res.*, **68**, 6083, 1963
- Farley D. T.**, Theory of equatorial electrojet plasma waves: new developments and current status, *J. Atmos. Terr. Phys.*, **47**, 729, 1985
- Fejer J. A.**, Ionospheric instabilities and fine structure, *J. Atmos. Terr. Phys.*, **41**, 895, 1979
- Fejer B. G. and M. C. Kelley**, Ionospheric irregularities, *Rev. of Geophys. Sp. Phys.*, **18**, 401, 1980
- Fejer B. G., J. Providakes and D. T. Farley**, Theory of plasma waves in the auroral E region, *J. Geophys. Res.*, **89**, 7487, 1984a
- Fejer B. G., R. W. Reid, D. T. Farley, W. E. Swartz and M. C. Kelley**, Ion cyclotron waves as a possible source of resonant auroral radar echoes, *J. Geophys. Res.*, **89**, 187, 1984b
- Fejer B. G.**, Small scale plasma irregularities in the auroral ionosphere, *Proceedings of the 1982-1984 MIT Symposia*, **5**, 73, 1985

- Fejer B. G., J. F. Providakes, D. T. Farley and W. E. Swartz**, Auroral E-region plasma waves and elevated electron temperatures, *J. Geophys. Res.*, **91**, 13583, 1986
- Fejer B. G. and J. F. Providakes**, High latitude E-region irregularities: new results, *Phys. Scripta*, **T18**, 167, 1987
- Fialer P. A.**, Field-aligned scattering from a heated region of the ionosphere – Observations at HF and VHF, *Radio Science*, **9**, 923, 1974
- Gordon W. E. and H. C. Carlson jr.**, Arecibo heating experiments, *Radio Science*, **9**, 1041, 1974
- Greenwald R. A., W. L. Ecklund and B. B. Balsley**, Auroral currents, irregularities and luminosity, *J. Geophys. Res.*, **78**, 8193, 1973
- Greenwald R. A., W. L. Ecklund and B. B. Balsley**, Radar observations of auroral electrojet currents, *J. Geophys. Res.*, **80**, 3635, 1975
- Greenwald R. A., W. Weiss, E. Nielsen and N. R. Thomson**, STARE: A new radar auroral backscatter experiment in northern Scandinavia, *Radio Science*, **13**, 1021, 1978
- Greenwald R. A., K. B. Baker, R. A. Hutchins and C. Hanuise**, An HF-phased array radar for studying small-scale structure in the high-latitude ionosphere, *Radio Science*, **20**, 63, 1985
- Greenwald R. A., K. B. Baker, J. R. Dudeney, M. Pinnock, T. B. Jones, E. C. Thomas, J.-P. Villain, J.-C. Cerisier, C. Senior, C. Hanuise, R. D. Hunsucker, G. Sofko, J. Koehler, E. Nielsen, R. Pellinen, A. D. Walker, N. Sato and H. Yamagishi**, DARN/SuperDARN: A global view of the dynamics of high-latitude convection, *Space Science Reviews*, **71**, 761, 1995
- Grésillon D. and B. Cabrit**, Collective scattering and fluid velocity fluctuations, *A variety of plasmas (Proceed. of the Internat. Conf. on Plasma Physics, New Delhi)*, 1991
- Grésillon D., B. Cabrit, J.-P. Villain, C. Hanuise, A. Truc, C. Laviron, P. Hennequin, F. Gervais, A. Quemeneur, X. Garbet, J. Payan and P. Devynck**, Collective scattering of electromagnetic waves and cross-B plasma diffusion, *Plasma Phys. Contr. Fusion*, **34**, 1985, 1992
- Gurevich A. V.**, *Nonlinear Phenomena in the Ionosphere*, Springer, 1978
- Gurevich A. V. and A. N. Karashtin**, Small-scale thermal diffusion instability in the lower ionosphere, *Geomagn. Aeron.*, **24**, 733, 1984
- Gurevich A. V., A. V. Lukyanov and K. P. Zybin**, Anomalous absorption of powerful radio waves on the striations developed during ionospheric modification, *Phys. Lett. A*, **211**, 363, 1996

References

- Hagfors T.**, Electromagnetic wave propagation in a field-aligned-striated cold magnetoplasma with application to the ionosphere, *J. Atmos. Terr. Phys.*, **46**, 211, 1984
- Haldoupis C. and G. J. Sofko**, VHF double-peak spectra in the morning sector of radio aurora, *Planet. Space Sci.*, **27**, 233, 1979
- Haldoupis C., E. Nielsen and C. K. Goertz**, Experimental evidence on the dependence of 140 MHz auroral backscatter characteristics on ionospheric conductivity, *J. Geophys. Res.*, **87**, 7666, 1982
- Haldoupis C., G. J. Sofko, J. A. Koehler, P. Prikryl and A. G. McNamara**, High resolution Doppler spectrum measurements of 3-m auroral irregularities at large magnetic aspect angles, *Phys. Scripta*, **35**, 910, 1987
- Haldoupis C.**, A review on radio studies of auroral E-region ionospheric irregularities, *Ann. Geophys.*, **7**, 239, 1989
- Hall G. E., J. W. MacDougall, D. R. Moorcroft, J.-P. St.-Maurice, A. H. Manson and C. E. Meek**, Super Dual Auroral Radar Network observations of meteor echoes, *J. Geophys. Res.*, **102**, 14603, 1997
- Hanuse C.**, High latitude ionospheric irregularities: A review of recent results, *Radio Science*, **18**, 1093, 1983
- Hanuse C., J. P. Villain, D. Grésillon, B. Cabrit, R. A. Greenwald and K. B. Baker**, Interpretation of HF radar ionospheric Doppler spectra by collective wave scattering theory, *Ann. Geophys.*, **11**, 29, 1993
- Hedberg Å., H. Derblom, B. Thidé, H. Kopka and P. Stubbe**, Observations of HF backscatter associated with the heating experiment at Tromsø, *Radio Science*, **18**, 840, 1983
- Hedberg Å., H. Derblom, G. Wannberg, B. Thidé, H. Kopka and P. Stubbe**, Measurements of HF backscatter cross sections for striations created by ionospheric heating at different power levels, *Radio Science*, **21**, 117, 1986
- Henriksen K., W. Stoffregen, B. Lybekk and Å. Steen**, Photometer and spectrometer search of the oxygen green and red lines during artificial ionospheric heating in the auroral zone, *Ann. Geophys.*, **2**, 73, 1984
- Honary F., A. J. Stocker, T. R. Robinson, T. B. Jones, N. M. Wade, P. Stubbe and H. Kopka**, EISCAT observations of electron temperature oscillations due to the action of high power HF radio waves, *J. Atmos. Terr. Phys.*, **55**, 1433, 1993
- Honary F., A. J. Stocker, T. R. Robinson, T. B. Jones and P. Stubbe**, Ionospheric plasma response to HF radio waves operating at frequencies close to the third harmonic of the electron gyrofrequency, *J. Geophys. Res.*, **100**, 21489, 1995

- Huang J. and S. P. Kuo**, Cyclotron harmonic effect on the thermal oscillating two-stream instability in the high-latitude ionosphere, *J. Geophys. Res.*, **99**, 2173, 1994
- Hysell D. L., M. C. Kelley, Y. M. Yampolski, V. S. Beley, A. V. Koloskov, P. V. Ponomarenko and O. F. Tyrnov**, HF radar observations of decaying artificial field-aligned irregularities, *J. Geophys. Res.*, **101**, 26981, 1996
- Inhester B., A. C. Das and J. A. Fejer**, Generation of small-scale field-aligned irregularities in ionospheric heating experiments, *J. Geophys. Res.*, **86**, 9101, 1981
- Inhester B.**, Thermal modulation of the plasma density in ionospheric heating experiments, *J. Atmos. Terr. Phys.*, **44**, 1049, 1982
- Isham B., C. La Hoz, H. Kohl, T. Hagfors, T. B. Leyser and M. T. Rietveld**, Recent EISCAT heating results using chirped ISR, *J. Atmos. Terr. Phys.*, **58**, 369, 1996
- Jones T. B., T. Robinson, P. Stubbe and H. Kopka**, A hysteresis effect in the generation of field-aligned irregularities by a high-power radio wave, *Radio Science*, **18**, 835, 1983
- Kelley M. C.**, *The Earth's Ionosphere*, Academic Press, 1989
- Kintner P. M.**, Observations of velocity shear driven plasma turbulence, *J. Geophys. Res.*, **81**, 5114, 1976
- Kissack R. S., J.-P. St.-Maurice and D. R. Moorcroft**, The effect of electron-neutral energy exchange on the fluid Farley-Buneman instability threshold, *J. Geophys. Res.*, **102**, 24091, 1997
- Kivelson M. G. and C. T. Russell**, *Introduction to Space Physics*, Cambridge University Press, 1995
- Kleva R. G. and J. F. Drake**, Stochastic $E \times B$ particle transport, *Phys. Fluids*, **27**, 1686, 1984
- Kohl H., H. Kopka, P. Stubbe and M. T. Rietveld**, Introduction to ionospheric heating experiments at Tromsø – II. Scientific problems, **55**, 601, 1993
- Landau L. and E. Lifchitz**, *Electrodynamics of continuous media*, Mir, 1969
- Lundborg B. and B. Thidé**, Standing wave pattern of HF radio waves in the ionospheric reflection region 2. Applications, *Radio Science*, **21**, 486, 1986
- Meltz G., L. H. Holway jr. and N. M. Tomljanovich**, Ionospheric heating by powerful radio waves, *Radio Science*, **9**, 1049, 1974
- Milan S. E., T. K. Yeoman, M. Lester, E. C. Thomas and T. B. Jones**, Initial backscatter occurrence statistics from the CUTLASS HF radars, *Ann. Geophys.*, **15**, 703, 1997a

- Milan S. E., T. B. Jones, T. R. Robinson, E. C. Thomas and T. K. Yeoman**, Interferometric evidence for the observation of ground backscatter originating behind the CUTLASS coherent HF radars, *Ann. Geophys.*, **15**, 29, 1997b
- Milan S. E. and M. Lester**, A classification of spectral populations observed in HF radar backscatter from the E-region auroral electrojets, *Ann. Geophys.*, **19**, 189, 2001
- Milan S. E., M. Lester, N. Sato and H. Takizawa**, On the altitude dependence of the spectral characteristics of decametre-wavelength E region backscatter and the relationship with optical auroral forms, *Ann. Geophys.*, **19**, 205, 2001
- Minkoff J., P. Kugelmann and I. Weissman**, Radio frequency scattering from a heated ionospheric volume, 1, VHF/UHF field-aligned and plasma-line backscatter measurements, *Radio Science*, **9**, 941, 1974
- Mjølhus E.**, On linear conversion in a magnetised plasma, *Radio Science*, **25**, 1321, 1990
- Mjølhus E.**, On the small scale striation effect in the ionospheric radio modification experiments near harmonics of the electron gyro frequency, *J. Atmos. Terr. Phys.*, **55**, 907, 1993
- Monin A. S. and A. M. Yaglom**, *Statistical Fluid Mechanics*, MIT Press, 1971
- Moorcroft D. R.**, Dependence of radio aurora at 398 MHz on electron density and electric field, *Can. J. Phys.*, **57**, 687, 1979
- Nielsen E., M. Bruns, I. Pardowitz, H. Perplies, L. Bemannann, P. Janhunen and A. Huuskonen**, STARE: Observations of a field-aligned line current, *Geophys. Res. Lett.*, **26**, 21, 1999
- Noble S. T. and F. T. Djuth**, Simultaneous measurements of HF-enhanced plasma waves and artificial field-aligned irregularities at Arecibo, *J. Geophys. Res.*, **95**, 15195, 1990
- Ogawa T., H. Mori, S. Miyazaki and H. Yamagishi**, Electrostatic plasma instabilities in the highly active aurora observed by sounding rocket S-310JA-7, *Mem. Natl. Inst. Polar Res. Jpn.*, **18**, 312, 1981
- Perkins F. W.**, A theoretical model for short-scale field-aligned plasma density striations, *Radio Science*, **9**, 1065, 1974
- Prikryl P., J. A. Koehler, G. J. Sofko, D. J. McEwen and D. Steele**, Ionospheric ion cyclotron wave generation inferred from coordinated Doppler radar, optical and magnetic observations, *J. Geophys. Res.*, **92**, 3315, 1987
- Provan G.**, Coherent scatter radar observations of field lines resonances and flux transfer events, PhD. Thesis, Univ. of Leicester, 1998

- Providakes J. F.**, Radar interferometer observations and theory of plasma irregularities in the auroral ionosphere, PhD. Thesis, Cornell Univ., 1985
- Providakes J. F., D. T. Farley, W. E. Swartz and D. Riggin**, Plasma irregularities associated with morning discrete auroral arcs: Radar interferometry observations and theory, *J. Geophys. Res.*, **90**, 7513, 1985
- Quemada D.**, Ondes dans les plasma, Hermann, 1968
- Rietveld M. T., H. Kohl, H. Kopka and P. Stubbe**, Introduction to ionospheric heating at Tromsø – I. Experimental overview, *J. Atmos. Terr. Phys.*, **55**, 577, 1993
- Rishbeth H. and P. J. S. Williams**, The EISCAT ionospheric radar: the system and its early results, *Q. Jl R. astr. Soc.*, **26**, 478, 1985
- Robinson T. R.**, The heating of the high latitude ionosphere by high power radio waves, *Phys. Rep.*, **179**, 79, 1989
- Robinson T. R. and F. Honary**, A resonance broadening kinetic theory of the modified two-stream instability: Implications for radar auroral backscatter experiments, *J. Geophys. Res.*, **95**, 1073, 1990
- Robinson T. R.**, The role of natural E-region plasma turbulence in the enhanced absorption of HF radio waves in the auroral ionosphere: Implications for RF heating of the auroral electrojet, *Ann. Geophys.*, **12**, 316, 1994
- Robinson T. R., F. Honary, A. J. Stocker, T. B. Jones and P. Stubbe**, First EISCAT observations of the modification of F-region electron temperatures during RF heating at harmonics of the electron gyro frequency, *J. Atmos. Terr. Phys.*, **58**, 385, 1996
- Robinson T. R., A. J. Stocker, G. E. Bond, P. Eglitis, D. M. Wright and T. B. Jones**, O- and X-mode heating effects observed simultaneously with the CUTLASS and EISCAT radars and low power HF diagnostics at Tromsø, *Ann. Geophys.*, **15**, 134, 1997
- Robinson T. R.**, The effects of small scale field aligned irregularities on E-region conductivities: Implications for electron thermal processes, *Adv. Space Res.*, **22**, 1357, 1998
- Robinson T. R., R. Strangeway, D. M. Wright, J. A. Davies, R. B. Horne, T. K. Yeoman, A. J. Stocker, M. Lester, M. T. Rietveld, I. R. Mann, C. W. Carlson and J. P. McFadden**, FAST observations of ULF waves injected into the magnetosphere by means of modulated RF heating of the auroral electrojet, *Geophys. Res. Lett.*, **27**, 3165, 2000
- Rogister A. and N. D'Angelo**, Type 2 irregularities in the equatorial electrojet, *J. Geophys. Res.*, **75**, 3879, 1970

- Rose G., B. Grandal, E. Neske, W. Ott, K. Spenner, J. Holtet, K. Måseide and J. Trøim**, Experimental results from the HERO project: in situ measurements of ionospheric modifications using sounding rockets, *J. Geophys. Res.*, **90**, 2851, 1985
- Schunck and Nagy**, Electron Temperatures in the F Region of the Ionosphere: Theory and Observation, **16**, 355, 1978
- St.-Maurice J.-P. and D. G. Torr**, Nonthermal rate coefficients in the ionosphere: The reactions of O^+ with N_2 , O_2 and NO , *J. Geophys. Res.*, **83**, 969, 1978
- St.-Maurice J.-P., P. Prikryl, D. W. Danskin, A. M. Hamza, G. J. Sofko, J. A. Koehler, A. Kustov and J. Chen**, On the origin of narrow non-ion-acoustic coherent radar spectra in the high-latitude E region, *J. Geophys. Res.*, **99**, 6447, 1994
- St.-Maurice J.-P. and R. S. Kissack**, The role played by thermal feedback in heated Farley-Buneman waves at high latitudes, *Ann. Geophys.*, **18**, 532, 2000
- Stubbe P. and H. Kopka**, Ionospheric modification experiments in northern Scandinavia – a description of the heating project, Report MPAE-W-02-79-04, Max-Planck-Institut für Aeronomie, F. R. G., 1979
- Stubbe P., H. Kopka, T. B. Jones and T. R. Robinson**, Wide band attenuation of radio waves caused by powerful HF waves: saturation and dependence on ionospheric variability, *J. Geophys. Res.*, **87**, 1551, 1982
- Stubbe P.**, Theory of electrostatic waves in an E region Plasma 1. General Formulation, *J. Geophys. Res.*, **94**, 5303, 1989
- Stubbe P., H. Kohl and M. T. Rietveld**, Langmuir turbulence and ionospheric modification, *J. Geophys. Res.*, **97**, 6285, 1992
- Stubbe P.**, Review of ionospheric modification experiments at Tromsø, *J. Atmos. Terr. Phys.*, **58**, 349, 1996
- Sudan R. N., J. Akinrimisi and D. T. Farley**, Generation of small-scale irregularities in the equatorial electrojet, *J. Geophys. Res.*, **78**, 240, 1973
- Sudan R. N.**, Unified theory of Type I and Type II irregularities in the equatorial electrojet, *J. Geophys. Res.*, **88**, 4853, 1983
- Thidé B., H. Kopka and P. Stubbe**, Observations of stimulated scattering of a strong high-frequency wave in the ionosphere, *Phys. Rev. Lett.*, **49**, 1561, 1982
- Thome G. D. and D. W. Blood**, First observations of RF backscatter from field-aligned irregularities produced by ionospheric heating, *Radio Science*, **9**, 917, 1974
- Thornhill S. G. and D. ter Haar**, Langmuir turbulence and modulational instability, *Phys. Rep.*, **43**, 43, 1978

- Tsunoda R. T. and R. I. Presnell**, On the threshold electric field associated with the 398 MHz diffuse radar aurora, *J. Geophys. Res.*, **81**, 88, 1976
- Tsunoda R. T., J. K. Olesen and P. Stauning**, Radar evidence for a new low-frequency crossed-field plasma instability in the polar mesopause region: A case study, *Geophys. Res. Lett.*, **24**, 1215, 1997
- Utlaut W. F. and E. J. Violette**, A summary of vertical incidence radio observations of ionospheric modification, *Radio Science*, **9**, 895, 1974
- Vas'kov V. V. and A. V. Gurevich**, Non-linear resonant instability of a plasma in the field of an ordinary electromagnetic wave, *Sov. Phys. JETP*, **42**, 91, 1976
- Vas'kov V. V. and A. V. Gurevich**, Resonance instability of small-scale plasma perturbations, *Sov. Phys. JETP*, **46**, 487, 1978
- Villain J.-P., R. A. Greenwald, K. B. Baker and J. M. Ruohoniemi**, HF radar observations of E region plasma irregularities produced by oblique electron scattering, *J. Geophys. Res.*, **92**, 12327, 1987
- Villain J.-P., R. André, C. Hanuise and D. Grésillon**, Observation of the high latitude ionosphere by HF radars: Interpretation in terms of collective wave scattering and characterisation of turbulence, *J. Atmos. Terr. Phys.*, **58**, 943, 1996
- Villante U.**, Some remarks on the structure of the distant neutral sheet, *Planet. Space. Sci.*, **23**, 723, 1975
- Wright D. M., J. A. Davies, T. R. Robinson, P. J. Chapman, T. K. Yeoman, E. C. Thomas, M. Lester, S. W. H. Cowley, A. J. Stocker, R. B. Horne and F. Honary**, Space plasma exploration by active radar (SPEAR): an overview of a future radar facility, *Ann. Geophys.*, **18**, 1248, 2000
- Yampolski Y. M., V. S. Beley, S. B. Kascheev, A. V. Koloskov, V. G. Somov, D. L. Hysell, B. Isham and M. C. Kelley**, Bistatic HF radar diagnostics induced field-aligned irregularities, *J. Geophys. Res.*, **102**, 7461, 1997